2021

Atomistic Simulation of Hydrogen Embrittlement of Grain Boundaries in Metals

Jiaqing Li
University of Wollongong

UNIVERSITY OF WOLLONGONG AUSTRALIA

Atomistic Simulation of Hydrogen Embrittlement of Grain Boundaries in Metals

Jiaqing Li

Supervisors:
Prof. Cheng Lu
Prof. Kiet Tieu

This thesis is presented as part of the requirement for the conferral of the degree:

Doctor of Philosophy

University of Wollongong

School of Mechanical, Materials, Mechatronic and Biomedical Engineering

January 2021

Table of Contents

Table of Contents III
Acknowledgments VI
Abstract VII
List of Publications IX
List of Tables and Illustrations XI
List of Figures and Illustrations XII
Chapter 1 Introduction 1
1.1 Research background 1
1.2 Research motivations and objectives 3
1.3 Structure of the thesis 6
Chapter 2 Literature review 7
2.1 Experimental techniques 8
2.2.1 Macro-scale experiments 8
2.2.2 Micro/nano-scale experiments 13
2.2 Theoretical modelling 18
2.2.1 Hydride formation and cleavage 18
2.2.2 Hydrogen-enhanced decohesion (HEDE) 18
2.2.3 Hydrogen-enhanced localised plasticity (HELP) 19
2.2.4 Adsorption-induced dislocation emission (AIDE) 20
2.2.5 Defactant theory 21
2.3 Simulations 22
2.3.1 Hydrogen trapping, diffusion and segregation 22
2.3.2 Hydrogen interaction with dislocations 29
2.3.3 Hydrogen interaction with crack tips/GBs 33
2.4 Summary 46
Chapter 3 Fundamentals of atomistic simulations 48
3.1 MS and MD simulations 48
3.2 Potential selection 49
3.3 Ensemble 51
3.4 Boundary conditions 51
3.5 Visualisation Methods 52
3.5.1 Potential energy 53
3.5.2 Local stress 53

3.5.3 Centrosymmetric parameter 54
3.5.4 Common neighbour analysis 54
3.6 Dislocation extraction algorithm 55
3.7 Summary 56
Chapter 4 Influence of hydrogen segregation on tensile deformation behaviour of grain boundaries 57
4.1 Introduction 57
4.2 Simulation methodology 57
4.3 Results and discussion 59
4.3.1 GB structure and energy 59
4.3.2 H trapping map 62
4.3.3 Tensile response and deformation mechanisms of tilt GBs 66
4.3.4 Tensile response and deformation mechanisms of twist GBs 74
4.4 Summary 83
Chapter 5 Effect of H segregation on shear-coupled motion of ⟨110⟩ grain boundaries 85
5.1 Introduction 85
5.2 Simulation methodology 85
5.3 Results 87
5.3.1 GB structure and H trapping map 87
5.3.2 Shear response and GB motion of pure GBs 89
5.3.3 Shear response and motion of GBs with H content 92
5.4 Discussion 96
5.5 Summary 98
Chapter 6 Hydrogen-modified interaction between lattice dislocations and grain boundaries 100
6.1 Introduction 100
6.2 Simulation methodology 100
6.3 Results 102
6.3.1 GB structure and H trapping map 102
6.3.2 Shear response and interaction outcomes 104
6.3.3 Atomic mechanisms for dislocation-GB interactions 106
6.3.4 Interaction of dislocation pile-ups with the GB 112
6.4 Discussion 113
6.5 Summary 117
Chapter 7 Atomistic investigation of hydrogen induced decohesion of grain boundaries 119

7.1 Introduction 119
7.2 Computational approach 119
7.3 Results 123
7.3.1 H trapping map 123
7.3.2 Computational tensile tests 125
7.3.3 GB decohesion aided by plasticity 129
7.4 Discussion 131
7.5 Summary 133
Chapter 8 Hydrogen-modified behaviour of cracks along grain boundaries 134
8.1 Introduction 134
8.2 Computational approach 134
8.3 Results 136
8.3.1 Theoretical model for embrittlement 136
8.3.2 Dislocation emission and cleavage of crack tip under monotonic loading 138
8.3.3 Dislocation emission and cleavage of crack tip under cyclic loading 143
8.4 Discussion 145
8.5 Summary 146
Chapter 9 Conclusions and recommendations for future work 148
9.1 Conclusions 148
9.2 Recommendations for future work 150
References 152

Acknowledgments

First of all, I express my deepest and sincerest thanks to my supervisors Prof. Cheng Lu and Prof. Kiet Tieu for their guidance and advice during my doctoral study. They constantly give me courage, teach me how to research, and initiate very interesting and deep discussions to keep me on the right track. I am truly honoured to have them as my supervisors.

I also would like to thank my group mates, Che Zhang and Rui Wang for making a friendly research environment. Thanks for their thoughtful and insightful suggestions on my research. I also have the opportunity to make friends and collaborate with, Yu Liu, Peiyu He, Lin Teng, Zhou Li, Hui Fang, Yao Lu, Long Wang, Chunyang Xia and Nan Jiang in the lab. We have lots of valuable memories and fruitful discussions. Also, many thanks go to Post-docs Linqing Pei, Liang Zhang and Hui Wang who dedicatedly guide and help me perform atomistic simulations.

I also appreciate the support from China Scholarship Council (CSC) and University of Wollongong (UOW) for providing scholarships. This thesis is undertaken with the assistance of resources and services from the National Computational Infrastructure (NCI), which is supported by the Australian Government.

Last but definitely the best; I express my warmest respects and gratitude to my parents Xinling Liu and Ren Li, and my sisters Mengyun Li and Mengjun Li for their emotional support and patience.

Abstract

It has been known for about a century that hydrogen contamination causes severe degradation in the mechanical properties of metals. This phenomenon is generally termed as 'hydrogen embrittlement' (HE). In this thesis, the underlying mechanisms behind HE phenomenon were elucidated on an atomic scale. The H segregation at various grain boundaries (GBs) and its influence on the structure, mechanical properties, deformation mechanisms and failure response of GBs were examined by atomistic simulations.

First, H segregation at various GBs was studied in this thesis. The results indicated that H segregation properties were very sensitive to GB structures. The effects of H atoms on the mechanical behaviour and plastic deformation of GBs were then examined. It was shown that H atoms modified the behaviour of dislocation nucleation and caused the yield stress of dislocation nucleation to increase or decrease. Different deformation mechanisms were directly responsible for this modification. In addition, H segregation increased the critical shear stress and impeded the coupled GB motion, irrespective of the GB structures. During GB migration, H-vacancy clusters cannot grow, which suggests that the coupled GB motion may help to resist H-induced intergranular embrittlement.

The role of H atoms in changing the interaction of dislocations with GBs was also investigated. Several interaction mechanisms such as dislocation transmission, nucleation and reflection were reported for different glide planes and GB structures. Segregated H atoms transformed these interaction mechanisms into ones involving dislocation absorption for most of GBs. This disordered the atomic structure of GBs and established a local stress state, which promoted the ultimate failure of GBs due to the formation of vacancies.

The decohesion of Ni GBs in the presence of H was examined by direct simulations. Computational tensile tests showed that under the equilibrium concentration of H atoms typical of embrittlement in Ni, and in conjunction with the local H diffusion process, the maximum reduction of tensile strength and fracture energy was 6.60% and 15.75% for $\Sigma5$ (210) ⟨100⟩ and $\Sigma17$ (530) ⟨100⟩ GBs, respectively. Further calculations of these cohesive parameters aided by the dislocation-GB interactions revealed that the H embrittling effect in metallic materials was largely assisted by the plasticity process.

The ability of H segregation at GBs to modify both the ductile emission and brittle

cleavage of the intergranular cracks was studied. It was found that H segregation had a limited embrittling effect on the predicted ductile cracks along the GBs, but favoured the cleavage process in intrinsically brittle directions. Furthermore, cyclic loading can promote the accumulation of H into the GB region ahead of the crack tip and overcome crack trapping, thus inducing a ductile-to-brittle transformation.

Keywords: Hydrogen embrittlement; Grain boundary; dislocations; fracture mechanics; ductile to brittle transition

List of Publications

Li J, Lu C*, Wang L, Pei L, Godbole A, Michal G. The role of hydrogen on the behavior of intergranular cracks in bicrystalline α-Fe nanowires. Nanomaterials. 2021;11:294.

Li J, Pei L, Lu C*, Godbolea A, Michala G. Hydrogen effects on the mechanical behaviour and deformation mechanisms of inclined twin boundaries. Int J Hydrogen Energy. 2021;46:16127-16140.

Li J, Lu C*, Pei L, Zhang C, Wang R. Atomistic investigation of hydrogen induced decohesion of Ni grain boundaries. Mech Mater. 2020;150:103586.

Li J, Lu C*, Pei L, Zhang C, Wang R. Hydrogen-modified interaction between lattice dislocations and grain boundaries by atomistic modelling. Int J Hydrogen Energy. 2020;45:9174-87.

Li J, Lu C*, Pei L, Zhang C, Tieu K. Influence of solute hydrogen on the interaction of screw dislocations with vicinal twin boundaries in nickel. Scripta Mater. 2019;173:115-9.

Li J, Lu C*, Pei L, Zhang C, Wang R, Tieu K. Effects of H segregation on shear-coupled motion of <110> grain boundaries in α-Fe. Int J Hydrogen Energy. 2019;44:18616-27.

Li J, Lu C*, Pei L, Zhang C, Wang R, Tieu K. Influence of hydrogen environment on dislocation nucleation and fracture response of <110> grain boundaries in nickel. Comput Mater Sci. 2019;165:40-50.

Li J, Lu C*, Pei L, Zhang C, Wang R, Tieu K. Atomistic simulations of hydrogen effects on tensile deformation behaviour of [0 0 1] twist grain boundaries in nickel. Comput Mater Sci. 2019;159:12-23.

Li J, Zhang Z, Xu H, Feng Z. Dynamic characteristics of the vibratory roller test-bed vibration isolation system: Simulation and experiment, J Terramech. 2014;56:139-156.

Wang L, Tieu K*, Hai G, **Li J,** Zhu H, Sang T, Yang J. Na_2CO_3 and graphene nanocomposites toward efficient lubrication, Carbon. 2021;177:138-150.

Zhang C, Lu C*, Michal G, **Li J,** Wang R. Strong strain hardening in graphene/nanotwinned metal composites revealed by molecular dynamics simulations, Int. J. Mech. Sci. 2021;201:106460.

Zhang C, Lu C*, Pei L, **Li J,** Wang R. The structural rearrangement with secondary reinforcement in graphene/nanotwinned copper nanocomposites: A molecular dynamics study. Compos B Eng. 2020;182:107610.

Zhang C, Lu C*, Pei L, **Li J,** Wang R, Tieu K. The negative Poisson's ratio and strengthening mechanism of nanolayered graphene/Cu composites. Carbon. 2019;143: 125-137.

Zhang C, Lu C*, Pei L, **Li J,** Wang R, Tieu K. Molecular Dynamics Simulation of the Negative Poisson's Ratio in Graphene/Cu Nanolayered Composites: Implications for Scaffold Design and Telecommunication Cables. ACS Appl Nano Mater. 2019;3:496-505.

Zhang C, Lu C*, Pei L, **Li J,** Wang R. The wrinkling and buckling of graphene induced by nanotwinned copper matrix: A molecular dynamics study. Nano Mater Sci. 2021;3:95-103.

Pei L, Lu C*, Tang Q, Zhang Y, **Li J,** Zhang C, Zhao X, Tieu K. Effect of Temperature on Deformation and Fracture Behaviour of Nanostructured Polycrystalline Ni Under Tensile Hydrostatic Stress by Molecular Dynamics Simulation. J Nanosci Nanotechno.2019;19:2723-2731.

List of Tables and Illustrations

Table 2.1. Yield strength (YS) and work hardening (WH) values under different conditions. Work hardening rates are calculated at 6% and 8% strain……..13

Table 2.2. Work of separation for (a) pure GBs,W_0, (b) fast fracture at constant H concentration, W_Γ, and (c) slow fracture at constant chemical potential, W_μ……... 29

Table 2.3. Theoretical and simulated cleavage and emission stress intensities for all GBs [29]. ……44

Table 3.1. The parameters used to determine the embedded atom potential [160]….50

Table 3.2. Original and modified parameters for the Ni–H EAM potential based on the formulation of (Angelo et al.,[160]; Baskes et al.,[161]) [29]…….50

Table 4.1. Model parameters for twelve GBs after energy minimization……...60

Table 5.1. Model parameters for four GBs after energy minimization……...86

Table 6.1. Characterization of the GBs, including tilt angle, Σ value, model size and GB energies……102

Table 6.2. Summary of the interaction outcomes. The following abbreviations are used. D: Dislocation dissociation, N: Dislocation nucleation, T: Dislocation transmission, R: Dislocation reflection, A: Dislocation absorption……..106

Table 7.1. Characterization of the GBs, including Σ value, tilt angle, numbers of atoms and GB energies……..120

Table 7.2. Theoretical cohesive strength and fracture energy of GBs. The minimum values of cohesive properties for each GB are highlighted in bold. P1, P2 and P3 are the cleavage planes…….128

Table 7.3. Theoretical cohesive strength and fracture energy of bulk Ni……..129

Table 7.4. Theoretical cohesive strength of various GBs with different configurations. ……131

List of Figures and Illustrations

Fig. 2.1. Historical summary of approaches in HE literature [38]…….7
Fig. 2.2. (a) The variation in yield stress due to H absorption and desorption. (b) Hydrogen-induced hardening behavior explained by the relationship between the ratio of the hydrogen absorption depth to the plastic deformation depth and the ratio of the residual indentation depth before hydrogen charging to that after hydrogen charging [85]…….9
Fig. 2.3. Effect of hydrogenation time on (a) tensile strength, (b) yield strength, (c) breaking strength and (d) elongation of steel [86]……10
Fig. 2.4. The sequence of elemental processes that supply damaging H to the crack tip fracture process zone during either H environment assisted cracking for gaseous hydrogen, water vapour or an electrolyte, or internal hydrogen assisted cracking for a H precharged microstructure [87]…….11
Fig. 2.5. Stress-strain curves for single crystal, 1-mm grain size, and 35-μm and grain size Ni-201 at (a) 293 K and (b) 77 K, in the presence and absence of H…….13
Fig. 2.6. Time-resolved images of the dislocation motion in the presence of H [97]..15
Fig. 2.7. Generation of dislocation sources in Fe caused by H gas. Arrowheads indicate the sources, and arrows represent the dislocation motion direction [97]……...15
Fig. 2.8. H effects on the separation distance between dislocations. (a) Composite image of a dislocation pile-up in vaccum (black lines) and in the H environment with 95 torr (white lines). (b) Dislocation separation distance under varying H gas pressure [98].……...……..…15
Fig. 2.9. Load-depth curves for Ni at cathodic (a) and anodic (b) potentials [104]….16
Fig. 2.10. (a) The crack opening displacement of the intergranular crack observed in the H-charged polycrystalline Ni. (b) The fracture surface of the intergranular crack [106]…….16
Fig. 2.11. H-induced intergranular failure of Ni. (a) SEM micrograph of fracture surface. (b) TEM micrograph of microstructure immediately underneath the fracture surface. (c) TEM micrograph of microstructure away from the fracture surface [108, 109]……...17
Fig. 2.12. Hydride formation and cleavage mechanism [39]……18
Fig. 2.13. Decohesion process caused by weakening the inter-atomic bonds as a result

of (i) H in the lattice; (ii) adsorbed H; (iii) H at particle-matrix interfaces [39]……..19
Fig. 2.14. Illustration of the HELP mechanism associated with localised plasticity and microvoid coalescence in the region of high H concentrations [39]…….20
Fig. 2.15. Schematic diagram illustrating the AIDE mechanism involving crack growth and coalescence with voids formed in the plastic zone ahead of cracks [39]……21
Fig. 2.16. H atom diffusion path at the vicinity of (a) Σ5 twist GB, (b) Σ5 tilt GB and (c) twist+ tilt GB structure [117]……..23
Fig. 2.17. The calculated minimum energy paths for H atom diffusion (a) perpendicular to the plane of a twist GB, (b) parallel to the plane of the tilt GB and (c) the energy of sites and accumulated time at the twist + tilt GB as functions of the Z-coordinate of the H atom [117]…….23
Fig. 2.18. (a) Side view of Σ5 (310)/[001] tilt W GB. (b) Top view of the N atom layer of the W GB supercell [118]……..……...24
Fig. 2.19. Segregation energies as a function of occupation sites per H atom in a W GB for the interstitial, substitutional and vacancy cases [118]……24
Fig. 2.20. Hydrogen solution energies as a function of the distance from the grain boundary interface for investigated GBs in Fe [119]…….25
Fig. 2.21. Diffusion pathway for an H interstitial within the interface region of the investigated GBs in Fe [119]…….25
Fig. 2.22. Valence electron density plots for the Σ5 GB [120].……27
Fig. 2.23. Local atomic configuration for the minimum energy paths for H migration [120]……...……..27
Fig. 2.24. Potential energy surface for H along the Σ5 GB plane obtained by interpolation of several NEB calculations [120]……...27
Fig. 2.25. Schematic illustration of polyhedron in representative Σ5 (130) [100] GB and bulk lattice [121]……...28
Fig. 2.26. Relationship between hydrogen-trap energy and applied simple shear [128]…….31
Fig. 2.27. Relationship between hydrogen-trap energy and applied hydrogen static stress [128]……...…….31
Fig. 2.28. (a) MD simulation model of dislocation pile-ups in α-Fe. (b) Equilibrium separation distance between dislocations with various H coverage [36]……...32
Fig. 2.29. (a) Image of dislocation nucleation during nanoindentation without and with H. (b) The indentation load as a function of indentation depth in pure Ni and Ni-H [110].

……..32
Fig. 2.30. Configurations of (a) H-free and (b) H-charged edge dislocation in Fe under applied shear stress [131]……..33
Fig. 2.31. Models used to calculate the fracture energy (2γ) as a function of H coverage (Θ_H) from DFT: (a) Lu et al.'s model [132]; (b) Van der Ven and Ceder's model [133,134]……..35
Fig. 2.32. The Born-Haber cycle used to calculate the ideal fracture energy [$2\gamma(\Theta_H)$] along a certain plane of a single crystal at a hydrogen atom coverage Θ_H. ΔH_s: solution enthalpy of H2 in the bulk metal. $\gamma(0)$: surface energy of the pure metal without hydrogen. E_{ad}: dissociative adsorption energy of H_2 on metal surfaces [135]……..35
Fig. 2.33. Surface or fracture energy γ versus H concentration c for {1 0 0}, {1 1 0} and {1 1 1} surfaces, as calculated using the methods of Van der Ven et al and Jiang et al [26]……37
Fig. 2.34. GSF energy versus slip displacement δ on the {1 1 1} <1 1 2> slip system, for various H concentrations c. Unstable and stable stacking fault points are indicated by filled circles and filled triangles, respectively. a_0 is the equilibrium lattice parameter for Ni [26]……37
Fig. 2.35. Critical stress intensity factors K_I^c and K_I^e for brittle cleavage and dislocation emission, respectively, for various cleavage and slip planes, as a function of hydrogen concentration on the relevant plane. (a) Cleavage on plane {1 0 0} and (b) Emission in orientation (1 1 1)[1 1 2] [26]……38
Fig. 2.36. Example of evolution of the nanohydride phase around a geometry I crack tip with increasing load (a)–(d) and (e) configuration at 1.96 MPa pm after loading to K_I = 2.06 MPa pm, where cleavage through the nanohydride occurs. (f) Schematic of simple geometry for characterizing the size L of nanohydrides [28]…….40
Fig. 2.37. Example of evolution of the nanohydride phase around a geometry IV crack tip at with increasing load (a)–(d) and (e) configuration at 1.90 MPa pm after loading to K_I = 1.95 MPa pm, where cleavage through the nanohydride occurs [28]……40
Fig. 2.38. The geometry of a crack, where the orange circular region is the plastic zone, and the blue region is a circle region where the radius is equal to r_P. The red annulus region is to offer and deplete the hydrogen atoms [145]……41
Fig. 2.39. Snapshots of crack propagation behavior for the crystal orientation (B) at 400 K. (a) $x^0 = 1.0 \times 10^{-4}$ (b) $x^0 = 3.0 \times 10^{-4}$ (c)$x^0 = 0$ [127]……...42

Fig. 2.40. Snapshots illustrating the preferred locations for hydrogen segregation [152]…….45
Fig. 2.41. Dislocation structures for samples without GB H (left) and 3.2 H/nm^2 (right) [153]…….46
Fig. 2.42. Crack initiation and growth as a function of applied strain for various levels of H coverage at the GB [153]……..46
Fig. 3.1 (a) Two-dimensional periodic boundary condition where the central configuration is surrounded by its copies. (b) A cross section of polycrystal with periodic boundary condition…….52
Fig. 3.2. Four different methods of visualization of grain boundary and dislocation segment within a nanocrystalline environment. Atoms are shaded according to (a) potential energy, (b) local stress, (c) centrosymmetric parameter and (d) common neighbour analysis (CNA)……53
Fig. 3.2. Burgers circuit method to detect and identify a dislocation. A closed circuit around the dislocation is translated from (a) the dislocated crystal to (b) the perfect reference crystal. The closure failure is called the Burgers vector of the dislocation…56
Fig. 4.1. Schematic diagram of a bicrystal model with [11$\bar{0}$] tilt GB……..58
Fig. 4.2. The equilibrium [1$\bar{1}$0] GB structures with SUs (a) Σ11 (11-3) = 50.48°, (b) Σ153 (44-11) = 54.43°, (c) Σ57 (44-5) = 97.05°, (d) Σ3 (11-1) = 109.47°, (e) Σ171 (1111-10) = 114.53°, (f) Σ9 (22-1) = 141.06°, (g) Σ9 (11-4) = 38.94°, (h) Σ3 (11-2) = 70.53°, (i) Σ17 (22-3) = 86.63°, (j) Σ11 (33-2) = 129.52°, (k) Σ19 (33-1) = 153.48°, and (l) Σ73 (66-1) = 166.56°. The structures are shown along the [1$\bar{1}$0] tilt axis, where atoms are coloured according to their centro-symmetry parameter….....62
Fig. 4.3. H segregation energy maps for typical GBs, all cells are shown along the [1$\bar{1}$0] tilt axis. Larger spheres represent Ni atoms (green), and smaller ones indicate possible H trapping sites…….63
Fig. 4.4. Distribution of segregation energies as a function of distance from the GB plane. Atoms in the inset of (b) are coloured by the hydrostatic stress value……65
Fig. 4.5. Summary of segregation energy maps for 12 types of GBs. (a) GB energy and H segregation energy, with squares denoting GB energy, solid circles denoting lowest H segregation energy, and hollow circles denoting highest H segregation energy. (b) Maximum excess H concentration (triangles) and excess volume (pentagons)……66
Fig. 4.6. The stress-strain curves for typical GBs with different excess H concentrations.

The inserted figures show the dependency of the yield stress on H content…….68
Fig. 4.7. Dislocation activities and atomic configurations for Σ11 $(1\,1\,\bar{3})$ GB with various excess H concentrations during tensile deformation process: (a, c-e) without H, (b, f-g) with H of $C_H = 0.09$ Å^{-2}. All figures are coloured by CNA, where atoms with a perfect fcc structure are blue, the red atoms organize the GB plane and the dislocation core, the continuous light blue atoms represent the stacking fault, and H atoms are assigned in yellow. Three-dimensional polyhedrons shown in (f) and (g) include CTP (green) and OCT(magenta)……..70
Fig. 4.8. Dislocation activities and atomic configurations for Σ3 $(1\,1\,\bar{1})$ GB with various excess H concentrations during tensile deformation process: (a) and (b) without H, (c) and (d) with H of $C_H = 0.03$ Å^{-2}. All figures are coloured by CSP….....71
Fig. 4.9. Dislocation activities and atomic configurations for Σ9 $(2\,2\,\bar{1})$ GB with various excess H concentrations during tensile deformation: (a-e) without H and (f-j) with H of $C_H = 0.21$ Å^{-2}. All figures are coloured by CNA, the same as described in Fig. 2.7….....72
Fig. 4.10. Yield stress and the change of the energy of H segregation vs. excess H concentration….....74
Fig. 4.11. Stress-strain curves of bicrystal models with different bulk H concentrations: (a) Σ145 TGB, (b) Σ65 TGB and (c) Σ5 TGB….....75
Fig. 4.12. Yield stress vs. bulk H concentration for all models….....75
Fig. 4.13. Dislocation activities and atomic configurations for Σ145 (θ= 6.73°) TGB with various bulk H concentrations during tensile deformation process: (a)-(e) without H, and (f)-(h) with H of $C_{bulk} = 3.0 \times 10^{-5}$. All images are coloured by DXA. The blue lines are the perfect dislocations, the green lines represent the Shockley dislocations, the pink lines are the stair-rod dislocaitons, and the red lines are other types of dislocaitons. Stacking-fault atoms are shown in red, and H atoms are assigned in pink….....77
Fig. 4.14. Dislocation activities and atomic configurations for Σ65 (θ= 14.25°) TGB with various bulk H concentrations during tensile deformation process: (a-e) without H and (f-j) with H of $C_{bulk} = 3.0 \times 10^{-5}$. All images are coloured by DXA, the same as described in Fig. 2.13, except (e) and (j) coloured by the hydrostatic stress value…….81
Fig. 4.15. Dislocation activities and atomic configurations for Σ5 (θ= 36.87°) TGB with various bulk H concentrations during tensile deformation process: (a)-(c) without H,

(d)-(f) with H of $C_{bulk} = 6.0 \times 10^{-4}$, and (g)-(i) with H of $C_{bulk} = 3.0 \times 10^{-3}$. The insertions of (d) and (g) are coloured by the CSP value. All other images are coloured by CNA, the same as described in Fig. 2.7, and H atoms are assigned in green…….83

Fig. 5.1. Schematic diagram of a bicrystal model rotated around the $[1\bar{1}0]$ axis…....86

Fig. 5.2. The equilibrium $[1\bar{1}0]$ GB structures with SUs (a) Σ19 (11-6) = 26.53°, (b) Σ3 (11-2) = 70.53°, (c) Σ3 (11-1) = 109.47° and (d) Σ9 (22-1) = 141.06°. The structures are shown along the $[1\bar{1}0]$ tilt axis, and atoms are coloured according to their centro-symmetry parameters……87

Fig. 5.3. H segregation energy maps for four GBs, and all cells are shown along the $[1\bar{1}0]$ tilt axis. Larger spheres represent Fe atoms (green), and smaller ones indicate possible H trapping sites……...88

Fig. 5.4. Distribution of segregation energies as a function of distance from the GB…89

Fig. 5.5. Shear stress-time and GB displacement-time curves for pure GBs at 10K…90

Fig. 5.6. Dislocation mechanisms of $[1\bar{1}0]$ GBs in bcc α-Fe with ⟨100⟩ and ⟨111⟩ coupling shear modes….....91

Fig. 5.7. (a) shear stress-time and (b) GB displacement-time curves for Σ19 $(1\ 1\ \bar{6})$ GB under various H concentrations. (c) The critical shear stress vs. H concentration for Σ19 $(1\ 1\ \bar{6})$ GB. Σ9 $(2\ 2\ \bar{1})$ GB has the same descriptions as presented in (d)-(f)……93

Fig. 5.8. Dislocation activities and atomic configurations for Σ19 $(1\ 1\ \bar{6})$ GB: (a) without H and (b) with H of $C_H = 1.0 \times 10^{-3}$. (c) and (d) are atomic structures for Σ9 $(2\ 2\ \bar{1})$ GB without H and with H of $C_H = 1.0 \times 10^{-3}$, respectively. (e) and (f) are atomic details of Σ19 $(1\ 1\ \bar{6})$ GB and Σ9 $(2\ 2\ \bar{1})$ GB, respectively, at $C_H = 6.0 \times 10^{-3}$. Atoms are coloured by CNA, where atoms with a perfect bcc structure are dark yellow, green atoms organize the GB plane and the dislocation core, and H atoms are assigned in pink. Different types of dislocations are identified by DXA in Ovito….....95

Fig. 5.9. The evolution of vacancy concentration with simulation time for (a) Σ19 $(1\ 1\ \bar{6})$ GB and (b) Σ9 $(2\ 2\ \bar{1})$ GB under various H-charged concentrations…….98

Fig. 5.10. MD simulation snapshots of atomic configurations of Fe bicrystals containing (a) and (b) Σ19 $(1\ 1\ \bar{6})$ GB, (c) and (d) Σ9 $(2\ 2\ \bar{1})$ GB with different simulation time at $C_H = 1.0 \times 10^{-3}$. Atoms are coloured by CNA, the same as described in Fig. 3.8….....98

Fig. 6.1. Model box of Σ57 (4 4 5) GB for simulating the interaction between a screw dislocation and GBs. All images are coloured by the CNA, the same as described in Fig.

2.7….....101
Fig. 6.2. Atomic images of the equilibrium GB structures with SUs. The structures are viewed along the $[1\bar{1}0]$ tilt axis. Atoms on consecutive {110} planes are shown as blue and red. Several incoming glide planes are marked by solid lines and labelled as 1–3……..103
Fig. 6.3. H segregation energy maps for six typical GBs, all cells are shown along the $[1\bar{1}0]$ tilt axis. Larger spheres represent Ni atoms (green), and smaller ones indicate possible H trapping sites….....104
Fig. 6.4. (a) Shear stress-strain curves during the interaction between a screw dislocation and Σ9 (2 2 1) GB with different slip planes and H concentrations. P1, P2 and P3 are slip planes, and θ_{bulk} is H concentration. (b) Snapshots of atomic configuration for each stage of P2, θ_{bulk}= 0 case in (a)……105
Fig. 6.5. Interaction of a screw dislocation with Σ3 twin boundary: (a) θ_{bulk}= 0 and (b) θ_{bulk}= 0.001. H atoms are assigned in yellow. The direction of dislocation motion and GB migration is marked out by the yellow and red arrows, respectively……107
Fig. 6.6. Interaction of a screw dislocation with Σ11 (1 1 3) GB: (a) θ_{bulk}= 0 and (b) θ_{bulk}= 0.001. The direction of dislocation motion and GB migration is marked out by the yellow and red arrows, respectively……..108
Fig. 6.7. MD snapshots illustrating the interaction process between Σ57 (4 4 5) GB and a screw dislocation gliding on: (a) plane 1 without H, (b) plane 1 with H of θ_{bulk}= 0.001, (c) plane 2 without H and (d) plane 2 with H of θ_{bulk}= 0.001. The insets of each snapshot are coloured by the dislocation type. The light blue lines represent the Frank dislocations, the green lines represent the Shockley partial dislocations, the dark blue lines indicate the perfect dislocations, and the red line are the other types of dislocations. 110
Fig. 6.8. MD snapshots illustrating the interaction process between Σ171 (11 11 10) GB and a screw dislocation gliding on plane 3: (a) and (b) without H, (c) and (d) with H of θ_{bulk}= 0.001……..……111
Fig. 6.9. MD snapshots illustrating the interaction process between Σ451 (15 15 1) GB and a screw dislocation gliding on: (a) plane 1 without H, (b) plane 1 with H of θ_{bulk}= 0.001, (c) plane 2 without H and (d) plane 2 with H of θ_{bulk}= 0.001….....112
Fig. 6.10. MD snapshots illustrating the interaction process between Σ1241 (20 20 21) GB and 5-dislocation pile-up gliding on plane $\#L3$ with H of $C_H = 0.14$ Å^{-2} : (a)

absorption of the first three dislocations, (b) absorption of the fourth dislocation and (c) absorption of the fifth dislocation. All images except insets are coloured by CNA. The left and right insets of each snapshot are coloured by CSP and von-Mises shear stress, respectively. (d) Vacancy evolution with the number of incoming dislocations in the absence and presence of H. The large pink particles are vacancies detected by Atomviewer while the small yellow ones are H atoms……..113

Fig. 6.11. Shear stress component on GB dislocations of Σ451 (15 15 1): (a) without H and (b) with H of θ_{bulk}= 0.001. H atoms are removed to facilitate viewing of the defect structures…….115

Fig. 6.12. (a) Interaction of dislocation with Σ57 (4 4 5) GB in terms of the energy barrier to the applied shear strain. (b) Energy barrier for dislocation-GB interaction plotted against the static GB energy for various types of GBs without and with H……..116

Fig. 7.1. (a) Schematic illustration of the bicrystal sample. Atomic structure of (b) Ni bulk, (c) Σ5 (210) GB and (d) Ni (210) free surface….....121

Fig. 7.2. Schematic diagram of (a) the fracture paths for the Σ5 (210) ⟨100⟩ GB and (b) the totally separated two free surfaces. P1, P2 and P3 stand for the potential cutting planes separating two grains……...123

Fig. 7.3. H segregation energy maps for four types of GB/FS. Larger spheres represent Ni atoms, and smaller ones indicate possible H trapping sites….....124

Fig. 7.4. Summary of segregation energy maps for 20 types of GB and FS tilted around ⟨100⟩, ⟨110⟩ and ⟨111⟩ axis. Squares denote GB/FS energy, solid and hollow circles denote the lowest and highest H segregation energy, respectively, and triangles denote maximum excess H concentration….....125

Fig. 7.5. Rigid separation energy and tensile stress as a function of separation distance for different GBs under varying H concentrations: (a) and (d) Σ5 (210) ⟨100⟩ GB, (b) and (e) Σ3 (111) ⟨110⟩ GB, (c) and (f) Σ3 (121) ⟨111⟩ GB….....127

Fig. 7.6. Theoretical cohesive strength and fracture energy plotted as a function of misorientation angle with different tilt axes. The vertical dashed lines indicate the GBs of interest….....127

Fig. 7.7. Calculation for GB cohesive strength with various configurations: (a) Ni GB,. (b) Ni GB, maximum excess of H, (c) Ni GB, boundary disruption, (d) Ni GB, local stress state and (e) Ni GB, with three factors combined. Ni atoms are coloured according

to their centrosymmetry value, and H atoms are assigned in purple……130
Fig. 7.8. Tensile stress-separation distance curves for tensile stretching of various GBs: (a) Σ5 (210) ⟨100⟩, (b) Σ3 (111) ⟨110⟩, and (c) Σ3 (121) ⟨111⟩….....131
Fig. 8.1. MD simulation set-up for mode-I fracture along tilt boundary. (a) Geometry and crystallographic orientations of simulation model. (b) and (c) H distribution around the crack tip with 45 and 135 mppm H atoms. (d)-(g) Atomic configurations of the equilibrium structure of various GB types. Images are coloured by CNA, where atoms with bcc structure are coloured in blue, atoms at the GB and free surface are coloured in red, atoms with fcc structure are coloured in green, and H atoms are assigned in yellow. The structural units of each GB are outlined by the black line. Possible dislocation slip systems are indicated with pink arrows…….135
Fig. 8.2. Schematic representations of (a) a crack along a tilt GB and (b) dislocation emission on slip plane emanating from the crack tip. (c) Simulation model for calculating the generalized stacking fault in $(11\bar{2})[111]$ and $(110)[1\bar{1}\bar{1}]$ slip systems. Atoms with perfect bcc structure are coloured by dark blue, and the red atoms represent the stacking fault and the free surface. (d) The generalized stacking fault energy versus fractional displacement in $(11\bar{2})[111]$ slip system (blue circle) and $(110)[1\bar{1}\bar{1}]$ slip system (pink star). (e) Fracture energy of various GBs as a function of H concentration. 137
Fig. 8.3. MD snapshots illustrating the crack propagation in the simulations of Σ17 (2 2 3) GB along (a) [3 3 $\bar{4}$] direction with 0 mppm H atoms, (b) [3 3 $\bar{4}$] direction with 45 mppm H atoms, (c) [3 3 $\bar{4}$] direction with 180 mppm H atoms, (d) [$\bar{3}$ $\bar{3}$ 4] direction with 0 mppm H atoms and (e) [$\bar{3}$ $\bar{3}$ 4] direction with 180 mppm H atoms. (f) Overview of critical stress intensity factors K_{Ie} and K_{Ic}, and global applied stress intensity factor K_{Iapp} in dependence on crack orientation and H concentration. The partially filled diamonds indicate ductile emission, while solid diamonds indicate brittle cleavage. Crack propagation distance versus the stress intensity K_{Iapp} with various H concentrations along (g) [3 3 $\bar{4}$] direction and (h) [$\bar{3}$ $\bar{3}$ 4] direction……139
Fig. 8.4. MD snapshots illustrating the crack propagation in the simulations of Σ11 (5 5 7)$_A$($\bar{7}$ $\bar{7}$ 1)$_B$ GB along (a) [7 7 $\overline{10}$] direction with 0 mppm H atoms, (b) [7 7 $\overline{10}$] direction with 45 mppm H atoms, (c) [7 7 $\overline{10}$] direction with 180 mppm H atoms, (d) [$\bar{7}$ $\bar{7}$ 10] direction with 0 mppm H atoms and (e) [$\bar{7}$ $\bar{7}$ 10] direction with 180 mppm H atoms. (f) Overview of critical stress intensity factors K_{Ie} and K_{Ic}, and global applied

stress intensity factor K_{Iapp} in dependence on crack orientation and H concentration. The partially filled diamonds indicate ductile emission, while solid diamonds indicate brittle cleavage. Crack propagation distance versus the stress intensity K_{Iapp} with various H concentrations along (g) [7 7 $\overline{10}$] direction and (h) [$\bar{7}$ $\bar{7}$ 10] direction……141
Fig. 8.5. (a) and (d) Overview of critical stress intensity factors K_{Ie} and K_{Ic}, and global applied stress intensity factor K_{Iapp} in dependence on crack orientation and H concentration. The partially filled diamonds indicate ductile emission, while solid diamonds indicate brittle cleavage. Crack propagation distance versus the stress intensity K_{Iapp} with various H concentrations along (b) [1 1 $\bar{1}$] direction, (c) [$\bar{1}$ $\bar{1}$ 1] direction, (e) [$\bar{1}$ $\bar{2}$ 0] direction and (f) [1 2 0] direction……...142
Fig. 8.6. Cyclic loading spectra in the simulations….....144
Fig. 8.7. The volume density of H atoms in the GB and the grain interior region versus number of cycles…….144
Fig. 8.8. MD snapshots illustrating the crack propagation along the predicted ductile direction of (a) Σ17 (2 2 3) GB and (c) Σ11 (5 5 7)$_A$($\bar{7}$ $\bar{7}$ 1)$_B$ GB with 135 mppm H atoms during cyclic loading. The upper inserts are loading spectra, and lower inserts of each image represent stress field distribution and are coloured by hydrostatic stress value. (b) and (d) The corresponding H distribution maps under different stress intensity. Possible cracking path is marked by dark dash, and H diffusion is indicated with pink arrows……..145

Chapter 1 Introduction

1.1 Research background

In 1875, Johnson examined the way different acids affected the mechanical properties of iron and noted that after immersion in strong hydrochloric or dilute sulfuric acid, a piece of iron could be broken after being bent once, whereas it could be bent two or three times before immersion. It was shown that these effects on the toughness and breaking-strain were temporary, and the metal would regain its original character [1]. He attributed this phenomenon to hydrogen (H) segregation where the H atoms in acids entered the metal and hindered the movement of iron atoms, thus causing a temporary loss of toughness and strength. This was the first report of H-induced degradation in the mechanical performance of iron, and launched the field of study of hydrogen embrittlement (HE) of metals. Researchers then found that this H-induced failure was universal in metals, such as steels [2-4], aluminium [5-7] and titanium alloys [8-10].

High-strength steels and engineering alloys are widely used in aerospace engineering, oil and gas transportation, offshore platforms and nuclear energy, etc. However, HE phenomenon severely limits their industrial applications. During manufacturing and fabrication, the hydrogen molecular H_2 can be adsorbed on the metal surface and dissociated into H atoms. These H atoms then segregate into metals, diffuse within the lattice structure, and are eventually trapped by defects such as vacancies, dislocations and grain boundaries (GBs) [11]. When there is a large accumulation of H, crack initiation and propagation occur, which leads to the final rupture and catastrophic failure of metallic systems. For example, high-strength steels are preferred in the automotive industry to increase fuel efficiency by reducing weight while still meeting strength requirements. When exposed to an aggressive environment these steels endure the threat of HE due to the presence of H gas [12]. Moreover, with the fast development and increasing utilisation of H energy, the HE of steels is also becoming a severe challenge in the design and use of H-pressurised pipes and storage containers [13].

The activation of the HE phenomenon and its influence on the deterioration of mechanical properties in structural materials depends on factors such as [14]: (1) material microstructure, such as defects and impurity densities, (2) H charging and

diffusion, and H interaction with various traps and trapping conditions, (3) H coverage and its local distribution around defects, and (4) mechanical and environmental loading conditions at macro, micro, and nano scales. Due to its multi-faceted nature, there are still strong debates on the H-induced failure mechanisms and general HE models.

As an important ingredient of crystal imperfections, the GB significantly affects intergranular HE [14-20]. GBs can play a critical role in the transport and segregation of H and fracture patterns in polycrystalline materials [14], and "special" GBs are often utilised by GB engineering to increase resistance to intergranular HE in metallic systems [17]. For example, Bechtle et al. [17] used thermomechanical processing to engineer Ni-201 alloy. By comparing the mechanical properties and fractography of samples with low and high fractions of low-Σ boundaries, particularly Σ3 twins, they found that microstructures with a higher proportion of Σ3 boundaries displayed higher tensile ductility and fracture toughness. Therefore, a deeper understanding of the behaviour of GBs during the HE phenomenon is of significance to improved failure predictions and to design of HE-resistant materials. It has been proposed that the role of H is to weaken the cohesive bonding strength of GB planes, thereby facilitating GB separation or cleavage crack growth [15, 16]. This H-enhanced decohesion (HEDE) theory is commonly quoted to interpret experimentally-observed cleavage-like failure. However, recent studies of the microstructure beneath H-induced intergranular facets in structural materials such as Ni and Fe, and martensitic and austenitic steels suggest that ultimate failure cannot be caused by HEDE alone [6, 18-20]. H-enhanced localised plasticity (HELP) and dynamic dislocation-GB interactions probably play a decisive role in establishing conditions for intergranular failure by boundary decohesion. The plasticity helps accumulate sufficient H into the GB and change the boundary structure and local stress state, which facilitates the embrittlement process. Unfortunately, further details of how the dynamic plasticity process occurs on an atomic scale cannot be directly observed with experimental techniques.

With the advent of computational resources, atomistic simulations are increasingly being used to study the GB-mediated plasticity process and various HE mechanisms on an atomic scale. For example, Spearot et al. [21, 22] conducted a series of molecular dynamics (MD) simulations to investigate the nucleation events from GBs with <100> and <110> tilt axes over a wide range of misorientation angles.They found that the tensile stress for dislocation nucleation was directly correlated to the grain orientations and certain structural units of GBs. Cahn and Mishin [23] took

advantage of atomistic simulation on [001] symmetric tilt GBs to examine the shear-induced coupled motion. Two distinct coupling modes (positive and negative branches) were predicted based on the proposed geometric model of coupling. They revealed that GB migration was achieved by the deformation of structural units and collective glide of lattice dislocations on corresponding slip planes. Tehranchi and Curtin [24] calculated the reduction of theoretical strength on various symmetric tilt GBs and found that the theoretical strength was not significantly reduced by the presence of H atoms for all studied GBs. Song and Curtin [26-28] examined the H-triggered ductile-to-brittle transition in bulk Ni and Fe via finite-temperature coupled atomistic/discrete dislocation (CADD) multiscale method and MD simulations. They claimed that the formation of nano-hydride due to a substantial accumulation of H around the crack tip promoted brittle fracture by preventing the dislocation emission of crack tip. Moreover, the interactions between H and vacancies proved to be critical for failure [30-32]. H and vacancies preferred to accumulate as defect complexes near GBs, thereby producing damage and causing brittle fracture along the GBs [33].

1.2 Research motivations and objectives

In this thesis, MD simulations were employed to study the H segregation at various GBs and how it influenced the structure, mechanical properties, deformation mechanisms and failure response of GBs. It is envisioned that these simulation results can provide important insights into experimental observations and enrich our knowledge of the multifaceted problem of HE.

This thesis begins with an investigation of H segregation at various GBs and its influence on the mechanical response and plastic deformation of GBs. To advance GB engineering, characterising the GBs and related H adsorption behaviour becomes critical. Inspired by Ashby et al. [34], the structure of all GBs with a powerful geometrical approach of space tessellation was analysed. Based on the structural characterisation, a corresponding computational route to identify all possible H trapping sites at GBs was developed. Subsequently, molecular statics (MS) calculations were carried out to evaluate the energetics of H segregation at GBs. This method provides an atomistically-based thermodynamic framework to quantify the HE. As mentioned above, the HELP mechanism postulates that H atoms enhance dislocation mobility and generation. However, recently Xie et al. [35] conducted quantitative mechanical tests in an environmental transmission electron microscope to examine dislocation movement, and

found that mobile dislocations lost their mobility under H atmosphere, contrary to the HELP mechanism. In addition, Song and Curtin [36] proposed that H-formed Cottrell atmospheres following dislocations produced resistance to dislocation motion. As a consequence, these observations made the HELP mechanism controversial, and it still remains unclear whether solute H promotes or suppresses dislocation nucleation or movement. Motivated by this, tensile and shear deformation simulations of bicrystal models with tilt/twist GBs were performed to reveal the effects of H on the dislocation dominated plasticity in this thesis.

The H-modified interaction of dislocations with GBs was also studied. Recent experiments [18, 19] showed that the microstructure beneath H-induced intergranular facets was comprised of extremely high density of dislocations, suggestive of an acceleration of plasticity process (dynamic dislocation-GB interactions) and pre-failure deformation prior to crack initiation. However, the effects of H atoms on modifying the interaction mode of GBs and the accurate role of the interaction process in promoting ultimate failure are unknown. Dislocations can interact with GBs in various forms: (i) absorption followed by the formation of GB dislocations, (ii) direct transmission through the GB, (iii) reflection from the original grain, or (iv) nucleation from the GB [37]. The introduction of H atoms into the GB can modify the interaction mechanisms via several aspects. H atoms can produce pronounced changes in the atomic structure of the GB. The disordered atomic structure obviously serves as a dislocation sink or trap which absorbs the impinging dislocations. Furthermore, the segregation of H into the GB gives rise to a concentration of stress along the GB. These stress fields interact with the impinging dislocations, and change the initial slip and net Burgers vector along the GB. In addition, the dislocation dissociation into GB dislocations is suppressed by H atoms that cannot diffuse to lower-energy sites during GB migration. As the slip transfer is hindered, the strain energy and local stress within the GB is increased. To relieve the accumulated energy, an alternative response such as crack nucleation and propagation may be initiated, causing ultimate failure. In this thesis some aspects of this problem were investigated.

H-induced failure was examined by direct simulations of the decohesion of Ni GBs in the presence of H. The HEDE mechanism posits that segregated H atoms reduce the cohesive bonding strength of the GB, and increase the propensity for cleavage-like failure [15, 16]. While this theory is backed up by experimental observations of cleavage failure in metallic systems, it is insufficient and is open for more in-depth quantification and

analysis. By necessity, atomistic simulations can be used to directly assess the magnitude of the reduction in GB cohesive properties as a function of H concentrations and GB types during GB separation. Two parameters control the GB decohesion in the presence of H. One is the theoretical cohesive strength of the GB. Generally, the GB cohesive strength is higher than the plastic flow stress of metal, thus facilitating dislocation emission from the GB when subjected to tensile loading while preventing cleavage-like separation. The introduction of H atoms into the GB could change these properties, and thus encourage intergranular failure. The other is the fracture energy of the GB, which is the difference between intact and fully-separated system energies. This parameter is directly associated with the critical stress intensity factor for cleavage according to Griffith's theory. Given that dislocation-GB interactions could establish the conditions—stress state, boundary disruption and critical H concentration to cause the GB to become the weak link in metallic systems and therefore the source of crack nucleation, presumably these factors must aid the GB decohesion and change the two controlling parameters. Thus, this study aims to examine the H-induced reduction in theoretical cohesive strength and fracture energy, with contributions from dislocation-GB interactions.

Although the direct decohesion of GBs produces H-induced reduction in GB properties, it is abstruse to answer whether such reduction is sufficient to induce brittle fracture instead of ductile fracture today. When considering brittle fracture to happen via the propagation of sharp cracks, such a process is suppressed if dislocation emission blunts the crack tip. It seems to be vital to address the issue associated with the inherent competition between brittle cleavage and ductile emission at a sharp crack tip. If H segregation can decrease the fracture energy to a level at which the critical stress intensity factor for cleavage K_{Ic} falls below that for dislocation emission K_{Ie}, it is possible for brittle cleavage to occur. Otherwise, the sharp crack tip blunts by dislocation emission, decreasing the crack tip stress intensity and preventing cleavage process. As aforementioned, cleavage K_{Ic} is controlled by the fracture energy, which is reduced with increasing H concentration. Within Rice's theory, emission K_{Ie} is determined by the unstable stacking fault, which is increased or slightly decreased by H atoms depending on H concentration. Therefore, significant H aggregation around the crack tip is critical for $K_{Ic} < K_{Ie}$. This process can occur quasi-statically or dynamically, involving H diffusion from the bulk toward GB crack tips or dynamic crack growth. In this work, we

studied the influence of H atoms on modifying the behaviour of cracks under monotonic and cyclic loading.

1.3 Structure of the thesis

Most of the research outcomes of this thesis have been peer-reviewed and published in journals. The thesis begins with a literature review of the HE phenomenon that was studied using various progressive experimental techniques, theoretical modelling and simulations (Chapter 2). In Chapter 3, the fundamental features of MD simulations are described, and the details of MD model construction and other related techniques are explained. In Chapter 4 and 5, the effects of H segregation on the mechanical behaviour and plastic deformation of GBs in Ni and Fe are examined by direct simulations. The role of H atoms in changing the interaction of dislocations with GBs is demonstrated in Chapter 6. Chapter 7 examines the decohesion of Ni GBs in the presence of H via direct simulations. Chapter 8 is focused on the influence of H segregation at GBs in modifying both the ductile emission and brittle cleavage of the intergranular cracks. The conclusions and recommendations for future work are given in Chapter 9.

Chapter 2 Literature review

Since the HE phenomenon is of concern to industry, a great deal of research has been carried out. Fig. 2.1 summarises the approaches used in HE studies [38], where the scale of study shifted from macro, through to micro/meso, and up to the nano and atomic. These multi-disciplinary and multi-scale approaches provided a direct, or indirect characterisation of H effects and H-related deformation and damage in metallic materials. Various experimental techniques, theoretical modelling and simulations were utilised in HE literature, including: (i) scanning electron microscopy (SEM) [39, 40], (ii) transmission electron microscopy (TEM) [39, 41], (iii) environmental transmission electron microscopy (ETEM) [42-48], (iv) atomic force microscopy (AFM) [46, 47, 49], (v) focused-ion beam (FIB) microscope and machining [46, 47, 50], (vi) thermal desorption spectroscopy (TDS) analysis [51, 52], (vii) atom probe tomography (APT) [53, 54], (viii) modelling and simulation: density functional theory (DFT) and first principles modelling [55-59], cohesive zone modelling (CZM) [60-65], molecular dynamics (MD) and Monte Carlo (MC) simulation [35, 66-69], finite element (FE) simulation [55, 68, 70, 71]; (ix) progressive micro- and nano-mechanical testing, such as slow strain rate testing (SSRT) [72-74] and nanoindentation testing [55, 60, 63, 75-82]. In the following, some representative reviews are introduced and discussed to provide some insights into the HE problem.

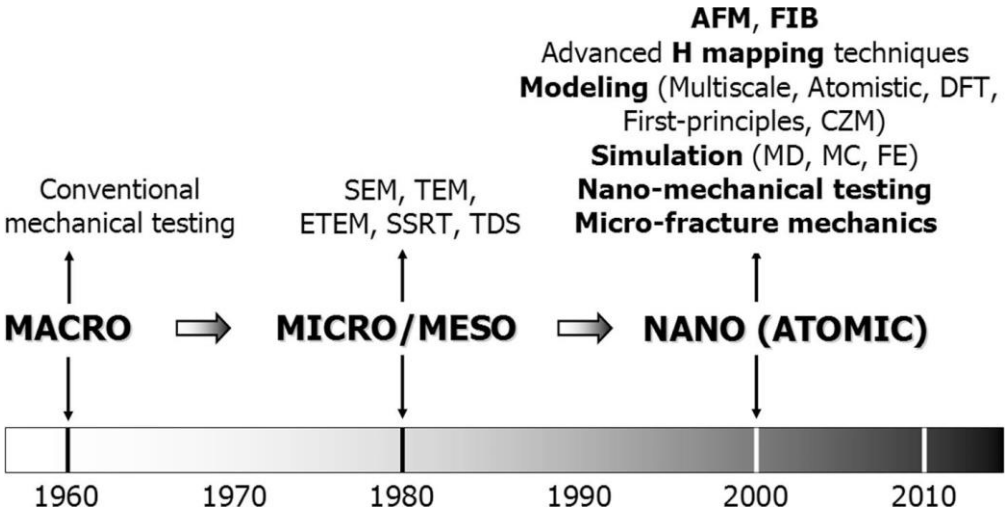

Fig. 2.1. Historical summary of approaches in HE literature [38].

2.1 Experimental techniques

2.2.1 Macro-scale experiments

Experiments revealed that material degradation due to H segregation under mechanical testing was characterised by changes in macromechanical properties. The effects of gaseous H on the mechanical properties include: (i) yield strength, (ii) tensile strength, (iii) elongation to failure, (iv) reduction of area, (v) fracture toughness, (vi) threshold stress-intensity factor, (vii) fatigue life, and (viii) crack propagation [83]. For example, Djukic et al. [84] conducted a comprehensive failure analysis of a damaged boiler tube made of grade 20 – St.20 (or 20G, equivalent to AISI 1020). Samples were chosen from the boiler tubes of a fossil fuel power plant, caused by high temperature H attack during service. Subsequent tensile testing, hardness measurement and impact strength testing (on instrumented Charpy machine) revealed that local hydrogenation reduced the ductility of the material (elongation to failure and reduction of the area). Takakuwa and Soyama [85] performed an indentation test with inverse problem analysis to uncover the influence of H on the local yield stress close to the surface of austenitic stainless steel. The indentation test was effective in detecting the variations in the mechanical properties of austenitic stainless steel caused by H as H was mainly distributed nearby the surface due to its low diffusion and high solubility. To establish a link between the absorption depth and H effects using the indentation test, a secondary ion mass spectrometry was used to measure the H depth data. As shown in Fig. 2.2, it is obvious that the yield stress rises prominently with increasing H charging time. The value reaches over 650 MPa after 48h of H charging, doubling the value of 304 MPa measured before H charging. Once the charging is terminated, the yield stress is ultimately reverted to its initial value due to H desorption from the charged surface. The H-induced hardening effects in the indentation test can be ascribed to H-dislocation interactions. There is a link between the H absorption profile and the plastic deformation depth in the indentation test. The hydrogen-induced hardening increases significantly as the hydrogen absorption depth increases up to the plastic deformation depth and then saturates when the hydrogen absorption depth goes beyond the plastic deformation.

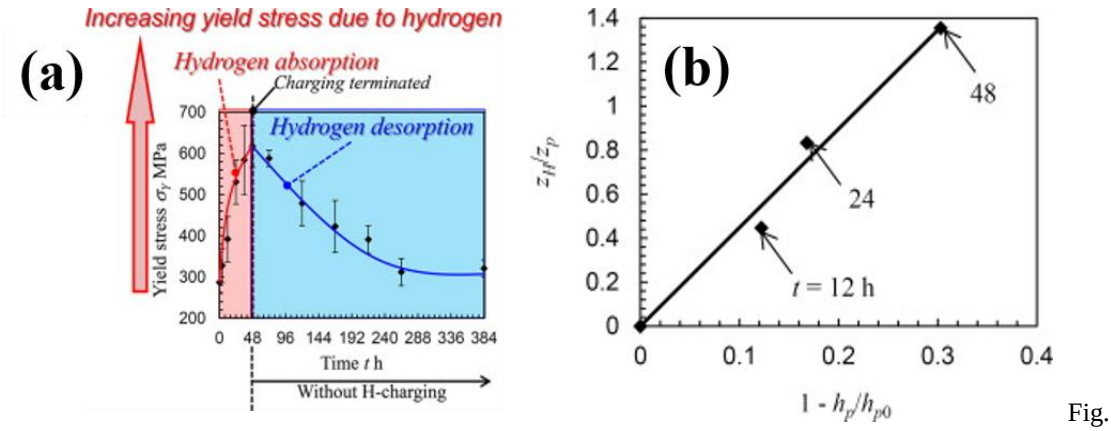

Fig. 2.2. (a) The variation in yield stress due to H absorption and desorption. (b) Hydrogen-induced hardening behaviour explained by the relationship between the ratio of the hydrogen absorption depth to the plastic deformation depth and the ratio of the residual indentation depth before hydrogen charging to that after hydrogen charging [85].

Siddiqui and Abdullah [86] carried out experiments to assess the effects of hydrogenation time on the mechanical behaviour of 0.31% carbon steel, independent of other processing and constitutional variables. The experimental results showed a complex phenomenon regarding H-modified plasticity. It is clear from Fig. 2.3(a) that as the charging time increases from 1 to 6 h, there is a gradual increase in tensile strength for all heat-treated specimens. When the H charging time further increases from 6 to 8 h, a small decrease in tensile strength is observed, in particular, for specimens tempered at 200 and 400 °C. In contrast, there is very little change in tensile strength of specimens tempered at 300 °C, but for hydrogenated specimens between 6 and 8 h and tempered at 500 °C, a constant increase in tensile strength is noticed. The yield stress as a function of H charging time is plotted in Fig. 2.3(b). The yield stress of 0.31% carbon steel shows a slow increase with the charging time increasing from 1 to 7h. Subsequently, a very small reduction in yield stress occurs for all tempered and received specimens when charged between 7 and 8 h. There is a similar behaviour in the breaking strength of the 0.31% carbon steel (Fig. 2.3(c)). Fig. 2.3(d) presents a modest decrease in elongation to failure after cathodic hydrogen charging. The ductility of quenched and hydrogenated specimens is the lowest compared to as-received cases. However, the overall trend is similar, i.e., as the hydrogenation time increases, the elongation decreases. They attributed the increase in tensile strength, yield stress, breaking strength and loss in elongation to failure when hydrogenated between 1 and 6 h to a number of factors. High H diffusion resulted in interactions of H atoms with various types of defects such as dislocations, GBs, precipitates interfaces, carbide matrix produced by the heat treatment.

Immobilising and interference with these defects changed the mechanical properties of the steel. After 6 h of H charging the decrease in tensile strength, yield stress, breaking strength and loss in elongation to failure was ascribed to H diffusion into pre-existing stressed micropores/voids. The exerted pressure due to the gas adds to the external applied load on the specimen. The fracture stress is therefore decreased.

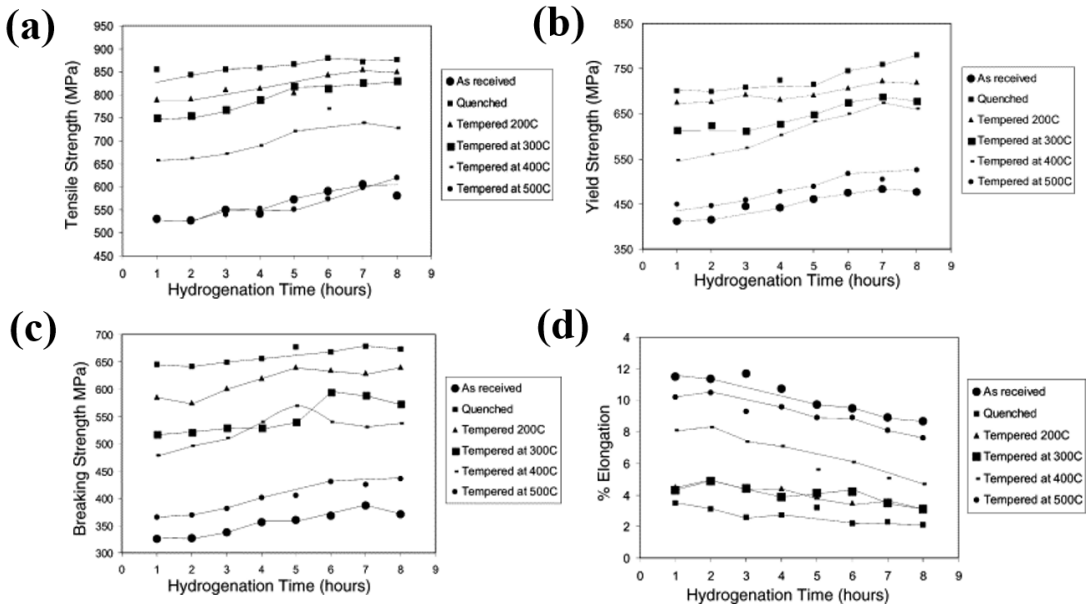

Fig. 2.3. Effect of hydrogenation time on (a) tensile strength, (b) yield stress, (c) breaking strength and (d) elongation of steel [86].

Gangloff and co-workers [4, 75, 78, 87] studied the H-assisted crack process of high strength alloys such as steels, superalloys, 7000 series aluminium alloys and Beta Titanium alloys in the presence of both internal and environmental hydrogen. For internal hydrogen assisted cracking, H atoms can be introduced globally throughout the microstructure by manufacturing operations such as casting, welding, surface-chemical cleaning, electrochemical machining, electroplating, and heat treatment, as well as by environmental exposure such as cathodic electrochemical reactions at low temperatures and gaseous hydrogen exposure at elevated temperatures. Subcritical crack growth occurs when the H-charged metal is subsequently stressed, as shown in the right-portion of Fig. 2.4. Loading causes a redistribution of dissolved hydrogen from the surrounding microstructure to the crack tip process zone to promote crack growth. Stress is not necessary during hydrogen uptake, and the production of environmental hydrogen at the crack tip during stressing is insignificant since the loading environment is typically benign. H environment assisted cracking involves a conjoint action of mechanical loading and chemical reaction where H atoms are mainly produced on clean crack

surfaces near the tip, followed by an uptake of H into the crack tip and subsequent embrittlement, as shown in the left and bottom portions of Fig. 2.4. The mass transport of elements of the surrounding environment is unique to the occluded crack volume and supplies surface reactions of the crack tip, as shown in three environments. From left to right, H is produced by dissociative chemical adsorption for H_2, by chemical reactions for gases such as water vapour or H_2S, or by electrochemical cathodic reactions for acidic or alkaline electrolytes. Once produced, the H diffuses ahead of the crack tip into the plastic zone to cause damage.

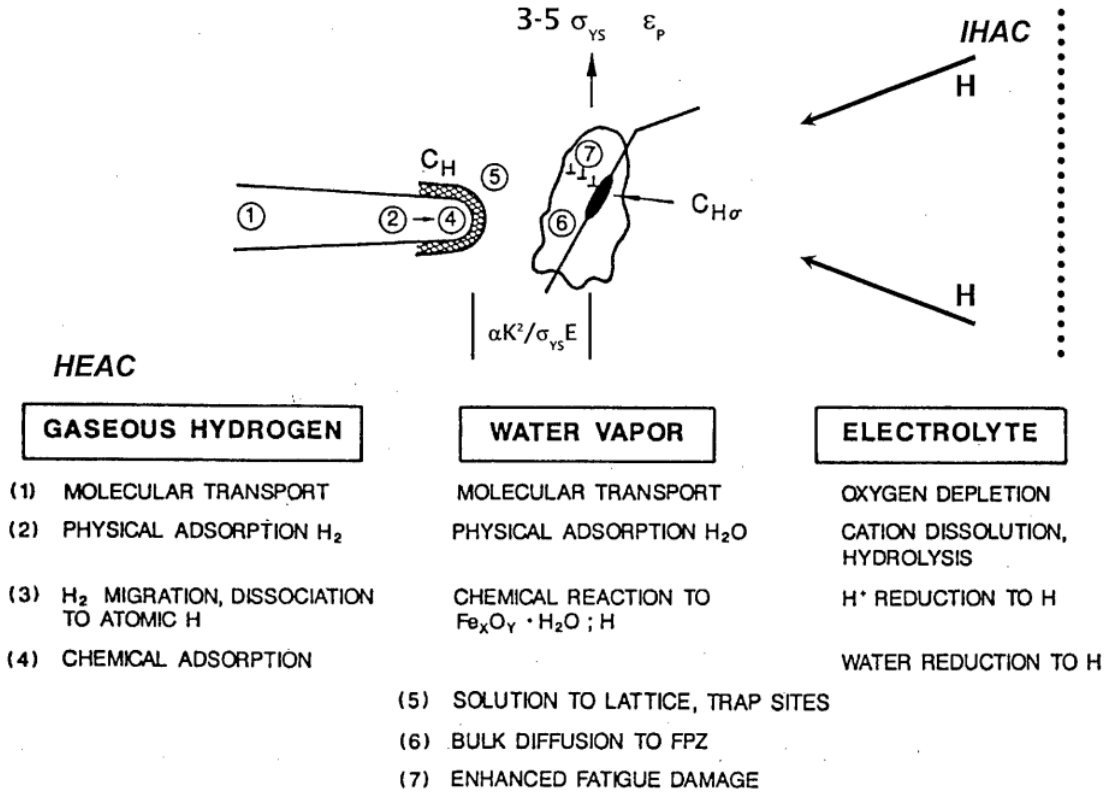

Fig. 2.4. The sequence of elemental processes that supply damaging H to the crack tip fracture process zone during either H environment assisted cracking for gaseous hydrogen, water vapour or an electrolyte, or internal hydrogen assisted cracking for a H pre-charged microstructure [87].

The crack growth behaviour was defined in three stages [87]: In stage I when the stress intensity factor was just above a threshold value less than the fracture toughness of the metal, the crack growth velocity increased prominently. In stage II the crack growth rate was independent of the stress intensity factor, and in stage III the crack growth rate increased as the stress intensity factor increased to values close to the fracture toughness. These studies showed that the presence of H promoted stage I cracking and reduced the fracture toughness of metals. They also stated that nano-scale investigations are required for the fundamental understanding of H-induced cracking.

H not only influences the tensile properties, it also influences ductility [13，88-90] and harness [91-93]. Depending on the H coverage, H-dislocation interaction and local H trapping conditions in different grades of steels, both hardening and softening effects due to H segregation were observed. By combining positron annihilation spectroscopy (PAS) and TDS experiments, Lawrence et al. [89] found that H charging increased the yield stress and work hardening rate of Ni single crystals and polycrystalline Ni-201 alloy samples. The stress-strain curves in Fig. 2.5(a) and (b) show that the yield stress of material with 1-mm grain size is generally lower than that with 35-μm grain size; this is in concordance with the Hall-Petch relationship and the well-annealed condition of the material with 1-mm grain size. For both the 1-mm grain size and 35-μm grain size cases, hydrogen charging increases the yield stress and work hardening rate, as calculated from the slope of the stress-strain curve at 6% and 8% true strain. At 77K the yield stress changes more prominent, with the increase of approximately 18% and 50% for the 1-mm and 35-μm grain size material, respectively (see Fig. 2.5(b) and Table 2.1). At room temperature, the work hardening increases more significant during deformation, with the increase of approximately 56% and 58% for the 1-mm and 35-μm grain size material, respectively (see Fig. 2.5(a) and Table 2.1). Samples of Ni single crystals were only loaded along the [001] crystallographic direction at 293K. The corresponding stress-strain curves in Fig. 2.5(a) show that significant increases in the yield strength (42%) and work hardening rates (approximately 50%) are caused by H charging. With these increases being dependent to temperature, it was postulated that at low temperature (77K), H enhanced and stabilized the formation of vacancies and vacancy clusters, which induced an ‘Orowan type’ hardening effect even when solute H was immobile in essence; at room temperature (297K), mobile H atoms interacted with mobile dislocations, restricting dislocation cross-slip and providing an additional hardening increase.

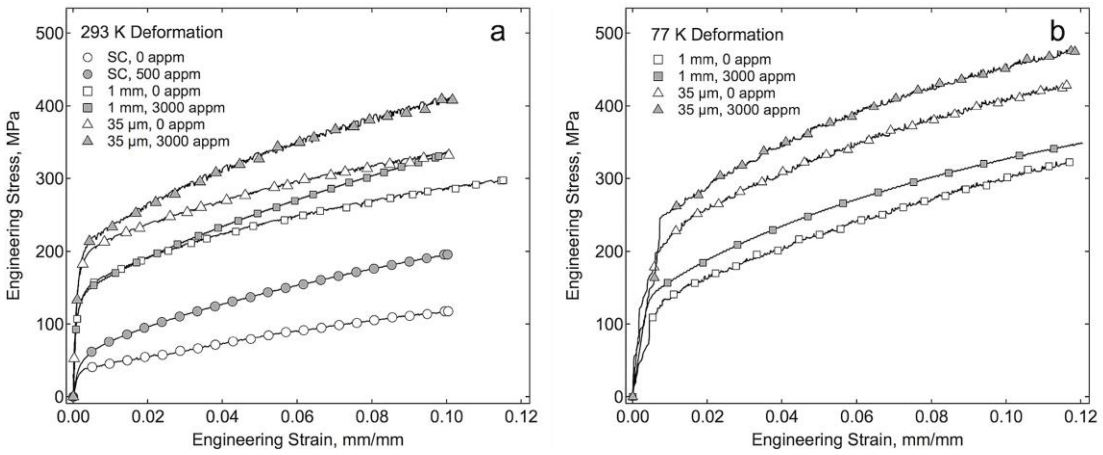

Fig. 2.5. Stress-strain curves for single crystal, 1-mm grain size, and 35-μm and grain size Ni-201 at (a) 293 K and (b) 77 K, in the presence and absence of H.

Table 2.1. Yield stress and work hardening values under different conditions. Work hardening rates are calculated at 6% and 8% strain.

Sample	Yield stress	Work hardening @ 6%	Work hardening @ 8%
SC[001], 293 K	42	48	55
1 mm, 293 K	5	56	86
1 mm, 77 K	19	7	29
35 μm, 293 K	8	58	69
35 μm, 77 K	52	16	12

The in-situ electrochemical nanoindentation by Stenerud et al. [92] made similar conclusions. They attributed the H-induced increase in the harness to either an enhanced slip planarity or a suppressed dislocation mobility in the presence of H. On the other hand, the introduction of H atoms caused softening [94-96] or no change [40] of the mechanical properties in some experiments. TDS and nanoindentation experiments were employed to elucidate the effects of electrochemical and gaseous H on the mechanical response of a low carbon steel [96]. While electrochemical charging enhanced hardening, gaseous charging induced softening. The results revealed that the hardening/softening behaviour was dependent on H concentration, i.e., hardening occurred at relatively higher H concentration by electrochemical charging, whereas softening occurred at lower H concentration by gaseous charging.

2.2.2 Micro/nano-scale experiments

Unlike the macro-scale experiments described above, micro/nano-scale techniques have been used to probe H effects on the material microstructure (GBs, dislocations, voids, etc.). Among all interactions of solute H with various defects, one of the most

important issues is how solute H modifies the behaviour of dislocations which are the main carriers of plastic flow. Through extensive in situ TEM experiments, the “Illinois group” led by Birnbaum, Robertson, and Sofronis [20, 97-103] provided direct evidence of H enhanced the mobility of dislocations. Two types of experiments were carried out. One involved introducing H gas while keeping the rate of displacement of the stage constant; this was characterised by a change in the dislocation velocity. The other experiment involved generating mobile dislocations. They stopped the dislocation motion by keeping the applied load constant, added a gas environment to the microscope, and then observed the change of stationary dislocations. Both experiments showed that the introduction of H increased the dislocation velocity. Fig. 2.6 shows an example of this effect. A Fe sample was deformed in a vacuum to generate dislocations, then the applied displacement of the stage was held and H gas was introduced after the dislocations stopped. H enhanced the dislocation motion, as evidenced by comparing the series of time-resolved images. The dislocation velocity is indicated by the times of each frame, as shown in Fig. 2.6.

Experiments also revealed that the presence of H atoms promoted the generation rate of dislocation sources. Fig. 2.7 shows an example of this effect. Three dislocation sources are formed by the introduction of H gas, as indicated by the arrowheads in Fig. 2.7(a). Source 3 evolutes by Fig. 2.7(h) and expands again in Fig. 2.7(i). Dislocation 1 expands and breaks into two segments propagating in different directions when it meets the free surface. Experimental observations also showed that the equilibrium separation distance between dislocations in an array was prominently changed by H gas [98]. Fig. 2.8 presents the separation distance between dislocations in S310 steels under varying H gas pressure. It is found that the distance between the dislocations is decreased with the increase of the H gas pressure. These experiments suggest that the introduction of H environment can lead to more compact dislocation pile-ups and weaken the dislocation–dislocation interactions, and thus localise the plastic deformation.

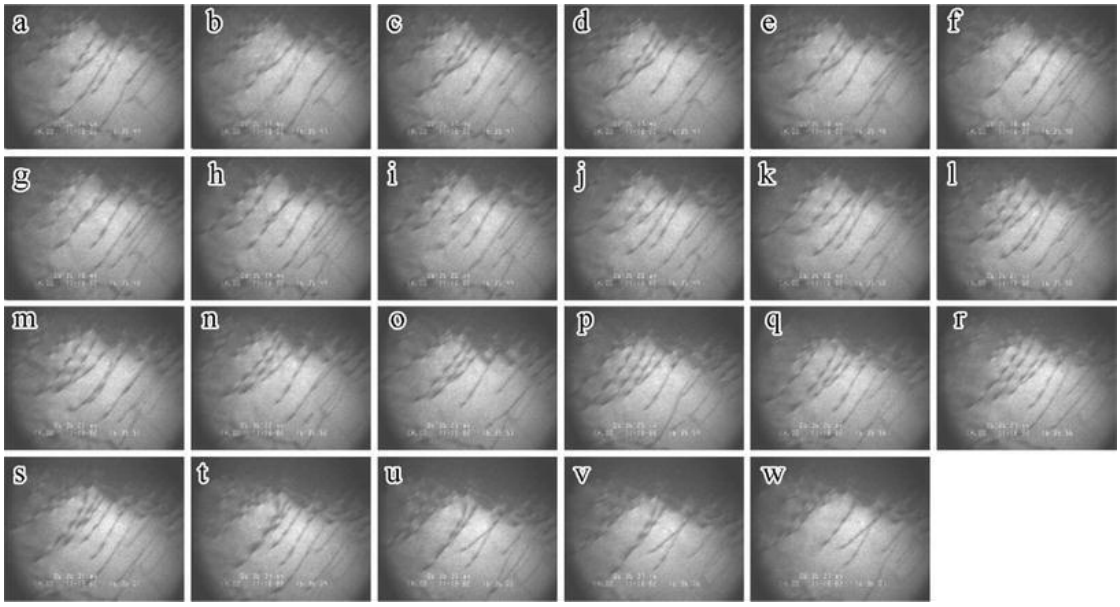

Fig. 2.6. Time-resolved images of the dislocation motion in the presence of H [97].

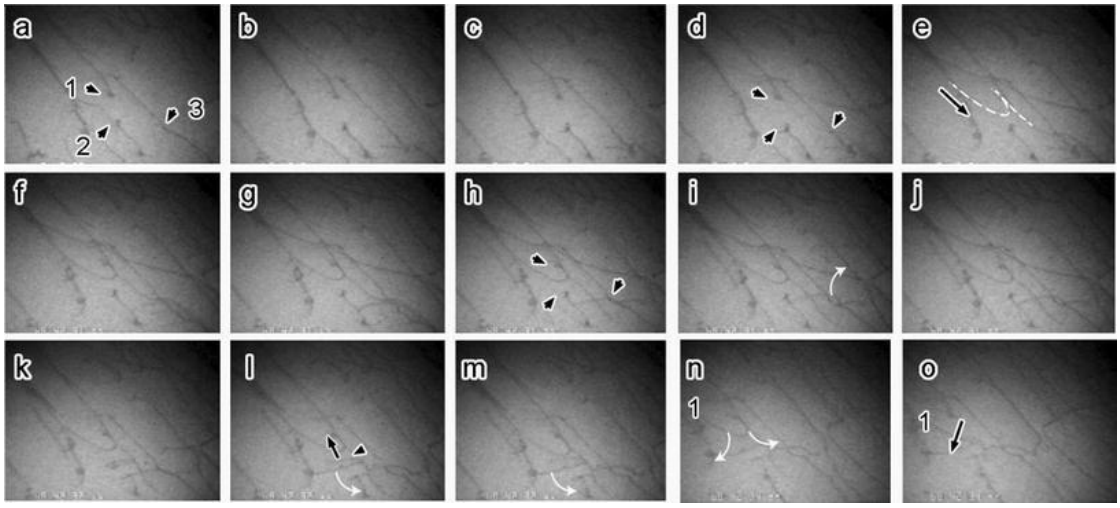

Fig. 2.7. Generation of dislocation sources in Fe caused by H gas. Arrowheads indicate the sources, and arrows represent the dislocation motion direction [97].

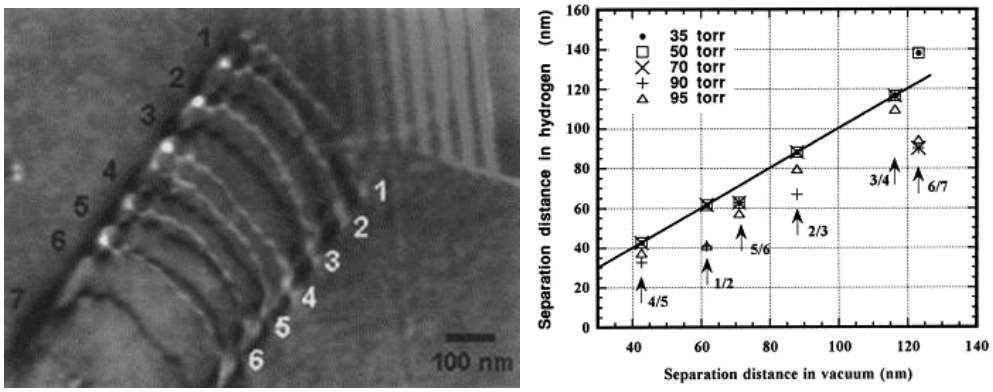

Fig. 2.8. H effects on the separation distance between dislocations. (a) Composite image of a dislocation pile-up in vacuum (black lines) and in the H environment with 95 torr (white lines). (b) Dislocation separation distance under varying H gas pressure [98].

The influence of H on the nucleation of dislocations was also investigated. Barnoush

and his co-workers [104, 105] probed dislocation nucleation behaviour and examined the dependence of the pop-in load on H charging by performing NI-AFM experiments on in situ H-charged samples under controlled electrochemical conditions. Typical load-depth curves of Ni samples under cathodic and anodic potentials are shown in Fig. 2.9. It can be seen that the pop-in load corresponding to the nucleation and formation of dislocation loops is reduced by the introduction of cathodically charged H. This reduction of the pop-in load in nickel was explained using homogenous dislocation nucleation theory where H resulted in the reduction of shear modulus and stacking fault energy in Ni.

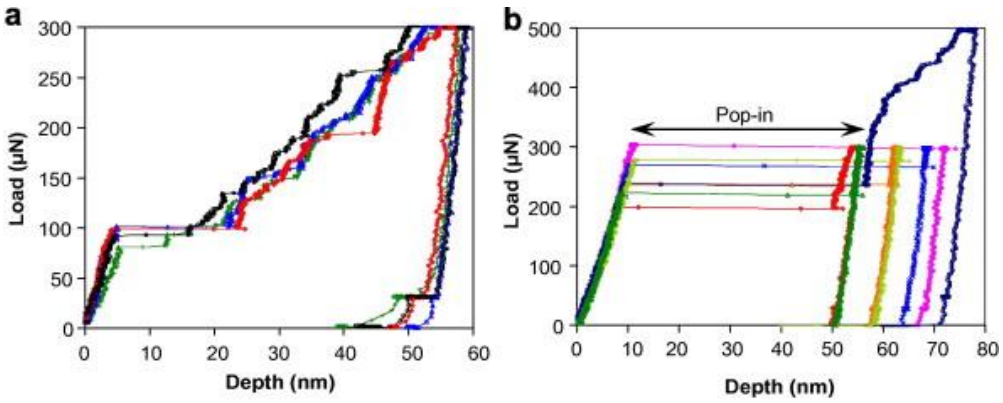

Fig. 2.9. Load-depth curves for Ni at cathodic (a) and anodic (b) potentials [104].

The HE process is associated with the competition between ductile transgranular and brittle intergranular failure in polycrystalline metals. In situ TEM deformation experiments showed the H-induced transition from ductile transgranular to brittle intergranular failure [106, 107]. For example, Lissila and Birnbaum studied the embrittlement of H charged Ni that had been heat treated to segregate S to the GBs using tensile tests at 77 K. The failure mode was transgranular in the absence of H and intergranular in the presence of H. Fig. 2.10 demonstrates a typical picture of the intergranular fracture in nickel with H.

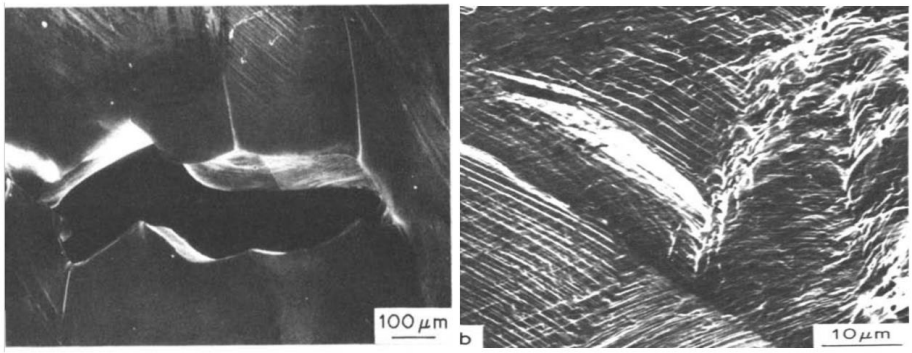

(a) (b)

Fig. 2.10. (a) The crack opening displacement of the intergranular crack observed in the H-charged polycrystalline Ni. (b) The fracture surface of the intergranular crack [106].

Perhaps, the challenge in HE analysis is how H-influenced dislocation gives rise to accelerated brittle-like intergranular failure. Recently, some experimental evidence from new fractographic analysis techniques contributes to understanding this question. Studies on Ni [108] and Fe [19] model systems analysed the slip traces on the fracture surface, suggesting enhanced plasticity activities. The high magnification SEM and TEM in Fig. 2.11 shows that dislocations cells are immediately beneath the fracture surface, and the plastic strain characterised by the size of dislocation cells is almost three times what the sample actually experienced macroscopically. In fact, for the Ni case this dislocation structure is found to extend over a significant distance from the fracture surface [109] (see Fig. 2.11c), suggestive of an acceleration of plasticity process and pre-failure deformation prior to crack initiation. It was proposed that H environment led to a dislocation structure in Ni at 15% strain at failure that would normally only occur at 40% strain without H [110]. The enhanced plasticity deformed the GBs, and transported large amounts of H atoms to the GBs, decreasing their cohesive strength and promoting failure.

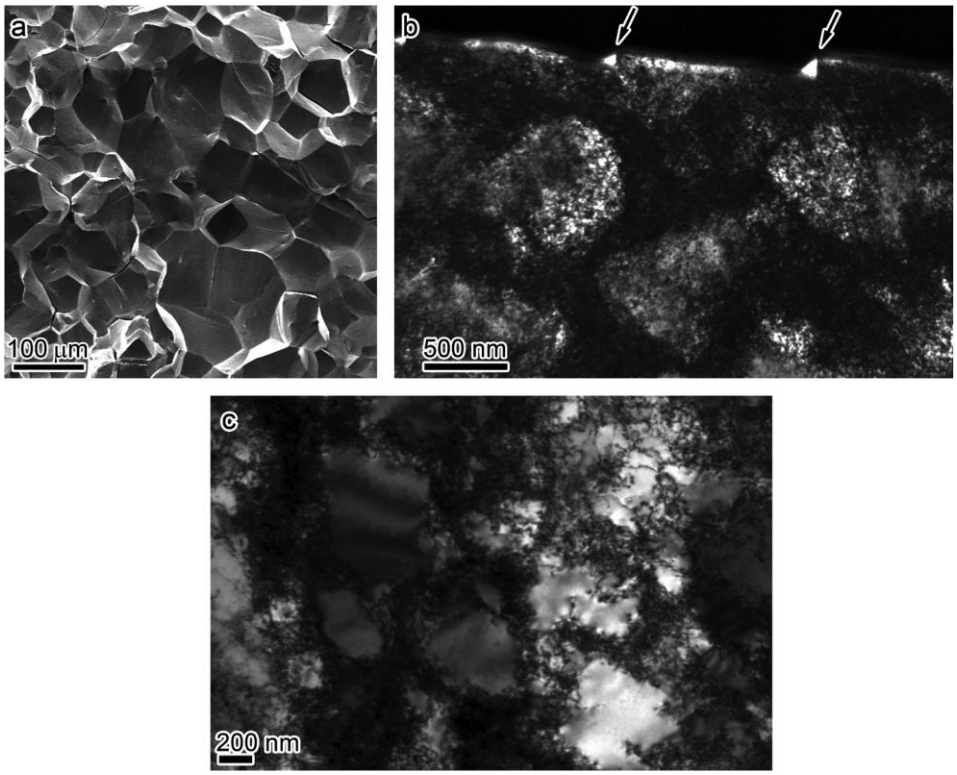

Fig. 2.11. H-induced intergranular failure of Ni. (a) SEM micrograph of fracture surface. (b) TEM micrograph of microstructure immediately underneath the fracture surface. (c) TEM micrograph of microstructure away from the fracture surface [108, 109].

In summary, experiments with various techniques have been conducted to deepen our understanding of HE process. However, the exact underlying mechanisms are still missing. Therefore, theoretical approaches exist in the field to uncover different aspects

of the HE phenomenon.

2.2 Theoretical modelling

There have been numerous HE mechanisms over the past few years, such as hydride formation and cleavage, H-enhanced decohesion (HEDE), H-enhanced localised plasticity (HELP), adsorption-induced dislocation emission (AIDE), and defactant theory.

2.2.1 Hydride formation and cleavage

The nucleation of hydrides was firstly observed in titanium alloy. It was postulated by Gahr [111], however, the hydrides are unstable and may dissolve quickly as the crack passes through them in steel [10]. This is a stress-intensity based mechanism. At low stress intensities, hydride formation decreases the local stress intensity at the crack tip and therefore continued fracture needs an increment in external stress. Once the local stress intensity is increased to exceed the intensity needed for hydride fracture, the crack can proceed by repeated hydride nucleation, growth and cleavage. At high stress intensities, failure is a constrained plastic mechanism in which the stress for plastic flow is reduced at a higher hydrogen concentration [10, 111]. This mechanism is illustrated in Fig. 2.12.

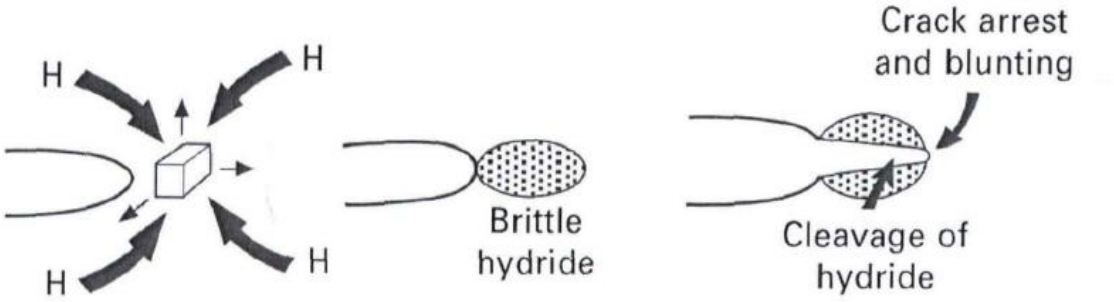

Fig. 2.12. Hydride formation and cleavage mechanism [39].

2.2.2 Hydrogen-enhanced decohesion (HEDE)

The hydrogen enhanced decohesion model proposed by Troiano and Oriani [15, 16] suggests that H atoms are to weaken the inter-atomic bonds in the steel, thereby facilitating grain boundary separation or cleavage crack growth. There is the same implication with the surface energy theory proposed by Petch and Stables [78]. Decohesion is generally assumed to be a simple and sequential tensile separation of atoms ahead of sharp crack tips, but dislocation activity at the crack tip in plastically

deforming metals is an intrinsic competition that dissipates energy and blunts the crack tip, thus inhibiting decohesion. Therefore, high concentrations of H are usually needed to reduce the fracture energy to a level where the critical stress intensity factor for cleavage falls below that for dislocation emission. H segregation and the decohesion typically occur at several positions: (i) tens of nanometers ahead of crack tips where the shielding effects of dislocation render a maximum stress, (ii) sharp crack tips caused by absorbed H, (iii) particle-matrix interfaces, as shown in Fig. 2.13.

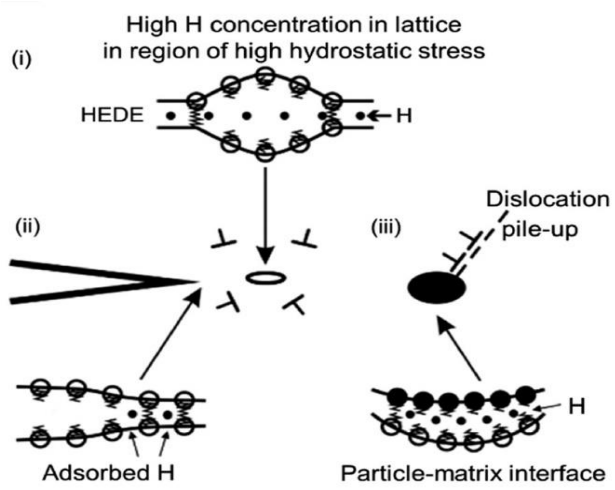

Fig. 2.13. Decohesion process caused by weakening the inter-atomic bonds as a result of (i) H in the lattice; (ii) adsorbed H; (iii) H at particle-matrix interfaces [39].

2.2.3 Hydrogen-enhanced localised plasticity (HELP)

Based on fractographic observations of the ductile features on failure surfaces, Beachem was the first to propose that H assisted cracking is directly related to the microstructural state. This finding changed our thinking about the HE mechanism. Birnbaum, Robertson, and Sofronis [97-103] developed this theory and proposed that as the hydrostatic stress around crack tips is high, H atoms easily accumulate near crack tips, which facilitates dislocation activities and localised plasticity ahead of crack tips, thus causing cracking. Subsequent crack propagation occurs due to more localised microvoid coalescence (MVC), as seen in Fig. 2.14. The HELP mechanism is entirely different from HEDE theory, as HELP postulates that failure of materials is due to local plasticity, not the simple decohesion of inter-atomic bonds.

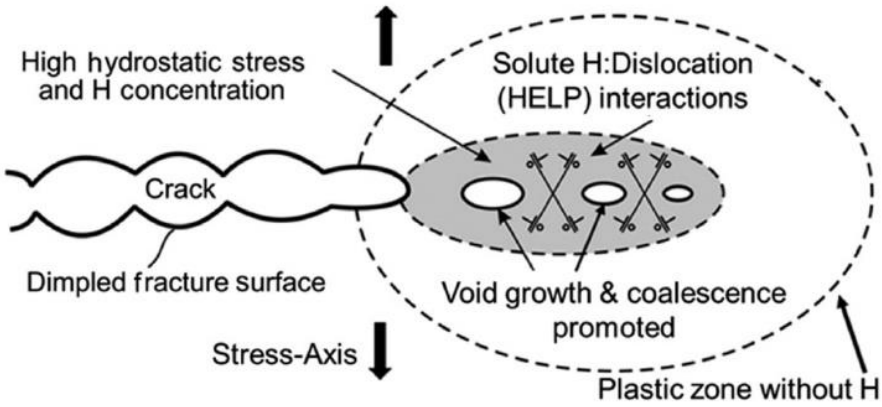

Fig. 2.14. Illustration of the HELP mechanism associated with localised plasticity and microvoid coalescence in the region of high H concentrations [39].

The main reasons for enhanced localised plasticity in the presence of H include: (i) H promotes the generation of dislocation sources: the introduction of H decreases the stacking fault energy and encourages the ejection of Frank-Read dislocation sources and local plasticity, (ii) H increases dislocation motion: H modifies the stress field such that the interaction energy between the dislocation and obstacles is reduced, enabling dislocation to move at a lower stress, (iii) H reduces the separation distance between dislocations: the H shielding model assumes that dislocation-dislocation interaction is influenced by H. One manifestation of such a model is that the separation between dislocation pile-ups is decreased with H.

2.2.4 Adsorption-induced dislocation emission (AIDE)

In 1976 Lynch first proposed the AIDE mechanism. This theory was further developed in subsequent research [112-114]. The so-called "dislocation emission" includes both dislocation nucleation and movement away from the crack tip. Once the dislocation is nucleated, external loading can easily drive it away from the crack tip. Consequently, dislocation nucleation is critical and promoted by H adsorption. The nucleation process is often accompanied by the synchronous formation of a dislocation core and surface step via the shearing of atoms (breaking of old atomic bonds and reforming of new atomic bonds). Thus, the weakening of inter-atomic bonds by H adsorption can facilitate the emission of dislocations, which further accelerates the expansion of cracks.

The AIDE mechanism posits that crack propagation involves not only dislocation emission emanating from the crack tip, but also the nucleation and growth of microvoids at tens of nanometers ahead of the crack tip. This is ascribed to the fact that in the plastic zone near the crack tip, the stress required for dislocation emission is sufficiently high

due to the absence of H adsorption. General dislocation activities thus occur before dislocation emission, which causes voids to nucleate and advance at slip-band intersections, second-phase particles, or positions in the plastic zone around cracks. The formation of voids contributes to crack propagation and ultimate failure.

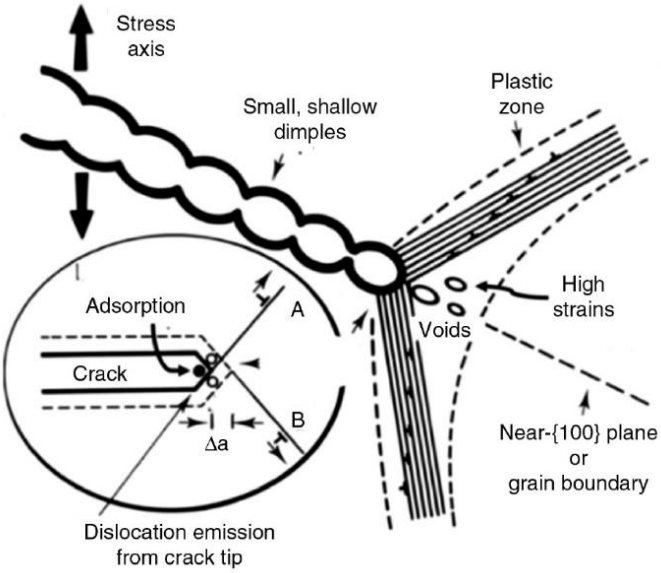

Fig. 2.15. Schematic diagram illustrating the AIDE mechanism involving crack growth and coalescence with voids formed in the plastic zone ahead of cracks [39].

2.2.5 Defactant theory

Based on equilibrium thermodynamics, Kirchheim [115, 116] proposed a general theory in which solute H atoms that segregate into defects in solids and reduce their formation energies are regarded as "defactants". Given a fixed chemical potential, the energy of a defect with H is lower than that without H, which promotes the formation of defects. Furthermore, H segregation increases and the free energies of defects decrease as the H chemical potential increases. If the defect is dislocation, defactant H can reduce the dislocation line energy. When the H chemical potential is high at which defactant effects are significant, dislocation nucleation becomes autonomous, and subsequently ductile failure occurs. From this perspective, the theory concurs with the HELP mechanism. Moreover, the defactants segregate into the newly-formed free surfaces and then reduce the surface energy and corresponding work of fracture, all of which promotes brittle cleavage. From this perspective, the theory is in line with HEDE mechanism. In addition, the defactants decrease the formation energies of dislocations at the crack tip and vacancies, thereby increasing the dislocation generation and equilibrium concentration of vacancies. In this sense, this theory is in accordance with AIDE

mechanism.

Note that the H chemical potential in the defactant theory is far higher than that in realistic experimental conditions. Such high H coverage is also used in recent atomistic simulations of H in GBs and related fracture. Besides, this theory is within the framework of equilibrium thermodynamics, so it does not address kinetics. There might be insufficient time for H to be transported into defects such as surfaces, dislocations and GBs to achieve equilibrium conditions where HE is observed.

Overall, each mechanism has different deeds, and some and multiple HE mechanisms may operate together. However, a quantitative prediction of fundamental mechanisms has not been completely resolved. More in-depth studies are required in this field.

2.3 Simulations

In line with experimental activities, simulations are effective in testing fundamental theories and conjectures, and quantifying embrittlement features. Herein, the atomistic simulations are mainly discussed to provide atomic details of H-related plasticity and fracture phenomenon.

2.3.1 Hydrogen trapping, diffusion and segregation

Pedersen and co-workers [117] carried out a simulation analysis using the adaptive kinetic Monte Carlo (AKMC) method to investigate the effect of GBs on the diffusion mechanism and diffusion rate. The diffusion paths for an H atom in the vicinity of three different GBs are presented in Fig. 2.16. Obviously, for the twist GB, the H atom prefers to stay in the upper grain and is blocked by the GB. For other two cases, the H atom crosses the GB. For the twist + tilt GB, the path shows that the density of stable sites for the H atom within the GB is higher than in the crystal grains.

In addition, the diffusion path was analysed from an energy perspective. For twist GB, the energy barrier for an H atom to enter a stable site within the GB is 0.45eV(see Fig. 2.17(a)), a significant increase in energy from the B-layer and inwards to the GB layer, which explains why the trajectory in Fig. 2.16(a) never crosses the GB. Fig. 2.17(b) shows that the influence of the tilt GB on the energy is greater than for the twist GB. For tilt + twist GB, the H atom spends more than 99% of the total time in the GB region because a large number of sites with low-energy in the GB region can serve as trapping sites so as to reduce diffusion.

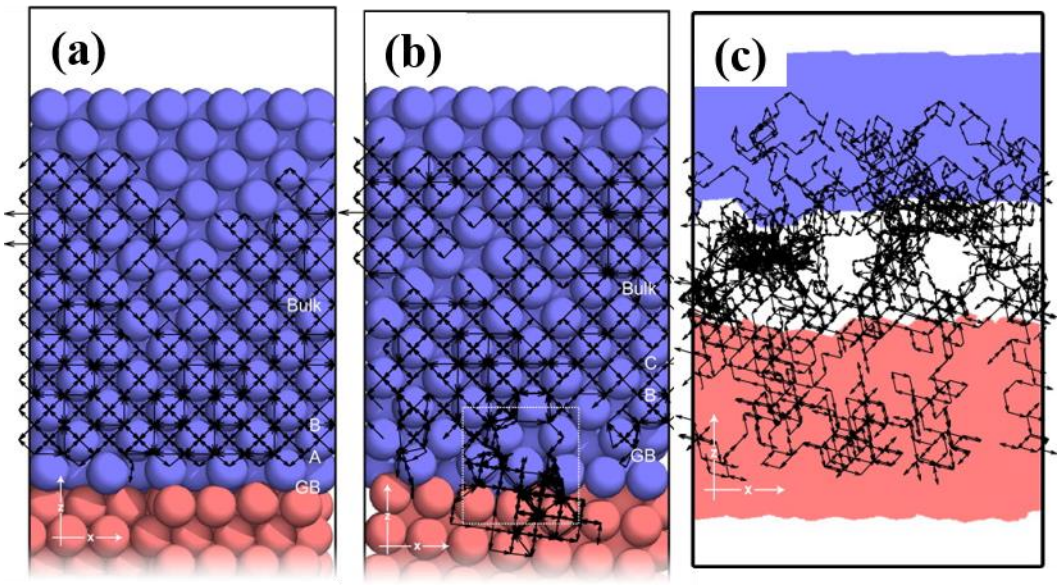

Fig. 2.16. H atom diffusion path at the vicinity of (a) Σ5 twist GB, (b) Σ5 tilt GB and (c) twist+ tilt GB structure [117].

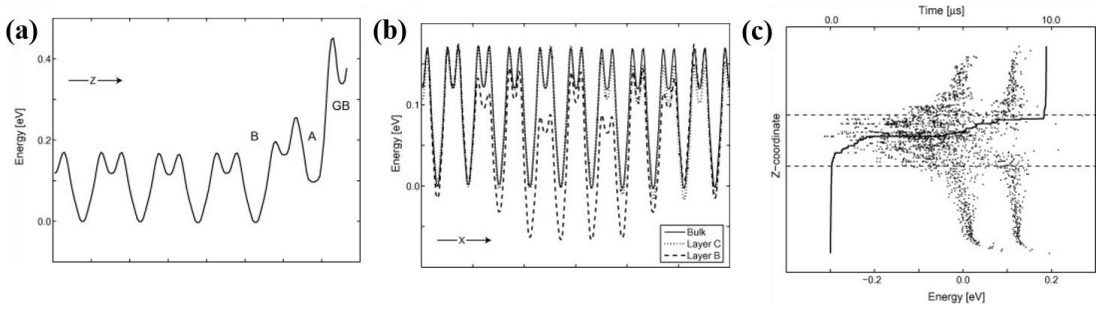

Fig. 2.17. The calculated minimum energy paths for H atom diffusion (a) perpendicular to the plane of a twist GB, (b) parallel to the plane of the tilt GB and (c) the energy of sites and accumulated time at the twist + tilt GB as functions of the Z-coordinate of the H atom [117].

Zhou et al. [118] studied the segregation and diffusion of H in tungsten GB using a first principles method in order to understand the GB trapping mechanism of H. They first examined the solution and segregation energies of all potential GB sites for H, including interstitial and substitutional cases (see Fig. 2.18). It can be seen from Fig. 2.19 that single H atom energetically prefers to occupy the interstitial site rather than the substitutional site in the GB. Dissolution and segregation of H are directly associated with the optimal charge density. W GB can act as a trapping centre which drives the H atom to segregate towards the GB, comparable to the monovacancy in the W bulk. This is because the most stable sites exist at the vacant space in the GB with the lowest solution and segregation energy. In addition, they concluded that H_2 molecule and H bubble cannot form in the W GB as the H–H equilibrium distance was 2.15 Å, much larger than that in a H_2 molecule. Taking into account the lower vacancy formation energy in the GB as compared with the bulk, they also proposed that experimentally-observed H bubble

formation in the W GB should be via a vacancy trapping mechanism.

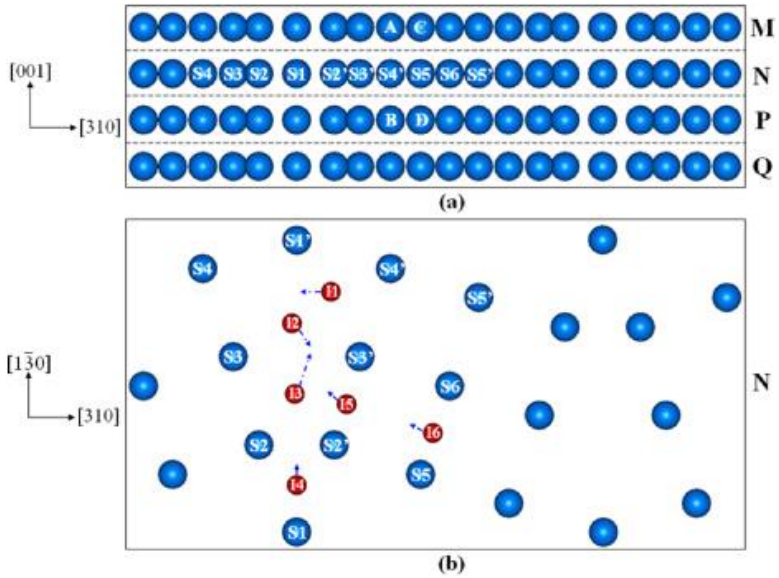

Fig. 2.18. (a) Side view of Σ5 (310)/[001] tilt W GB. (b) Top view of the N atom layer of the W GB supercell [118].

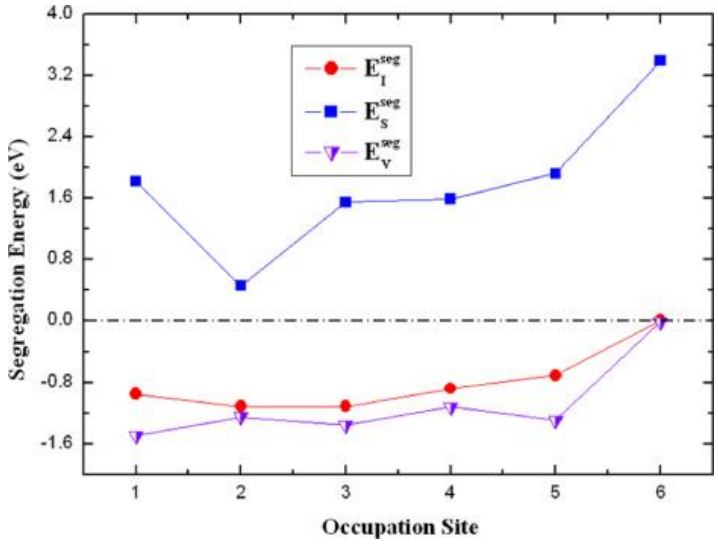

Fig. 2.19. Segregation energies as a function of occupation sites per H atom in a W GB for the interstitial, substitutional and vacancy cases [118].

Du and Ismer [119] studied the interaction of H interstitials with open and close-packed boundary structures within the ferritic α- and austenitic γ-Fe from three aspects: the stability of H in the vicinity of the GBs, the effect of H on the fracture strength of the interface, and the mobility of H towards and within the GB planes. Fig. 2.20 shows H solution energies as a function of the distance from the GB interface for the studied GBs in bcc (red dots) and fcc (blue squares) Fe. The solution energy of H within the different GB structures depends on the local coordination of the corresponding interstitial site and is only moderately correlated with the actual volume of the interstitial site. Within the

close-packed and low-energy Σ3 GBs, the available interstitial sites are very similar to the tetrahedral and octahedral sites in the corresponding bulk structures. Only at the interface different interstitial sites are available, which leads to H being attracted within the bcc Σ3 structure and being repulsed from the fcc Σ3 GB. Within the open GB structures, Σ5 bcc and Σ11 fcc, various interstitial sites are available, and generally provide favourable binding sites for H atoms; this implies that H is trapped at the GB.

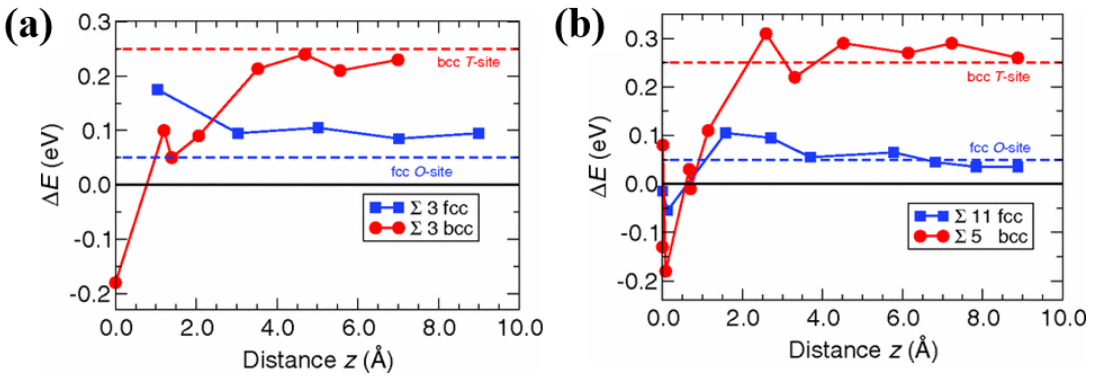

Fig. 2.20. H solution energies as a function of the distance from the boundary for investigated GBs in Fe [119].

The mobility of H within α- and γ-Fe GBs was also studied. As shown in Fig. 2.21, none of the GBs provides a fast diffusion channel for H atoms, but the more open structure, Σ5 bcc and Σ11 fcc, favour diffusion along the GB plane and might thus direct H diffusion towards other defects such as GB junctions or dislocations. These close-packed boundary structures do not promote H diffusion and might even represent two-dimensional barriers to H diffusion.

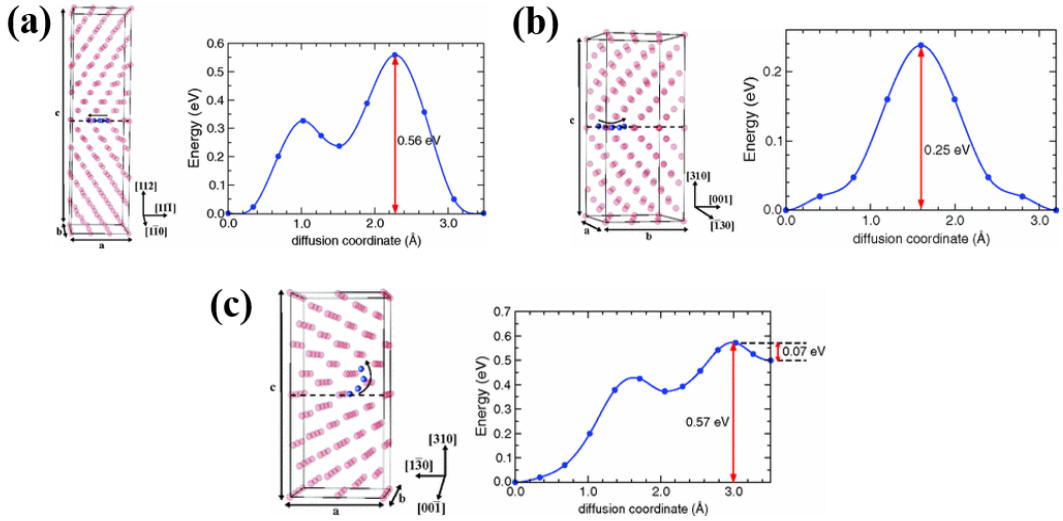

Fig. 2.21. Diffusion pathway for an H interstitial within the interface region of the investigated GBs in Fe [119].

Stefano and Mrovec [120] used density functional simulations to examine the

interaction of H with high-angle GBs in nickel. Two symmetric tilt GBs were selected for the study: Σ5 (210) [001] GB and Σ3 (111) [$\bar{1}$10] GB. Like the above studies, they first identified the various interstitial positions in the two GB supercells and calculated the H segregation. It is concluded from Fig. 2.22 that Σ3 does not attract H atoms, whereas Σ5 acts as an efficient two-dimensional sink for H. This is because the segregation energy for Σ3 GB is negligibly small, while Σ5 GB possesses multiple trapping sites with moderate segregation energies ranging from -0.09 to -0.23 eV. H migration across and along the GBs was then discussed. It can be seen from Fig. 2.23(a) that the H jump between two neighbouring octahedral sites parallel to Σ3 GB plane is equal to that in perfect crystal where the migration takes place through a metastable tetrahedral site, while H migration has a different path as the neighbouring octahedral sites across the GB plane share their faces instead of edges as in bulk (see Fig. 2.23(a) and (b)). Consequently, H migration across the GB plane between neighbouring octahedral sites without the intermediate tetrahedral site. The high migration energy barrier indicates that Σ3 GB acts as a two-dimensional barrier for H diffusion.

Fig. 2.23(c) gives the diffusion of H across Σ5 GB. The barrier for H migration from bulk towards the GB plane is very slow so that H atoms can easily reach the favourable segregation sites inside the GB cavities. In contrast, the GB can serve as an effective two-dimensional sink that H hardly escapes from the GB cavity, albeit the migration is not high. For H migration along the GB plane, the five locally stable sites inside the cavity are shown in Fig. 2.24. Obviously, H can move freely inside the cavity due to the low migration barrier. The estimated ratio value of diffusivity between the GB and bulk at room temperature suggests that the H diffusivity at the atomic scale along Σ5 GB is about two orders of magnitude greater than that in the perfect single crystal.

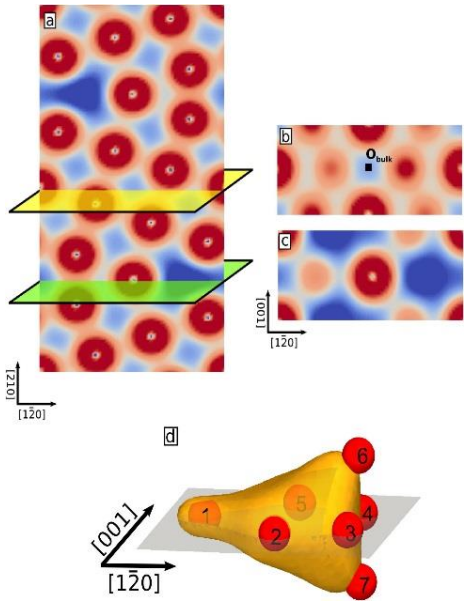

Fig. 2.22. Valence electron density plots for the $\Sigma 5$ GB [120].

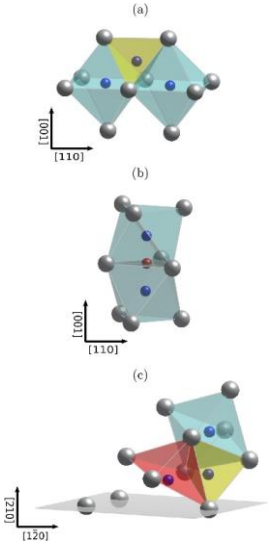

Fig. 2.23. Local atomic configuration for the minimum energy paths for H migration [120].

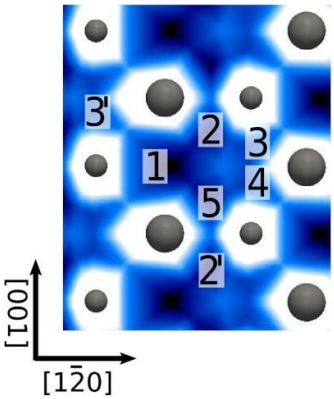

Fig. 2.24. Potential energy surface for H along the Σ5 GB plane obtained by interpolation of several NEB calculations [120].

Zhou and Song [121] used first principles calculations to examine H adsorption at GBs in a variety of fcc metals. A novel modelling approach that combined the space tessellation of polyhedral packing units and first principles calculation was developed. Using the geometric approach of space tessellation of polyhedral packing units, they identified potential H adsorption sites along GBs as only one interstitial site of H adsorption corresponded to the centroid of each polyhedron. Five types of polyhedrons are shown in Fig. 2.25: i.e., tetrahedron (TET), octahedron (OCT), pentagonal bipyramid (PBP), cap trigonal prism (CTP), and bitetrahedron (BTE).

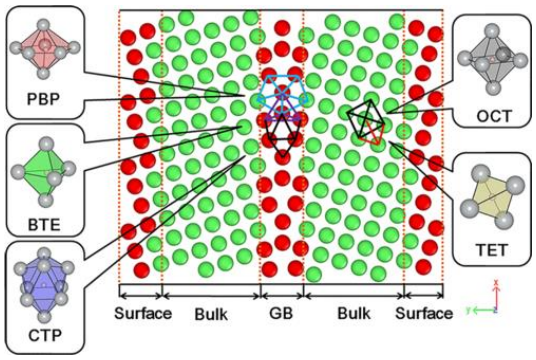

Fig. 2.25. Schematic illustration of polyhedron in representative Σ5 (130) [100] GB and bulk lattice [121].

A general physics-based formula was used to provide accurate assessments and reveal the chemomechanical origin of H trapping and segregation energetics at GBs (Eq. 2.1). This model was validated through the quantitative evaluation of hydrogen adsorption energies as a function of the volumetric deformation of polyhedral structural units at GBs for several fcc metals.

$$E^{ad} = E_0^{ad} - B\Omega_p \frac{dV_p}{V_p^0} \tag{2.1}$$

where E_0^{ad} is the chemisorption energy of hydrogen in a deltahedron, B is the bulk modulus, V_p^0 is the volume of the pristine polyhedron, Ω_p is the partial volume of the H atom.

In Zhou's further research [122], atomistic simulations were employed to identify the root cause underlying the volumetric distortion at those polyhedrons and attempt to explain the corresponding physical origin within continuum mechanics. Based on simulation result, the relation between the local hydrostatic stress (σ_h^p) and the local volumetric distortion ($\delta V_p/V_p^0$) was described by the following formula:

$$\sigma_h^p - s_0^p = C_0 \times \frac{\delta V_p}{V_p^0} \tag{2.2}$$

where C_0 and s_0^p are two constants. In particular, the s_0^p is dependent on the type of polyhedron. The linear relationship between local volumetric distortion at polyhedrons

and their associated hydrostatic stresses has been revealed. This linear relationship confirms the validity of continuum mechanism in describing the lattice deformation at atomistic (i.e., individual polyhedron) level at GBs, and suggests the crucial role of stress in determining H adsorption energetics.

Huang and Song [123] developed a computational route to divide a relaxed GB into deltahedral packing units by using an H atom as a probe. Similar to Zhou's result, five various deltahedral packing units were identified at selected tilt GBs. Besides, they also studied the fast and slow separation limits corresponding to GB fracture at fixed H concentration and fixed H chemical potential, respectively. The work of separation at fast fracture and low fracture was calculated and compared (see Table 2.2). It can be seen that the reduction of the GB separation energies due to H segregation was around 50% in the slow fracture limit, as opposed to about 10% in the fast fracture limit. Hence, these atomistic calculations demonstrated that the H embrittlement effects on GBs are more significant in the slow limit than the fast one.

Table 2.2. Work of separation for (a) pure GBs, W_0, (b) fast fracture at constant H concentration, W_Γ, and (c) slow fracture at constant chemical potential, W_μ.

	Σ5(310)[001]	Σ17(140)[001]	Σ11(113)[011]	Σ27(115)[011]
W_0	3.60	3.46	4.29	3.93
W_Γ	3.24	3.06	3.99	3.43
$(W_\Gamma - W_0)/W_0$	−10%	−12%	−7%	−13%
W_μ	1.94	1.64	2.27	1.44
$(W_\mu - W_0)/W_0$	−46%	−53%	−47%	−63%

The above energetics set a benchmark for the time scales for H diffusion. The H segregation to free surfaces provides thermodynamic limits for cleavage failure. The interaction of H atoms with GBs gives rise to diffusion-independent fracture energies for intergranular failure. H segregation to vacancies has implications for the enhancement of vacancy concentrations as a result of the decreased formation energy for vacancy and H-vacancy complexes. The interaction between H atoms and dislocations forms the basis of understanding the hardening, softening, H transport by dislocations, and dislocation pinning effects that set H diffusion rates. Nevertheless, these simulations cannot directly reveal the overall plastic flow behaviour or underlying mechanisms behind the HE processes.

2.3.2 Hydrogen interaction with dislocations

With high computational costs of DFT calculations, it is impossible to simulate plastic flow behaviour involving long-range of H-dislocation interactions and motions.

More sophisticated simulation techniques are thus required. Zhao et al. [124] examined the interactions between the impurities (H and He) with dislocations (edge and screw) in α-Fe using a multiscale quantum-mechanics/molecular mechanics (QM/MM) approach. They found that H and He both favoured the tetrahedral sites at the dislocation core by calculating the impurity-dislocation binding energy and the impurity solution energy. This was consistent with many of the studies mentioned above [119-121]. The impurity diffusion along the dislocation core was investigated using the QM/MM nudged-elastic band method. It was concluded that H and He both diffused between adjacent tetrahedral sites along the dislocation line, although the diffusion barrier along the screw dislocation was lower than the bulk value for both impurities. With the edge dislocation, although H had similar diffusion barriers as in the bulk, He had much higher diffusion energy barriers than the bulk. The H enhanced dislocation mobility was consistent with experimental observations. Although these simulations could compute the interaction of H atoms with dislocations, it is still impossible to simulate larger and more complex interaction processes such as dislocation glide.

As computing power increases, atomistic simulations such as MS and MD based on semi-empirical interatomic potentials have been developed to study long-range phenomena such as the dislocation interaction with multiple H atoms and H diffusion into defects [125-129]. For example, Taketomi and Matsumoto [128] carried out MS analyses of the H-trap energy around a {112}<111> edge dislocation in alpha iron. By comparing the H-trap energy for the tetrahedral (T) and octahedral (O) sites under shear stress and hydrostatic static stress, it was revealed that H distribution was also sensitive to shear stress for the crystal orientation analysed here. This indicated that strong trap sites were distributed across a wide range on the slip plane around the dislocation core. Fig. 2.26 and Fig. 2.27 shows that the shear stress effect on the trap-energy of an O site type A is much stronger than the hydrostatic effect.

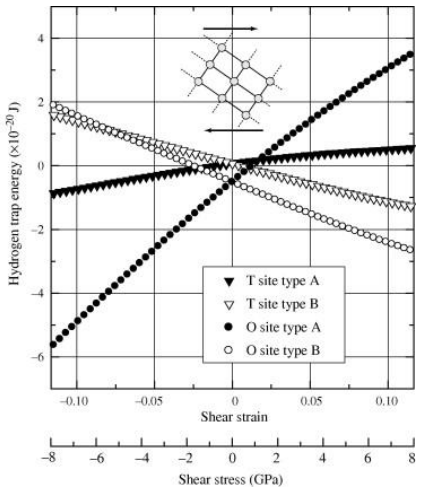

Fig. 2.26. Relationship between hydrogen-trap energy and applied simple shear [128].

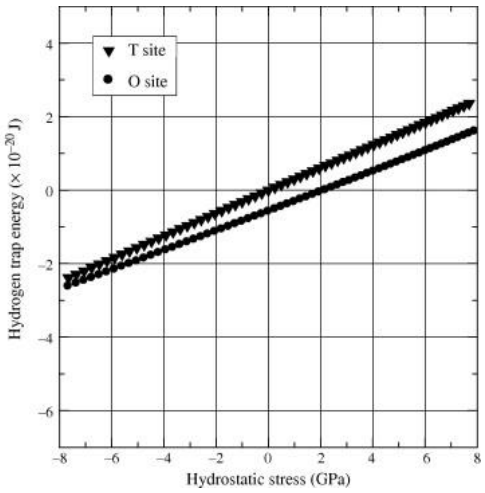

Fig. 2.27. Relationship between hydrogen-trap energy and applied hydrogen static stress [128].

Song and Curtin [36] performed MD simulations of dislocation pile-ups in α-Fe. Three equally spaced edge dislocations were placed into the periodic simulation model at zero shear stress. H atoms with a wide range of concentrations were randomly inserted into tetrahedral sites and equilibrated at room temperature to generate Cottrell atmospheres. A dislocation obstacle was created ahead of the first dislocation by freezing some atoms. Under shear deformation the second and third dislocations were driven to pile-up against the first dislocation. For different H concentrations and shear stresses, the pile-up configurations were the same, suggestive of that H had no shielding effect on dislocation-dislocation interactions (see Fig. 2.28). Understanding the HELP mechanism thus requires examination of more complex dislocation/H interactions. Zhou et al. [130] analysed the effects of H charging on the mechanical behaviour of fcc Ni and Pd under nanoindentation. They found that H segregation slightly reduced the pop-in load for dislocation nucleation, and hardly influenced the indentation response after pop-in (see Fig. 2.29). Furthermore, the results showed that the change in pop-in load was directly

correlated with the H-induced swelling of the lattice. In other words, the presence of H simply showed lattice dilation, and no direct effects on dislocation plasticity. This information suggests that rate-dependent mechanisms related to fluctuating nucleation and H diffusion are presumably the cause of experimental observations of H-induced reduction in the pop-in load.

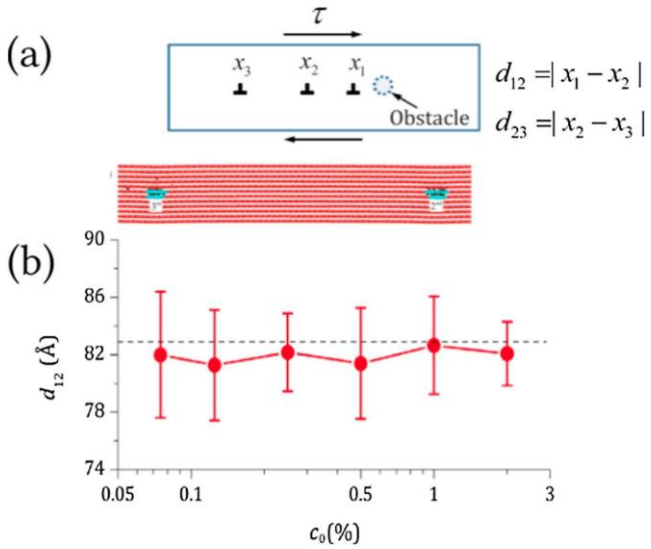

Fig. 2.28. (a) MD simulation model of dislocation pile-ups in α-Fe. (b) Equilibrium separation distance between dislocations with various H coverage [36].

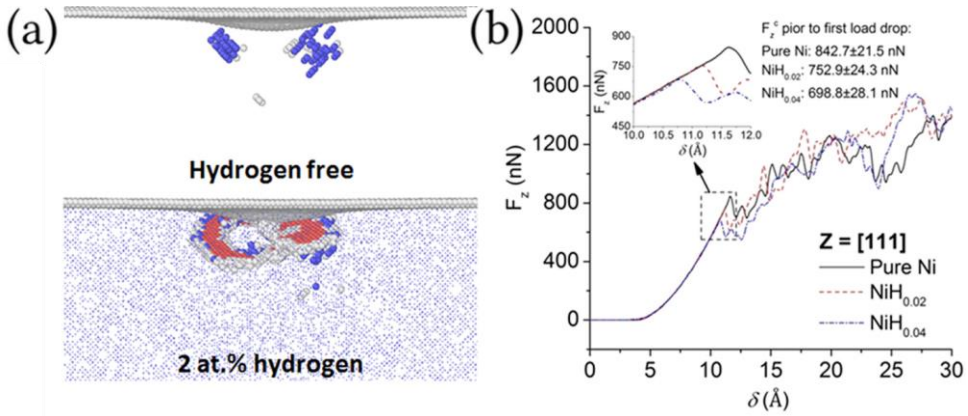

Fig. 2.29. (a) Image of dislocation nucleation during nanoindentation without and with H. (b) The indentation load as a function of indentation depth in pure Ni and Ni-H [110].

Tehranchi [131] studied the bow-out behaviour of an edge dislocation in Fe with and without H. Fig. 2.30(a) shows the H-free dislocation configuration subjected to shear stress. The bowed dislocation is asymmetric and mainly contains ≈70° and 45° segments connected via an intermediate edge segment. When the critical applied stress is reached, Orowan dislocation loops are formed around each obstacle, and the remaining dislocation glides through the simulation cell. The presence of H leads to a different result. Fig. 2.30(b) shows an H-charged dislocation configuration where the H diffusion is

asymmetric along the dislocation line. It is energetically unfavourable for H atoms to segregate to the 70° segment, and therefore H diffusion into the intermediate edge segment occurs. In contrast, H atoms prefer to remain in the 45° segment during the simulation. The high H diffusion barrier at glide direction of the 45° edge segments hinders the bow-out process. In particular, the intermediate edge segment acts as a secondary pinning point for the dislocation. Meanwhile the 70° segment containing less H atoms, can bow-out more easily. Thus overall, the shear stress required for dislocation escaping from the obstacle was pronouncedly increased in the presence of H atoms.

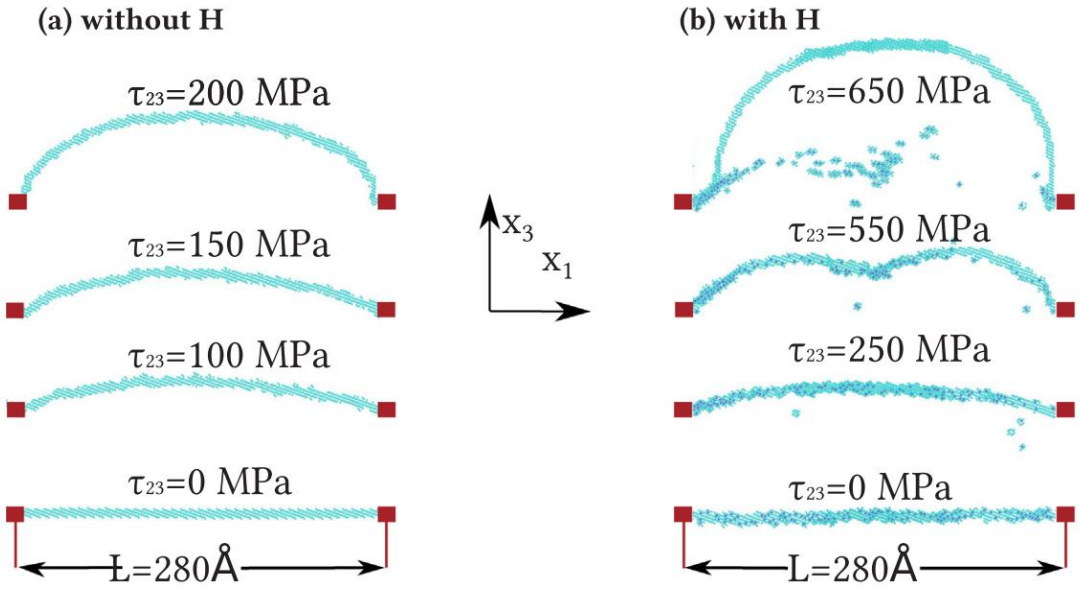

Fig. 2.30. Configurations of (a) H-free and (b) H-charged edge dislocation in Fe under applied shear stress [131].

2.3.3 Hydrogen interaction with crack tips/GBs

2.3.3.1 Basic theoretical framework

Before proceeding to the interaction between hydrogen and crack tips, the Griffith and Rice criteria for cleavage and dislocation emission must be reviewed. The influence of interstitial H atoms on the key parameters in each criterion is also presented. According to Griffith's theory, cleavage occurs when the rate of energy release at the crack tip $G = \alpha K_{Ic}^2$ reaches the critical value, $G_c = 2\gamma_i = \gamma_{s_1} + \gamma_{s_2}$(for single crystal), $G_c = 2\gamma_i = \gamma_{s_1} + \gamma_{s_2} - \gamma_{GB}$(for grain boundary), where γ_{s_i}(i = 1,2), and γ_{GB} are the energies of the surfaces made after cleavage and grain boundary energy, respectively. The critical stress intensity factor for cleavage can be determined as

$$K_{Ic} = \sqrt{\frac{2\gamma_i}{\alpha}} \tag{2.3}$$

The calculation of α has been well established, depending on the anistropic plane-strain moduli c_{ij} as [132].

$$\alpha = [\frac{\sqrt{c_{22}}}{2} \sqrt{2c_{11} + 2c_{12} + c_{44}}] \quad (2.4)$$

An important subtlety in using Eq. 2.3 is that the value of γ_i is required but the proper fracture surface for many intergranular crack problems is not well defined. The surface with the lowest energy may be kinked (non-flat), which changes the local crack tip stress intensity. The GB structure can also have a long periodic repeat distance, so the crack could be "trapped" in some local region of the GB where the local energy needed to extend the crack exceeds the average surface energy. Thus, the critical K_{Ic} computed by Griffith's theory may not be accurate, and could be lower or higher than an assessment based on an assumed fracture surface. The presence of H makes this problem even more complicated because H atoms generally reduce the surface energy and the GB energy, so it is not guaranteed that $2\gamma_i = \gamma_{s_1} + \gamma_{s_2} - \gamma_{GB}$ decreases in all cases.

Several models have been proposed to obtain the fracture energy in the presence of impurities [132-135]. Fig. 2.31 shows two of those models, proposed by Lu et al. [132] and Van der Ven and Ceder [133]. Starting from a layer of H atoms in the bulk metal, Lu et al. [132] simulated crystal decohesion by introducing a thick layer of vacuum and letting the H atoms remain on the surface. The advantage of this model was that it was straightforward to use DFT to directly calculate such a fracture energy ($2\gamma_i$) in one step, while the disadvantage was that the initial state was not a mechanically stable distribution of H in the bulk metal. As a result, in the high coverage regime, the initial states in this model became unstable due to the repulsion between H atoms. As shown below, this state needed not be invoked because H in particular was a very mobile impurity, freely diffusing from one interstitial site to another.

Van der Ven and Ceder [133,134] also investigated the effects of hydrogen impurities on the decohesion of a pair of Al (1 1 1) planes by an equilibrium thermodynamic description. They determined the energy and grand force potential of the cohesive zone as a function of lattice plane separation and hydrogen coverage using the first principles DFT and a lattice gas model Hamiltonian.

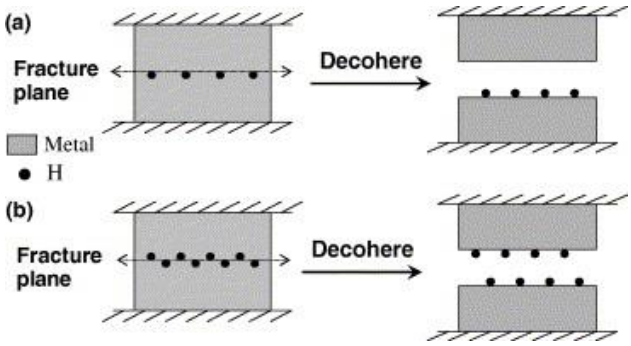

Fig. 2.31. Models used to calculate the fracture energy (2γ) as a function of H coverage (Θ_H) from DFT: (a) Lu et al.'s model [132]; (b) Van der Ven and Ceder's model [133,134].

Jiang and Carter [135] proposed an alternative means and computed the ideal fracture energy of metals (Fe and Al) in the presence of varying amounts of H, using periodic DFT. The ideal fracture energy as a function of H coverage can be expressed as follows:

$$2\gamma_i(\Theta_H) = -\Delta H_s + 2\gamma(0) + E_{ad}(\Theta_H) \quad (2.5)$$

The approaching using a Born-Haber thermodynamic cycle is illustrated in Fig. 2.32.

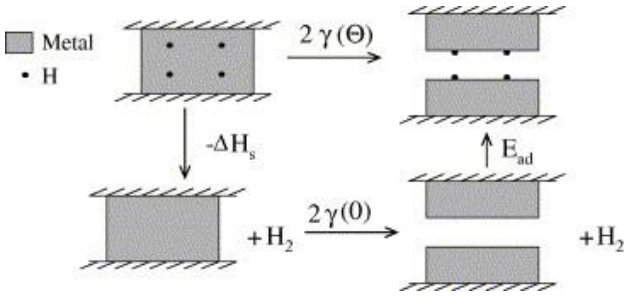

Fig. 2.32. The Born-Haber cycle used to calculate the ideal fracture energy $2\gamma_i(\Theta_H)$ along a certain plane of a single crystal at a hydrogen atom coverage Θ_H. ΔH_s: solution enthalpy of H_2 in the bulk metal. $\gamma(0)$: surface energy of the pure metal without hydrogen. E_{ad}: dissociative adsorption energy of H_2 on metal surfaces [135].

Yamaguchi and his teammates [136] calculated the change of $2\gamma_i$ from the GB and fracture-surface segregation energies of hydrogen and found that the cohesive energy (work of fracture) of the GB can be reduced significantly if many H atoms segregated at GBs and fracture surface. The cohesive energy can be expressed using the following equation:

$$2\gamma_i = (2\gamma_s + \Delta E^{seg,1}_{FS,total}/A + \Delta E^{seg,2}_{FS,total}/A) - (\gamma_{GB} + \Delta E^{seg}_{GB,total}/A) \quad (2.6)$$

here, A is the area of GB and surface plane of the unit cell.

Under pure mode-I loading, dislocations can be emitted along a slip plane inclined at an angle θ with respect to the crack plane if the critical stress intensity reaches a critical value K_{Ie}. In fcc materials, dislocation emission often proceeds via the nucleation of a leading partial dislocation which generates a stacking fault between the crack tip and

emitted dislocation [137, 138]. Within a Peierls model for the sliding of two surfaces and for an elastically anisotropic material, Rice [139] developed an approximate expression for K_{Ie} that depends on the unstable stacking fault γ_{usf} as

$$K_{Ie} = f_1(\theta)^{-1}\sqrt{\frac{2\mu}{1-v}\gamma_{usf}[1+(1-v)tan^2\emptyset]} \quad (2.7)$$

where

$$f_1(\theta) = cos^2(\theta/2)\sin(\theta/2) \quad (2.8)$$

where μ is the shear modulus, v is Poisson's ratio, θ and $\emptyset$ is the angle between the dislocation burgers vector in the slip plane under consideration and the vector perpendicular to the crack front in the slip plane [139-141]. For anisotropic materials, the effective value of μ is calculated using the convention from Zimmerman and Gao [142]. The introduction of H along the slip plane is envisioned to change γ_{usf} as a function of the H concentration, $\gamma_{usf}(c)$, and thus to change $K_{Ie}(c)$. Here, c is the number of H per surface metallic atom that would exist if the material were separated along the plane of interest. As for cleavage, this model neglects any other effects induced by the H, such as its effect at the surface step created upon dislocation nucleation or the modification of the local elasticity and/or stress field due to H, among other possibilities.

2.3.3.2 Hydrogen-assisted ductile-to-brittle transition

Because of the high mobility of H in metals [143], it is natural to postulate that ductile-to-brittle transition is related to hydrogen diffusion and accumulation [144]. In addition, MD simulations suggest that HE is related to the accumulation of H atoms in a tensile stress field. This accumulation not only enhances the pinning effect to dislocations, which can harden the material, it also decreases the free surface energy and stacking fault energy near the crack tip [26]. This mechanism can be expressed using two parameters, K_{Ie} and K_{Ic}, the stress intensity factors associated with the emission of first dislocation from the crack and with the initiation of crack cleavage, respectively. For a given material, if K_{Ie} is smaller than K_{Ic}, it will deform plastically near a crack tip. However, if K_{Ic} is smaller than K_{Ie}, it will start cleavage near a crack tip. Note here that any change in H concentration would likely change the free surface energy and stacking fault energy, which would then affect the relative values of K_{Ic} and K_{Ie}. As a result, a ductile material may have K_{Ic} smaller than K_{Ie}, which results in a ductile-to-brittle transition [26-28]. Song and Curtin [26] made continuum predictions for emission and cleavage using computed generalised stacking fault energies and surface energies in a

model Ni-H system, and then used an atomistic model to investigate actual crack tip behaviour in the presence of controlled arrays of H atoms around the crack tip. The procedure proposed by Van der Ven[133, 134] and standard method [28] were used to calculate the fracture energy and unstable stacking fault in the presence of hydrogen, as shown in Fig. 2.33 and Fig. 2.34.

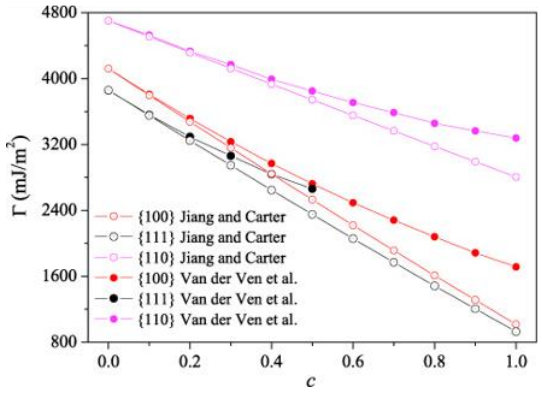

Fig. 2.33. Surface or fracture energy versus H concentration for {1 0 0}, {1 1 0} and {1 1 1} surfaces, as calculated using the methods of Van der Ven et al and Jiang et al [26].

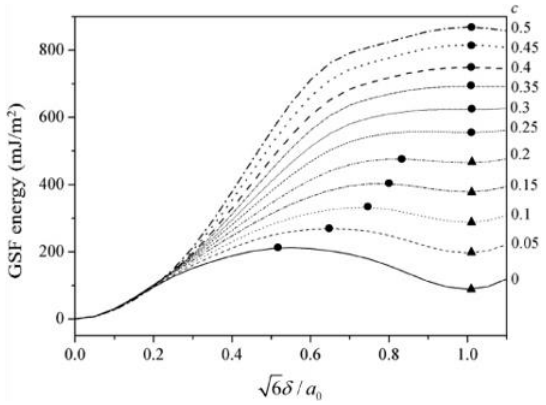

Fig. 2.34. GSF energy versus slip displacement δ on the {1 1 1} <1 1 2> slip system, for various H concentrations c. Unstable and stable stacking fault points are indicated by filled circles and filled triangles, respectively. a_0 is the equilibrium lattice parameter for Ni [26].

Fig. 2.33 shows that the (100) and (111) surface energies are not widely different, and neither is the effective elastic constant for fracture along these planes, leading to relatively small differences in the predicted values of K_{Ic} (c). However, the (110) surface energy is much higher. This indicates that it is more difficult to cleavage along the (110) surface than (100) or (111) surfaces. Fig. 2.34 shows that both unstable stacking fault γ_{usf} and stable stacking fault γ_{sf} increase with increasing H concentration, and that a stable stacking fault energy barely exists for concentration above $c > 0.15$, which indicates that the critical stress intensity for emission increases so as to make it difficult for dislocation emission. Simulations were then performed in the framework of the

coupled atomistic/discrete-dislocation (CADD) multiscale method, which consisted of a fully atomistic region around the crack tip surrounded by a continuum region that can contain discrete dislocations. Both brittle and ductile fracture were considered. As shown in Fig. 2.35(a), the measured K_{Ic} values deviate somewhat from the predicted values as H atoms are introduced along the crack plane, with discrepancy becoming larger as c increases. The origin of the discrepancy is likely associated with the local volume expansion due to introduction of H atoms, which leads to an additional compressive stress along the crack plane. In the ductile orientation, dislocation emission is observed along slip plane. Fig. 2.35(b) shows that K_{Ie} increases with increasing H concentration and closely follows the prediction value.

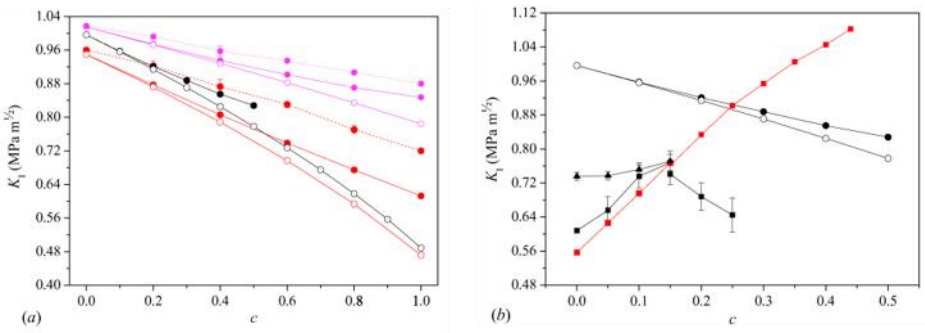

Fig. 2.35. Critical stress intensity factors K_{Ic} and K_{Ie} for brittle cleavage and dislocation emission, respectively, for various cleavage and slip planes, as a function of hydrogen concentration on the relevant plane. (a) Cleavage on plane {1 0 0} and (b) Emission in orientation (1 1 1)[1 1 2] [26].

In Song's further work [28], the HE problem in the presence of equilibrium H distributions around the crack tip was examined. Specifically, a new model was proposed wherein the diffusion of H to a crack tip led to a very high local H concentration that corresponded, essentially, to the formation of a "nanohydride" material. The key to this "nanohydride" material (e.g. H concentrations approaching those of the accepted bulk hydride phase) was its ability to prevent dislocation emission or absorption at the crack tip, thereby suppressing the blunting of cracks, inhibiting ductile fracture mechanisms, and driving cleavage failure. The analysis was performed in single crystal Ni and for several tilt GBs and several initial crack notch radii, using MS and embedded-atom-method interatomic potentials. Hydride formation was created with equilibrium segregation of H. With a simple solution model, the equilibrium H concentration $c(x)$ at site x can be determined by the difference in energy $\Delta E(x)$ between an H atom at position x and an H atom in the bulk crystal under zero load as:

$$c(x) = \frac{c_0 \exp[\Delta E(x)/K_B T]}{1 + c_0 \exp[\Delta E(x)/K_B T]} \tag{2.9}$$

where c_0 is the equilibrium H concentration (H atoms per Ni) in an unstressed bulk crystal, T is the temperature, and the positive $\Delta E(x)$ corresponds to binding, thus favouring segregation to site x relative to the bulk crystal. In any given system, c_0 is determined by an externally imposed chemical potential μ at temperature T. In the presence of a loaded crack, a major component of the energy is the elastic interaction energy $p(x)\Delta V$ where $p(x) = \sum_{i=1}^{3} \sigma_{ii}(x)/3$ is the crack-induced field at position x and ΔV is the misfit volume of the H atom. In the presence of H around the crack tip, dislocation emission can be inhibited such that the applied load can be increased beyond K_{Ie}. Increased loading then allows for a further accumulation of H atoms near the crack tip, which can further suppress dislocation emission. Fig. 2.36 and Fig. 2.37 illustrate the embrittlement mechanism explicitly for two different crack geometries. Obviously, with increasing load, the crack tip becomes completely surrounded by a growing nanohydride, which prevents dislocation emission and finally culminates in brittle cleavage through most of the nanohydride phase (see Fig. 2.36(e) and Fig. 2.37(e)).

In addition, Song and Curtin also calculated the size of the "nanohydride" formed at the crack tip as a function of hydrogen chemical potential, temperature, H diffusion rate, load level and loading rate. As Fig. 2.36 shows, the size of the nano-hydride is L and H atoms will move into this region and saturate it at an atomic ratio of 1.

$$\frac{\pi}{2}(L+R)^2 - \frac{\pi}{2}R^2 = 2.1c_0\left(\frac{5(1+v)D\Omega\dot{K}_I}{12\sqrt{2\pi}k_BT}t^2\right)^{\frac{4}{5}} \tag{2.10}$$

Using $K_I = \dot{K}_I t$, the nanohydride size L as a function of K_I can be obtained by

$$L = \sqrt{R^2 + (\frac{K_I}{A_0})^{\frac{8}{5}}} - R \tag{2.11}$$

where

$$A_0 = \left(\frac{1.67\sqrt{2\pi}k_BT}{(1+v)D\Omega}\right)^{1/2} c_0{}^{-\frac{5}{8}}\dot{K}_I{}^{\frac{1}{2}} \tag{2.12}$$

A_0 is the single parameter that combines the effects of concentration, diffusion coefficient, stress intensity loading rate, and temperature that controls the kinetics of formation of the nanohydride, where R is the inner radius of crack tip, as shown in Fig. 2.36, c_0 is the H concentration far away from crack tip, v is Poisson's ratio, D is the diffusivity of H atom, Ω is the partial volume of hydrogen, $\dot{K}_I$ is the changing rate of stress intensity and k_B is the Boltzmann constant.

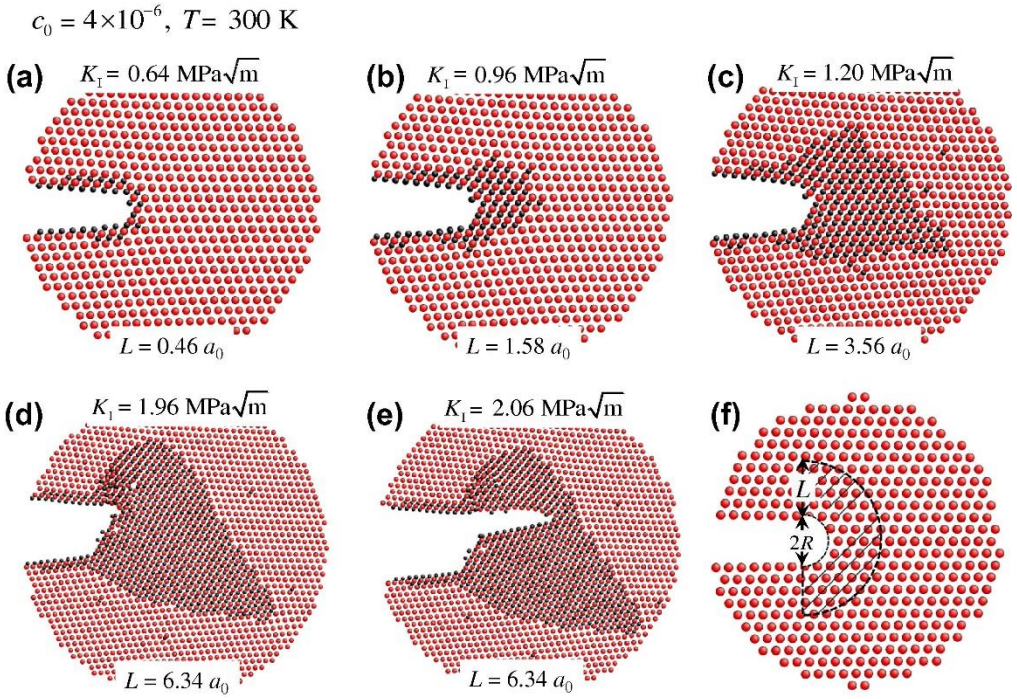

Fig. 2.36. Example of evolution of the nanohydride phase around a geometry I crack tip with increasing load (a)–(d) and (e) configuration at 1.96 MPa pm after loading to K_I = 2.06 MPa pm, where cleavage through the nanohydride occurs. (f) Schematic of simple geometry for characterizing the size L of nanohydrides [28].

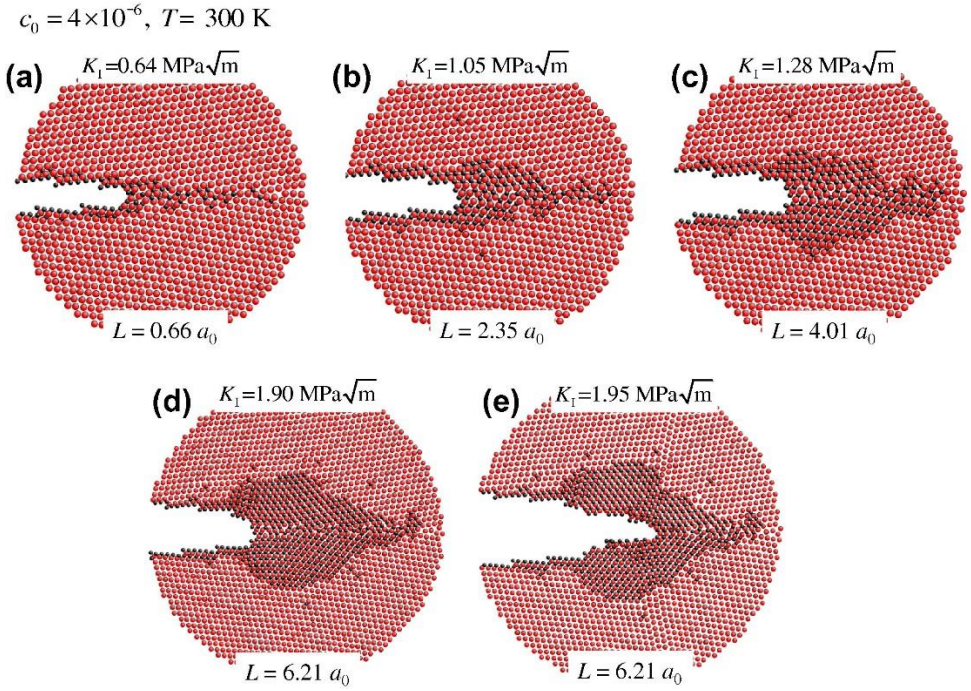

Fig. 2.37. Example of evolution of the nanohydride phase around a geometry IV crack tip at with increasing load (a)–(d) and (e) configuration at 1.90 MPa pm after loading to K_I = 1.95 MPa pm, where cleavage through the nanohydride occurs [28].

Xing et al. [145-147] investigated H-assisted ductile-to-brittle transition in α-iron under cyclic loading. An H concentration that corresponded to ductile-to-brittle transition

was predicted. Based on the estimated critical H concentration , the number of H atoms required to saturate the plastic zone and allowed for ductile-to-brittle transition to occur under specific experimental condition was calculated according to Eq. 2.13,

$$N_H^{total} = \frac{c_{critical} l_z [\pi (r_p + \bar{V}_r * t_{critical})^2 - \pi {r_p}^2]}{a_0^3/2} \quad (2.13)$$

where $c_{critical}$ is the theoretical value, $t_{critical}$ is the loading time corresponding to the critical loading frequency, l_z is the thickness of the specimen, and $\bar{V}_r$ is the average velocity of H movement at the boundary of the plastic zone.

Fig. 2.38 shows a crack growth model. The plastic zone under plain strain conditions can be approximated as a circular region with radius r_p. To reach the dynamic equilibrium of H concentration in the plastic zone during cyclic loading, an annulus region with an inner radius r_p and an outer radius R_{eq} is needed to supply and deplete the H atoms. The H concentration outside of plastic zone is estimated to be c_0. Therefore, the minimum time, $t_{critical}$, for H diffusion in/out of circular region during cyclic load to satisfy the dynamic equilibrium hydrogen concentration in plastic zone is related to critical frequency through $f_{critical}$=1/(2$t_{critical}$). The diffusivity of H atoms outside the plastic zone is assumed to be constant since these regions are not stress concentrated. As the stress intensity changes from K_{min} to $K_{\max}$ in a range of time t, the H atoms can diffuse into the plastic zone from a farthest position r_p +R_{eq}. The total volume of the annulus red region in Fig. 2.38 which offers H atoms to the plastic zone during loading can be estimated as $l_z[\pi(r_p + R_{eq})^2 - \pi {r_p}^2]$, where $R_{eq} = \bar{V}_r * t$ and $\bar{V}_r$ is the average velocity of H movement. The total number of Fe atoms contained in the red region is $l_z\left[\pi\left(r_p + R_{eq}\right)^2 - \pi {r_p}^2\right]/(a_0^3/2)$, where $a_0^3/2$ is the volume taken by each Fe atom. The total number of H atoms needed to saturate the plastic zone is equal to an atomic ratio of H/Fe (c_0) multiplied by the number of Fe atoms.

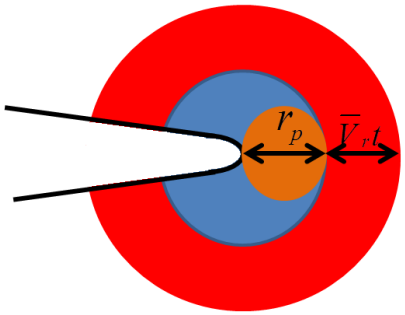

Fig. 2.38. The geometry of a crack, where the orange circular region is the plastic zone, and the blue region is a circle region where the radius is equal to r_p. The red annulus region is to offer and deplete the hydrogen atoms [145].

Matsumoto and Taketomi [127] applied the MD method to examine the mode I crack growth in α-Fe single crystals with and without H. With the same orientation (ductile orientation), crack propagation was carried out at 100K and 400K. The simulation results showed that there was no dislocation emission at 100K because of a lower temperature than the ductile-to-brittle transition temperature, while at 400K, dislocation emission from the crack tip and crack propagation along the {112} slip plane were observed at high frequency with H atoms. Fig. 2.39 shows the crack propagation for three cases of H concentrations. It is clear that dislocations are first emitted from a crack tip along the slip plane, and the crack propagation is then promoted along the slip plane. They analysed the interaction between dislocation and H atoms [128] and concluded that the H atoms at a dislocation cores reduced the energy barrier for dislocation motion and increased dislocation mobility. The crack propagation (separation of the slip plane) was mainly due to the H atoms trapped at dislocation cores, and such separation was connected among pile-up dislocations. The above mechanism was a hybrid of the HELP and the HEDE. The fracture was related to the HELP mechanism in that plastic deformation with dislocations was needed prior to the fracture. On the other hand, the fracture was associated with the HEDE mechanism in that the fracture resulted from the separation of a slip plane.

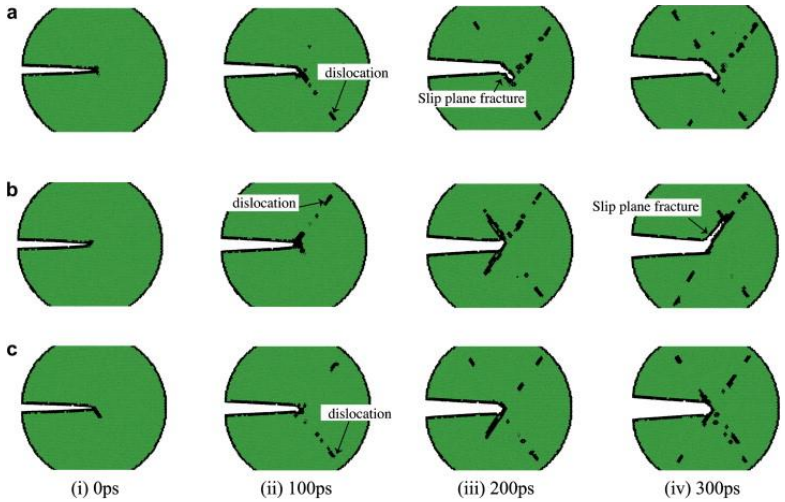

Fig. 2.39. Snapshots of crack propagation behavior for the crystal orientation (B) at 400 K. (a) $x^0 = 1.0 \times 10^{-4}$ (b) $x^0 = 3.0 \times 10^{-4}$ (c)$x^0 = 0$ [127].

In Matsumoto's further study [147], the effect of H on dislocation emission from a mode II crack in α-Fe was investigated using an atomistic model. It was found that H reduced the stacking fault energy of α-Fe, resulting in an enhancement of dislocation emission, but the distance from the H atoms to the crack tip was only limited to a few angstroms. They also confirmed that dislocation enhancement can occur at realistic H

concentrations of H gaseous under thermal equilibrium conditions.

2.3.3.3 Intergranular fracture/decohesion along GBs

The HE is often prone to cleavage-like failure, frequently along GBs in polycrystalline metals [148, 149]. Cleavage-like failure implies that sharp cracks can propagate without blunting, and this points towards studying crack-tip specific phenomena associated with H. Based on the analysis in Section 2.3.3.2, the same competition between dislocation emission and cleavage is expected to be relevant, with the expectation that (i) cleavage along a GB is easier than in the bulk crystal, (ii) dislocation emission which occurs into the grains is similar to emission in the bulk crystal, (iii) H segregation to the GB should decrease the stress intensity required for cleavage, and (iv) emission may be influenced by H on the cleaved GB surfaces, but perhaps not by H accumulation along the slip plane.

Tehranchi and Curtin [29] performed atomistic simulations to study the effects of segregated H on the behaviour of cracks along various symmetric tilt GBs in fcc Ni. The existing EAM potential was modified by changing some parameters that described the Ni-H interactions. The binding energy of H atoms to various atomic sites in studied GBs, and to various surfaces created by separating these GBs into two possible fracture surfaces were computed and used to determine equilibrium H concentrations at bulk H concentrations typical of embrittlement in Ni. Table 2.3 shows the results of the theoretical predictions of the Griffith's and Rice's theories as well as the simulation results, which indicates that no ductile-to-brittle transition is observed for the predicted ductile cracks in the presence of segregated H atoms along any of the GBs studied. However, H atoms make cleavage easier for crack growth in the intrinsically brittle directions. For example, for Ni Σ99(557)⟨110⟩ GB, the predicted cleavage load decreases from 1.00 $MPa\sqrt{m}$ in pure Ni to 0.92 $MPa\sqrt{m}$ in the presence of H. Simulations in pure Ni show partial cleavage at 0.912 $MPa\sqrt{m}$, with cleavage finally occurring at 1.52 $MPa\sqrt{m}$. In the presence of H, the final cleavage load to 1.072 $MPa\sqrt{m}$, approaching the predicted values. It is worth noting that the simulated value is larger than the Griffith's prediction. This can be attributed to crack trapping within the GB structure. Griffith's theory considers only the surface energy, which is an average over the various structural units in the GB, while crack tip can be arrested within the higher-tougher regions in the simulation cases. With trapping, a higher K^+ is required for crack growth. If $K^+$is higher than the critical emission load($K^+ > K_{Ie}$), local plastic events can occur

prior to cleavage. In pure Ni Σ9(221)⟨110⟩ GB, the final event in the predicted cleavage direction is actually emission ahead of the crack tip and thus no cleavage is observed. In the presence of H, the cleavage occurs along the GB in place of dislocation emission. The only ductile-to-brittle transition arises from the reduction of trapping effects rather than reduction in the fracture energy, which is so different from the results observed in Ni single crystal [28].

Barrows [150,151] employed a statistical approach combined with MD simulations to explore the influence of H on intergranular decohesion from atomistic simulation data during steady-state crack propagation along the GB. A range of <110> symmetric tilt GBs in Ni were studied, with H coverages and favourable sites for H segregation motivated by Monte Carlo calculations. Decohesion was assessed through extraction of a traction–separation relationship in a statistically meaningful approach based upon atomistic cohesive zone volume elements (CZVEs). They discussed how the H coverage influenced the details of crack propagation along the Σ3(112) symmetric tilt GB and concluded that increasing H asymmetrically influenced the crack tip velocity during propagation, which led to a general decrease in the work of separation required for crack propagation, and provided a reduction in the peak stress in the extracted traction-separation relationship.

Table 2.3. Theoretical and simulated cleavage and emission stress intensities for all GBs [29].

	c_0	Rice's theory (MPam)	Griffith's theory (MPam)	Simulation results (MPam)
NiΣ3(111)⟨110⟩	0.0	**1.01**	1.03	1.20 Cleavage
	0.001	**1.01**	1.03	1.20 Cleavage
	0.0	**0.38**	1.03	0.62 Emission
	0.001	**0.38**	1.03	0.58 Emission
NiΣ9(221)⟨110⟩	0.0	1.500	**0.98**	1.49 Rearrangement
	0.001	1.50	**0.97**	1.39 Cleavage
	0.0	**0.64**	0.98	0.72 Emission
	0.001	**0.64**	0.97	0.93 Emission of two partials
NiΣ99(557)⟨110⟩	0.0	1.41	**1.00**	1.52 Cleavage
	0.001	1.41	**0.92**	1.07 Cleavage
	0.0	**0.62**	1.00	0.63 Emission
	0.001	**0.62**	0.92	0.58 Emission
NiΣ5(120)⟨100⟩	0.0	N.A.	0.92	0.91 Cleavage

0.001	N.A.	0.75	0.65 Cleavage
0.0	N.A.	0.92	1.38 Cleavage
0.001	N.A.	0.75	1.20 Cleavage

2.3.3.4 Effects of H on the structure and deformation of GBs

One manifestation of H-induced failure is a transition in the failure mode from ductile transgranular to brittle intergranular. Although H-induced reduction in the cohesive strength is ultimately the cause of failure, the conditions for establishing this failure mode are driven by H-enhanced plasticity processes [106, 108, 109]. This includes the changes in the GB structure and local H concentration associated with slip transfer, as well as the increase in local stress around the GB due to the H-accelerated plasticity that occurs prior to the initiation of an intergranular crack.

O'Brien et al. [152] examined H segregation to misoriented GBs vicinal to the $\Sigma 3(111)[1\bar{1}0]$(coherent-twin) boundary. Results showed that the presence of H affected a change in structure of the boundaries with increasing concentration. Fig. 2.40 shows the preferred locations for H segregation in the case of low-angle boundaries. It can be seen that the structure of the boundary differs from that the H-free boundary. This structural change is due to the increasing concentration of H reducing the length of the extended stacking faults in Fig. 2.40(a)-(d).

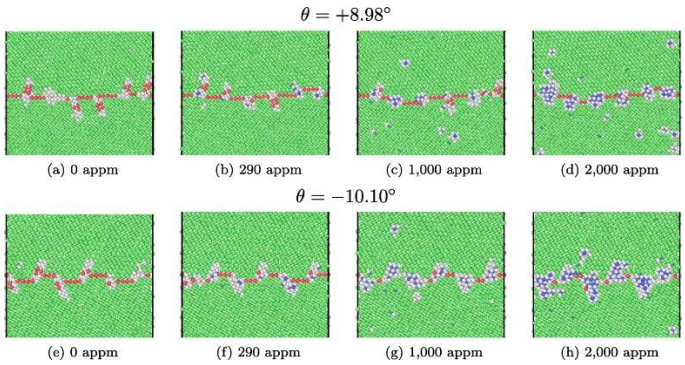

Fig. 2.40. Snapshots illustrating the preferred locations for H segregation [152].

Recently, Kuhr and Farkas [153] reported fully three-dimensional atomistic MD studies of the mechanical response of identical samples with and without H in the GBs. They selected random boundaries and applied tensile deformation in a strain-controlled virtual tensile test to examine the response of polycrystalline samples. The presence of H in the GBs can change the grain boundary structure, creating regions of high free volume at the sites of H clusters. Fig. 2.41 shows the overall distribution of dislocations in the H-free sample and H coverages of 3.2 H/nm^2. By comparing the deformation in each grain at various strains, it can be seen that the number of slip systems activated as

well as the number of events is greater in the sample with 3.2 H/nm^2 than in H-free material.

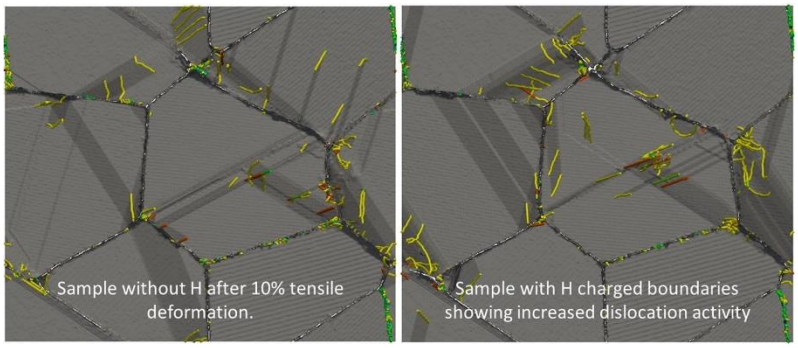

Fig. 2.41. Dislocation structures for samples without GB H (left) and 3.2 H/nm^2 (right) [153].

Fig. 2.42 shows the crack growth as a function of applied strain for various levels of H coverage at the GB. The results indicate that crack initiation on the GB is relatively insensitive to H coverage. Once cracks are nucleated in the GB, their growth is significantly enhanced by the presence of intergranular H. A further visual inspection suggests that the cracks nucleate in a region of high dislocation activity and close to the location at which a dislocation pile-up forms against the boundary.

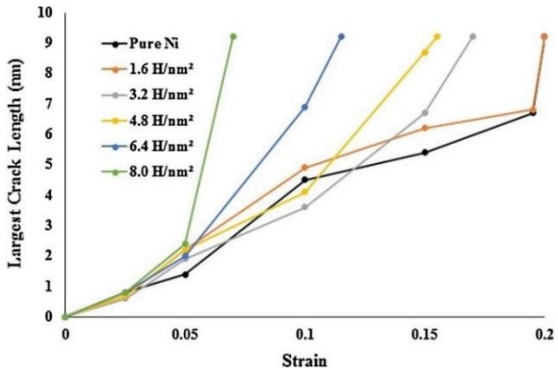

Fig. 2.42. Crack length as a function of applied strain for various levels of H coverage at the GB [153].

2.4 Summary

Notwithstanding such a rich literature explaining H-related phenomenon using experimental techniques, theoretical modelling and simulations, there are still strong debates and polarization of opinions on the underlying HE mechanisms [20, 35, 36, 39, 41, 131, 154]. Particularly, a comprehensive investigation on the role of GBs in the H-related deformation and failure is lacking. Some questions still remain open: (1) what atomic mechanism is responsible for H interaction with GBs and (2) how does the interaction process contribute to H embrittlement failure? In this thesis, the technique of MD simulations was used to study H segregation at various GBs and its influence on the

structure, mechanical properties, deformation mechanisms, and failure response of GBs. It is envisioned that these simulation results can provide important insights into experimental observations and enrich our knowledge of the multifaceted problem of HE.

Chapter 3 Fundamentals of atomistic simulations

As mentioned before, atomistic simulations such as MS and MD can provide information on the nanoscale H distribution around various defects, and probe the mechanical behaviour and fracture mechanisms in the presence and absence of H. In this chapter, basic research fundamentals such as the simulation method, potential selection, visualisation tools, and structure and defects identification are briefly introduced.

3.1 MS and MD simulations

In this thesis, MS simulations were performed to generate GBs with minimum energy, or the most favourable interface structures. MS simulations are a form of classical atomistic simulations that are implemented to determine minimum energy structures in the absence of temperature effects, i.e., they are performed at 0K. Energy minimisation is a process in which atoms can move from their initial positions with increments and directions that result in a decrease in the overall potential energy of the system. The energy minimisation approach used here utilises the conjugate gradient minimisation method. The conjugate gradient method can solve large systems of linear equations for a set of inputs and atom positions, and minimise a desired quantity and the potential energy. Ultimately, this is achieved using an iterative approach with minimum potential energy determined once the difference between the potential energy at one step and the potential energy at the next step is less than the user-defined threshold value. A more detailed explanation of the atomistic conjugate gradient method, and other minimisation methods for solving systems of equations, can be found in Shewchuk [90].

MD simulations were carried out to investigate the fundamental mechanisms of GBs in the presence of H. As classical mechanics based simulations, model atoms are modelled as unified spheres with a defined mass, and their trajectories and interactions are determined in accordance with Newton's 2nd law of motion and an interatomic potential:

$$m_i \frac{d^2 r_i(t)}{dt^2} = f_i \tag{3.1}$$

where m_i and r_i are the mass and position of the atom i. The fore f_i through which the particles interact with each other derives from the interaction potentials:

$$f_i = -\frac{\partial}{\partial r_i} U(r_1, \dots, r_N) \tag{3.2}$$

where U is potential energy, and $r_1, \dots, r_N$ consists of 3N spatial coordinates of the atomic

configuration.

All simulations were carried out using the Large-scale Atomic/Molecular Massively Parallel Simulator (LAMMPS) [155]. As a classical MD simulation code with a focus on materials modelling, LAMMPS was originally developed at Sandia National Laboratories, a US Department of Energy facility, and was designed to run efficiently on parallel computers. Performing a MD simulation requires three basic steps. First, a system of atoms must be created and assigned initial positions or velocities if necessary. Next, the thermodynamic state of the system must be fixed. Fixing the thermodynamic state of the system defines the equations of motion that the trajectories of the atoms will follow. Finally, the equations of motion that are defined by fixing the thermodynamic state of the system must be solved or integrated every timestep to update the positions and velocities of the atoms. The initial positions are determined by put atoms on the lattice sites with a crystallographic orientation. The velocities are randomly chosen from a Gaussian distribution with a mean of 0.0 and a sigma scaled to produce the required temperature:

$$\frac{3N}{2} k_B T = \frac{1}{2} \sum_{i=1}^{N} m_i \dot{r}_i^2(t) \tag{3.3}$$

where k_B is the Boltzmann constant and T is the temperature.

The Verlet algorithm is used to solve the equations of motion. Through Tayler expansion of the coordinate of a particle around time $t + \Delta t$ and $t - \Delta t$, the particle coordinate at time $t + \Delta t$ can be calculated by:

$$r_i(t + \Delta t) = 2r_i(t) - r_i(t - \Delta t) + \frac{f_i}{m_i} \Delta t^2 + o(\Delta t^4) \tag{3.4}$$

The velocity of the particle can be derived from:

$$v_i(t) = \frac{r_i(t+\Delta t) - r_i(t-\Delta t)}{2\Delta t} + o(\Delta t^2) \tag{3.5}$$

3.2 Potential selection

Semi-empirical interatomic potentials have been widely used in atomistic simulations such as MS and MD to study long-range phenomena including dislocation interaction with multiple H atoms and the H diffusion process into defects [26, 29, 125-127, 129, 147, 156-159]. The development of metal-H potentials is mainly based on the embedded atom method (EAM), with fitting of parameters to first-principle energetic calculations and experimental results. To date, Ni-H and Fe-H EAM potentials have been widely used in the literature. Notwithstanding some shortcomings, these potentials can be used to investigate specific deformation and failure mechanisms with carefully designed

simulations.

The well-established Ni-H EAM potential was first introduced by Angelo et al. [160]. This potential includes Ni-Ni, Ni-H, H-H interactions. As shown in Table 3.1, the parameters c_1, c_2, c_3, c_5, and r_{cut} are used to define the Ni-Ni interactions. The interactions of Ni and H are fitted by allowing c_1, c_2 and c_3 for the Ni-H pair interaction, c_4 and c_5 for the hydrogen electron density, and c_6, c_7, c_8, c_9 for the hydrogen embedding energy to vary. The cut-off distance for all interactions involving hydrogen is fixed at r_{cut} = 2.8 Å. Recently, Tehranchi and Curtin [29] made modifications to better reproduce the results obtained from the DFT method for H in the Σ5 boundary. The misfit volume of 3.27 $Å^3$ and H migration barrier in the modified potential agree well with the experimental values. Also, the H-H interaction energy is in good agreement with DFT calculations and energies required for the NiH hydrides. Consequently, this Ni-H potential is effective in probing various mechanics issues and phenomena such as H interaction with the stress field related to defects. Table 3.2 shows the original and revised values for the modified parameters in the potential and the relevant bulk properties of Ni.

Table 3.1. The parameters used to determine the embedded atom potential [160].

	Ni-Ni	Ni-H	H-H
$\boldsymbol{c_1}$	5.6411172	6.6090538	0.12027801
$\boldsymbol{c_2}$	1.4136118	1.0256391	0.00000000
$\boldsymbol{c_3}$	1.1333300	2.1101256	0.00000000
$\boldsymbol{c_4}$	1.0000000		5.5854322
$\boldsymbol{c_5}$	2.8448303		75.998895
$\boldsymbol{c_6}$			0.53419208
$\boldsymbol{c_7}$			13.526207
$\boldsymbol{c_8}$			22.592082
$\boldsymbol{c_9}$			1.1292331
$\boldsymbol{c_{10}}$	-19.743089		0.0000000
$\boldsymbol{r_{cut}}$(Å)	4.84	2.8	2.8

Table 3.2. Original and modified parameters for the Ni–H EAM potential based on the formulation of (Angelo et al.,[160]; Baskes et al.,[161]) [29].

Parameter	Original [160,89]	Modified
c_{10}^{H} (eV)	13.26	13.85
c_6(eV)	0.53419208	0.52
c_9	1.1292331	1.092
r_c^H (Å)	2.8	2.7
c_{11} (GPa)	251.7	251.7
c_{12} (GPa)	147.3	147.3
c_{44} (GPa)	130.6	130.6
γ_{usf} (mJ/m^2)	276	276

The currently used Fe-H potential was developed by Ramasubramaniam et al. [162] on the basis of the Fe potential by Ackland [163]. Song and Curtin [27] further modified the potential to eliminate unphysical H clustering at high H concentrations by introducing an additional repulsive term into the pairwise for H-H interaction in the form of a Weibull function,

$$f(r_{ij}, \lambda, k, C_0, B_0, r_0, r_1) = \begin{cases} C_0 \left[\frac{(r_{ij}-r_0)}{\lambda}\right]^{k-1} exp\left[-\left(\frac{r_{ij}-r_0}{\lambda}\right)^k - B_0(r_{ij}-r_1)^2\right] \; if \; r_{ij} \geq r_1, \\ C_0 \left[\frac{(r_{ij}-r_0)}{\lambda}\right]^{k-1} exp\left[-\left(\frac{r_{ij}-r_0}{\lambda}\right)^k\right] \; if \; r_0 \leq r_{ij} < r_1, \\ 0 \quad if \; r_{ij} < r_0. \end{cases} \tag{3.6}$$

where r_{ij} $(i \neq j)$ denotes the distance between H atoms i and j, with $\lambda, k, C_0, B_0, r_0$ and r_1 constant parameters. The second exponential term for $r_{ij} \geq r_1$is a tail treatment to ensure smooth termination of the function at the potential cutoff distance. This potential has reasonable bcc Fe properties, surface energy in the presence and absence of H, low H diffusion barrier, and stable FeH hydrides.

3.3 Ensemble

To solve or integrate the equations of motion, the positions and velocities of the atoms are updated every timestep under ensembles. There are three important thermodynamics ensembles used in MD simulations: microcanonical ensemble (NVE); isothermal ensemble (NVT); and isothermal-isostress ensemble (NPT) where N is the number of atoms, V is the volume, E is the energy, T is the temperature, and P is the pressure. The microcanonical ensemble (NVE) represents constant number of atoms, volume, and energy, and the sum of kinetic and potential energy is conserved. This ensemble is not suitable for cases with a desired temperature or pressure. The isothermal ensemble (NVT) can keep the system temperature constant by rescaling the temperature with the Nose-Hoover thermostat, the Berendsen thermostat, or the Langevin thermostat. In contrast, the isothermal-isostress ensemble (NPT) can control the temperature and the pressure by Nose-Hoover barostat or Berendsen barostat.

3.4 Boundary conditions

To save computing time and eliminate the influence of surface force, the periodic boundary condition is usually applied to the simulation model. Under periodic boundary conditions, particles interact across the boundary, and then exit from one end of the box

and re-enter at the other end. As shown in Fig. 3.1, the simulation box is repeated by copying itself 9 times for a two-dimensional system. The atom-a1 indicated by a green circle exits from one side of the box boundary and re-enter the box on the opposite side (atom-a2 marked by a purple circle).

Sometimes, to focus on the individual boundary and exclude the effects of secondary boundary, free boundary conditions are set to encompass the atoms in that dimension, no matter how far they move.

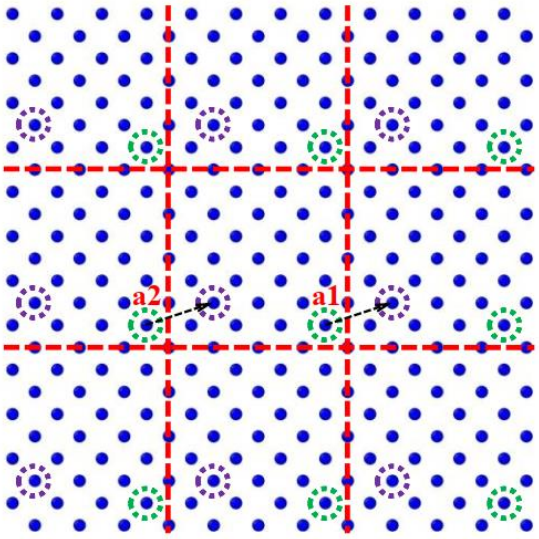

Fig. 3.1. Two-dimensional periodic boundary condition where the central configuration is surrounded by its copies.

3.5 Visualisation Methods

After the set-up of suitable models, MD calculations usually produce huge amounts of data, i.e., position and velocity components are available for thousands of atoms and for thousands of time steps. To go into the detailed properties of a nanocrystalline, the essential information for whole atoms must be captured. This process often includes a great deal of grains within the atomic configuration and in turn involves a large number of atoms. Atomeye [164], AtomViewer [165] and Ovito [166] are used for visualisation and data analysis for output by large-scale MD/MS and Monte-Carlo simulations. They provide many customised functions to identify and accentuate certain structural characters of an atomistic configuration. These methods facilitate the observation of atomic scale processes related to thermal processes during sample annealing or to deformation mechanisms during plastic deformation. The major visualisation methods used in this thesis to calculate potential energy, local stress and strain, centrosymmetric parameter and

common neighbour analysis (CNA) parameter are summarised in the following.

3.5.1 Potential energy

Atoms can be coloured by their local potential energy and viewed in visualisation software. In nanocrystalline systems, structural defects such as GBs can be identified by only showing the atoms with potential energies higher than a certain threshold. Note that care must be taken in using this method to identify the GB region because by definition, only those atoms in a high energy configuration are considered, which naturally biases the probed GB structure to more disordered configurations. Fig. 3.2(a) shows the atomic positions of those atoms with a cohesive energy of approximately 0.1 eV higher than the fcc crystalline energy. With this criterion the GB and partial dislocation core are visible.

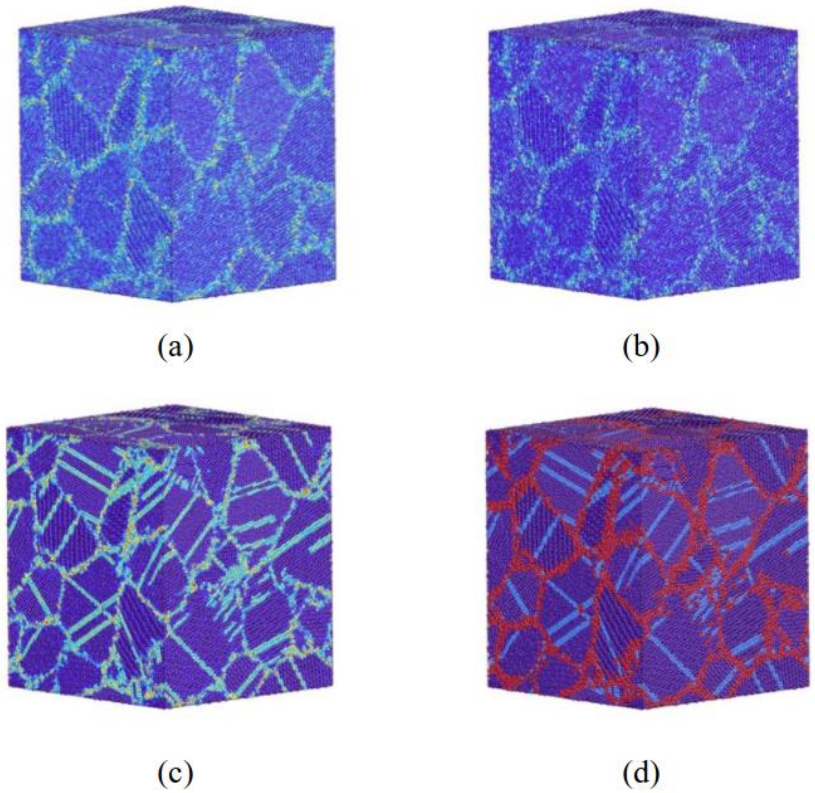

Fig. 3.2. Four different methods of visualization of grain boundary and dislocation segment within a nanocrystalline environment. Atoms are shaded according to (a) potential energy, (b) local stress, (c) centrosymmetric parameter and (d) common neighbour analysis (CNA).

3.5.2 Local stress

The instantaneous stress tensor of each atom can be calculated by the virial stress [167]:

$$\sigma_{ij} = \frac{1}{V}\left(\frac{1}{2}\sum_j \sum_{i \neq j} \frac{U'}{r^{ij}} r_\alpha^{ij} r_\beta^{ij} - \sum_i m^i v^i v^i\right) \quad (3.7)$$

Here, V stands for the volume of partition element, U' is the derivative of the potential energy with respect to position. α and β denote the indices in the Cartesian coordinates and i and j are atom index numbers. r^{ij} is the distance between atom i and j. m and v indicate the mass and velocity of the atom. Fig. 3.2b shows how the atoms are shaded according to local stress.

3.5.3 Centrosymmetric parameter

In solid-state systems the centrosymmetry parameter (CSP) [168] is a useful measure of the local lattice disorder around an atom and therefore can be used to characterise whether the atom is part of a perfect lattice, a local defect (e.g. a dislocation or stacking fault), or is located at a surface. The CSP value of an atom having N nearest neighbours (N = 12 for fcc cubic, N = 8 for bcc lattices) is given by:

$$P_{CSP} = \sum_{i=1}^{N/2} \left| r_i + r_{i+N/2} \right|^2 \tag{3.8}$$

where r_i and $r_{i+N/2}$ are vectors pointing from the central atom to a pair of opposite neighbours. For lattice sites in an ideal centrosymmetric crystal, the contributions of all the neighbour pairs in this formula will be cancelled, and the resulting CSP value will be zero. Atomic sites within a defective crystal region, in contrast, typically have a disturbed, non-centrosymmetric neighbourhood. In this case the CSP becomes positive. Using an appropriate threshold, to allow for small perturbations due to thermal displacements and elastic strains, the CSP can be used as an order parameter to filter out atoms that are part of crystal defects.

3.5.4 Common neighbour analysis

To identify the defective structure and its evolution during the simulations, the common neighbour analysis (CNA) technique [169] is used. It gives a classification of all the atoms by their local crystallinity. This visualisation of grain and GB structures has been greatly facilitated by a medium range order analysis of all atoms within the sample, which ascribes a local crystallinity class to each atom. This is carried out by selecting the common neighbours of a pair of atoms separated by no more than a second nearest neighbour distance, and introducing a classification scheme for the nearest-neighbour bond pathways between the two atoms.

The structural type determined by the algorithm is encoded as an integer value:

1 = fcc, face-centred cubic

2 = hcp, hexagonal close-packed

3 = bcc, body-centred cubic

4 = ico, icosahedral coordination

5 = other, unknown coordination structure

The CNA calculation can be sensitive to the specific cutoff value. It should be insured that the appropriate nearest neighbours of an atom are found within the cutoff distance for the presumed crystal structure, e.g. 12 nearest neighbours for perfect fcc crystals, and 14 nearest neighbours for perfect bcc crystals. The following formulae can be used to obtain a good cutoff distance:

$$r_c^{fcc} = \frac{1}{2}\left(\frac{\sqrt{2}}{2} + 1\right) a_0 \approx 0.8536a \tag{3.9}$$

$$r_c^{bcc} = \frac{1}{2}\left(\sqrt{2} + 1\right) a \approx 1.207a \tag{3.10}$$

where a_0 is the lattice parameter for the crystal structure.

3.6 Dislocation extraction algorithm

The authors of Ovito developed a computational method, namely, dislocation extraction algorithm (DXA) to identify all the dislocation line defects in an atomistic crystal, determine their Burgers vectors, and output a line representation of the dislocations [165, 170]. This algorithm can recognise partial dislocations and also certain secondary grain boundary dislocations (such as twinning dislocations in fcc).

The fundamental concept underlying the DXA is the Burgers circuit construction [171], which is the canonical method already proposed in the 1950s to discriminate dislocations from other crystal defects, and to determine their Burgers vectors. In the formulation employed in the dislocation analysis, a Burgers circuit C is a path in the dislocated crystal consisting of a sequence of atom-to-atom steps (line elements ΔX), as shown in Fig. 3.3. Assuming there is a mapping $\Delta X \rightarrow \Delta X'$ that translates each line element of the path to a corresponding image $\Delta X'$ in a perfect crystal lattice. Summing these transformed line elements algebraically along the associated path C', gives the true Burgers vector of the dislocation enclosed by C:

$$b = -\sum_{C'} \Delta X' \tag{3.11}$$

The Burgers vector b is the closure failure of the path after transferring it to the perfect reference crystal. Notably, the resulting vector b stays the same if we change the original circuit C, as long as it still encloses the same dislocation. On the other hand, if $b = 0$, it is known that the Burgers circuit did not enclose any defect with dislocation

character (deliberately ignoring the possibility that the circuit encloses multiple dislocations whose Burgers vectors cancel).

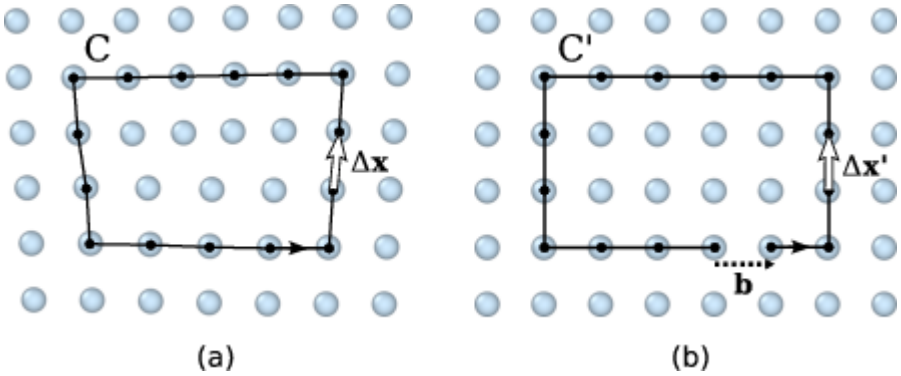

Fig. 3.3. Burgers circuit method to detect and identify a dislocation. A closed circuit around the dislocation is translated from (a) the dislocated crystal to (b) the perfect reference crystal. The closure failure is called the Burgers vector of the dislocation.

3.7 Summary

Molecular dynamics simulations can provide important insights by supporting or contradicting conjectures and concepts to rationalise experiments. For HE phenomenon, they can provide information on the nanoscale H distribution around various defects, and probe the mechanical behaviour and fracture mechanisms in the presence and absence of H. In this chapter, basic fundamentals such as the simulation method, potential selection, visualisation tools, and structure and defects identification have been introduced in detail.

Chapter 4 Influence of hydrogen segregation on tensile deformation behaviour of grain boundaries

This chapter is extracted from the following publications:

1. **Li J,** Lu C*, Pei L, Zhang C, Wang R, Tieu K. Influence of hydrogen environment on dislocation nucleation and fracture response of <110> grain boundaries in nickel. Comput Mater Sci. 2019;165:40-50.

2. **Li J,** Lu C*, Pei L, Zhang C, Wang R, Tieu K. Atomistic simulations of hydrogen effects on tensile deformation behaviour of [0 0 1] twist grain boundaries in nickel. Comput Mater Sci. 2019;159:12-23.

4.1 Introduction

The segregation of solute H has a profound effect on mechanical properties of GBs. In this chapter, systematic MD simulations were performed to investigate H segregation at various GBs and its influence on mechanical response and dislocation nucleation of different GBs in Ni. The results showed that the trapping ability of H was strongly dependent on GB structures. GBs containing more open structure or significant excess volume had higher maximum excess H concentration. Analysis of stress-strain curves showed that the segregation of H resulted in a decrease/increase in the yield stress of GBs depending on different GB types. This phenomenon was directly associated with different deformation mechanisms in the presence of H. The remainder of this chapter is organized as follows. The simulation methodology is described in Section 4.2, H segregation maps, mechanical response and deformation mechanisms are presented in Section 4.3, followed by our summary in Section 4.4.

4.2 Simulation methodology

All simulations were implemented with MD simulator LAMMPS [155]. The semi-empirical EAM potential for Ni-H used in the present study was first introduced by Angelo et al. [160] and then modified by Curtin et al. [28，29] to eliminate the instability of NiH hydrides. Twelve types of $[1\bar{1}0]$ symmetric tilt GBs were constructed by rotating grain-A above the interface plane around the Z axis by θ/2 clockwise, while rotating

grain-B underneath the grain boundary by θ/2 counterclockwise, as shown in Fig. 4.1. The simulation cell was modelled with periodic boundaries along X and Z directions and free boundary condition in Y direction. After GB initialization, various in-plane rigid body translation of grain-A with respect to grain-B combined with atom deletion criteria were adopted to determine optimal GB structures.

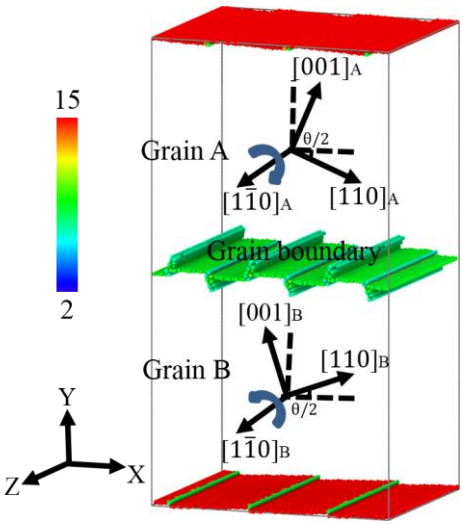

Fig. 4.1. Schematic diagram of a bicrystal model with [1$\bar{1}$0] tilt GB.

In order to search all possible trapping sites for H atoms at each GB type, the Voronoi tessellation of atoms was constructed with Voro++ code [172]. The each Voronoi vertex was concerned as a specific trapping site for solute H. After placing H atom at a particular site α, initial Ni-H configuration was constructed and optimized via the conjugate gradient process. The segregation energy for one H atom at the one type of trapping site α is calculated by

$$E_{\alpha}^{seg} = (E_{GB}^{\alpha} - E_{GB}) - (E_{O-site} - E_{bulk}) \quad (4.1)$$

where E_{GB}^{α} and E_{GB} represent the total system energies of GB structures with and without H atom, respectively. E_{O-stie} is the system energy associated with H atom trapped into a lattice octahedral site in the single crystal bulk, and E_{bulk} is the total energy of a single crystal bulk.

The considered GBs are characterized by the excess enthalpy (GB energy) defined as

$$\gamma_{GB} = \frac{E_{slab} - N_{Ni}E_{atom}}{A} \quad (4.2)$$

where E_{slab} is the total potential energy of Ni atoms within a slab extending $\pm$15 Å normal to the boundary plane, N_{Ni} means the number of Ni atoms within the slab, E_{atom} is the cohesive energy per Ni atom in the bulk, and A is the area of boundary plane. In general, a higher value of γ_{GB} indicates a weaker cohesive strength of GBs. Excess

volume is also introduced to characterize the GBs as

$$\Delta V_{GB} = \frac{V_{slab} - N_{Ni} V_{atom}}{A} \quad (4.3)$$

where V_{slab} is the total Voronoi volume of Ni atoms within the slab, and V_{atom} is the Voronoi volume per Ni atom in the bulk. A lower value of ΔV_{GB} indicates a more compact boundary structure.

The efficiency of H segregation into GBs, referred to excess H concentration, is expressed as

$$C_H = \frac{N_H}{A} \quad (4.4)$$

where N_H is the number of H atoms within the slab.

Based on the segregation energy map, a series of Ni-H interactions under various excess H concentrations were created by successively adding one H atom into 'favourable' trapping sites until all 'favourable' sites were occupied. Herein we define all sites with segregation energy lower than zero (octahedral sites in bulk) as 'favourable'.

For all cases, the simulation cell was equilibrated within isobaric-isothermal (NPT) ensemble at desired temperature and pressure for 0.1 ns (*i.e.*, $T = 10K, \sigma_{xx} = \sigma_{zz} = 0$ GPa) prior to tensile loading. Then, the tensile deformation was applied along *Y* axis for each case to investigate the H effect on mechanical response of GBs. Atoms within 10 Å of the top and bottom were frozen, and did not enter into MD simulations. The simulation cell was subjected to a successive incremental loading (about 10^8 s^{-1} constant tensile strain rate) by displacing frozen atoms (top and bottom) in opposite directions. During the MD simulations, the temperature was kept at 10 K via the Nose–Hoover thermostat, and the time increment of simulation was set 1 fs.

4.3 Results and discussion

4.3.1 GB structure and energy

All GBs considered in the present study are listed in Table 4.1, and atomic configurations of typical equilibrium GB structures are illustrated in Fig. 4.2. Five basic structural units (SUs) are identified and labelled among these GBs. Specifically, C, D and E SUs correspond to Σ11 (1 1 $\bar{3}$), Σ3 (1 1 $\bar{1}$) and Σ9 (2 2 $\bar{1}$) GBs, A and A' SUs are basic units of Σ1 (001) θ = 0° and Σ1 (110) θ = 180° perfect crystal orientations. Other GBs with non-preferred misorientation come from a combination of these basic SUs with complexity. For example, Σ153 (4 4 $\overline{11}$) GB is composed of C and D SUs (7C + D), Σ11 (3 3 $\bar{2}$) GB contains a combination of D and E SUs (D + E), and GBs with $\theta > 141.06°$

contain E and A/A' SUs. Note that the dissociated boundary structures are observed in three GBs: Σ3 (1 1 $\bar{2}$), Σ153 (4 4 $\overline{11}$) and Σ171(11 11 $\overline{10}$), where D SUs extend from one or two sides of the boundary, resulting in intrinsic stacking fault (ISF) facets inside lattice region. Table 4.1 lists the GB energy and excess volume for each case in the [$1\bar{1}0$] system. It can be seen that both GB energy and excess volume exhibit two minor cusps with respect to the favoured Σ11 (1 1 $\bar{3}$) GB and Σ3 (1 1 $\bar{1}$) GB (coherent twin boundary), which own very simple boundary structures (C and D SUs).

Table 4.1. Model parameters for twelve GBs after energy minimization.

Tilt angle θ (°)	GB normal $(hkl)_A/(hkl)_B$	Model size $\boldsymbol{Lx, Ly, Lz(nm)}$	$\boldsymbol{\gamma_{GB}}$ $\boldsymbol{(mJ \cdot m^{-2})}$	GB atoms (%)	$\boldsymbol{\Delta V_{GB}}$ (Å)
38.94	Σ9(1 1 -4)/(1 1 4)	13.72, 23.71, 10.95	800.97	3.1	0.3333
50.48	Σ11(1 1 -3)/(1 1 3)	13.20, 23.30, 10.95	375.80	2.5	0.1962
54.43	Σ153(4 4 -11)/(4 4 11)	12.31, 26.08, 10.95	617.27	2.6	0.2066
70.53	Σ3(1 1 -2)/(1 1 2)	13.41, 22.24, 10.95	806.91	3.9	0.2661
86.63	Σ17(2 2 -3)/(2 2 3)	12.31, 22.95, 10.95	870.27	3.0	0.3041
97.05	Σ57(4 4 -5)/(4 4 5)	15.03, 21.02, 10.95	731.82	3.1	0.2577
109.47	Σ3(1 1 -1)/(1 1 1)	13.79, 22.58, 10.95	50.39	1.8	0.0803
114.53	Σ171(11 11 -10)/(11 11 10)	13.80, 25.85, 10.95	419.64	2.8	0.2440
129.52	Σ11(3 3 -2)/(3 3 2)	13.99, 22.81, 10.95	920.38	2.6	0.3641
141.06	Σ9(2 2 -1)/(2 2 1)	13.43, 22.99, 10.95	1097.49	4.1	0.3743
153.48	Σ19(3 3 -1)/(3 3 1)	12.99, 24.21, 10.95	1081.91	3.3	0.3884
166.56	Σ73(6 6 -1)/(6 6 1)	12.75, 24.06, 10.95	877.01	1.7	0.3342

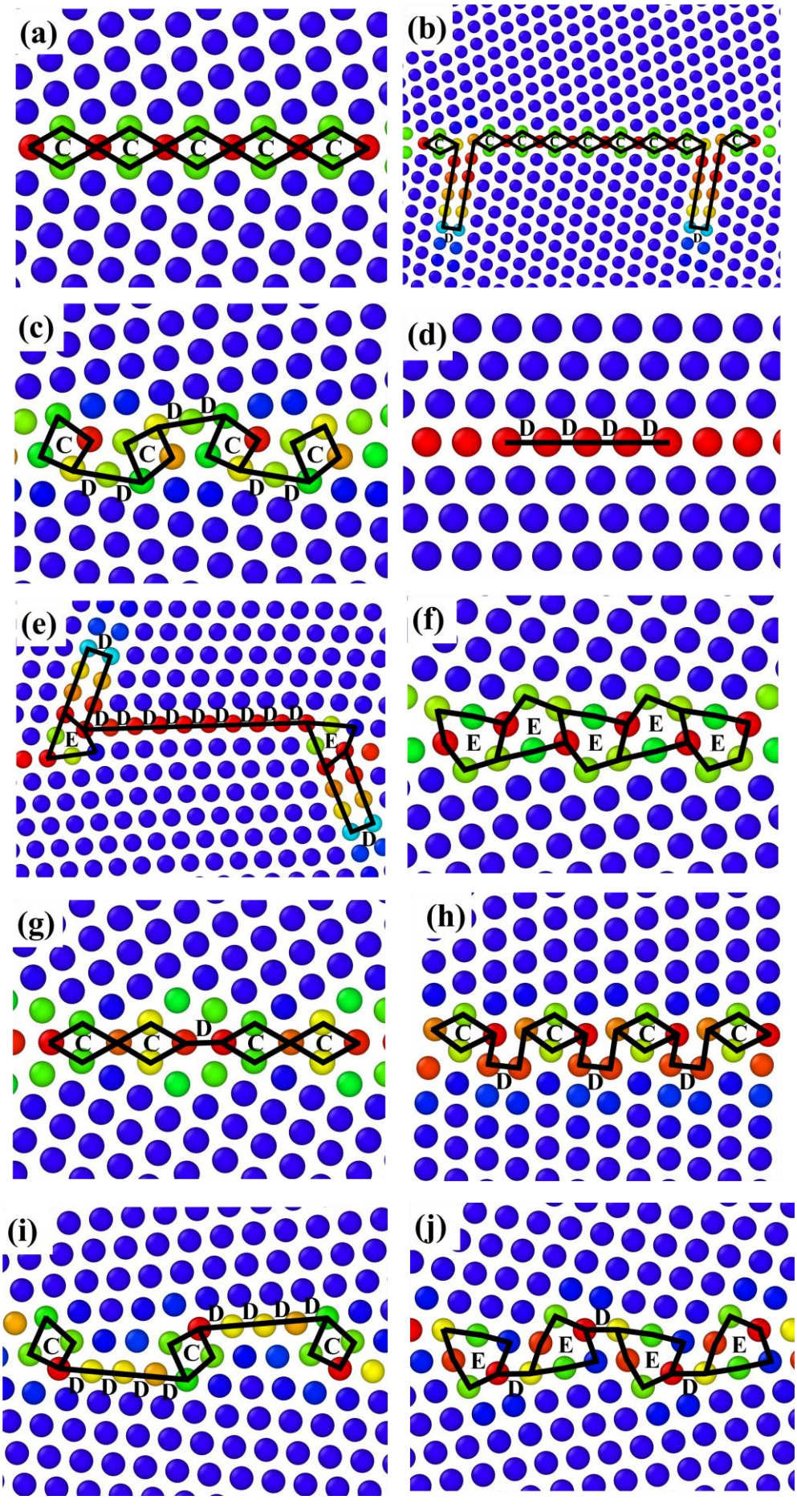
(a)
C C C C C
(b)
C C C C C C C C C
D D
(c)
D D
C C C C
D D D D
(d)
D D D D
(e)
D
D D D D D D D D D
E E
D
(f)
E E E E E E
(g)
D
C C C C
(h)
C C C C
D D D
(i)
D D D D
C C C
D D D D
(j)
D
E E E E E
D D

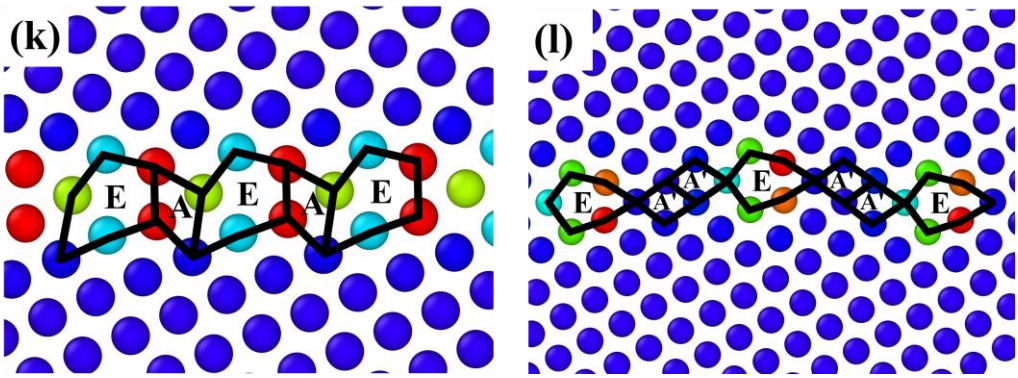

Fig. 4.2. The equilibrium [$1\bar{1}0$] GB structures with SUs (a) Σ11 (11-3) = 50.48°, (b) Σ153 (44-11) = 54.43°, (c) Σ57 (44-5) = 97.05°, (d) Σ3 (11-1) = 109.47°, (e) Σ171 (1111-10) = 114.53°, (f) Σ9 (22-1) = 141.06°, (g) Σ9 (11-4) = 38.94°, (h) Σ3 (11-2) = 70.53°, (i) Σ17 (22-3) = 86.63°, (j) Σ11 (33-2) = 129.52°, (k) Σ19 (33-1) = 153.48°, and (l) Σ73 (66-1) = 166.56°. The structures are shown along the [$1\bar{1}0$] tilt axis, where atoms are coloured according to their centro-symmetry parameter.

4.3.2 H trapping map

Based upon identified equilibrium structures of GBs, we plot H segregation energy maps for typical GBs in Fig. 4.3. The possible trapping sites are indicated by small spheres and coloured according to the segregation energy. As shown in Fig. 4.3, different GBs possess unique H trapping maps. Combined with segregation energy distribution curves in Fig. 4.4, it is found that trapping sites with the lowest segregation energy are located at the boundary planes except Σ3 (1 1 $\bar{1}$) coherent twin boundary. For coherent twin boundary, GB plane contains no octahedral interstitial sites as local stacking sequence of (111) layers is A-B-A rather than A-B-C. Thus, H atoms occupy exclusively at the octahedral sites located in between the twin boundary plane and its adjacent (111) plane (see Fig. 4.3). Fig. 4.4 also presents that possible H trapping sites with low segregation energy are generally distributed within a region $\pm$5 Å from the boundary planes for most of GBs, and the segregation energy at sites located far away from GB planes approaches 0 eV. This manifests a driving force for the segregation of H atoms from the bulk into the GB region, being consistent with previous observations [173]. It is worth noting that two GBs, *i.e.,* Σ153 (4 4 $\overline{11}$) and Σ171 (11 11 $\overline{10}$), provide a wider region within $\pm$15 Å of the GB planes, where H atoms favourably occupy. Further examination of Fig. 4.3(b) and (e) indicates that, apart from GB regions, H atoms also occupy at the right side of intrinsic stacking fault (ISF) facets. The main reason is that high hydrostatic stress on the right side of ISF facets drives more H atoms to segregate (see the inset of Fig. 4.4).

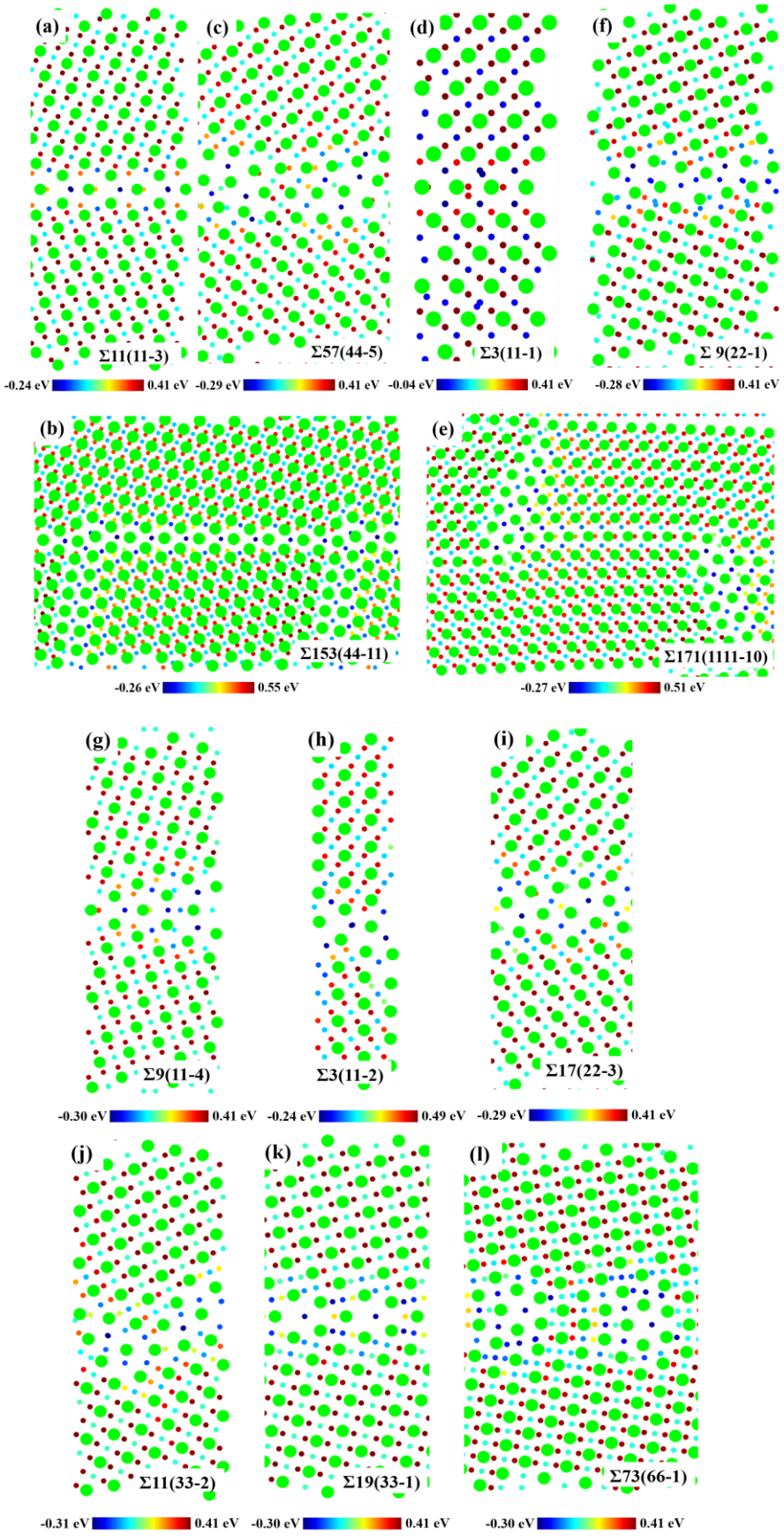

Fig. 4.3. H segregation energy maps for typical GBs, all cells are shown along the $[1\bar{1}0]$ tilt axis. Larger

spheres represent Ni atoms (green), and smaller ones indicate possible H trapping sites.

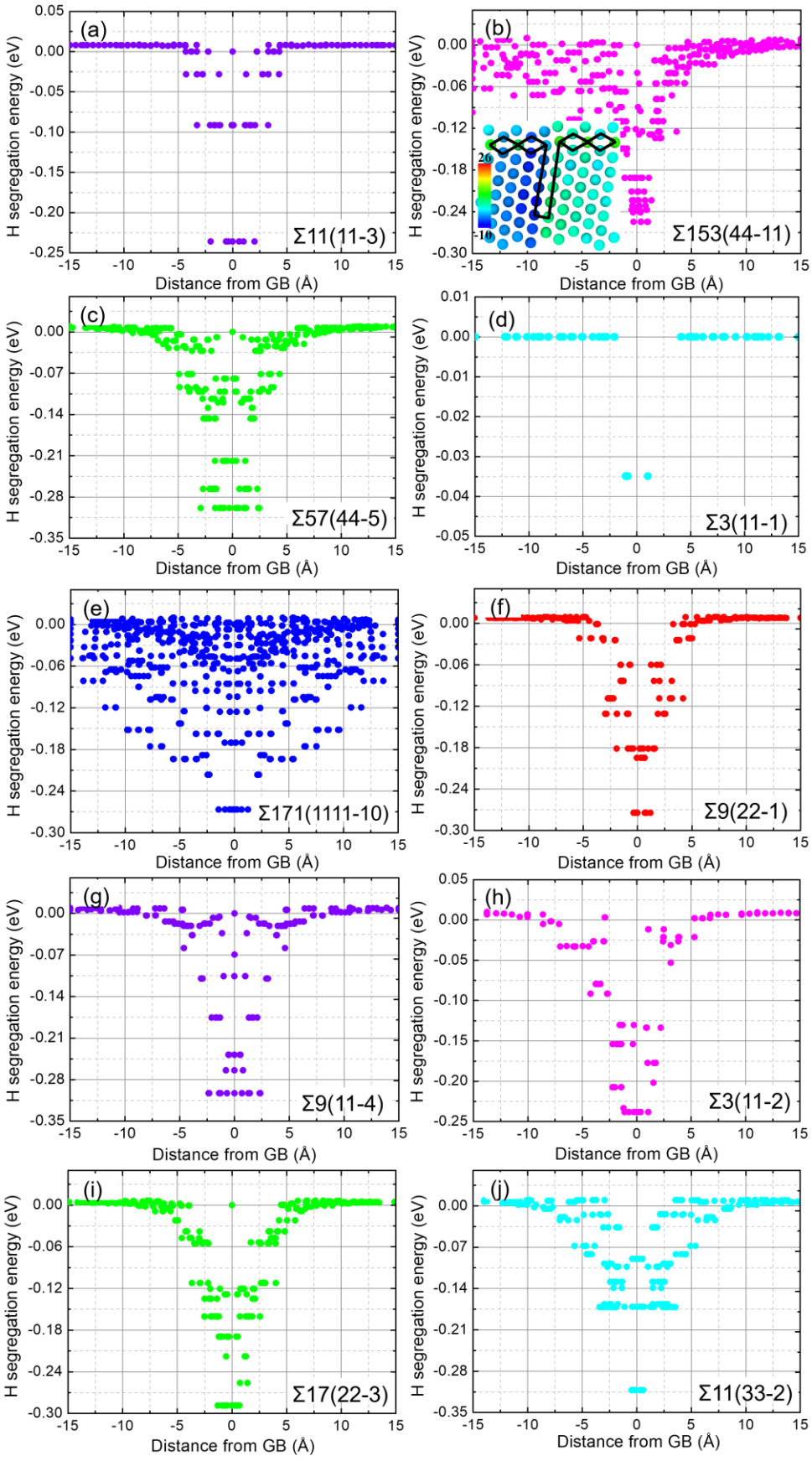

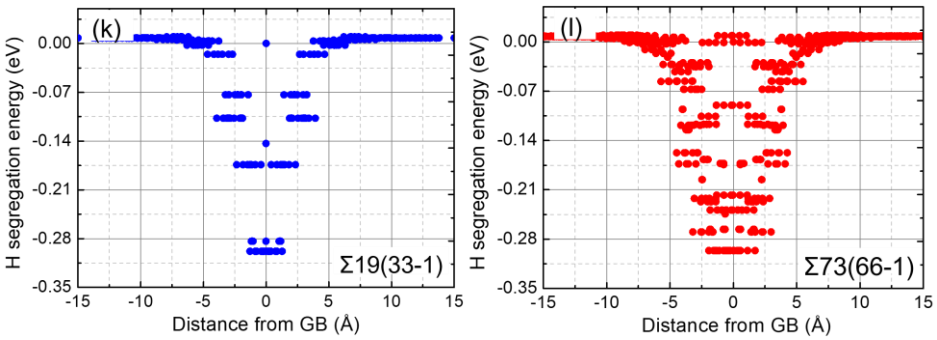

Fig. 4.4. Distribution of segregation energies as a function of distance from the GB plane. Atoms in the inset of (b) are coloured by the hydrostatic stress value.

The segregation energy maps including GB energies, H segregation energies, excess volume as well as maximum excess H concentrations are summarized in Fig. 4.5. It can be seen from Fig. 4.5(a) that, for most of GBs, the lowest and highest segregation energy varies somewhat over the entire misorientation range, but there are some interesting and notable exceptions. Specifically, the lowest segregation energy (-0.04 eV) of Σ3 (1 1 $\bar{1}$) GB is much higher than that of other GBs, *i.e.,* Σ9 (2 2 $\bar{1}$) with the segregation energy of -0.28 eV, indicating that the trapping ability of Σ3 (1 1 $\bar{1}$) GB is almost negligible. The highest segregation energy of three GBs, *i.e.,* Σ153 (4 4 $\overline{11}$), Σ3 (1 1 $\bar{2}$) and Σ171 (11 11 $\overline{10}$), is apparently different from that of other GBs, which is attributable to the presence of ISF facets. To quantitatively evaluate the trapping ability of GBs, the maximum excess H concentration is introduced and calculated by dividing the number of favourable sites by the GB area. As seen in Fig. 4.5(b), the trapping ability of H is strongly dependent on the GB structure, evidenced by that the maximum excess H concentration is changed pronouncedly as the misorientation angle increases. Intriguingly, GBs with E SUs ($\theta > 109.47°$) have higher maximum excess H concentration than other GBs with C and D SUs. When correlated with GB character, it becomes clear that E SUs contain more open structure or significant excess volume, where H atoms prefer to attach. To the contrary, due to compact structure or low excess volume, Σ11 (1 1 $\bar{3}$) and Σ3 (1 1 $\bar{1}$) GBs expectantly have poor H trapping ability.

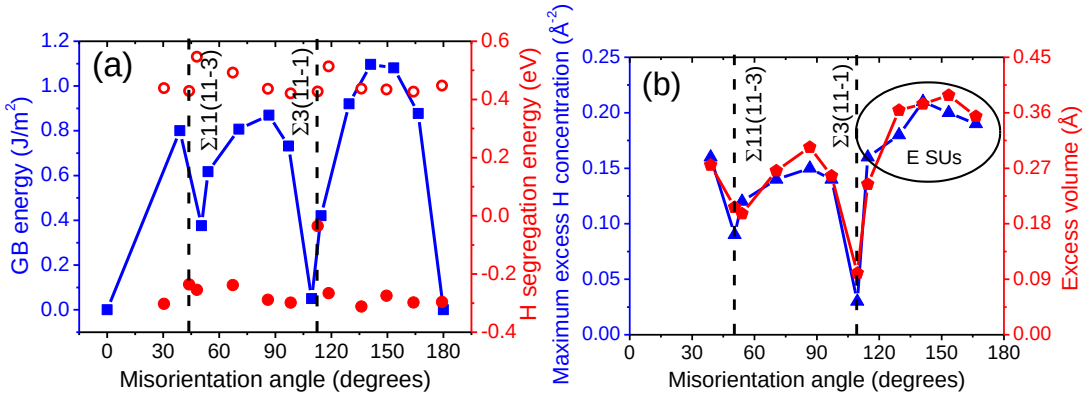

Fig. 4.5. Summary of segregation energy maps for 12 types of GBs. (a) GB energy and H segregation energy, with squares denoting GB energy, solid circles denoting lowest H segregation energy, and hollow circles denoting highest H segregation energy. (b) Maximum excess H concentration (triangles) and excess volume (pentagons).

4.3.3 Tensile response and deformation mechanisms of tilt GBs

After examining H segregation into various GB types, influence of H segregation on tensile deformation behaviour of Ni-H system is discussed in the following paragraphs. The stress-strain curves with different excess H concentrations are demonstrated in Fig. 4.6. The stress components were calculated using the expression taken from the Virial theorem, and the average atom volume was used in the stress calculations. The strain was calculated from the applied strain rate multiplied by the deformation time. All curves manifest a range of stress drops, which correspond to dislocation nucleation, multiplication and annihilation [21, 22]. Particularly, the first stress drop is associated with the incipience of dislocation plasticity, we thus denote the point of the maximum stress just prior to the first stress drop as the yield stress. The insets of Fig. 4.6 display the dependency of yield stress on excess H concentration. For GBs containing C and/or D SUs (Σ11, Σ153, Σ57, Σ3, Σ9, Σ3 and Σ17), the segregation of H results in a considerable decrease in the yield stress, while the yield stress of GBs with E SUs (Σ171, Σ9, Σ11, Σ19 and Σ73) increases significantly with increasing excess H concentration. The seemingly inverse observations suggest that the effect of solute H on the nucleation of dislocations is strongly sensitive to GB types. In the following three different GBs (Σ11, Σ3 and Σ9) are taken as examples to elucidate the role of H in the plastic deformation process. As other GBs are composed of these three basis GBs, it is believed that specific properties of these three GBs are applicable to and characteristic for all considered GBs.

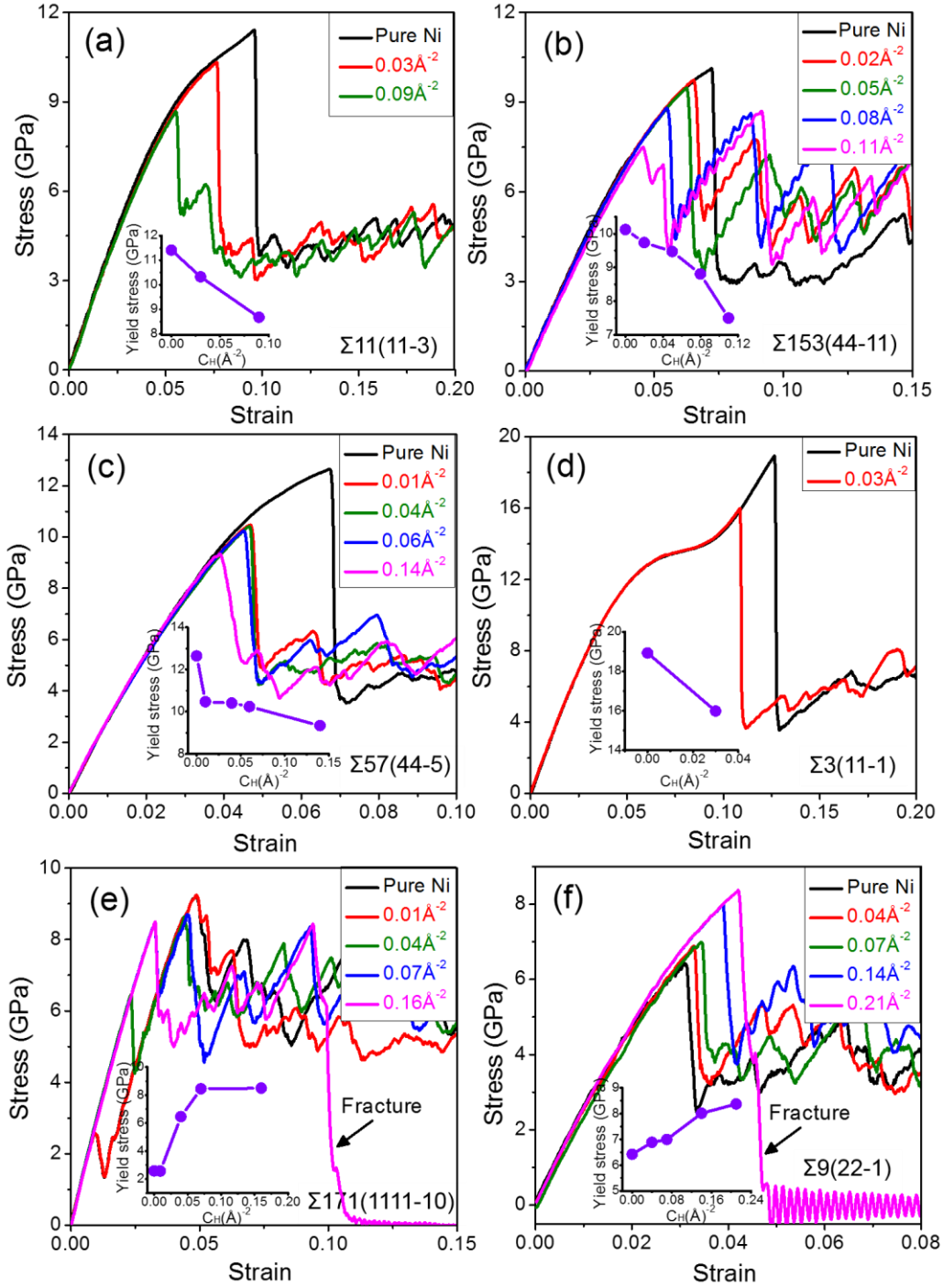
(a)
Pure Ni
0.03Å^{-2}
0.09Å^{-2}
Σ11(11-3)
Yield stress (GPa)
C_H(Å^{-2})
Stress (GPa)
Strain
(b)
Pure Ni
0.02Å^{-2}
0.05Å^{-2}
0.08Å^{-2}
0.11Å^{-2}
Σ153(44-11)
(c)
Pure Ni
0.01Å^{-2}
0.04Å^{-2}
0.06Å^{-2}
0.14Å^{-2}
Σ57(44-5)
(d)
Pure Ni
0.03Å^{-2}
Σ3(11-1)
(e)
Pure Ni
0.01Å^{-2}
0.04Å^{-2}
0.07Å^{-2}
0.16Å^{-2}
Fracture
Σ171(1111-10)
(f)
Pure Ni
0.04Å^{-2}
0.07Å^{-2}
0.14Å^{-2}
0.21Å^{-2}
Fracture
Σ9(22-1)

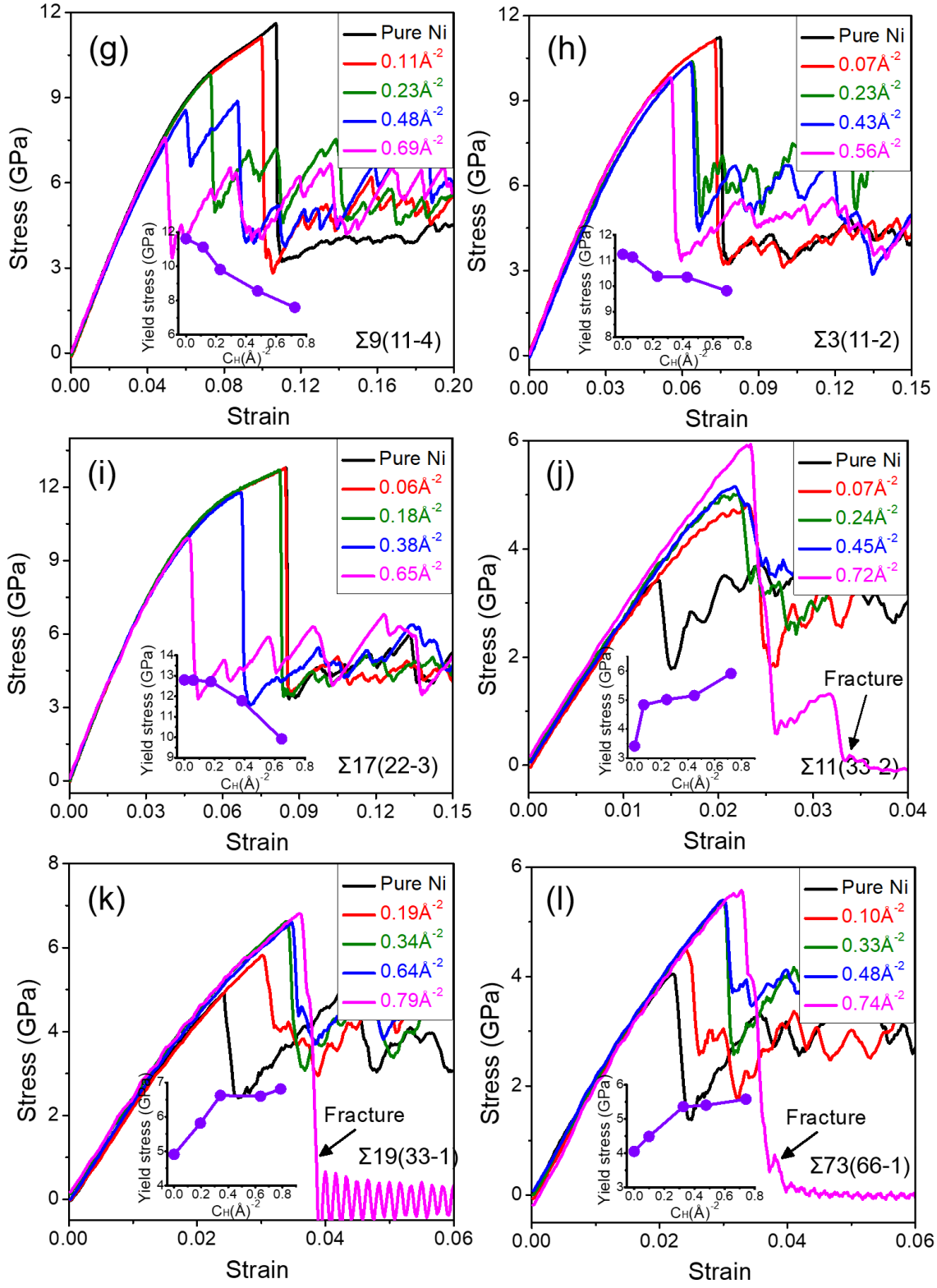

Fig. 4.6. The stress-strain curves for typical GBs with different excess H concentrations. The insets show the dependence of the yield stress on H content.

GBs with C and D SUs (Σ11 and Σ3)

To demonstrate the possible impact of H atoms on the dislocation emission from GBs with C SUs, we begin with the analysis of nucleation from the interface without H. In the

case of Σ11 (1 1 $\bar{3}$) GB in the absence of H shown in Fig. 4.7(a), when the maximum stress is reached at $\varepsilon = 9.60\%$, two partial dislocations with the Burgers vectors of 1/6[1 1 2] and 1/6[1 1 $\bar{2}$] nucleate and slip on the (1 1 $\bar{1}$) and (1 1 1) planes in the grain-A and grain-B, respectively, with a set of extrinsic stacking faults (ESFs) left behind. Aside from ESFs, the twin is also formed at the GB during tensile deformation. The evolution of C SUs leading to ESFs and twin is interpreted in Fig. 4.7(c)-(e). On the whole, the uniaxial tension causes the bicrystal model to elongate in *Y* direction and shorten in *X* and *Z* directions. Further examination of MD simulations suggests that the reduction of size in *X* direction shrinks C SUs, resulting in dislocation nucleation. Specifically, as presented in Fig. 4.7(c), atom-a translates along the negative *X* direction as the first C unit shrinks, which causes atoms residing on the plane 1 gliding towards the interface, and atoms on the plane 2 slipping away from the interface. As a result of this relative shift of the slip systems, the first partial dislocation is nucleated with the ISF left behind. Following the same mechanism, the movement of atom-b leads to the second nucleation of partial dislocation through a relative shift of atoms on the plane 2 and the plane 3. It is worth noting that atoms on the plane 2 first move out of the interface due to the translation of atom-a, and then return to the initial position (perfect fcc structure) driven by the movement of atom b, forming an ESF. The continuous shrinkage of C SUs provides the sources of consecutive dislocation nucleation events, resulting in the broadening of twin region. As shown in Fig. 4.7(d) and (e), the translation of atom-c and atom-d along the negative *X* direction leads to the broadening of twin region with the lattice spacing of five{1 1 1} planes.

As can be seen in Fig. 4.7(b), the onset of plasticity is associated with the nucleation of a series of ISFs in the presence of H, unlike the H-free case. H atoms segregate exclusively into the centre of capped trigonal prism (CTP) and octahedron (OCT) at boundary plane, indicated by green and magenta lines [121]. This segregation has the effect on changing GB structure, as the thickness of identified GB region increases with H concentration. As the tensile deformation proceeds, atom a moves along the negative *X* direction, pushing H atom 1 translating together. As a result, atoms residing on the plane 1 shift towards the interface, while atoms on the plane 2 slip in the opposite direction. The only discrepancy between Fig. 4.7(f) and (c) is that the shift of atoms on the plane 2 away from the boundary is driven by the H atom-1 in the presence of H, rather than atom-a without H. It is easier for H atom-1 to nucleate the first partial dislocation

(the relative slip of plane 2) than atom-a, since shorter translating distance is required. After dislocation emission, the interstitial site of H atom-1 changes from CTP centre to OCT centre. Also, H atom-4 locally moves for accommodating GB reconstruction, with one OCT site transformed into another. As displayed in Fig. 4.7(g), the final position of H atom-4 at the centre of new OCT apparently hinders the return of plane 2, which makes it difficult for the nucleated ISF to transform into an ESF/twin.

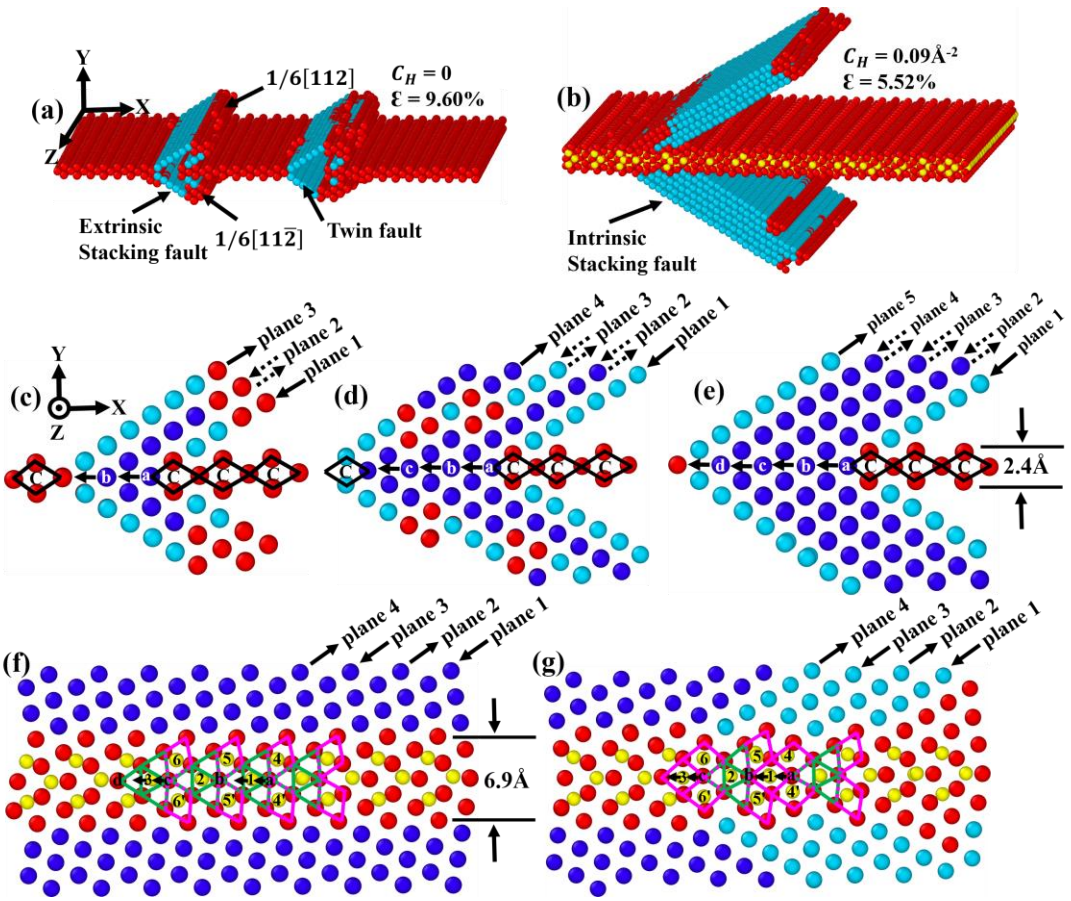

Fig. 4.7. Dislocation activities and atomic configurations for Σ11 $(1\,1\,\bar{3})$ GB with various excess H concentrations during tensile deformation process: (a, c-e) without H, (b, f-g) with H of $C_H = 0.09$ Å^{-2}. All figures are coloured by CNA, where atoms with a perfect fcc structure are blue, the red atoms organize the GB plane and the dislocation core, the continuous light blue atoms represent the stacking fault, and H atoms are assigned in yellow. Three-dimensional polyhedrons shown in (f) and (g) include CTP (green) and OCT (magenta).

Fig. 4.8 shows dislocation activities and atomic configurations for Σ3 $(1\,1\,\bar{1})$ GB (D SUs) without and with H during tensile deformation. This type of boundary has a simple GB structure and the lowest GB energy, which provides no free volume for atoms to move or rearrange when subjected to uniaxial tension. It is difficult therefore for partial dislocations to nucleate or emit from the GB. To accommodate continued tensile strain, lattice dislocation loops with the Burgers vectors of $1/6[112]$, $1/6[\bar{1}2\bar{1}]$ and $1/6[\bar{2}\bar{1}\bar{1}]$

are nucleated from three activated slip systems $(11\bar{1})$, $(1\bar{1}1)$, and $(\bar{1}11)$ in the grain interior at $\varepsilon = 12.68\%$, as demonstrated in Fig. 4.8(b). According to Schmid factor analysis, all activated planes are primary slip planes with the maximum Schmid factor $SF^{max}_{(11\bar{1})} = SF^{max}_{(1\bar{1}1)} = SF^{max}_{(\bar{1}11)} = 0.314$. During the whole deformation process, no dislocations appear to nucleate from the twin boundary. Fig. 4.8(c) shows that local atomic structures of twin boundary are pronouncedly modified in the presence of H. Besides thicker GB region, GB atoms are more disordered with higher CSP values. When the tensile strain reaches $\varepsilon = 10.84\%$, Shockley dislocations are directly nucleated from the disordered twin boundary, different from H-free case. Due to that the interface provides the source of dislocation nucleation, the yield stress is decreased from 18.92 GPa to 15.77 GPa.

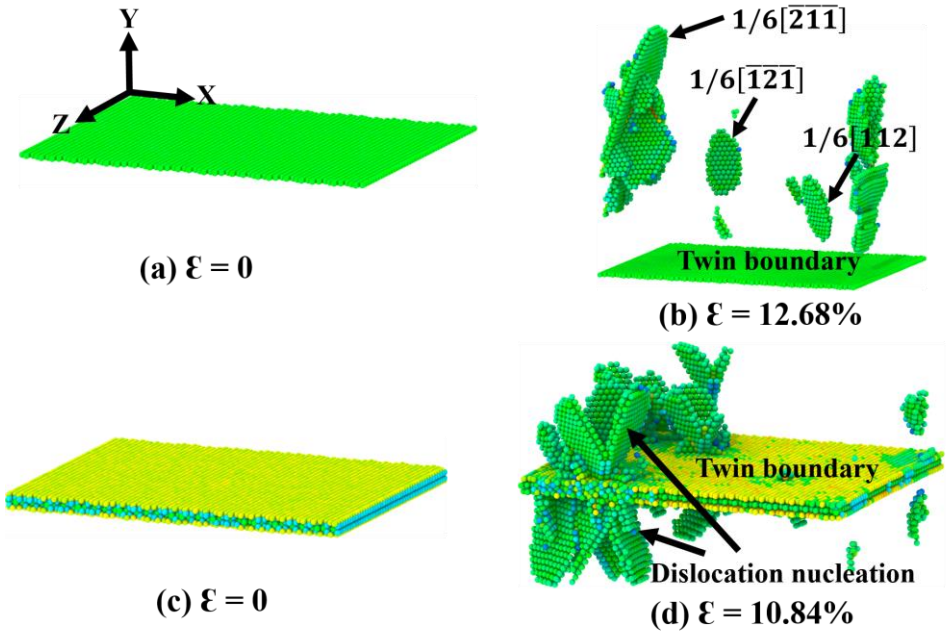

Fig. 4.8. Dislocation activities and atomic configurations for Σ3 (1 1 $\bar{1}$) GB with various excess H concentrations during tensile deformation process: (a) and (b) without H, (c) and (d) with H of C_H = 0.03 Å^{-2}. All figures are coloured by CSP.

GBs with E SUs (Σ9)

Fig. 4.9 demonstrates dislocation activities and atomic configurations for Σ9 (2 2 $\bar{1}$) GB without and with H during tensile deformation. As seen in Fig. 4.9(b), a series of very short ISF facets are first emitted from the boundary prior to yielding in the absence of H. According to the DXA analysis, these facets are Shockley partials with the Burgers vectors of $1/6[11\bar{2}]$ and $1/6[112]$ nucleating from the GB and gliding on (111) and $(11\bar{1})$ planes in the grain-A and grain-B, respectively, both of which are primary slip

planes with the Schmid factor of $SF_{(111)}^{max} = SF_{(11\bar{1})}^{max} = 0.471$. Later on, only certain partial dislocations propagate away from the boundary at the expense of other nucleated ISF facets. Spearot and Tschopp [21, 174] concluded that the evolution of E SUs was responsible for dislocation nucleation events. Specifically, as seen in Fig. 4.9(d), atom-d slips out of the downward E SU while atom-e slips into the downward E SU along the (1 1 1) plane when subjected to a tensile loading. Similarly, atom-j slips out of the upward E SU while atom-i slips into the upward E SU along the $(11\bar{1})$ plane. The relative motion of atoms-d, -e, -i and -j reduces and collapses the free volume of E SUs positioned at the end of the {111} plane, and eventually evolves E SUs into C SUs.

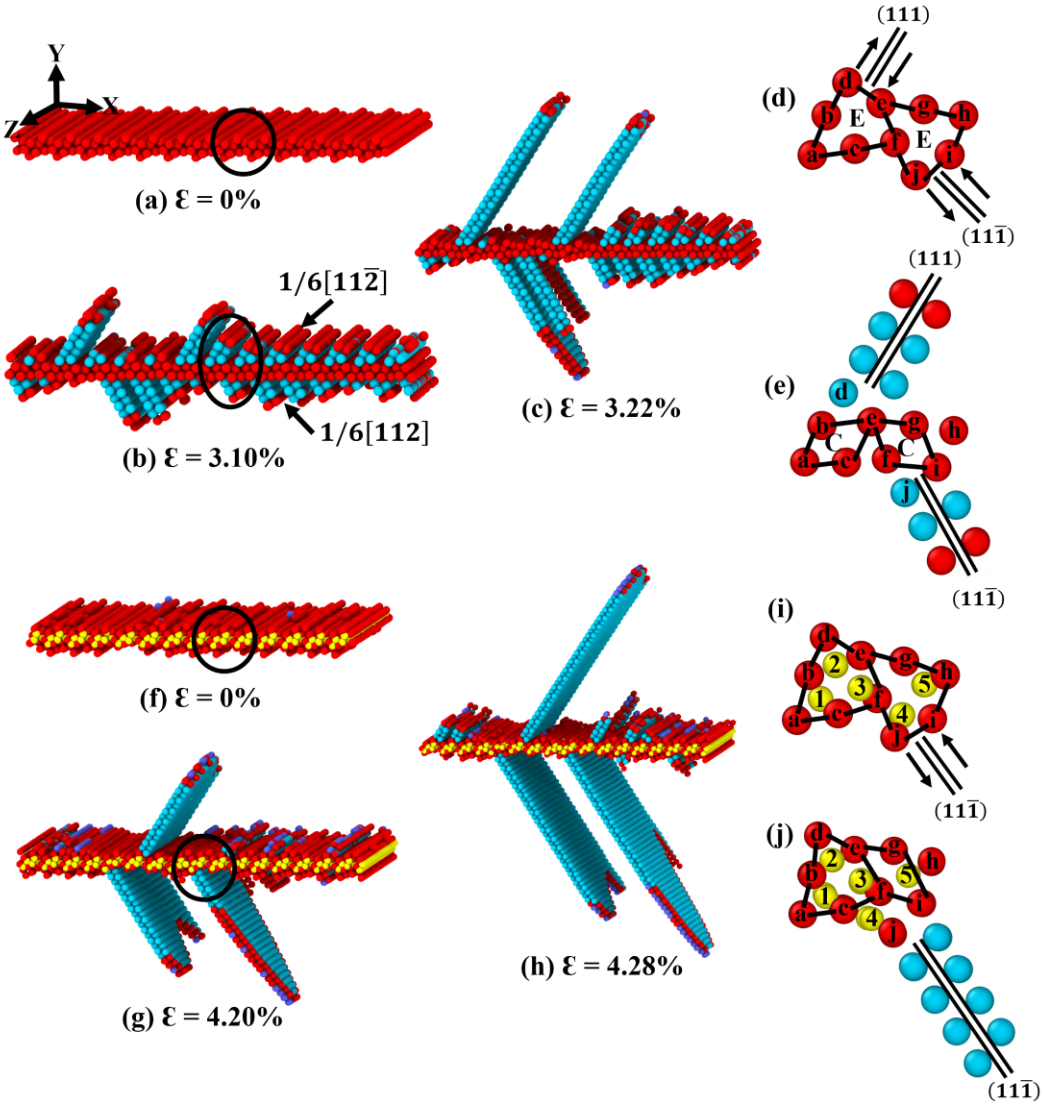

Fig. 4.9. Dislocation activities and atomic configurations for Σ9 (2 2 $\bar{1}$) GB with various excess H concentrations during tensile deformation: (a-e) without H and (f-j) with H of $C_H = 0.21$ Å^{-2}. All figures are coloured by CNA, the same as described in Fig. 4.7.

Regarding Fig. 4.9(f)-(j), one can find that the presence of H in the boundary can make it difficult for E SUs to nucleate Shockley partial dislocations, evidenced by a higher yield stress/strain and less frequency of nucleation events. Furthermore, short ISF facets cannot nucleate from the interface until the onset of plasticity, unlike the H-free cases. As shown in Fig. 4.9(i) and (j), five segregation sites are identified in one structural period of GB (downward and upward E SUs) according to H trapping map and marked with numbers 1 to 5. As the imposed tensile strain increases, atom-i attempts to slip into the H-segregated upward E SU, but this movement is effectively hindered by H atoms-4 and -5. With the help of high tensile stress, atom-i eventually squeezes into the space between H atoms-4 and -5, evolving E SU into C SU. As a consequence, H atoms-4 and -5 are pushed away from their original sites. In contrast to the upward E SU, the downward E SU consisting of atoms a-f are occupied with more H atoms (H atoms 1-3), therefore, the tensile stress required to activate the relative shift of atoms-d and -e becomes higher. Although not shown in Fig. 4.9, the downward E SU is ultimately collapsed, with a Shockley partial dislocation emitted. Overall, the segregated H atoms constrain the collapse of the free volume within E SUs, and result in a postponed dislocation nucleation event.

Note that, during dislocation emission, GB atoms rearrange themselves and push the segregated H atoms to move. Therefore, H atoms probably end up in the new locations that are less favourable for segregation than their original sites. For example, it can be clearly clued from Fig. 4.9(j) that H atom-4 finally occupies a new position out of the boundary plane (new-formed C SU). To characterize this effect, we consider the change of the energy of H segregation associated with dislocation nucleation process: $\Delta E = [(E_d^H - E^H) - (E_d^P - E^P)]/N_{GB}^H$. where E_d^H and E_d^P are the system energies after dislocation nucleation with and without H, E^H and E^P are the system energies before dislocation nucleation with and without H, and N_{GB}^H is the number of H atoms at GBs. As seen in Fig. 4.10, GBs with higher ΔE value generally correspond to higher yield stress. During dislocation nucleation process (the collapse of E SUs), a higher value of ΔE suggests an increased energy of H segregation, being indicative of an increased energy barrier for pushing solute H from initial positions to less favourable sites, thus a higher yield stress is required to overcome this higher energy barrier in such a way as to activate the nucleation event.

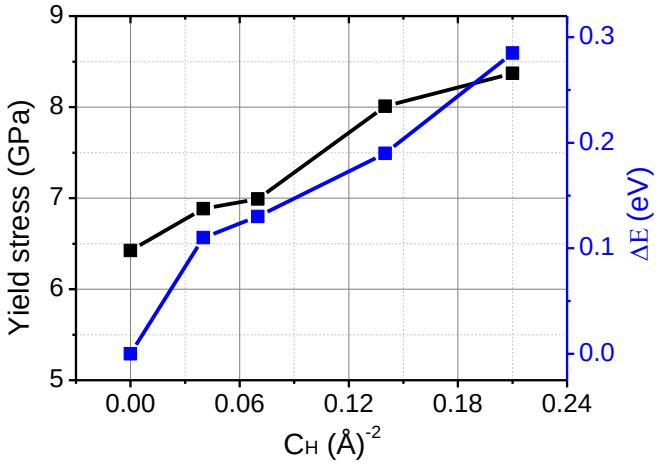

Fig. 4.10. Yield stress and the change of the energy of H segregation vs. excess H concentration.

4.3.4 Tensile response and deformation mechanisms of twist GBs

For generality, we also investigate the effects of H atoms on the mechanical behaviour and plastic deformation of twist GBs (TGBs). The stress-strain curves obtained with different bulk H concentrations are demonstrated in Fig. 4.11. Fig. 4.12 shows that the addition of H into the Σ65 and Σ5 TGBs results in a decrease in the yield stress, while the yield stress of Σ145 TGB rises significantly with increasing bulk H concentration. As a high-angle TGB, Σ5 has no pre-existing dislocations. Thus the reduction in yield stress due to the presence of H suggests that H facilitates dislocation nucleation and enhances local plasticity around the TGB. However, for low-angle TGBs (Σ65 and Σ145), it is invalid for predicting H-induced local plasticity simply based on the decrease/increase of the yield stress, as the equilibrium structures of these TGBs are accommodated by dislocation networks. Therefore, a closer examination of dislocation activities and atomic movement is required to identify the role of H in the plastic deformation process at different TGBs.

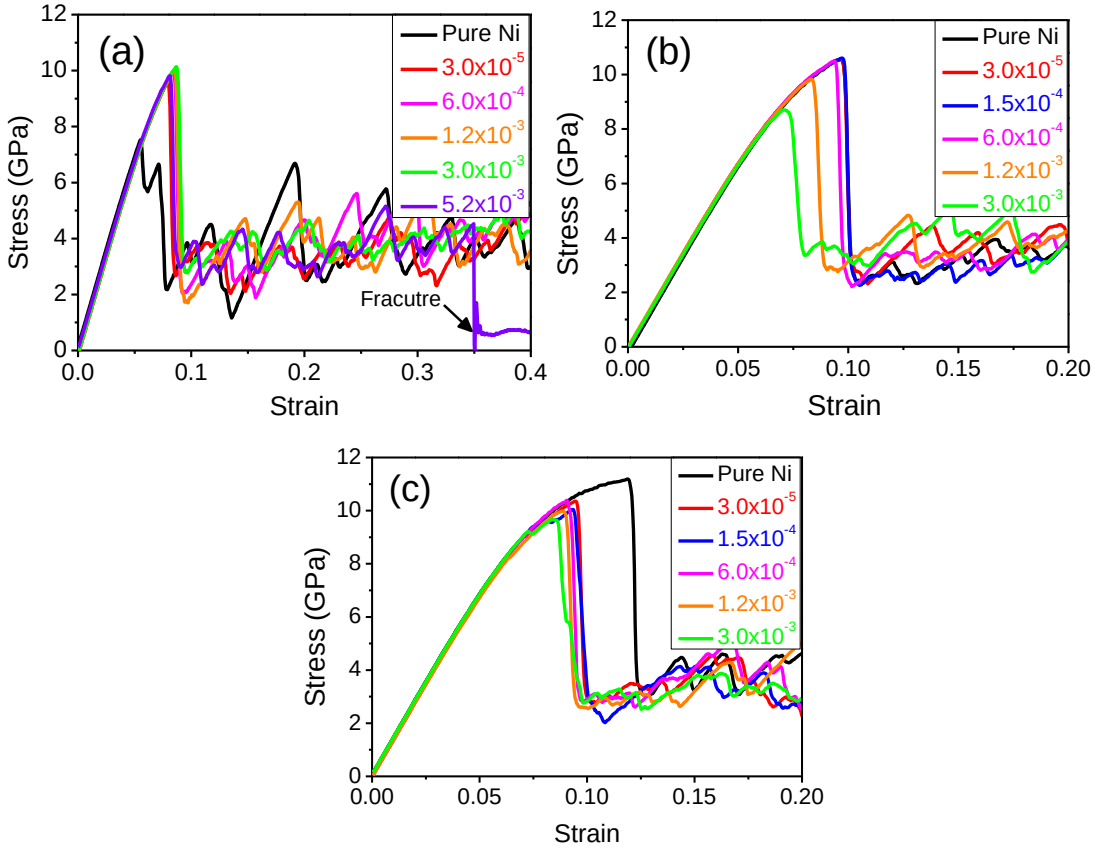

Fig. 4.11. Stress-strain curves of bicrystal models with different bulk H concentrations: (a) Σ145 TGB, (b) Σ65 TGB and (c) Σ5 TGB.

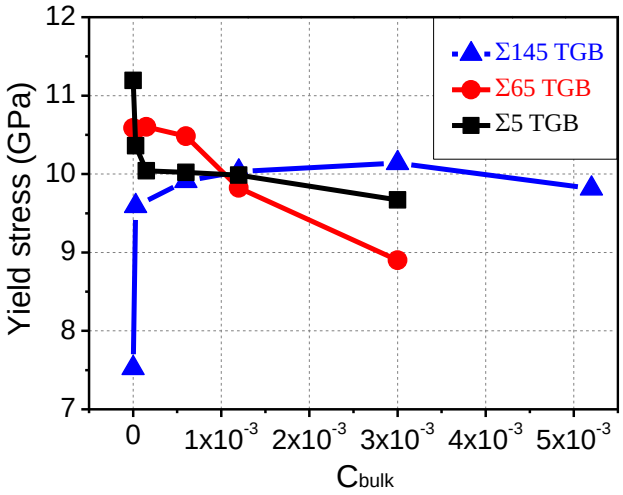

Fig. 4.12. Yield stress vs. bulk H concentration for all models.

Σ145 (θ = 6.73°) TGB. Fig. 4.13 shows the dislocation activities and atomic configurations for Σ145 ($\theta = 6.73°$) TGB with and without H during tensile deformation process. Dislocation activities at point 2 from Fig. 4.13(b)-(e) are circled for further analysis. Fig. 4.13(a) shows the initial configuration prior to tensile deformation in the absence of H. Clearly, the screw dislocations have already split into two partials separated

by a stacking fault in each square network unit. For example, a $1/2[110]$ pure screw dislocation dissociates into two Shockley partials ($1/6[121]$ and $1/6[21\bar{1}]$) residing on $(1\bar{1}1)$ plane at point 1, bounding an intrinsic stacking fault. It should be noted that the $1/2[110]$ perfect screw dislocation is common to $(1\bar{1}1)$ and $(\bar{1}11)$ two slip planes, which makes it possible for dislocation dissociation to happen on both planes, marked as points 1 and 2. Similarly, the dissociation from $1/2[\bar{1}10]$ perfect screw dislocation into partials occurs on (111) and $(11\bar{1})$ planes at points 3 and 4. As deformation proceeds, continued tensile stress leads to the further dislocation dissociation and the expansion of intrinsic stacking fault. At a strain of 3.04% in Fig. 4.13(b), dislocation dissociation at point 2 has been fully completed, and dissociated partial dislocations will no longer glide away from the TGB into lattice regions. The above reaction can be expressed in vector form:

$$1/2[110]_{(\bar{1}11)} \rightarrow 1/6[211]_{(\bar{1}11)} + 1/6[12\bar{1}]_{(\bar{1}11)} \tag{4.5}$$

To mediate the additional tensile strain, the leading partial dislocation further splits into a stair-rod dislocation and a Shockley dislocation as shown in Fig. 4.13(c). This dissociation process is given as:

$$1/6[211]_{(\bar{1}11)} \rightarrow 1/6[1\bar{1}0]_{(001)} + 1/6[121]_{(1\bar{1}1)} \tag{4.6}$$

The formed Shockley partial $1/6[121]$ glides on the cross-slip plane $(1\bar{1}1)$, while the produced stair-rod partial $1/6[1\bar{1}0]$ lies on the (001) plane. This dislocation is sessile as (001) plane is not a slip plane. But later on, the trailing partial dislocation on the primary plane catches up and reacts with the stair-rod dislocation at the intersection of the $(1\bar{1}1)$ and $(\bar{1}11)$ planes, with another Shockley partial formed on the cross-slip plane. This reaction is summarised as:

$$1/6[1\bar{1}0]_{(001)} + 1/6[12\bar{1}]_{(\bar{1}11)} \rightarrow 1/6[21\bar{1}]_{(1\bar{1}1)} \tag{4.7}$$

The interaction process is energetically favourable from the perspective of Frank energy criteria. In addition, the elastic energy is further released by the swipe of the trailing partial dislocation eliminating the bounded intrinsic stacking fault. A new extended dislocation has transferred totally to the cross-slip plane in Fig. 4.13(d), and is free to glide on this plane in Fig. 4.13(e). This observed cross-slip involving a stair-rod dislocation in Ni is a new finding in MD simulations, which can approve the model proposed by Fleischer [175].

As shown in Fig. 4.13(f)-(h), the presence of H can make a difference during the tensile deformation process. At low bulk H concentration, an H-enhanced dislocation dissociation (local plasticity) is observed at the elastic stage (see Fig. 4.13(f) and (g)).

Analogous to the H-free case, continued tensile strain causes the leading partial to dissolve into a star-rod dislocation and a Shockley partial dislocation (see Fig. 4.13(h)), shown as following:

$$1/6[12\bar{1}]_{(\bar{1}11)} \rightarrow 1/6[\bar{1}10]_{(001)} + 1/6[21\bar{1}]_{(1\bar{1}1)} \quad (4.8)$$

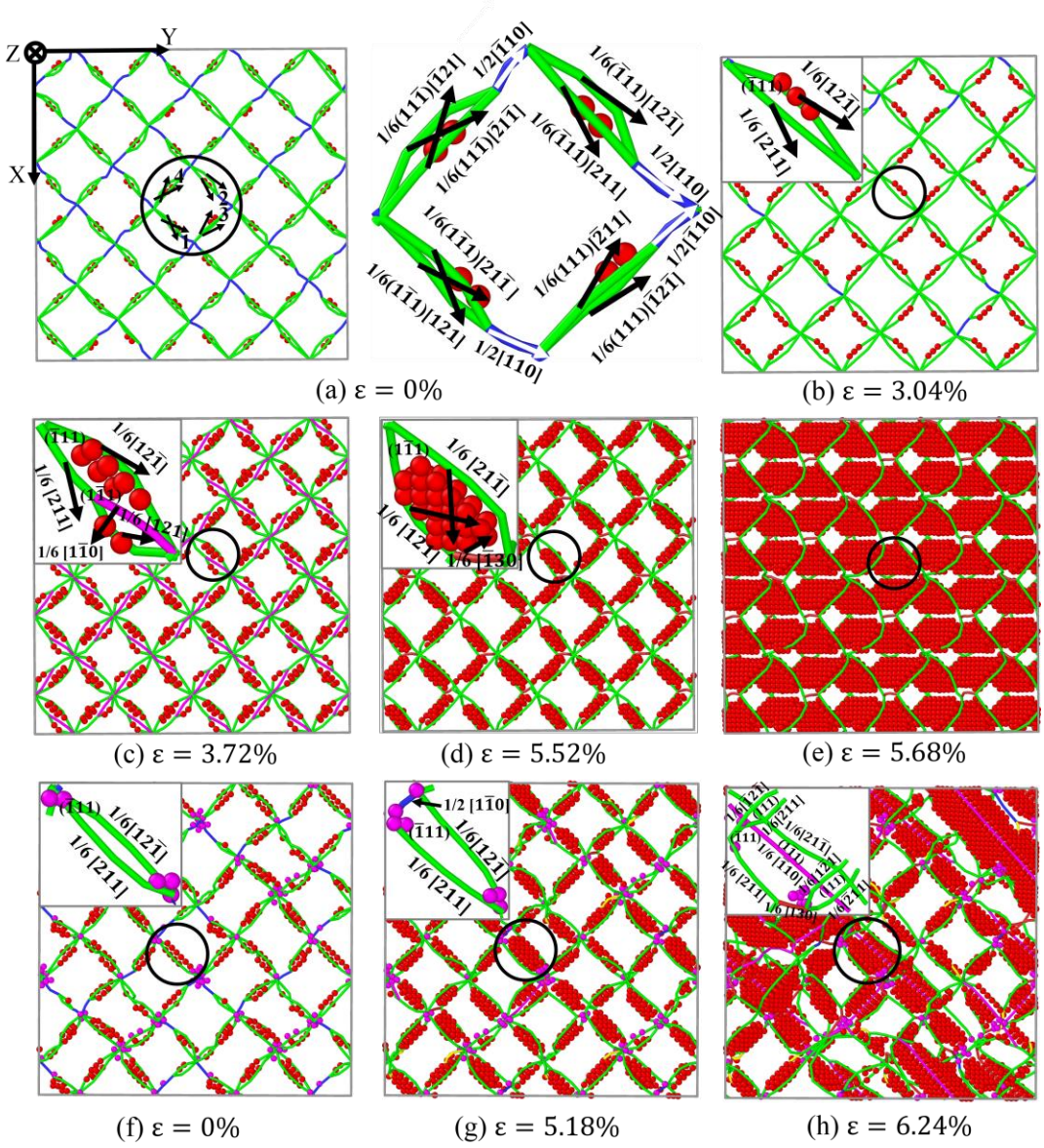

Fig. 4.13. Dislocation activities and atomic configurations for Σ145 (θ= 6.73°) TGB with various bulk H concentrations during tensile deformation process: (a)-(e) without H, and (f)-(h) with H of $C_{bulk} = 3.0 \times 10^{-5}$. All images are coloured by DXA. The blue lines are the perfect dislocations, the green lines represent the Shockley dislocations, the pink lines are the stair-rod dislocaitons, and the red lines are other types of dislocaitons. Stacking-fault atoms are shown in red, and H atoms are assigned in pink.

However, in contrast to H-free case, the trailing partial $1/6[211]$ on the primary plane cannot 'catch' the produced stair-rod dislocation to form a new partial on cross-slip plane. This observed H-induced slip planarity at the expense of cross-slip is interpreted that H

reduces the stacking-fault energy [176], which decreases the tendency for cross-slip by increasing the separation distance between the trailing partial and stair-rod dislocation. Moreover, H-enhanced dislocation dissociation on the (111) plane blocks the movement of newly-dissociated Shockley partial $1/6[21\bar{1}]$ on cross-slip plane. Consequently, stair-rod dislocation$1/6[\bar{1}10]$, trailing dislocation $1/6[211]$ and newly-dissociated Shockley partial $1/6[21\bar{1}]$ form a stable and sessile arrangement (Lomer-Cottrell lock), acting as a strong barrier to the further glide of dislocations on the $(1\bar{1}1)$ and $(\bar{1}11)$ planes. This exactly explains that the higher tensile stress is required to activate the onset of yielding in the presence of H, compared to the H-free case.

Σ65 (θ = 14.25°) TGB. The detailed deformation process of Σ65 (θ = 14.25°) TGB in the presence and absence of H is presented in Fig. 4.14. In the absence of H, the equilibrium TGB structure is composed of two series of screw dislocations $b_1 = 1/2[110]$ and $b_2 = 1/2[\bar{1}10]$, as marked in Fig. 4.14(a). Prior to yielding point, it is found that dislocation dissociation events occur onto {111} planes in network units as shown in Fig. 4.14(b), *i.e.* 1/2[110] pure screw dislocation dissolves in its glide plane $(\bar{1}11)$ into two Shockley partial dislocations: $1/6[211]$ and $1/6[12\bar{1}]$; $1/2[\bar{1}10]$ screw dislocation dissociates into $1/6[\bar{1}21]$ and $1/6[\bar{2}1\bar{1}]$ partials on plane $(11\bar{1})$. The atomic mechanism responsible for this dislocation dissociation is illustrated in Fig. 4.14(e). Four groups of atoms have been marked, specifically, atoms L ~ P reside on one $(\bar{1}11)$ plane; atoms A ~ F rest in the second $(\bar{1}11)$ plane; the third takes the positions Q ~ R, and atoms F ~ K are located at $(11\bar{1})$ plane. It's worth noting that atom-A is common to planes $(\bar{1}11)$ and (111), while atom-F lies in the intersection line [101] between planes $(\bar{1}11)$ and $(11\bar{1})$. With the increase of the imposed tensile stress, the hydrostatic stress of all atoms increase, and atoms A ~ C and F ~ I have the highest stress values (see Fig. 4.14(e2)). Driven by high hydrostatic stress, atoms-B, -C, -G and -H make movement to find stable positions, while atoms-A, -F and -I are sessile due to coplanar constrains. This can be clued that, after dislocation dissociation, atoms-B, -C, -G and -H change in colour from near-red in Fig. 4.14(e2) to near-yellow in Fig. 4.14(e3), while the colours of atoms-A, -F and -I are nearly kept the same. The movement path of atoms-B and -C has been indicated by black arrows in Fig. 4.14(e4). Instead of jumping from the site-B to the site-C over the top of the atom-M (vector $\overrightarrow{BC}$), atom-B moves to the nearby site-R along the 'valley' between the atoms-M and -O(vector $\overrightarrow{BR}$). Likewise, atom-C attempts to jump to

the new site-Q via a valley between the atoms-N and -P (vector $\overrightarrow{CQ}$) rather than vector $\overrightarrow{CF}$. This zig-zag motion results in dislocation dissociation from a pure screw dislocation into two Shockley partial dislocations onto {111} planes (see Fig. 4.14(b)). However, further dissociation no longer continues as the movement of atom-B from site-R to site-C (vector $\overrightarrow{RC}$) and atom-C from site-Q to site-F (vector $\overrightarrow{QF}$) is blocked by the sessile atom-F. When the strain increases to yielding point of 9.64%, the dissociated partials begin to interact with other dislocations in the neighbouring network units and further dislocation emission are observed in Fig. 4.14(d).

Fig. 4.14(f)-(j) show the dislocation activities and atomic mechanisms during tensile deformation process at low bulk H concentration ($C_{bulk} = 3.0 \times 10^{-5}$). Initially, H atoms segregate exclusively to the intersections of dislocation network, as shown in Fig. 4.14(f). It is very interesting to notice that dislocation dissociation events occur at a much lower tensile strain ($\varepsilon = 2.04\%$), compared to H-free case, implying that H can promote earlier dislocation dissociation and enhance dislocation plasticity around the TGB. To explain this phenomenon, atomic configuration of $\Sigma 65$ TGB in the presence of H is illustrated in Fig. 4.14(j). It is clearly seen that introduction of H (atoms-A and -E) into TGBs has the profound effect of changing local stress state and atomic structure: H increases local stress (see atom-B in Fig. 4.14(j1)) and promotes the generation of vacancy (see Fig. 4.14(j3)). Due to the high hydrostatic stress, atom-B attempts to move to the nearby stable position, even though at low tensile stress. Meanwhile, the H-generated vacancy facilitates the motion of atom-D as indicated by black arrow in Fig. 4.14(j3), which in turn accelerates the motion of atom-B. Finally, the zigzag motion of atoms-B and -D releases their stresses to a lower level (see Fig. 4.14(j2)) and causes the screw dislocation to dissociate into two Shockley partial dislocations (see Fig. 4.14(g)). Following the same mechanism, the motion of atoms-F and -I makes the dislocation dissociation happen on the (111) plane. Note that, even though H-enhanced dislocation dissociation exists at the elastic stage, the onset of yielding of H-charged cases at low bulk H concentration is still correlated to dissociated dislocation interactions as well as dislocation emission, like the H-free case. Therefore, the initial yield stress is reduced slightly with the increase of bulk H concentration ($C_{bulk} \leq 6.0 \times 10^{-4}$), as shown in Figs. 4.11 and 4.12. However, at high bulk H concentration, a totally different tensile deformation mechanism is observed. Here, no H-enhanced dislocation dissociation events can be observed at the elastic stage. When the yielding point is reached ($\varepsilon =$

8.44%), $1/6[\bar{1}12]$ and $1/6[1\bar{1}\bar{2}]$ Shockley partials directly nucleate from the TGB plane into the grain-A and grain-B, with an extrinsic stacking fault left behind. In summary, as the H content is increased, planar defect is gradually formed at the expense of dislocation network, leading to a change in plasticity mode from one dominated by dissociated dislocation interactions to the other controlled by dislocation nucleation from the boundary plane. This H-induced plasticity mode change is the main reason why the yield stress of Σ65 TGB at high bulk H concentration is much lower than that at low bulk H concentration and H-free case.

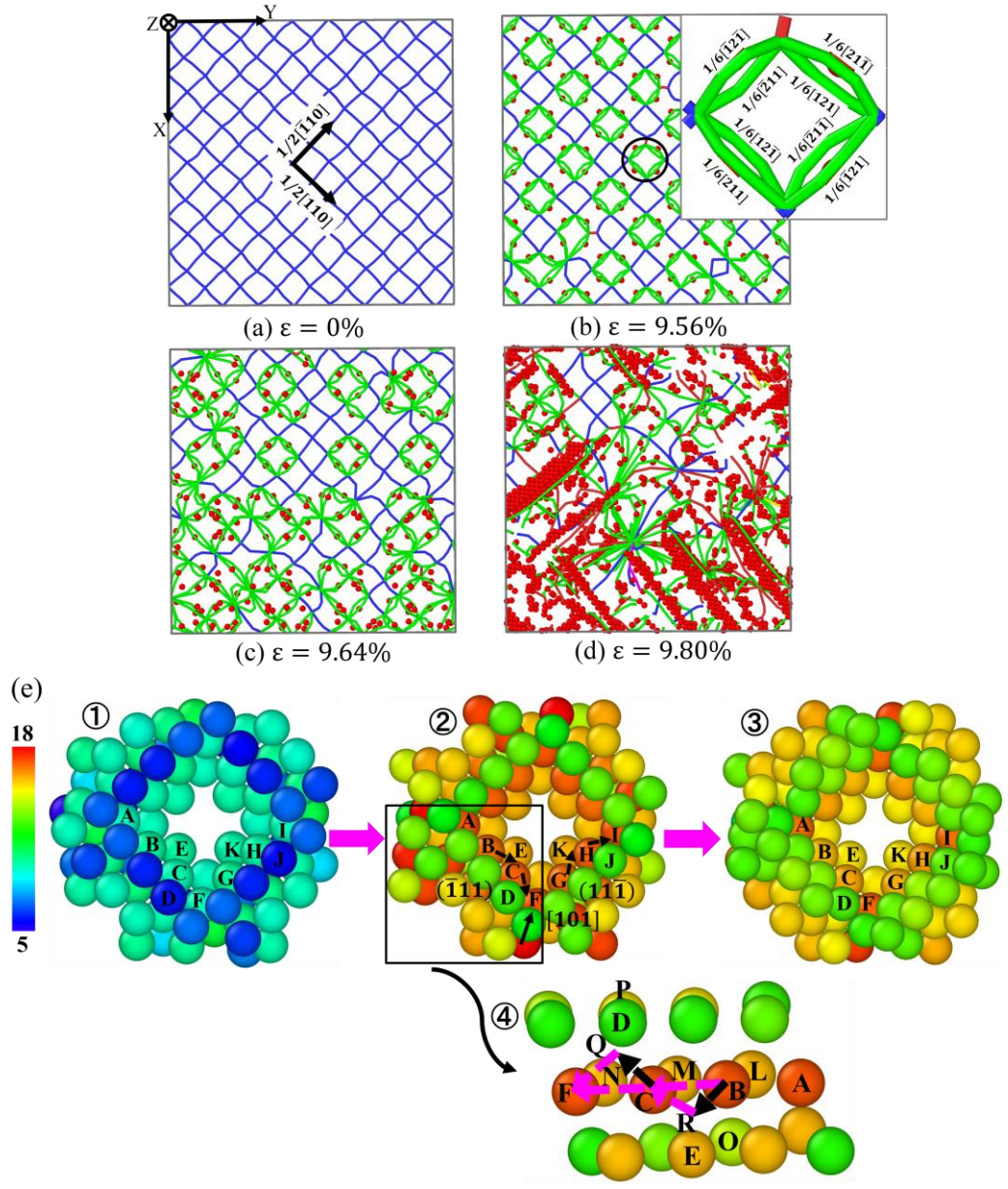

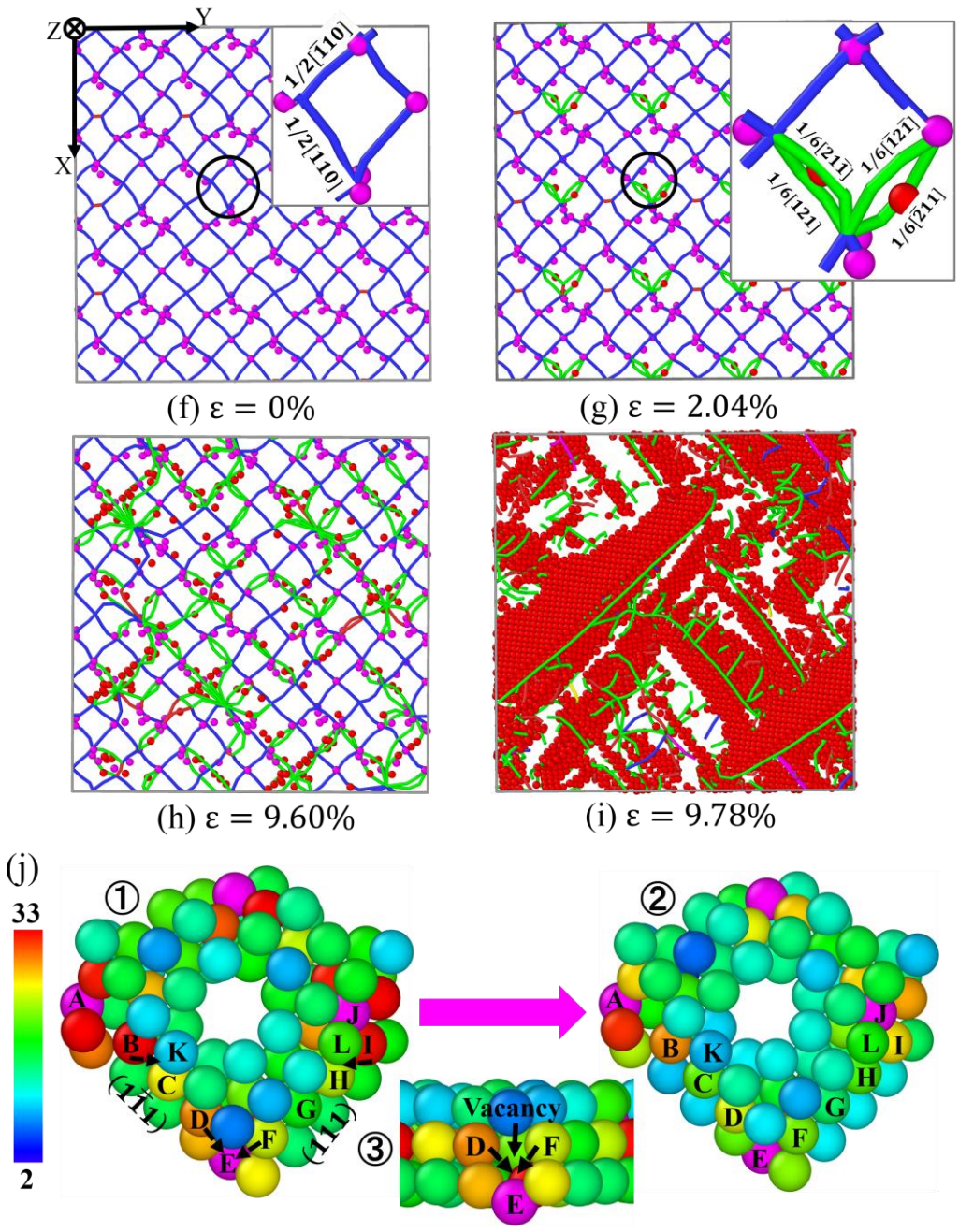

Fig. 4.14. Dislocation activities and atomic configurations for Σ65 (θ= 14.25°) TGB with various bulk H concentrations during tensile deformation process: (a-e) without H and (f-j) with H of $C_{bulk} = 3.0 \times 10^{-5}$. All images are coloured by DXA, the same as described in Fig. 4.13, except (e) and (j) coloured by the hydrostatic stress value.

Σ5 (θ = 36.87°) TGB. Fig. 4.15 shows the dislocation activities for Σ5 (θ = 36.87°) TGB with and without H at different deformation stages, respectively. For the H-free cases (see Fig. 4.15(a)-(c)), the boundary composed of planar defect gradually becomes coarsened before reaching the yielding point as the tensile deformation proceeds. In Fig. 4.15(b), the onset of plasticity is activated by an array of nucleation of partial dislocation

loops with edge and screw characters from the interface plane into grain-A and grain-B simultaneously. It can be seen that dislocation slip occurs on four {111} planes, leading to four nucleated partial dislocations ($1/6[\bar{1}12]$,$1/6[1\bar{1}2]$, $1/6[\bar{1}\bar{1}2]$ and $1/6[112]$) linked back to the TGB plane by extrinsic stacking faults. According to Schmid factor analysis, they are all the favourable slip planes with the maximum Schmid factor $SF_{(1\bar{1}1)}^{max} = SF_{(\bar{1}11)}^{max} = SF_{(111)}^{max} = SF_{(11\bar{1})}^{max} = 0.471$. As the tensile strain carries on, the intersection of operative slip systems leads to dislocation interactions. Furthermore, the presence of abundant extrinsic stacking faults in bicrystal model also blocks the movement of newly nucleated partial dislocations from the TGB plane, as shown in Fig. 4.15(c).

For H-charged cases (see Fig. 4.15(d)-(i)), different tensile deformation mechanisms are observed. As shown in Fig. 4.15(d) and (g), some ledges occur within the boundary planes, and the spacing between ledges decreases as the bulk H concentration is increased, which arises as a result of heterogeneous distribution of H atoms along TGB plane. The formation of GB ledges related to dislocation nucleation is already reported [177]. At low bulk H concentration ($C_{bulk} = 6.0 \times 10^{-4}$), when the yield stress is reached ($\varepsilon = 9.08\%$), a series of Shockley dislocations with the Burgers vector of $1/6[\bar{1}12]$ and $1/6[\bar{1}\bar{1}2]$ nucleate from H-induced GB ledges and slip on $(1\bar{1}1)$ and (111) planes in grain-A and grain-B, respectively. Continued tensile strain leads to dislocation nucleation events on other possible slip systems (see Fig. 4.15(f)). Theoretically, dislocation slip should occur on four {111} planes simultaneously as the maximum Schmid factor is identical on different slip systems, whereas, in the presence of H, partial dislocations nucleate on one certain slip system earlier than other slip planes. Moreover, the tensile stress/strain for dislocation nucleation is lower than that of H-free case. This implies that the configuration of H-induced GB ledges facilitates easier dislocation nucleation event. Further evidence supporting this point is presented in Fig. 4.15(g)-(i). More GB ledges created by high H concentration trigger the nucleation of $1/6[\bar{1}\bar{1}2]$ and $1/6[\bar{1}1\bar{2}]$ partials from the boundary plane at a lower tensile strain, with an array of extrinsic stacking faults left behind. To accommodate additional tensile deformation, another two groups of partial dislocations ($1/6[112]$ and $1/6[1\bar{1}\bar{2}]$) on $(11\bar{1})$ and $(1\bar{1}1)$ slip planes are also activated from dislocation interaction sites, as shown in Fig. 4.15(i).

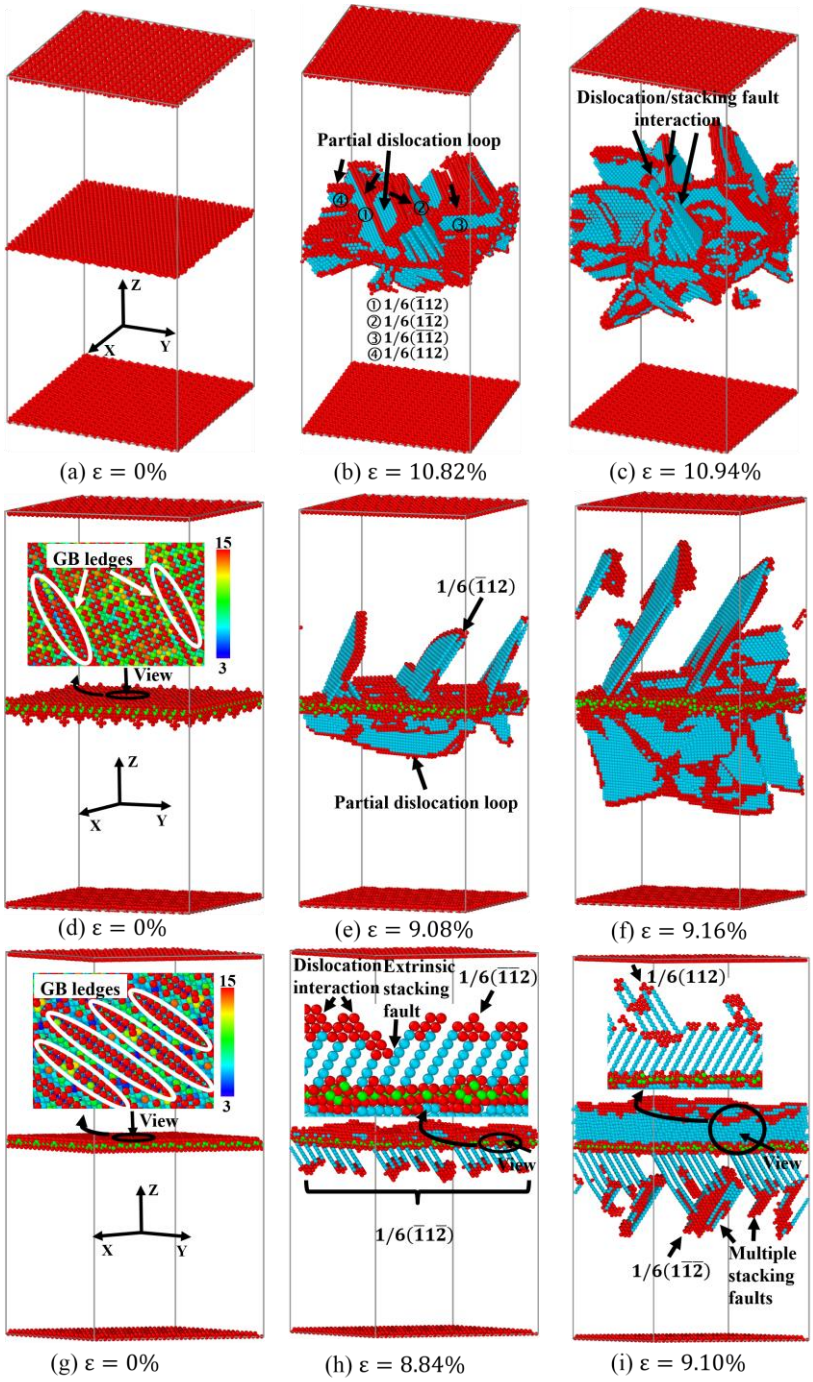

Fig. 4.15. Dislocation activities and atomic configurations for Σ5 (θ= 36.87°) TGB with various bulk H concentrations during tensile deformation process: (a)-(c) without H, (d)-(f) with H of $C_{bulk} = 6.0 \times 10^{-4}$, and (g)-(i) with H of $C_{bulk} = 3.0 \times 10^{-3}$. The insertions of (d) and (g) are coloured by the CSP value. All other images are coloured by CNA, the same as described in Fig. 4.7, and H atoms are assigned in green.

4.4 Summary

MD simulations were carried out to elucidate the influence of solute H on tensile deformation mechanisms of various types of GBs in Ni. For tilt GBs, H segregation energy maps demonstrated that the trapping ability of H was strongly dependent on GB

structures. GBs with E SUs had higher maximum excess H concentration than those with C and D SUs, since E SUs contained more open structure relative to other SUs. Analysis of stress-strain curves shown that the segregation of H resulted in a considerable decrease in the yield stress of GBs with C and D SUs, while the yield stress of GBs with E SUs increased significantly with increasing excess H concentration. The difference was likely attributed to different deformation mechanisms: (a) H can facilitate dislocation nucleation via changing local atomic structures of GBs with C and D SUs; (b) for GBs with E SUs, the segregated H atoms constrained the reduce of the free volume within E SUs so as to result in a postponed dislocation nucleation event. In terms of energy, the increase in the yield stress was correlated with the ultimate collapse of E SUs leading to an increase in the energy of H segregation during dislocation emission. As with tilt GBs, the H-modified mechanical response of twist GBs was also sensitive to the GB character. Different deformation mechanisms such as easier dislocation nucleation due to the presence of H, H-enhanced dislocation dissociation, and H-induced slip planarity were directly responsible for this modification.

Chapter 5 Effect of H segregation on shear-coupled motion of ⟨110⟩ grain boundaries

This chapter is extracted from the following publication:

Li J, Lu C*, Pei L, Zhang C, Wang R, Tieu K. Effects of H segregation on shear-coupled motion of <110> grain boundaries in α-Fe. Int J Hydrogen Energy. 2019;44:18616-27.

5.1 Introduction

Under shear stress a GB can move in its normal direction, leading to one grain growing into another. Such shear-driven GB migration operates as an important mechanism during plastic deformation, grain growth, recrystallization and phase transformation. In a system with impurities, the driven migration of a GB together with its absorbed impurity atoms is an activated process. By contrast, the impurity atoms may be left behind by the moving GB, leading to non-activated GB migration. At low temperatures, H atoms are immobile, thereby suppressing the GB migration and strengthening H-segregated metals. This chapter aims to study these aspects. To this end, the simulation methodology is described in Section 5.2; H segregation maps and shear deformation mechanisms without and with solute H are given in Section 5.3; the role of H in the damage of GBs in α-Fe is discussed in Section 5.4; and a summary of findings is presented in Section 5.5.

5.2 Simulation methodology

All simulations were implemented with MD simulator LAMMPS [155] by using the widely-used EAM interatomic potentials for Fe-H developed by Ramasubramaniam et al. [162] and further modified by Song and Curtin [27] to prevent the unrealistic clustering of H atoms. The bicrystal models with $[1\bar{1}0]$ STGBs were constructed by rotating grain-A above the interface plane by $\theta/2$ clockwise around the Z axis, while rotating grain-B underneath the grain boundary by $\theta/2$ counterclockwise (see Fig. 5.1). The simulation cell was modelled with periodic boundaries along the X and Z directions and a free boundary condition in Y direction. Four types of STGBs were considered in

this work, as listed in Table 5.1. After GB initialization, various in-plane rigid body translations of grain-A with respect to grain-B combined with atom deletion criteria were adopted to find optimal GB structures.

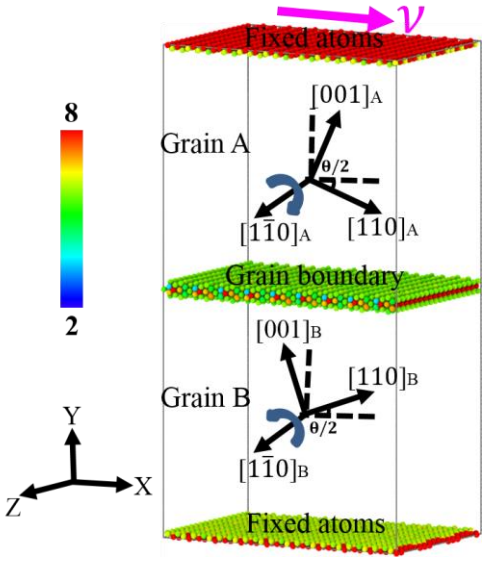

Fig. 5.1. Schematic diagram of a bicrystal model rotated around the [1$\bar{1}$0] axis.

Table 5.1. Model parameters for four GBs after energy minimization.

Tilt angle θ (°)	GB normal $(hkl)_A/(hkl)_B$	Model size $\boldsymbol{Lx, Ly, Lz(nm)}$	GB energy $(\boldsymbol{mJ \cdot m^{-2}})$	Excess volume (Å)
26.53	Σ19(1 1 -6)/(1 1 6)	13.20, 23.30, 10.95	1157.21	0.23
70.53	Σ3(1 1 -2)/(1 1 2)	12.31, 22.95, 10.95	262.80	0.01
109.47	Σ3(1 1 -1)/(1 1 1)	12.31, 22.95, 10.95	1310.72	0.36
141.06	Σ9(2 2 -1)/(2 2 1)	13.43, 22.99, 10.95	1288.50	0.19

In order to search all possible trapping sites for H atoms at each GB type, the Voronoi tessellation of atoms was constructed with Voro++ code [172]. Each Voronoi vertex was concerned as a specific trapping site for solute H. After placing H atoms at a particular site α, the initial Fe-H configuration was obtained and optimized via conjugate gradient process. The segregation energy for one H atom at trapping site α within the GBs is given by: $E_{\alpha}^{seg} = (E_{GB}^{\alpha} - E_{GB}) - (E_{T-site} - E_{bulk})$, where E_{GB}^{α} and E_{GB} represent the total system energies with and without H atom at GBs respectively, E_{T-site} is the system energy associated with the H atom trapped into the lattice tetrahedral site in a single crystal bulk, and E_{bulk} is the total energy of a single crystal bulk. Based on calculated segregation energy maps, a series of Fe-H interactions under various H concentrations (C_H ranging from 10^{-4} to 10^{-3} in atomic ratio) were created by successively adding one H atom into 'favourable' trapping sites until all 'favourable' sites were occupied. Here

we define all sites with segregation energy lower than zero as 'favourable'. Prior to the shear deformation, the constructed simulation cell with different H concentrations was first heated up to 300 K over 100 ps, then cooled down to 10 K for 100 ps.

The atoms within 12 Å thick region on the top of grain-A and the bottom of grain-B were fixed and frozen by setting the interatomic force to zero. A constant shear velocity of $v = 0.8\ \mathrm{m/s}$ was subsequently applied to the upper slab along the *X* direction, while the lower slab remained stationary. Under shear loading, the temperature was kept at 10 K via the NVT ensemble, and the time increment of simulation was set 1 fs.

5.3 Results

5.3.1 GB structure and H trapping map

Typical equilibrium GB structures are shown in Fig. 5.2. Herein, the SU model proposed by Sutton and Vitek [178] is used to characterize the local atomic structure within each GB. In the SU model, certain GBs correspond to favoured SUs, while all other GBs are characterized by two neighbouring favoured SUs. For the $[1\bar{1}0]$ α-Fe system, two Σ3 GBs are clearly favoured boundaries with B and C SUs, respectively. Also, the A and A' SUs are basic units of $\theta = 0°$ and 180° perfect crystals. The other GBs with non-preferred misorientation come from a combination of these basic SUs with complexity. For example, Σ19 $(1\ 1\ \bar{6})$ GB is composed of A and B SUs (2A + B), and Σ9 $(2\ 2\ \bar{1})$ GB contains C and A' SUs (C + 2A'), as shown in Fig. 5.2.

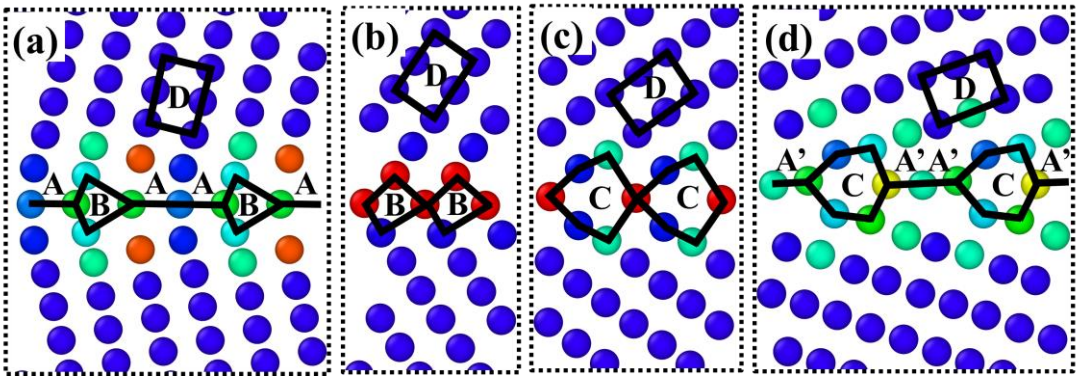

Fig. 5.2. The equilibrium $[1\bar{1}0]$ GB structures with SUs (a) Σ19 (11-6) = 26.53°, (b) Σ3 (11-2) = 70.53°, (c) Σ3 (11-1) = 109.47° and (d) Σ9 (22-1) = 141.06°. The structures are shown along the $[1\bar{1}0]$ tilt axis, and atoms are coloured according to their centro-symmetry parameters.

To uncover the interplay between GB structures and H trapping, H segregation energy maps for four identified GBs are presented in Fig. 5.3. The possible trapping sites are indicated by small spheres and coloured according to the segregation energy. It can be seen from Fig. 5.3 that different GBs possess unique H trapping maps. Combined with

the segregation energy distribution curves in Fig. 5.4, it is found that there exists a symmetric relationship with segregation energy at a distance of GB plane. For all considered GBs, boundary sites (a region ±5 Å from GB planes) correlated with atoms in the B and C SUs tend to have much lower segregation energy than those in the bulk lattice. This manifests an energetically favourable driving force for the segregation of H atoms from the bulk into the GB region, being consistent with previous observations [173]. In addition, the lowest and highest segregation energy varies somewhat over the entire misorientation ranges, but there is one exception. The lowest segregation energy (-0.25 eV) of Σ3 (1 1 $\bar{2}$) GB is much higher than that of the other GBs, *i.e.,* Σ19 (1 1 $\bar{6}$) GB with the segregation energy of -0.56 eV, indicating that the trapping ability of this twin boundary is almost negligible. The main reason is that Σ3 (1 1 $\bar{2}$) twin boundary has the most compact structure or lowest excess volume, as seen in Table 5.1.

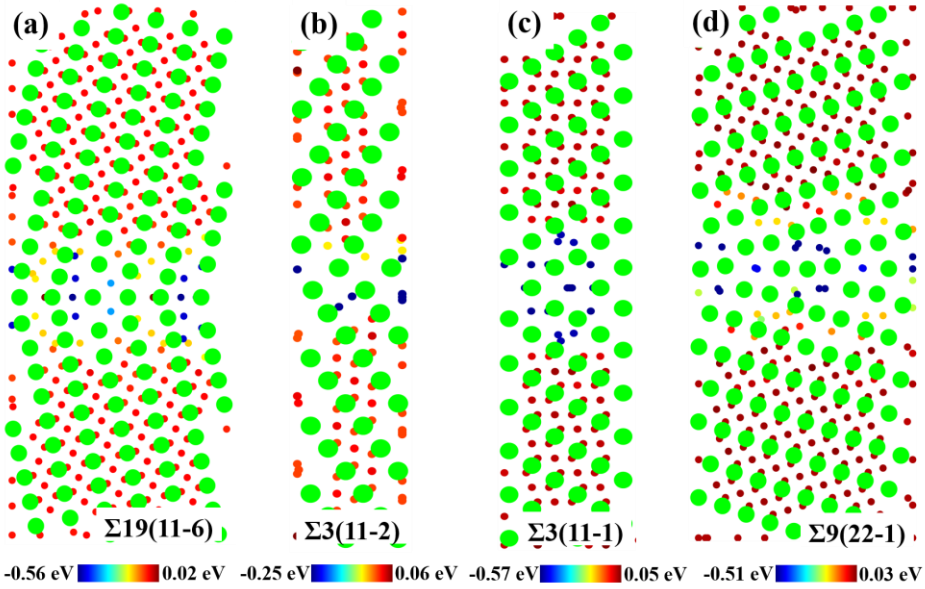

Fig. 5.3. H segregation energy maps for four GBs, and all cells are shown along the [1$\bar{1}$0] tilt axis. Larger spheres represent Fe atoms (green), and smaller ones indicate possible H trapping sites.

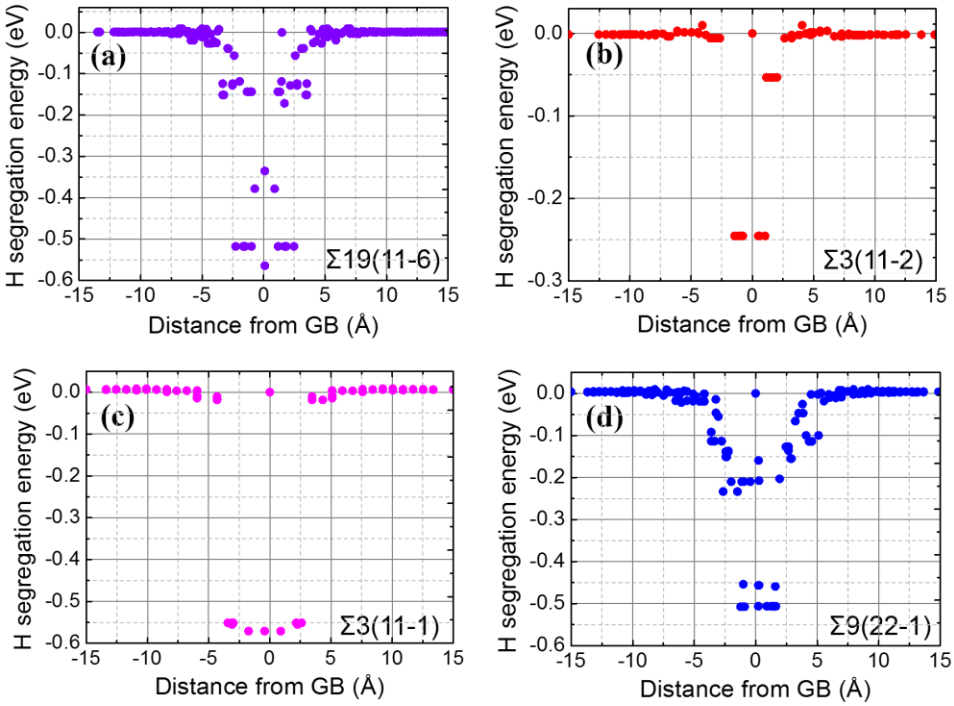

Fig. 5.4. Distribution of segregation energies as a function of distance from the GB.

5.3.2 Shear response and GB motion of pure GBs

Fig. 5.5 shows the shear stress and GB displacement of bicrystal models with four pure GBs as functions of simulation time. The stress components were calculated using the expression taken from the virial theorem, and the average atom volume was used in the stress calculations. One can see that for most scenarios, the shear stress initially rises without GB motion until reaching a peak value where GBs collectively move upwards or downwards. We denote the peak value as the critical shear stress in this work. Concomitant with each GB motion, the shear stress drops abruptly, followed by a long period of elastic loading stage where the stress gradually builds up. By consecutively applying the shear strain, the entire stick-slip dynamics is repeated, issuing in a sawtooth behaviour for shear stress and a stop-and-go GB migration. It is worthy to note that, with regard to Σ3 (1 1 $\bar{1}$) GB, a pure sliding event can be observed since it is accompanied by relative grain translation and a drop of the shear stress without normal GB migration.

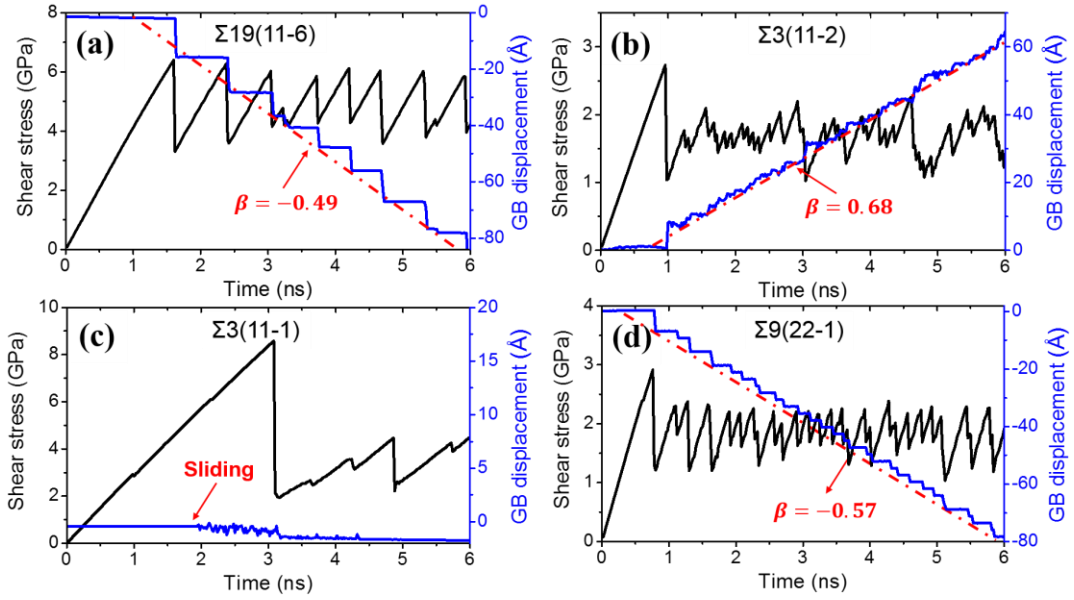

Fig. 5.5. Shear stress-time and GB displacement-time curves for pure GBs at 10K.

The coupling factor β of various GBs is determined by the slope of the dashed line. According to the MD simulation results, they are -0.49, 0.68 and -0.57 for Σ19 (1 1 $\bar{6}$), Σ3 (1 1 $\bar{2}$) and Σ9 (2 2 $\bar{1}$) GBs respectively. For Σ3 (1 1 $\bar{1}$) GB, there is no coupling factor for pure sliding. In terms of [001] tilt GBs in fcc Cu, Cahn et al. [179] proposed geometric model of coupling to describe the coupling factor β based on the Frank-Bilby equation [180, 181]. The Frank-Bilby approach indicated that different Burgers vector contents of the GBs can be determined solely by geometric considerations, resulting in a multivalued β. For a [001] fcc system, two Burgers vector contents (⟨100⟩ and 1/2⟨110⟩) were identified and described by corresponding coupling factors: $\beta_{<100>} = 2\tan(\frac{\theta}{2})$ and $\beta_{<110>} = -2\tan(\frac{\pi}{4} - \frac{\theta}{2})$. Homer et al. [182] went further and examined the generality of shear coupling mechanism over three typical tilt GBs ([001], [1$\bar{1}$0] and [111]) in fcc Ni. They reported that [1$\bar{1}$0] and [111] GBs did not follow the predicted coupling model. Recently, Niu et al. [183] claimed that the shear coupling of [001] GBs in bcc W obeyed the same derivation procedure as predicted in Cahn's investigation. In our case, [1$\bar{1}$0] boundaries in bcc α-Fe were chosen for simulation. Therefore, it is very necessary to examine whether the geometric theory holds valid in [1$\bar{1}$0] GBs in bcc metals. According to the most commonly-known dislocations (⟨100⟩ and 1/2⟨111⟩) in bcc crystals, we predict two shear coupling modes as seen in Fig. 5.6.

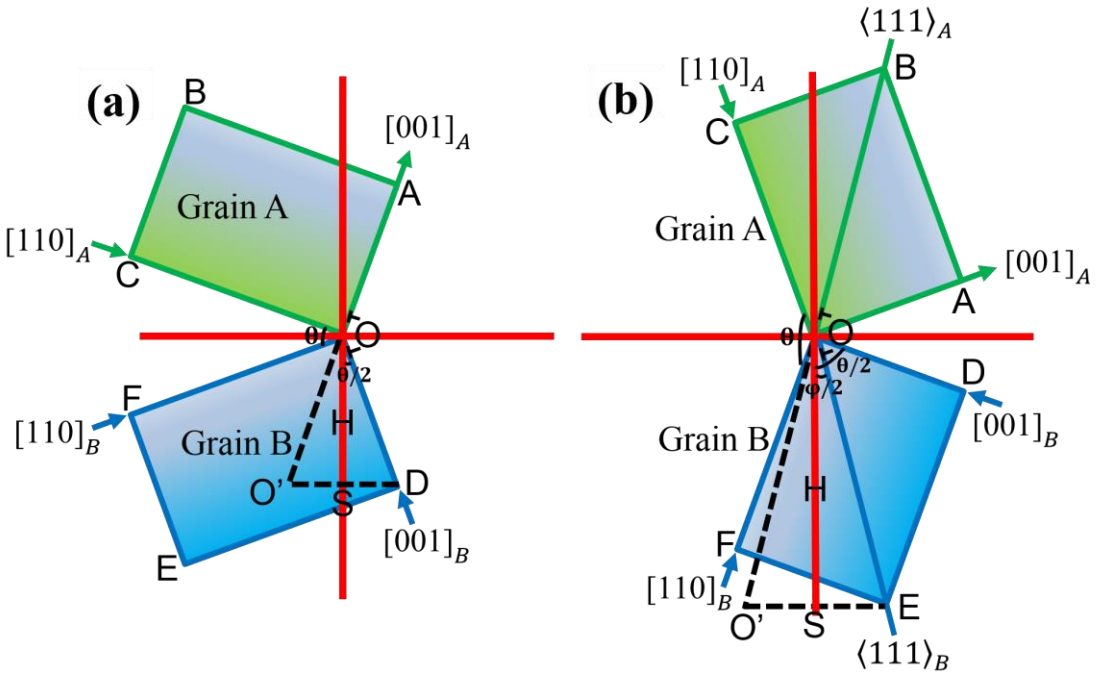

Fig. 5.6. Dislocation mechanisms of $[1\bar{1}0]$ GBs in bcc α-Fe with ⟨100⟩ and ⟨111⟩ coupling shear modes.

Considering two grains, grain-A (OABC) and grain-B (ODEF) rotate around the $[1\bar{1}0]$ tilt axis and form a symmetric tilt GB with misorientation angle θ. When subjected to shear deformation, the ⟨100⟩ GB dislocations of grain-A first advance along the slip direction. For example, segment AO undergoes a translation to a new position OO'. To align with the lattice of grain-B, the segment OO' then rotates counterclockwise by the tilt angle θ, conforming the segment OD. During the whole deformation process, the grain translation and normal GB displacement can be obtained from the relations: $S_{<100>} = 2a\sin(\frac{\theta}{2})$, $H_{<100>} = -a\cos\left(\frac{\theta}{2}\right)$, where a is the lattice constant. Therefore, the corresponding ⟨100⟩ coupling factor of $[1\bar{1}0]$ GBs in bcc α-Fe can be given as: $\beta_{<100>} = S_{<100>}/H_{<100>} = -2\tan(\frac{\theta}{2})$. Following a similar mechanism, we obtain the tangential translation and normal GB motion of the ⟨111⟩ coupling mode: $S_{<111>} = a\sqrt{3}\sin(\frac{\varphi}{2})$, $H_{<111>} = -(\sqrt{3}a/2)\cos(\frac{\varphi}{2})$. The relative coupling factor is readily derived from the ratio: $\beta_{<111>} = S_{<111>}/H_{<111>} = -2\tan(\frac{\varphi}{2})$, where $\frac{\varphi}{2} = \frac{\theta}{2} - \tan^{-1}\sqrt{2}$. Therefore, the coupling factor can be also expressed as: $\beta_{<111>} = 2\tan(\tan^{-1}\sqrt{2} - \frac{\theta}{2})$. Based upon the predicted coupling modes, the theoretical β value of each GB type is calculated as -0.47, 0.71 and -0.57, matching perfectly with the MD simulation results. As shown in Fig. 5.5, Σ19 $(1\ 1\ \bar{6})$ GB belongs to ⟨100⟩ mode, whereas Σ3 $(1\ 1\ \bar{2})$ and Σ9 $(2\ 2\ \bar{1})$ GBs migrate in ⟨111⟩ mode. Furthermore, it is found that the

critical shear stress of Σ19 (1 1 $\bar{6}$) GB is twice as high as that of Σ3 (1 1 $\bar{2}$) and Σ9 (2 2 $\bar{1}$) GBs, which is likely attributable to the fact that ⟨100⟩ dislocations are more difficult to glide than 1/2⟨111⟩ ones [179].

5.3.3 Shear response and motion of GBs with H content

Fig. 5.7 shows the influence of H atoms on the coupled GB motion in terms of the shear stress and GB displacement vs. simulation time, as well as the dependence of the critical shear stress on H concentration. It is clear that the critical shear stress of both ⟨100⟩ and ⟨111⟩ mode GBs (Σ19 and Σ9) in the presence of H is increased when compared to H-free cases, indicating that H impedes the local mobility of GBs. As seen in Figs. 5.7 and 5.8, GBs are pinned by the segregated H in the initial stress-accumulation stage, and the elastic loading time becomes longer than that without H. To overcome the pinning effect of H on GB mobility, a higher critical shear stress is needed for the normal GB displacement. For example, regarding the Σ9 (2 2 $\bar{1}$) GB at $C_H = 3.0 \times 10^{-3}$, there is an elastic loading stage lasting 1.2 ns, in which the critical shear stress increases up to 5.1 GPa, more than two orders of magnitude higher than the H-free case. Once the critical shear stress is reached, the coupled GB motion takes place, with a series of H-vacancy clusters left behind. It has been proven that H-vacancy clusters can serve as the primary cause for microstructural damage [184]. However, in the present work it is seen that these H-vacancy clusters fail to contribute to the ultimate failure. More details on this observation will be provided in Section 5.4. It should be mentioned that, after introducing H atoms, the subsequent grain translation is longer and the normal GB displacement is shorter in comparison to that of H-free case, which causes the coupling factor β to decrease (see Fig. 5.7(b) and (e)). When the H concentration exceeds a certain value, *i.e.,* 1.5×10^{-3} for Σ19 (1 1 $\bar{6}$) GB, and 5.5×10^{-3} for Σ9 (2 2 $\bar{1}$) GB, the GB coupling disappears, and a transition from the coupled GB motion to pure GB sliding is observed.

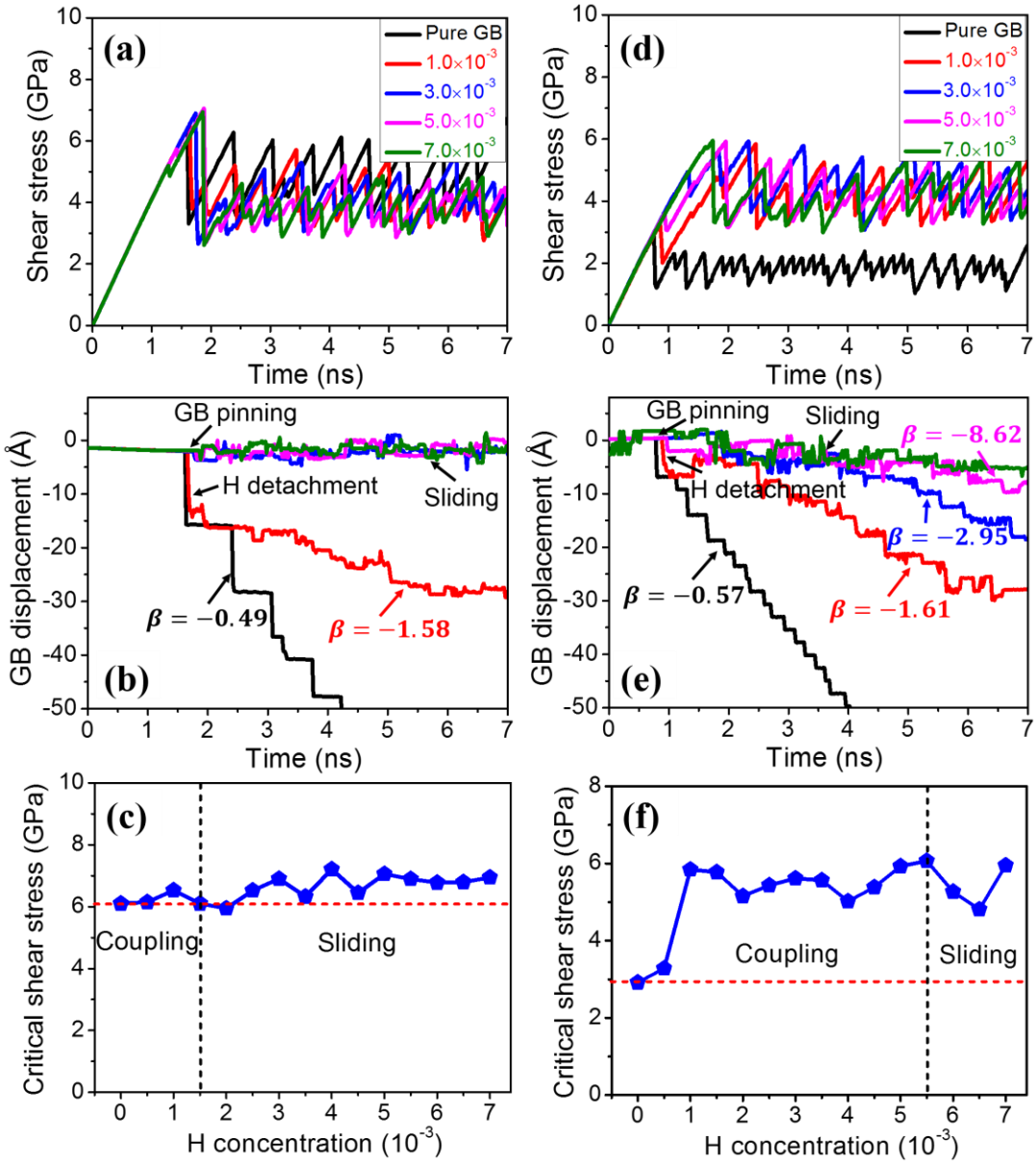

Fig. 5.7. (a) shear stress-time and (b) GB displacement-time curves for Σ19 (1 1 $\bar{6}$) GB under various H concentrations. (c) The critical shear stress vs. H concentration for Σ19 (1 1 $\bar{6}$) GB. Σ9 (2 2 $\bar{1}$) GB has the same descriptions as presented in (d)-(f).

Cahn et al. [179] revealed that the GB migration was achieved by the deformation of GB dislocation structures. Does the presence of H change the local dislocation structures of the GBs so as to affect their motion? To answer this, we begin with the analysis of atomic mechanisms responsible for the GB motion without and with H. In terms of Σ19 (1 1 $\bar{6}$) GB, the GB motion is in fact the collective gliding of an array of straight dislocations. From the extracted dislocation lines in Fig. 5.8(a), one can observe that these dislocations are ⟨100⟩-type, agreeing well with the predicted coupling mode. In the presence of H ($C_H = 1.0 \times 10^{-3}$), it can be seen from Fig. 5.8(b) that these ⟨100⟩-type dislocations interact with each other. This behaviour is generally in accordance with the

shielding concept of the HELP model, in which H reduces the interaction distance between dislocations [98]. A strong interaction force among dislocations seems to make it difficult to drive the gliding of ⟨100⟩-type dislocations, thus hindering the GB motion. Also, upon further shear loading the dislocation dissociation event occurs, for example, the ⟨100⟩-type dislocation splits into a ⟨111⟩-type dislocation and an other-type dislocation($[001] \rightarrow 1/2[\bar{1}\bar{1}\bar{1}] + 1/2[113]$), which further prevents the GB migration. Regarding Σ9 (2 2 $\bar{1}$) GB in Fig. 5.8(c), the boundary is composed of A' and C SUs. Two perfect D SUs are adjacent to the GB unit C and located at the upper and lower grains, respectively. During the GB migration, these SUs (C and D) can be transformed into each other by relatively small in-plane atomic displacements. Specifically, unit C composed of Fe atoms 5, 6 and 9-12 is transformed into D SU in the upper grain and the rectangular D SU consisting of Fe atoms 2-7 in the lower grain becomes six-member kite-shaped C SU. This unit transformation makes the GB plane move downward, accompanied by a lateral translation of the upper grain. Note that at $C_H = 1.0 \times 10^{-3}$, the coupled motion is still dominated by the unit transformation (see Fig. 5.8(d)). Concomitant with each GB migration step, the GB structure along the *Y* direction is converted from |DCD| to |DDC′|. The C' SU is regarded as a distorted C SU, arising from the H detachment during the GB migration. With the disordered structure, the difficulty for structural transition from D SU to C' SU is increased, which may explain why the presence of H results in a higher critical shear stress. In the case of high H concentration, a totally different phenomenon is observed. After the addition of H atoms, the local atomic configurations of the GB are significantly destroyed, with C and D SUs disappearing (see Fig. 5.8(f)). Under this condition, it is impossible to achieve GB migration via a unit transformation, instead, a pure sliding event occurs.

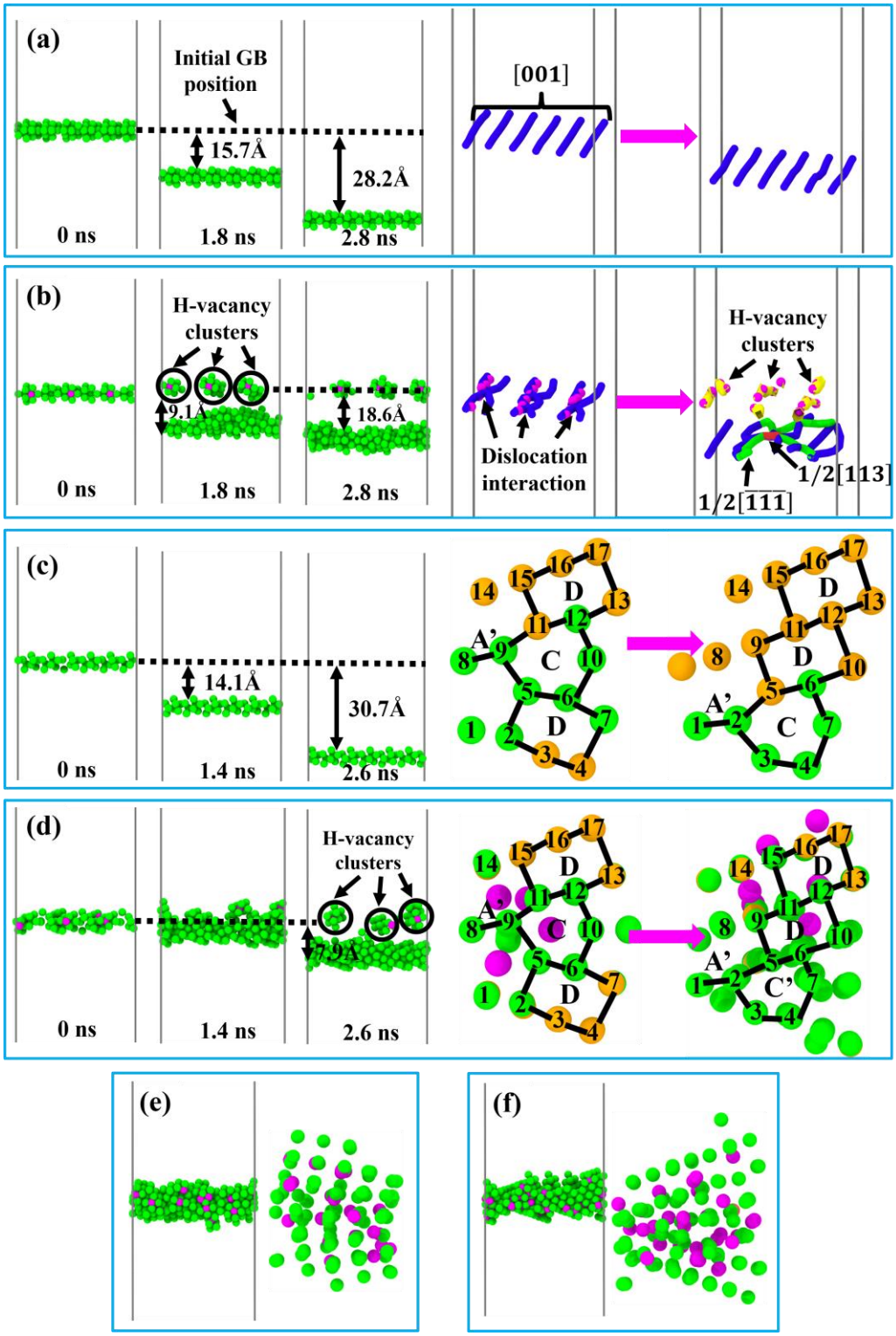

Fig. 5.8. Dislocation activities and atomic configurations for Σ19 (1 1 $\bar{6}$) GB: (a) without H and (b) with H of $C_H = 1.0 \times 10^{-3}$. (c) and (d) are atomic structures for Σ9 (2 2 $\bar{1}$) GB without H and with H of $C_H = 1.0 \times 10^{-3}$, respectively. (e) and (f) are atomic details of Σ19 (1 1 $\bar{6}$) GB and Σ9 (2 2 $\bar{1}$) GB, respectively, at $C_H = 6.0 \times 10^{-3}$. Atoms are coloured by CNA, where atoms with a perfect bcc structure are dark yellow, green atoms organize the GB plane and the dislocation core, and H atoms are assigned in pink. Different types of dislocations are identified by DXA in Ovito.

5.4 Discussion

Solute H atoms were introduced into two types of $[1\bar{1}0]$ STGBs, namely ⟨100⟩ and ⟨111⟩ mode GBs, in order to study their possible influence on the coupled GB motion. In all investigated cases, the GB migration process is markedly impeded, independent of GB structures. The present findings are in line with the observations on other impurities in metallic systems, like Mg in Al [185], O in Al [186], and He in W [187]. These studies have suggested that local structural changes caused by segregated impurities play a decisive role in the GB mobility. For example, Niu et al. [187] reported that He trapping could have an effect on changing GB dislocation structures by the formation of jogs and He-vacancy clusters. The critical shear stress was governed by a competition between the impeding effect of He and the facilitating effect of jogs. In the cases investigated in the present work, GB dislocation structures are modified by H-enhanced dislocation interaction events at ⟨100⟩ mode Σ19 GB within the framework of the HELP mechanism. These dislocation intersections can serve as dislocation sources owing to high local stress and disordered atomic structure. Proceeding to higher shear deformation, dislocation dissociation occurs at the expense of dislocation gliding, thereby inhibiting GB migration. Specifically, the dissociation process is energetically unfavourable according to the Frank energy criteria, a high system energy is therefore consumed to activate this event. Consequently, the residual energy required for normal dislocation gliding becomes low so as to suppress GB motion. Regarding ⟨111⟩ mode Σ9 GB, H throws the atomic structures of GBs into disarray, which prevents the GB structural transformation and changes the coupling mode.

As mentioned before, abundant vacancies were generated and stabilized by H in the form of H-vacancy clusters when subjected to shear deformation (see Fig. 5.8). This has been revealed to play a crucial role in embrittling metallic materials in previous experiments [188, 189] and MD simulations [125, 190-192]. Motivated by this, we further discuss the effects of segregated H atoms on the vacancy evolution during the coupled GB motion. As shown in Fig. 5.9, for H-free cases, there are no vacancies nucleated from either ⟨100⟩ or ⟨111⟩ mode GBs under shear deformation. Hirth and Lothe [193] concluded that vacancy generation typically originates from dislocation plasticity including the growth of prismatic loops, dislocation-dislocation interactions, etc. However, in our case, the shear plasticity is mainly controlled by the collective gliding of a series of parallel dislocations in the absence of H, without dislocation interactions or

other dislocation forms nucleating vacancies. In contrast, for all H-charged samples, extensive dislocation interaction events occur via the HELP mechanism, thus increasing the generation rate of vacancies. And more importantly, a certain number of these vacancies are combined with H and transformed into H-vacancy clusters, as demonstrated in Fig. 5.8. In this way, vacancies can be largely preserved during dislocation sinks and annihilation [125]. Attributed to these aspects, the vacancy nucleation rate is increased while the vacancy annihilation rate is decreased with increasing H concentrations, rendering that GBs with a higher H concentration have a higher vacancy concentration. However, a careful observation on Fig. 5.9 indicates that vacancies are mainly formed at the initial shear stage (H detachment process) in the presence of H, and there are few vacancies newly generated during the subsequent GB migration. Two factors could have contributed to the observed behaviour: firstly, since almost all solute H atoms are detached from GBs at initial shear stage, new vacancies are hardly nucleated or stabilized nearby the migrating GBs. Secondly, the detached H-vacancy clusters at the initial GB position cannot tend to grow in size via vacancy accumulation due to a lack of dislocation plasticity activities when the GBs migrate away. These points are also beneficial for us to understand why no ultimate failure occurs in our simulation models, as seen in Fig. 5.10. Li et al. [191] revealed that the growth of H-vacancy clusters activated the nucleation event of proto nanovoids, which further led to the occurrence of macroscopic fracture via nanovoid growth and coalescence. In the present work, although some H-vacancy clusters are found in the models, their growth is not encouraged as aforementioned. Accordingly, the voids are not triggered and HE does not eventuate (see Fig. 5.10). In view of this, it seems that the deformation mechanism dominated by the coupled GB motion is beneficial to reduce the susceptibility to H-induced intergranular embrittlement, which may prove to be fruitful in designing new metallic materials with high resistance to HE.

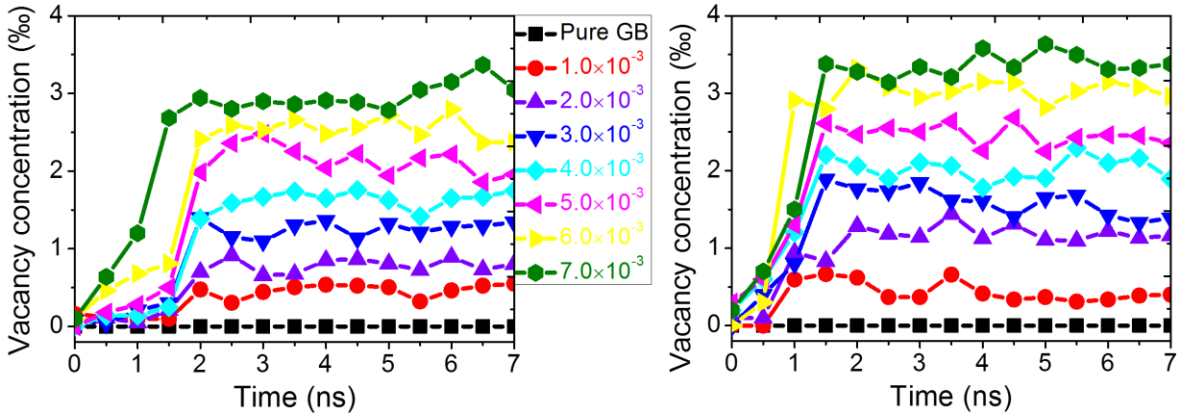

Fig. 5.9. The evolution of vacancy concentration with simulation time for (a) Σ19 (1 1 $\bar{6}$) GB and (b) Σ9 (2 2 $\bar{1}$) GB under various H-charged concentrations.

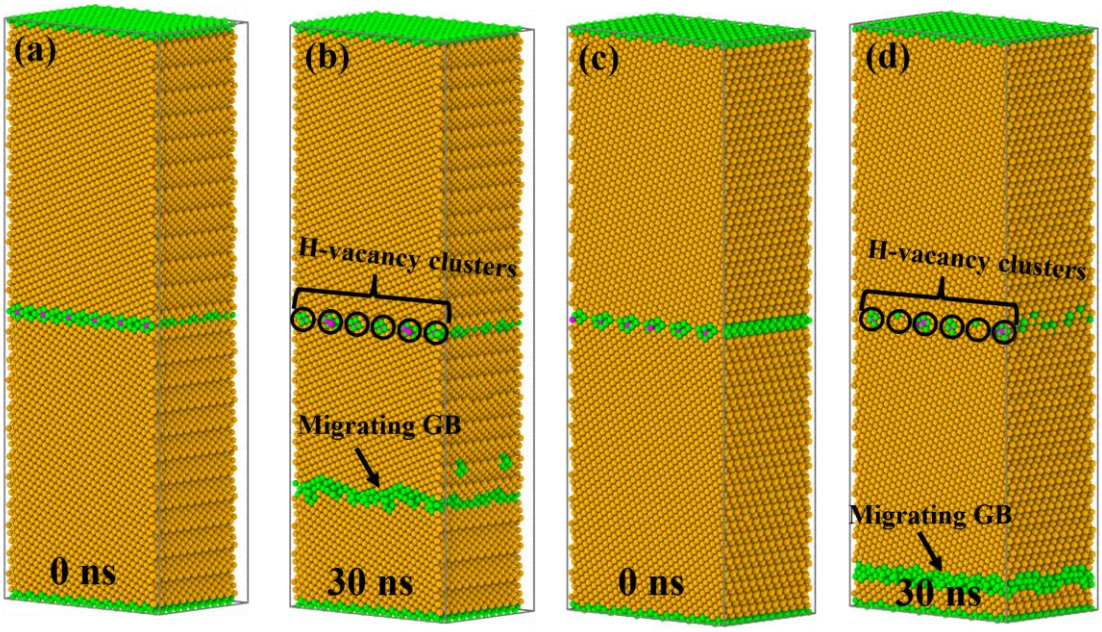

Fig. 5.10. MD simulation snapshots of atomic configurations of Fe bicrystals containing (a) and (b) Σ19 (1 1 $\bar{6}$) GB, (c) and (d) Σ9 (2 2 $\bar{1}$) GB with different simulation time at $C_H = 1.0 \times 10^{-3}$. Atoms are coloured by CNA, the same as described in Fig. 3.8.

5.5 Summary

MD simulations were carried out to elucidate the influence of H segregation into several typical [1$\bar{1}$0] STGBs on the shear response and coupled GB motion of bicrystals in α-Fe. The major conclusions can be summarized as follows:

(1) Under shear loading, the deformation modes of GBs except Σ3 (1 1 $\bar{1}$) GB were found to operate by normal GB migration coupled to tangential translation of grains. Depending on our geometric model of coupling for [1$\bar{1}$0] STGBs in bcc metals, two different coupling branches (⟨100⟩ and ⟨111⟩) were predicted and further validated by the

simulation results. Furthermore, it was found that the critical shear stress of ⟨100⟩ mode GBs is twice as high as that of ⟨111⟩ mode ones.

(2) Solute H had a considerable impeding effect on the coupled GB motion, irrespective of GB structures. In contrast to H-free cases, H segregation increased the critical shear stress and decreased the coupling factor. When the H concentration reached a critical value, the response of GBs to shear deformation changed from coupling to pure GB sliding. It was confirmed from atomic mechanisms that the impeding effect of H mainly originated from the fact that H severely damaged the local atomic structures of GBs. Regarding ⟨100⟩ mode Σ19 GB, solute H enhanced dislocation interactions by modifying the GB dislocation structures, and thus prevented the collective gliding of GB dislocations responsible for GB migration. In terms of ⟨111⟩ mode Σ9 GB, the presence of H disordered local structures of the GB, thereby suppressing the GB structural transformation and changing the coupling mode.

(3) It was revealed that the vacancy concentration increases with increasing solute H concentration. Although H-vacancy clusters were formed by the solute H stabilizing the vacancies, they cannot grow larger via vacancy accumulation as GBs with extensive dislocation plasticity migrate away, which directly suppressed the occurrence of ultimate failure. Therefore, it seems that the coupled GB motion may be beneficial to resist H-induced intergranular embrittlement.

Chapter 6 Hydrogen-modified interaction between lattice dislocations and grain boundaries

This chapter is extracted from the following publications:

1. **Li J,** Lu C*, Pei L, Zhang C, Wang R. Hydrogen-modified interaction between lattice dislocations and grain boundaries by atomistic modelling. Int J Hydrogen Energy. 2020;45:9174-87.

2. **Li J,** Lu C*, Pei L, Zhang C, Tieu K. Influence of solute hydrogen on the interaction of screw dislocations with vicinal twin boundaries in nickel. Scripta Mater. 2019;173:115-9.

6.1 Introduction

Experimental evidence of the microstructure beneath H-induced intergranular facets has shown an acceleration of plasticity process and pre-failure deformation prior to crack initiation, suggestive of the significance of dislocation-GB interactions on establishing the conditions for intergranular fracture. However, the effects of H atoms on modifying the interaction mode of GBs and the accurate role of the interaction process in promoting ultimate failure are unknown. In view of this, here a nanoscale understanding for the H-modified dislocation-GB interaction in Ni was developed using MD simulations. Particularly, the influence of H on the interaction mechanisms between the screw dislocation and various $[1\bar{1}0]$ symmetric tilt GBs on an atomic scale was studied. The remainder of this chapter is organized as follows. The details of simulation setup are described in Section 6.2. H segregation maps and dislocation-GB interaction mechanisms without and with solute H are given in Section 6.3. The simulation results are discussed in Section 6.4, followed by the main summary in Section 6.5.

6.2 Simulation methodology

MD simulations were carried out using the software package LAMMPS [155] with the EAM potential for Ni-H [28, 29, 160]. The bicrystal model was used to study the dislocation-GB interaction because it enables a well-controlled investigation of specific GB properties. The initial structures of nine $[1\bar{1}0]$ STGBs were constructed on the basis of the coincidence site lattice (CSL) and then equilibrated by energy minimisation using

a nonlinear conjugate gradient method. The crystallographic orientations of grain-A along *X*-[112], *Y*-[$\bar{1}\bar{1}$1], *Z*-[1$\bar{1}$0] in Fig. 6.1 were the same for all GBs; the orientations of grain-B were changed depending on the misorientation angle, refer to Table 6.1. Free boundary conditions were applied in the *X* and *Y* directions to minimise the effect of image forces, while a periodic boundary condition was prescribed along the *Z* direction. A single screw dislocation with Burgers vector of $a_0/2[\bar{1}10]$ was placed on the $(\bar{1}\bar{1}1)$ slip plane within the grain-A via a rigid-displacement procedure [194, 195] at a distance of 80 Å away from the GBs, where a_0 is the lattice parameter. With this separation distance, no attractive or repulsive forces were detected between the dislocation and GBs during relaxation. The core of the screw dislocation can split into two Shockley partials (leading and trailing partial dislocations) according to $1/2[\bar{1}10] \rightarrow 1/6[\bar{1}21] + 1/6[\bar{2}1\bar{1}]$.

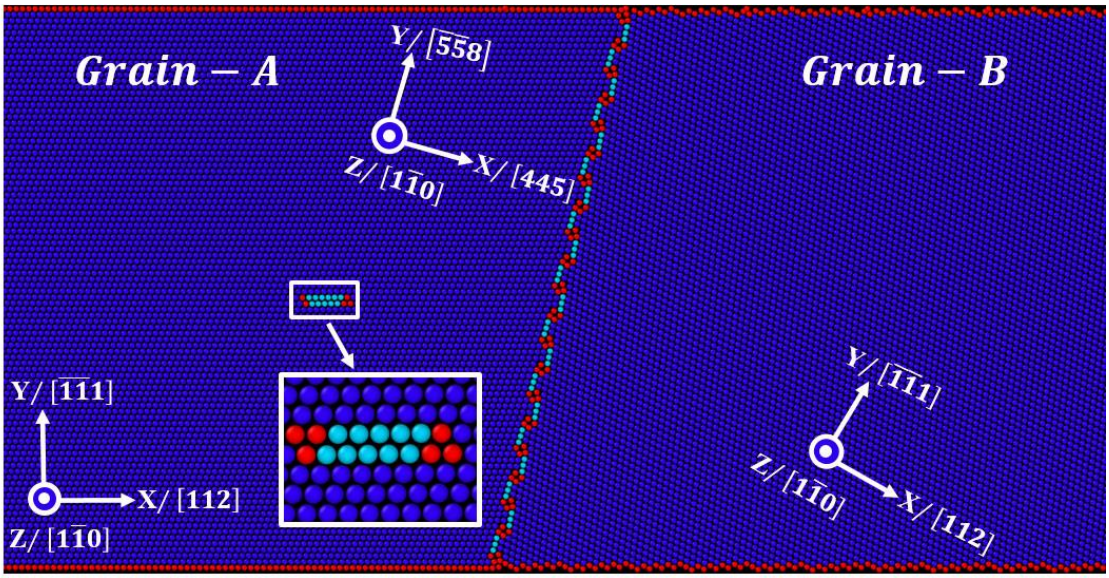

Fig. 6.1. Model domain of Σ57 (4 4 5) GB for simulating the interaction between a screw dislocation and GBs. All atoms are coloured by the CNA, the same as described in Fig. 4.7.

To study the effect of solute H on the dislocation-GB interactions, all possible trapping sites for H atoms at each GB type were first identified through Voronoi tessellation [172]. The H segregation maps were then plotted based on the calculated segregation energy E_α^{seg} for one H atom at one type of trapping site α, see more details in Chapter 4. Subsequently, the H occupation probability at site α was calculated as

$$\theta_\alpha = \frac{\theta_{bulk}\exp(-E_\alpha^{seg}/K_BT)}{1+\theta_{bulk}\exp(-E_\alpha^{seg}/K_BT)} \quad (6.1)$$

where θ_{bulk} is bulk H concentration in atomic ratio, K_B is Boltzmann's constant and T is the temperature. The Ni-H interactions were finally created by adding H atoms into

'favourable' trapping sites according to the occupation probability θ_α. Here we define all sites with segregation energy lower than zero as 'favourable'. The bulk H concentration and temperature is set at $\theta_{bulk} = 0.001$ and $T = 300$K, respectively. Prior to the MD shear simulations, energy minimisation was imposed again, followed by a heating process to bring the H distribution to a state of equilibrium.

The atoms within the 10 Å thick region near the free surfaces along the *Y* direction were fixed and frozen by setting the interatomic force to zero. The shear strain at a constant rate 10^8 s^{-1} was applied to the simulation cell on the *Y-Z* shear plane by rigidly displacing the upper frozen atoms along the *Z* direction. MD simulations were carried out under constant energy ensemble (NVE) with a timestep of 1 fs. Note that the H segregation into GBs was performed at 300 K but the shear deformation was started at 0.1 K to suppress any thermal activation of dislocation processes.

Table 6.1. Characterization of the GBs, including tilt angle, Σ value, model size and GB energies.

Tilt angle (°)	CSL value ($\boldsymbol{\Sigma}$)	Model size $\boldsymbol{Lx, Ly, Lz(nm)}$	GB energy $(\boldsymbol{mJ \cdot m^{-2}})$
26.53	Σ19(1 1 6)	39.06, 18.41, 1.99	904.52
50.48	Σ11(1 1 3)	38.19, 18.06, 1.99	375.80
70.53	Σ3(1 1 2)	38.80, 18.29, 1.99	806.91
97.05	Σ57(4 4 5)	38.70, 18.99, 1.99	731.82
109.47	Σ3(1 1 1)	39.43, 18.38, 1.99	50.39
114.53	Σ171(11 11 10)	38.71, 19.19, 1.99	419.64
141.06	Σ9(2 2 1)	39.01, 18.98, 1.99	1097.49
153.48	Σ19(3 3 1)	38.36, 19.53, 1.99	1081.91
174.60	Σ451(15 15 1)	38.09, 18.40, 1.99	547.31

6.3 Results

6.3.1 GB structure and H trapping map

Atomic configurations of several typical GB structures are illustrated in Fig. 6.2. Five basic SUs are identified and labelled among these GBs. Specifically, C, D and E SUs correspond to Σ11 (1 1 3), Σ3 (1 1 1) and Σ9 (2 2 1) GBs. A and A' SUs are basic units of Σ1 (001) θ = 0° and Σ1 (110) θ = 180° perfect crystal orientations. Other GBs with non-preferred misorientations come from a combination of these basic SUs with complexity. For example, Σ57 (4 4 5) GB is composed of C and D SUs, and Σ171 (11 11 10) GB contains a combination of D and E SUs. Note that Σ171 (11 11 10) GB has the dissociated

structure that D SUs extend from two sides of the boundary, resulting in ISF facets inside lattice region. For convenience of further discussion, we refer Σ11 (1 1 3), Σ3 (1 1 1) and Σ9 (2 2 1) boundaries as 'singular' GBs, and classify others as 'general' GBs.

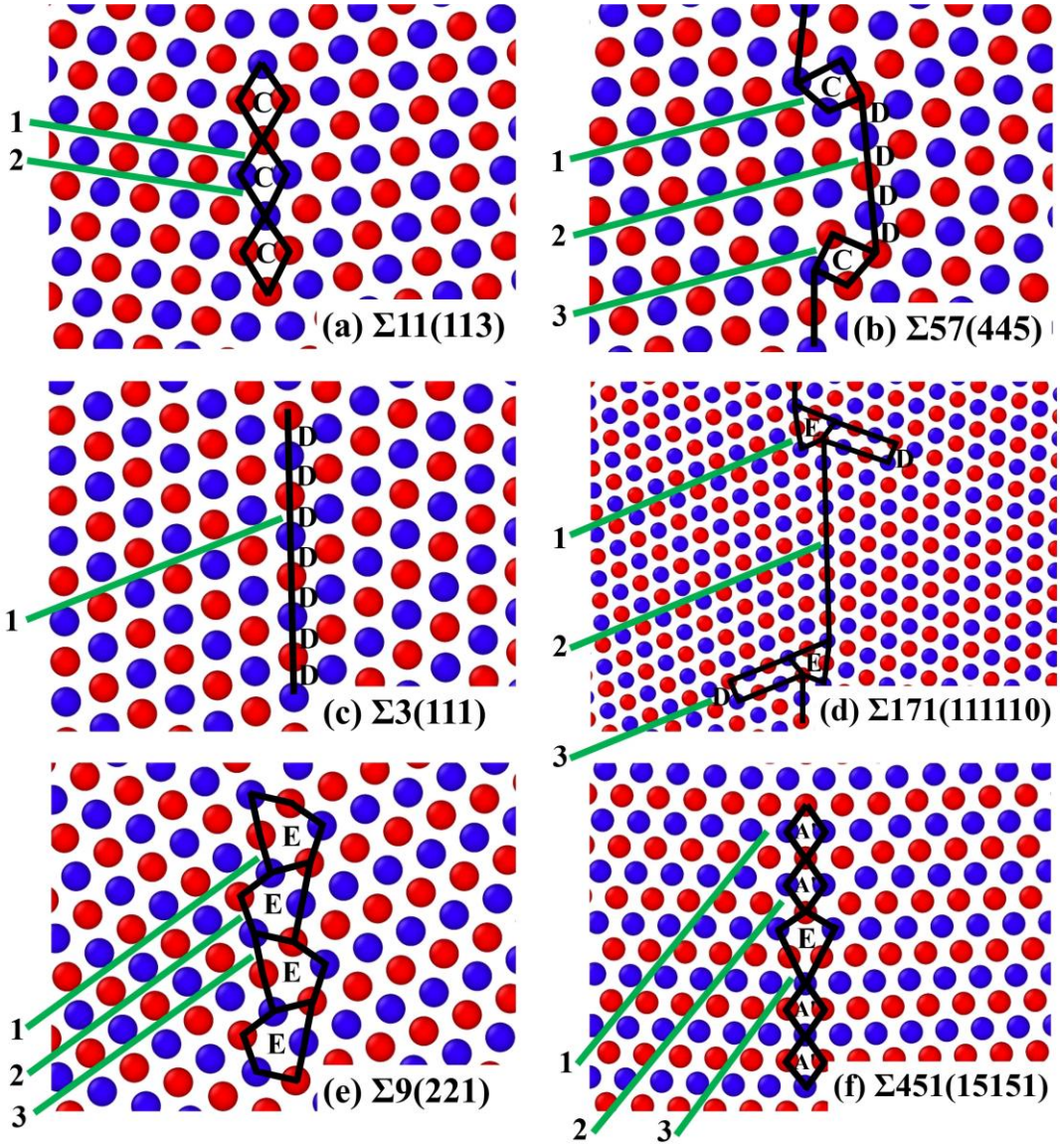

Fig. 6.2. Atomic images of the equilibrium GB structures with SUs. The structures are viewed along the [1$\bar{1}$0] tilt axis. Atoms on consecutive {110} planes are shown as blue and red. Several incoming glide planes are marked by solid lines and labelled as 1–3.

The H segregation energy maps are depicted in Fig. 6.3. The possible trapping sites are indicated by small spheres and coloured according to the segregation energy. Since different GBs possess different SUs, the segregation energy distribution of each GB type is unique. For instance, the lowest segregation energy of Σ9 (2 2 1) GB is -0.28 eV, and the sites with this energy are located within E SUs. In contrast, the lowest segregation energy of Σ3 (1 1 1) GB is only -0.04 eV, and H atoms occupy exclusively at the

octahedral sites located in between the twin boundary plane and its adjacent (1 1 1) plane. By comparing the segregation energy, it is found that Σ3 (1 1 1) GB has much higher segregation energy than other types of GBs, indicating that the trapping ability of this twin boundary is almost negligible. This concurs with many experimental results that CTBs are inherently resistant to H embrittlement due to their low H solubility [197-199].

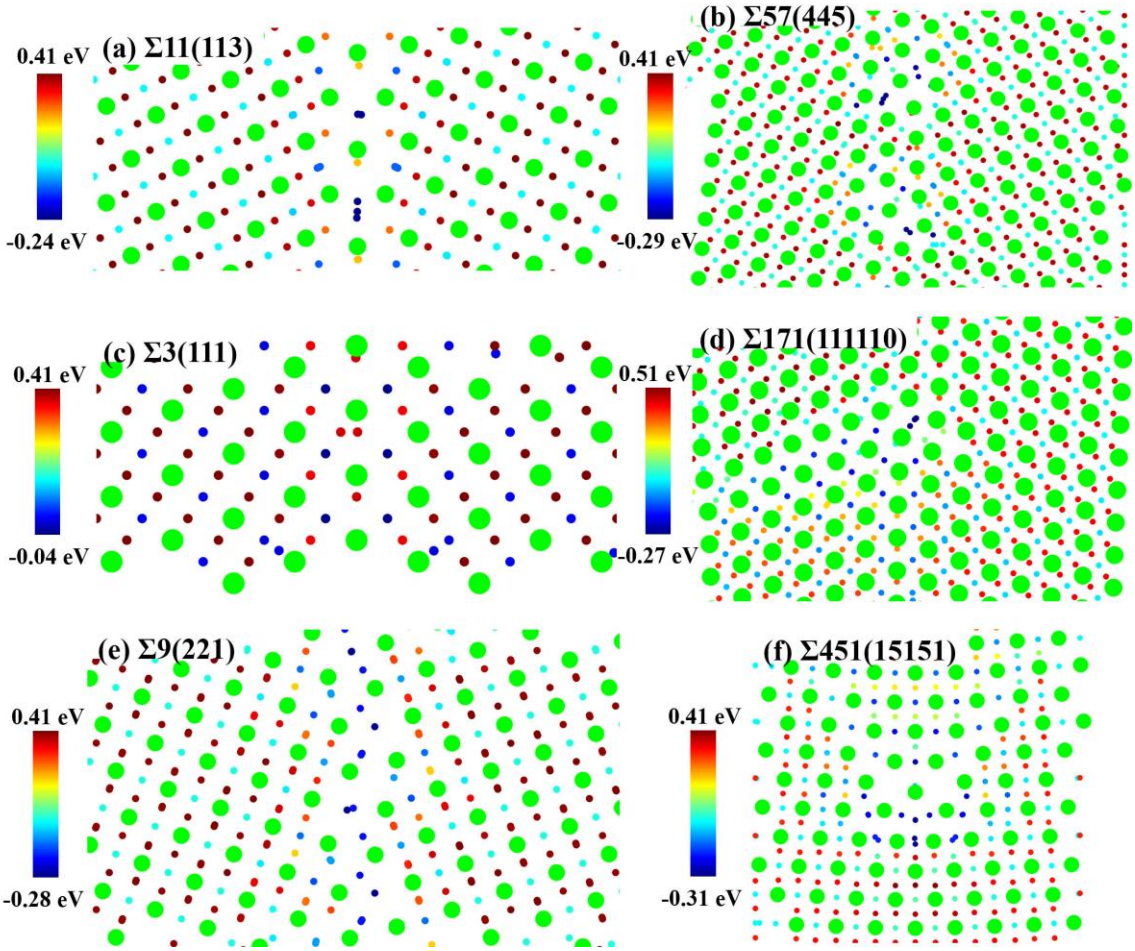

Fig. 6.3. H segregation energy maps for six typical GBs, all cells are shown along the [1$\bar{1}$0] tilt axis. Larger spheres represent Ni atoms (green), and smaller ones indicate possible H trapping sites.

6.3.2 Shear response and interaction outcomes

Taking Σ9 (2 2 1) GB as an example, the dislocation-GB interaction occurs in five stages, as divided by the dashed line in Fig. 6.4(a). The corresponding atomic configurations are illustrated in Fig. 6.4(b). In stage-①, the shear stress linearly rises without dislocation motion. A stress drop on the shear stress-strain curves is evident when incoming screw dislocation moves towards the boundary, as shown in stage-②. Once the dislocation impinges on the GB, the stress increases again in order to overcome high GB repulsion until it reaches a peak value (stage-③). This value is taken as the critical shear

stress in this study. For Σ9 (2 2 1) GB, the dislocation is eventually incorporated into the GB, and then dissociates into GB dislocations (stage-④). This observation is in concordance with the formal theory of crystalline interfaces that while impinging onto a GB, the lattice dislocation can dissociate or redistribute itself into GB dislocations with the total Burgers vector conserved [200]. With further shear deformation, the dissociated GB dislocations repel each other and propagate along the boundary plane (see Fig. 6.4(b) at a strain of 1.69%). In stage-⑤, the dislocation propagation is hindered when GB dislocations arrive at the fixed area of the simulation model. The stress curves reach the strain-hardening stage with a continuous increase of stress without any new deformation mechanisms to release the system stress.

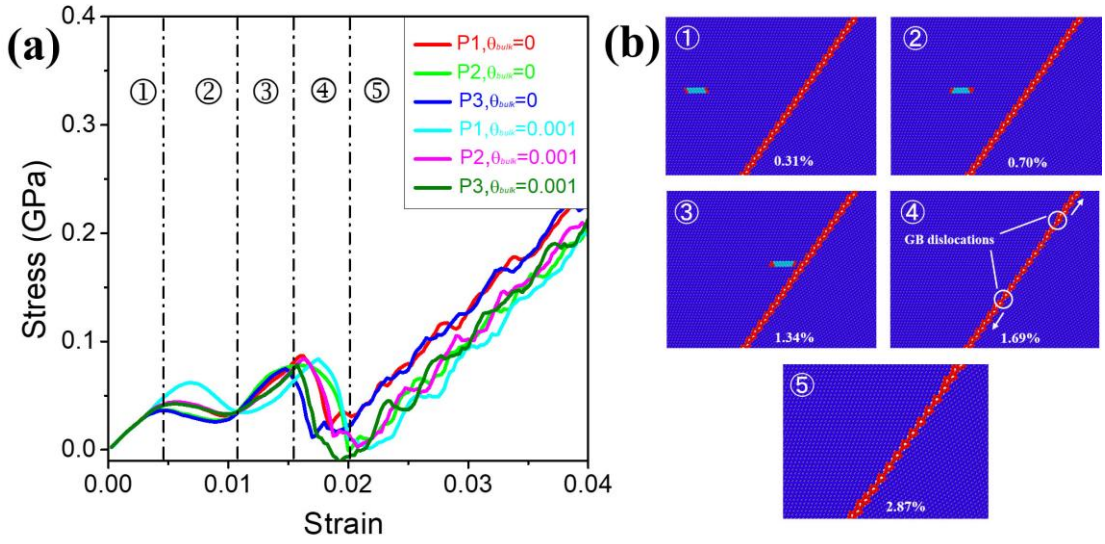

Fig. 6.4. (a) Shear stress-strain curves during the interaction between a screw dislocation and Σ9 (2 2 1) GB with different slip planes and H concentrations. P1, P2 and P3 are slip planes, and θ_{bulk} is H concentration. (b) Snapshots of atomic configuration for each stage of P2, θ_{bulk}= 0 case in (a).

All possible dislocation-GB interaction outcomes for different types of GBs with various incoming planes without and with H are listed in Table 6.2. In the absence of H, it is found that for 'singular' GBs (Σ3, Σ9 and Σ11), dislocation dissociation from the screw dislocation into GB dislocations is the interaction mechanism regardless of incoming planes. In the case of 'general' GBs (Σ57, Σ171 and Σ451), with different glide planes the shear loading may lead to different interaction outcomes due to the complexity of GB structures. For example, when the incident dislocation glides on the plane 1 and reacts with the Σ171 (11 11 10) GB, a new partial dislocation is nucleated from the boundary, whereas dislocation dissociation and reflection dominate the deformation process when the incoming slip is on plane 2 and 3, respectively. In contrast to H-free

cases, absolutely different interaction mechanisms are observed in the presence of H. For most of the scenarios, H segregation tends to transform these interactions into ones involving dislocation absorption. There are two exceptions: Σ3 (1 1 1) GB and Σ171 (11 11 10) GB with slip plane 2. The main reason is that the twin boundary and the twin segments of Σ171 (11 11 10) GB hardly trap H atoms, the interaction mechanism therefore does not change.

Table 6.2. Summary of the interaction outcomes. The following abbreviations are used. D: Dislocation dissociation, N: Dislocation nucleation, T: Dislocation transmission, R: Dislocation reflection, A: Dislocation absorption.

GBs	Incoming planes	$\boldsymbol{\theta_{bulk}}$= 0		$\boldsymbol{\theta_{bulk}}$= 0.001	
		Critical shear stress (MPa)	Reaction types	Critical shear stress (MPa)	Reaction types
Σ11(1 1 3)	1	109	D	114	A
	2	102	D	105	A
Σ57(4 4 5)	1	81	N	87	A
	2	82	T	89	A
	3	84	N	86	A
Σ3(1 1 1)	1	132	D	132	D
Σ171(11 11 10)	1	102	N	104	A
	2	98	D	98	D
	3	103	R	112	A
Σ9(2 2 1)	1	85	D	87	A
	2	78	D	81	A
	3	74	D	76	A
Σ451(15 15 1)	1	91	T	99	A
	2	89	N	89	A
	3	93	N	97	A

6.3.3 Atomic mechanisms for dislocation-GB interactions

'Singular' GBs

In the following we analyse atomic mechanisms responsible for dislocation-GB interactions without and with H. Herein, the Thompson tetrahedron is referred to elucidate the dislocation reaction paths [195]. Fig. 6.5(a) presents that the screw dislocation on plane 1 with the Burgers vector AB approaches and reacts with Σ3 (1 1 1) GB in the absence of H. It can be seen that this dislocation moving towards the twin boundary is constricted, and the two separated partials (γB and $A\gamma$) are recombined into a full dislocation AB at the intersection. At a shear strain of 1.73%, the constricted full dislocation AB dissociates into two GB dislocations (twinning partials $A\delta$ and δB) propagating in opposite directions along the twin boundary. The dissociation mechanism

can be summarised as: $\gamma B + A\gamma \rightarrow AB \rightarrow A\delta + \delta B$, or $1/6[\bar{1}21] + 1/6[\bar{2}1\bar{1}] \rightarrow 1/2[\bar{1}10] \rightarrow 1/6[\bar{1}2\bar{1}] + 1/6[\bar{2}11]$. A step height of one (111) atomic layer is associated with each twinning partial, indicating that the propagation of these partials results in a GB migration that expands the grain-B at the expanse of the grain-A. For the H-charged case, the dissociation behaviour at the intersection is identical to that without H since the twin boundary hardly absorbs H atoms (see Fig. 6.5(b)).

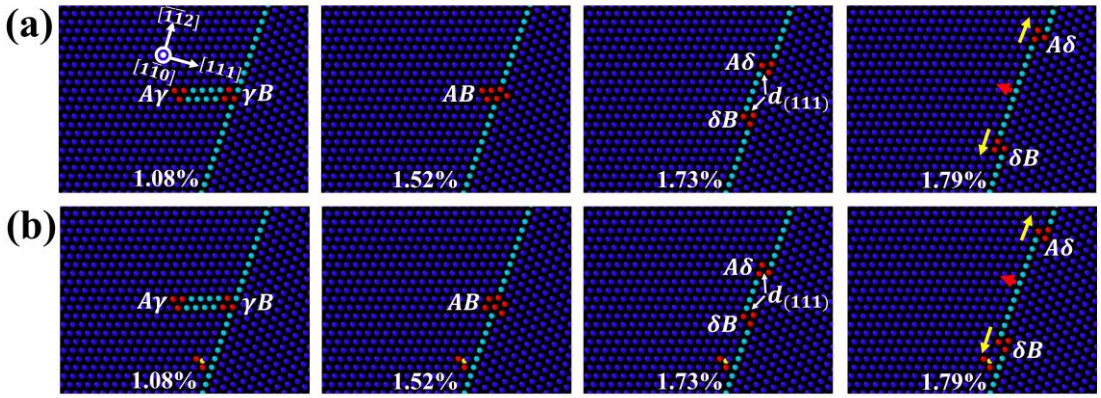

Fig. 6.5. Interaction of a screw dislocation with Σ3 twin boundary: (a) θ_{bulk}= 0 and (b) θ_{bulk}= 0.001. H atoms are assigned in yellow. The direction of dislocation motion and GB migration is marked out by the yellow and red arrows, respectively.

For the interaction with Σ11 (1 1 3) GB, our MD simulation results in Fig. 6.6 show a more complex process. Without H, the leading partial γB first intersects the boundary plane, and then generates two GB disconnections. These disconnections are single-layer GB dislocations with Burgers vector **b** = $1/22 < 471 >$ (denoted as GB dislocation 1 and 2). When the shear strain is increased up to 1.71%, the trailing partial $A\gamma$ is incorporated. Meanwhile, a new single-layer GB dislocation 4 is formed, introducing one new GB plane indexed as GB_3. Due to the GB migration (the occurrence of GB_3), the single-layer GB dislocation 2 is transformed into a double-layer GB dislocation 3, which has the height of two (1 1 3) atomic layers. MD simulations reveal that the double-layer disconnection possesses tiny Burgers vector **b** = $1/22 < 332 >$. Upon further shear deformation, GB dislocation 4 proceeds upwards gradually along the $[\bar{3}\bar{3}2]$ direction, resulting in a leftward migration of the boundary from GB_1 to GB_3 for a distance of one (1 1 3) lattice spacing. Similarly, associated with the lateral motion of GB dislocation 1 is a leftward migration of the boundary from GB_2 to GB_1. It is noticed that the double-layer GB dislocation 3 remains static until it meets the moving single-layer GB dislocation 1. At a shear strain of 1.98%, the single-layer GB dislocation 1 composes promptly with the double-layer GB dislocation 3 (1 + 3) into a new single-layer GB

dislocation 5. Subsequently, the dislocation 5 glides continuously along the $[33\bar{2}]$ direction and contributes to the GB migration from GB_1 to GB_3. From the above analysis, it appears that the interaction outcome of a screw dislocation with Σ11 (1 1 3) GB is dislocation dissociation and nucleation of different types of GB dislocations (single-layer and double layer). Through the lateral motion of GB dislocations, continuous and smooth migration of the Σ11 (1 1 3) GB occurs. For the interaction with H, Fig. 6.6(b) suggests no dislocation dissociation when only absorption mechanism is involved. The incident dislocation (γB and $A\gamma$) is completely absorbed by the boundary without nucleating the GB dislocations. This behaviour originates from the fact that dislocation dissociation (the nucleation of GB dislocations) usually triggers GB migration (see Fig. 6.6(a)), which is not correlated with any atomic diffusion or mass transport. H segregation can impede the GB motion since the migration of the GB needs diffusion of H atoms to the newly appearing stable sites (i.e., newly-formed C SUs). Due to the suppressed GB migration, the dislocation dissociation process is hindered, and the incident dislocation is enforced to get absorbed into the boundary. Following the same mechanism, the addition of H atoms transforms dislocation dissociation into dislocation absorption when the incoming dislocation interacts with Σ9 (2 2 1) GB.

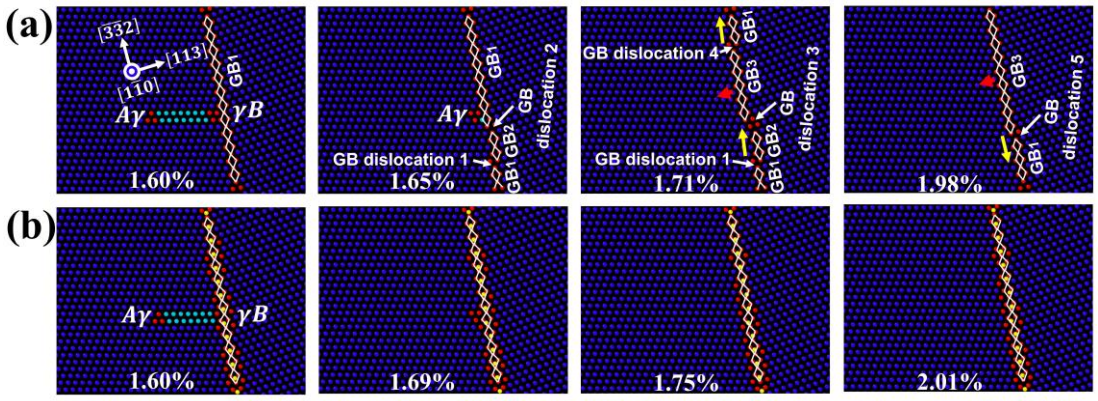

Fig. 6.6. Interaction of a screw dislocation with Σ11 (1 1 3) GB: (a) θ_{bulk}= 0 and (b) θ_{bulk}= 0.001. The direction of dislocation motion and GB migration is marked out by the yellow and red arrows, respectively.

'General' GBs

Due to small deviations in the lattice orientation relative to the twin boundary, Σ57 (4 4 5) and Σ171 (11 11 10) GBs are considered to be vicinal twin boundaries [201]. For simplicity, we refer the boundary steps of Σ57 (4 4 5) as 'interior' disconnections and Σ171 (11 11 10) GB as 'exterior' disconnections. Fig. 6.7 presents the simulations of a screw dislocation interacting with the Σ57 (4 4 5) GB without and with H. When inhabited on glide plane 1, the leading partial γB combines with one 'interior'

disconnection δD to emit a twinning partial δB along the twin segment, leaving behind a Shockley partial dislocation γD at the initial interaction site. The corresponding dislocation reaction can be written as: $\gamma B + \delta D \rightarrow \gamma D + \delta B$, or $1/6[\bar{1}21] + 1/3[\bar{1}\bar{1}\bar{1}] \rightarrow 1/6[\bar{1}\bar{1}\bar{2}] + 1/6[\bar{2}11]$. Proceeding to a higher shear loading, the twinning partial δB glides towards the 'interior' disconnection $D'\delta$ and eventually nucleates an extended dislocation into the adjacent twin lattice (grain-B). DXA indicates that this extended configuration contains a 30º leading partial $\gamma' A'$, a 90º trailing partial $D'\gamma'$, and a bounded stacking fault ribbon. This nucleation process can be expressed as: $D'\delta + \delta B \rightarrow D'B(D'A') \rightarrow \gamma' A' + D'\gamma'$. In contrast to the H-free case, an absolutely different interaction mechanism is observed in the presence of H. As shown in Fig. 6.7(b), the 'interior' disconnection completely absorbs the whole incident dislocation (γB and $A\gamma$). This occurs because H segregation produces pronounced changes in the atomic structure of disconnections. The disordered atomic structure of disconnections obviously serves as a dislocation sink or trap which effectively absorbs the impinging dislocations. After dislocation absorption, the newly-nucleated dislocation $A\delta/BD$ releases a twinning partial δB, with a perfect dislocation AD formed at the interaction site. The twinning partial δB is finally absorbed by the 'interior' disconnection $D'\delta$ in the form of a perfect dislocation $D'B$ without nucleating new partials into the twin lattice. With different glide planes the shear loading may lead to different dislocation interactions. Fig. 6.7(c) demonstrates a direct dislocation transmission when the incident slip is on plane 2. The 'interior' disconnection $D'\delta$ first attracts the leading partial γB, moving the incoming dislocation downwards by the two $(\bar{1}\bar{1}1)$ atomic layers. Continued shear deformation then results in the transmission of the leading partial γB through the 'interior' disconnection $D'\delta$ into the neighbouring grain. Along with the further movement, the trailing partial $A\gamma$ approaches the 'interior' disconnection $D'\delta$ and eventually becomes trapped. The addition of H atoms increases the difficulty of slip transmission across the Σ57 (4 4 5) GB. It is found that in Fig. 6.7(d), the leading and trailing partial dislocations are successively absorbed by the 'interior' disconnection $D'\delta$, which transforms the Frank dislocation into perfect one according to the equation: $AB + D'\delta \rightarrow A\delta + D'B$.

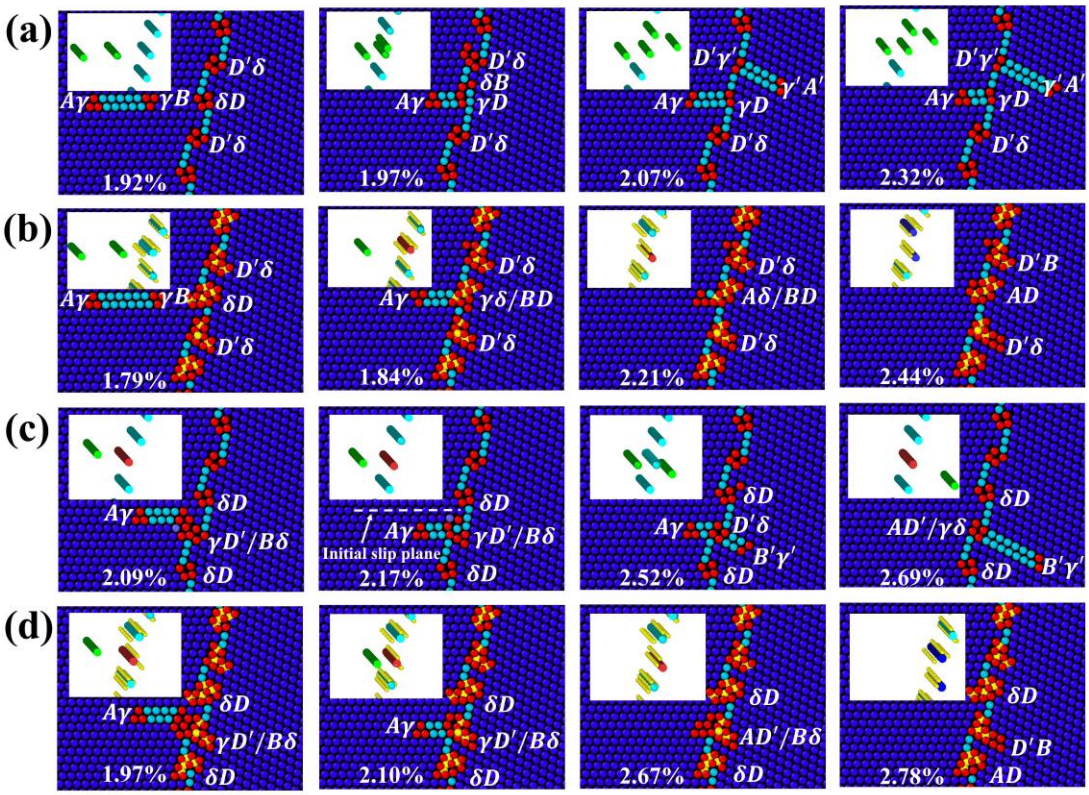

Fig. 6.7. MD snapshots illustrating the interaction process between Σ57 (4 4 5) GB and a screw dislocation gliding on: (a) plane 1 without H, (b) plane 1 with H of θ_{bulk}= 0.001, (c) plane 2 without H and (d) plane 2 with H of θ_{bulk}= 0.001. The insets of each snapshot are coloured by the dislocation type. The light blue lines represent the Frank dislocations, the green lines represent the Shockley partial dislocations, the dark blue lines indicate the perfect dislocations, and the red line are the other types of dislocations.

For Σ171 (11 11 10) GB, 'exterior' disconnections can relax into Shockley partial dislocations and stair-rod dislocations, with a series of ISFs left in grains, as illustrated in Fig. 6.8(a) and (b). The dislocation nucleation event occurring at glide plane 1 resembles that for the 'interior' disconnections with plane 1. When the incident dislocation intersects the twin segment on plane 2, the dislocation dissociation is identical to the case of Σ3 (1 1 1) GB. However, the dislocation slip on plane 3 produces a new interaction mechanism. As seen in Fig. 6.8(a) and (b), the dislocation is first constricted into a perfect dislocation due to strong repulsive force from the dissociated ISF, and then reflected into a different {111} slip plane in the initial matrix lattice (grain-A) via splitting into two Shockley dislocations ($A\delta$ and δB): $\gamma B + A\gamma \rightarrow AB \rightarrow A\delta + \delta B$, or $1/6[\bar{1}21] + 1/6[\bar{2}1\bar{1}] \rightarrow 1/2[\bar{1}10] \rightarrow 1/6[\bar{1}2\bar{1}] + 1/6[\bar{2}11]$. It is worth noting that there is a substantial decrease in the length of ISFs as the H concentration increases in Fig. 6.8(c) and (d). When the length of ISFs is very short, the emitted Shockley partials can react with the residual stair-rod dislocations and then generate $1/3[111]$ disconnections.

This structural change due to H segregation can prominently affect the dislocation-GB interaction. Instead of dislocation reflection, the impinging screw dislocation is totally absorbed by the Σ171 (11 11 10) GB.

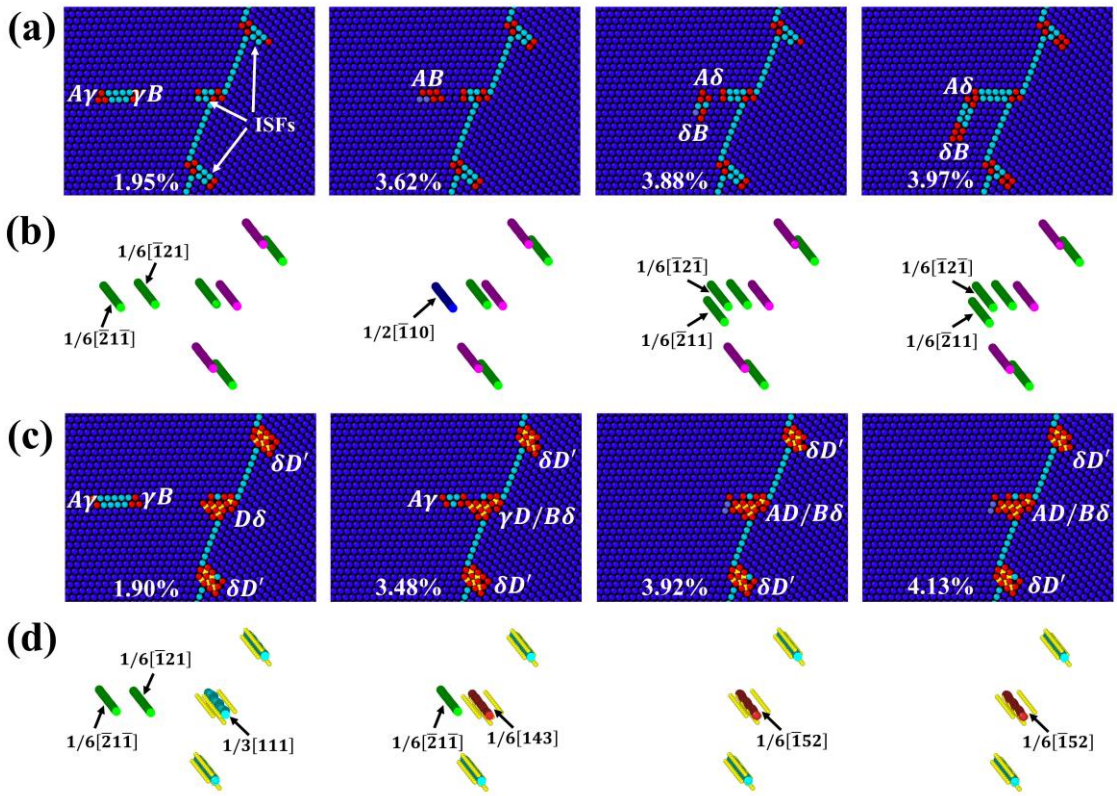

Fig. 6.8. MD snapshots illustrating the interaction process between Σ171 (11 11 10) GB and a screw dislocation gliding on plane 3: (a) and (b) without H, (c) and (d) with H of θ_{bulk}= 0.001.

As for Σ451 (15 15 1) GB, Fig. 6.9(a), the dislocation on slip plane 1 is found to directly pass through the GB without reacting with neighbouring GB dislocations, underlying free slip transmission. Nevertheless, when the incoming dislocation approaches the boundary, GB dislocations transform from pure Lomer locks into Lomer-Cottrell ones: $CD \rightarrow C\delta + \delta\gamma + \gamma D$, or $1/2[\bar{1}\bar{1}0] \rightarrow 1/6[\bar{1}\bar{1}2] + 1/6[\bar{1}\bar{1}0] + 1/6[\bar{1}\bar{1}\bar{2}]$. This Lomer-Cottrell lock has been observed in many metals through in-situ experiments and been proven to contribute to work hardening [202]. After complete slip transmission, the dissociated Lomer-Cottrell locks can recombine into a series of pure Lomer locks. Under H environment, Fig. 6.9(b) suggests no slip transmission during interaction process when only dislocation absorption mechanism is involved. It can be therefore concluded that the presence of H atoms increases the barrier for slip transmission across the Σ451 (15 15 1) GB. On glide plane 2, Fig. 6.9(c), the leading partial γB combines with the pure Lomer lock, and nucleates a partial δB with a stair-rod dislocation $2\delta\gamma$ left at the intersection. The stair-rod dislocation $2\delta\gamma$ is of edge

character and is sessile because it locates on the unfavourable (001) slip plane. This nucleation process can be expressed as: $\gamma B + CD \rightarrow 2\delta\gamma + \delta B$, or $1/6[\bar{1}21] + 1/2[\bar{1}\bar{1}0] \rightarrow 1/3[\bar{1}\bar{1}0] + 1/6[\bar{2}11]$. The dislocation configuration contains two 30º partials ($A\gamma$ and δB) and one stair-rod dislocation $2\delta\gamma$, which can be identified as a Hirth lock. The presence of H atoms again changes the interaction process into dislocation absorption where the lattice dislocation is fully absorbed by the H-charged GB (see Fig. 6.9(d)).

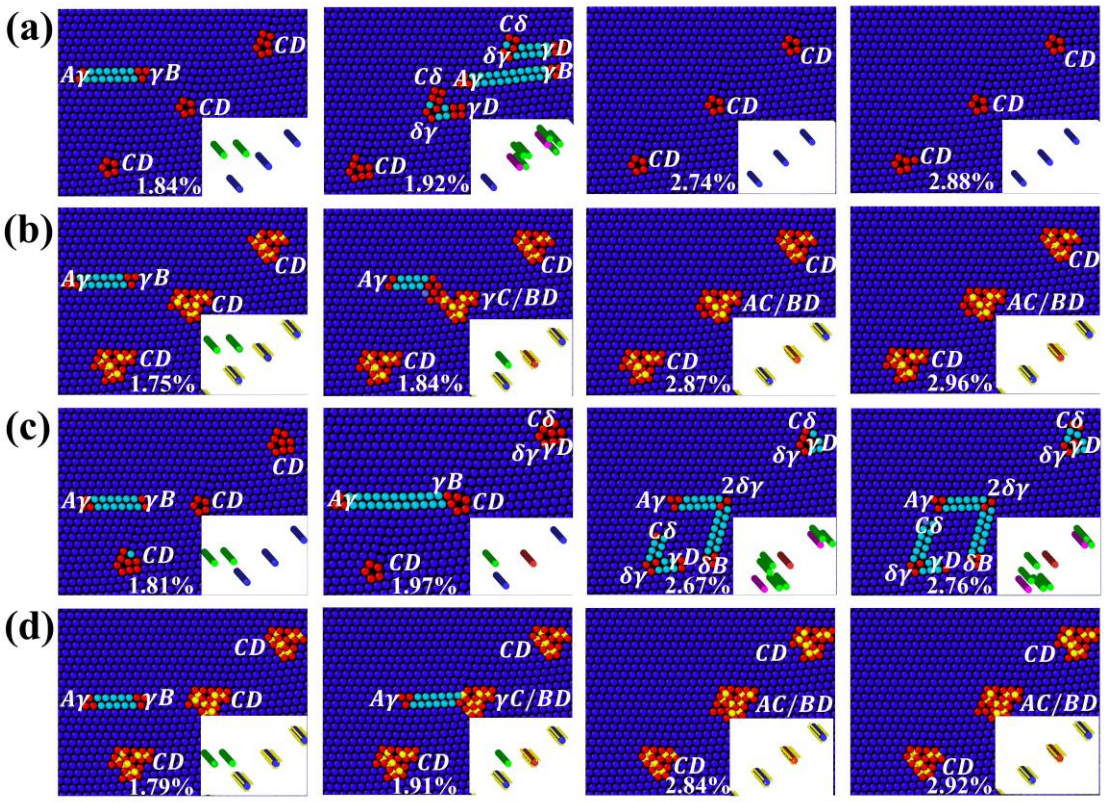

Fig. 6.9. MD snapshots illustrating the interaction process between Σ451 (15 15 1) GB and a screw dislocation gliding on: (a) plane 1 without H, (b) plane 1 with H of θ_{bulk}= 0.001, (c) plane 2 without H and (d) plane 2 with H of θ_{bulk}= 0.001.

6.3.4 Interaction of dislocation pile-ups with the GB

The interaction between dislocation pile-ups of five dislocations and vicinal twin boundaries in the presence of H is presented in Fig. 6.10. Taking 'interior' disconnections as an example, the interaction mechanisms of the first three dislocations are essentially the same as the single dislocation case where the incoming dislocations are thoroughly absorbed by the boundary. As a consequence of dislocation absorption, the GB structure becomes more disordered and the local dilative stress at the reaction site is considerably increased. When two additional dislocations impinge on the GB, after absorption, new

partial dislocations are emitted from the 'interior' disconnection into the twin grain, with the local stress relieved to a large extent. It needs to be mentioned that during the stress relief process, vacancies are generated by dislocation plasticity due to dynamic dislocation-GB interaction, and some of them are transformed into H-vacancy complexes by combing with H atoms, as seen in the insets in Fig. 6.10(d). Previous research by Li et al. [191] revealed that the nucleated vacancies were naturally stabilised by solute H to H-vacancy complexes, serving as the embryos for the nucleation of proto nano-voids. The growth and coalescence of nano-voids could contribute to the ultimate failure of metallic materials [3, 191]. It is believed that the vacancy formation under the environment where dislocation-GB interaction determines the atomic structure of GBs and establishes the local stress state is one possible factor for the experimentally-observed quasi-brittle fracture surfaces of H embrittled steels [46, 106, 203].

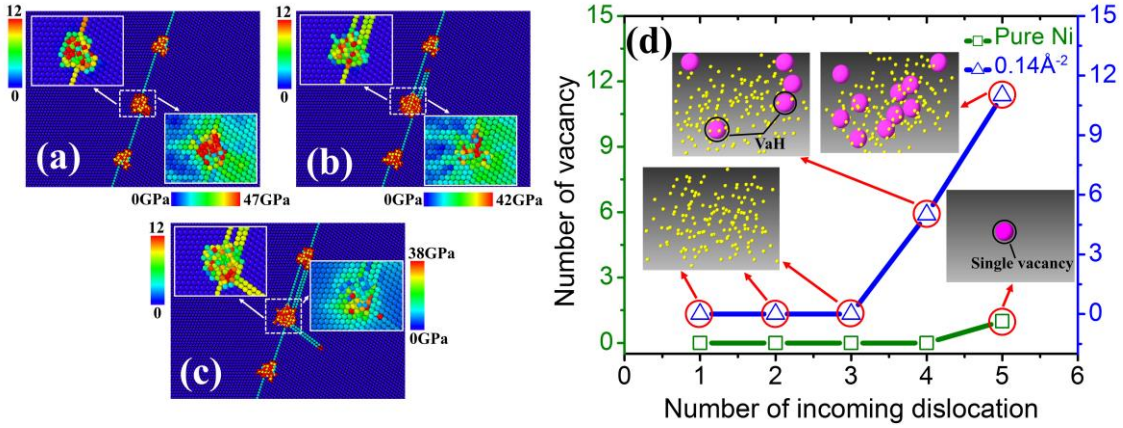

Fig. 6.10. MD snapshots illustrating the interaction process between Σ1241 (20 20 21) GB and 5-dislocation pile-up gliding on plane #$L3$ with H of $C_H = 0.14$ Å^{-2} : (a) absorption of the first three dislocations, (b) absorption of the fourth dislocation and (c) absorption of the fifth dislocation. All images except insets are coloured by CNA. The left and right insets of each snapshot are coloured by CSP and von-Mises shear stress, respectively. (d) Vacancy evolution with the number of incoming dislocations in the absence and presence of H. The large pink particles are vacancies detected by Atomviewer while the small yellow ones are H atoms.

6.4 Discussion

In this study, the interaction between a screw dislocation and $[1\bar{1}0]$ STGBs under shear deformation without and with H has been investigated. In the absence of H, it is found that dislocation-GB interactions are sensitive to GB structures and glide planes where the incoming dislocation propagates. This dependency was elegantly demonstrated by Bachurin et al., who showed that the misorientation angle of the GB, the sign of the

Burgers vector of the incoming dislocation and the exact site where the dislocation intersected the GB all played important roles in governing dislocation-GB interactions [204]. The analysis of the interaction of dislocation with 'singular' GBs shows that the dislocation dissociation predominates the deformation mechanism. This dissociation is achieved through the nucleation and lateral motion of GB disconnections, which contributes to the GB migration. By comparison, 'general' GBs are of more complicated atomic structures as they are a combination of these 'singular' GBs with complexity (see Fig. 6.2). As a consequence, different glide planes mean different interaction sites where the dislocation meets the GB, thereby leading to different interaction mechanisms. The reaction outcomes include dislocation nucleation, transmission, dissociation and reflection (see Figs. 6.7-6.9). Although extensive dislocation-GB interaction simulations have been done to reveal these reactions, most of them are focused on one or two mechanisms [194, 195, 205-208]. To our knowledge, such systematic investigation of dislocation-GB interactions is the first time conducted by far.

In the presence of H, the interaction mechanism is dislocation absorption for the vast majority of cases. The leading and trailing partials are successively absorbed by the H-charged GBs. In the case of Σ11 GB, the interaction is transformed from dislocation dissociation to absorption since the presence of H hampers the GB migration. In essence, the impeded GB migration is associated with changes of the GB structure during the dislocation-GB interaction, leading to the increase in heats of segregation of the solute atoms, which cannot diffuse to lower-energy sites within the timeframe of MD simulations. This effect has been characterized by $\Delta E = [(E_d^H - E^H) - (E_d^P - E^P)]/N_{GB}^H$ in our previous study [209], where E_d^H and E_d^P are the system energies after the dislocation-GB interaction with and without H, E^H and E^P are the system energies before the dislocation-GB interaction with and without H, and N_{GB}^H is the number of H atoms at GBs. The slip transmission of dislocation occurs when the dislocation intersects Σ57 GB along plane 2 and Σ451 GB along plane 1 without H (see Fig. 6.7(c) and 6.9(a)). It is clear that the former one is partial transmission where only leading partial is transferred to the neighbouring grain, whereas the latter one is complete transmission where the whole incident dislocation penetrates through the GB. H segregation enables the initial GB dislocations to trap and absorb the incoming dislocation (see Fig. 6.7(d) and 6.9(b)). In current study, the attachment of H to the initial GB dislocations modifies the local stress field, reducing it along the dislocation glide plane, as seen in marked

region of Fig. 6.11. This has always been an assumption of the HELP mechanism [20, 210-212]. Owning to the shielding effect, GB dislocations tend to move along the glide plane and interact with the incident dislocation, thereby hindering slip transmission. The interaction with Σ171 GB shows that H atoms change the boundary structure and shorten the length of ISFs, suppressing dislocation reflection while driving dislocation absorption. To account for this it is necessary to consider the influence of H on the dislocation spacing. Ferreia et al. showed that the presence of H was observed to reduce the elastic interactions between obstacles and perfect and partial dislocations; thus, reducing the equilibrium separation distance between dislocations [98]. In our simulation case, H reduces the spacing (the length of ISFs) between the emitted Shockley partials and residual stair-rod dislocations. Due to the disappearance of ISFs, instead of dislocation reflection, the dislocation is absorbed by the GB. Additionally, it is found that H stabilizes the configurational structure of dislocations, for example, the pure Lomer locks always dissociate into Lomer-Cottrell locks without H, Fig. 6.9(a) and (c), whereas they hold in their initial configurations with H, Fig. 6.9(b) and (d). This observation was revealed by Ferreira et al. [213], who demonstrated that solute H could stabilize dislocations and stop the dislocation cross-slipping. This locking of dislocations by H can also be evident in Figs. 6.7-6.9 where after dislocation absorption, the newly-formed GB dislocations stay at their positions without further nucleation or transmission into the neighbouring grain.

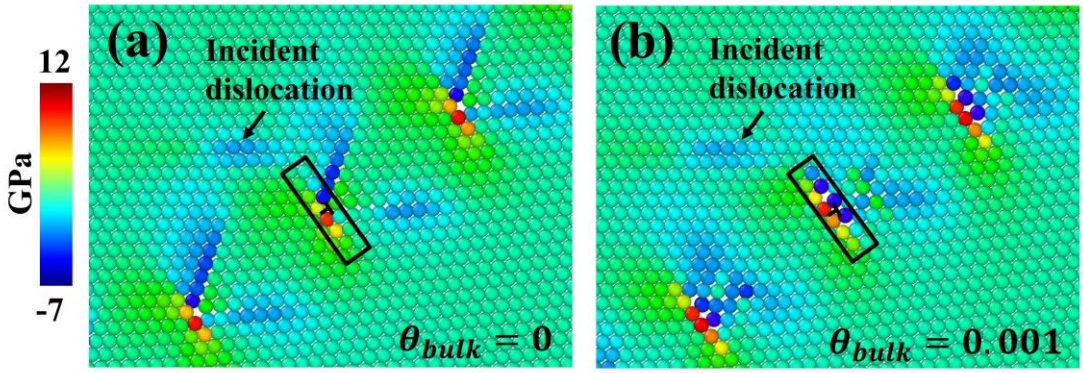

Fig. 6.11. Shear stress component on GB dislocations of Σ451 (15 15 1): (a) without H and (b) with H of θ_{bulk}= 0.001. H atoms are removed to facilitate viewing of the defect structures.

As aforementioned, there is a tendency for solute H to increase the difficulty of dislocation reactions (transmission, nucleation, dissociation and reflection). To quantify this effect, we introduced a control box at the intersection to measure the energy barrier for the dislocation-GB interaction [214]. The defect atoms within the control box were identified by CSP value ($P > 0.5$), and the energy barrier was calculated by considering

the net change in potential energy of the defect atoms during the dislocation-GB interaction normalized by the atomic volume of defect atoms: $E_{barrier} = \frac{\sum_i^n E_{load}^i - E_s}{V}$, where E_{load}^i is the real-time potential energy of defect atom i upon shear loading, E_s is the static energy, and V is the total volume of defect atoms in the static configuration. Fig. 6.12(a) plots the evolution of energy barrier for dislocation interaction with Σ57 GB during deformation. After the dislocation intersects the boundary, there is a sharp increase of the energy until a maximum value where the dislocation reaction occurs. Subsequently, the energy plummets, corresponding to the completion of the interaction. The maximum value is taken as the energy barrier for dislocation-GB interaction. To link this with intrinsic GB parameter, we rationalise the energy barrier for various types of GBs with initial GB energy in Fig. 6.12(b). For each type of GB, there is a strong inverse relationship between the energy barrier for dislocation-GB interaction and the GB energy; that is, the GBs with lower GB energy provide a higher energy barrier for dislocation interaction, which is in concordance with Sangid's conclusion [214]. However, the fitted power law function in current study is slightly different from Sangid's model as we adopt a different potential for Ni and use different GB types.

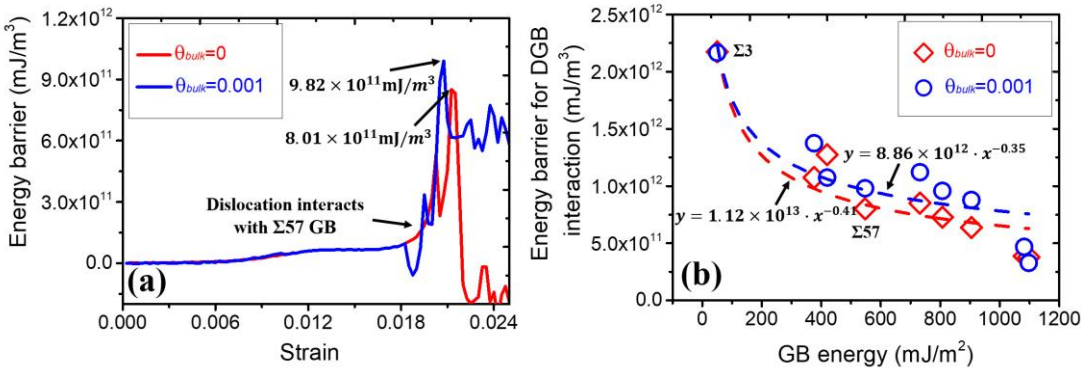

Fig. 6.12. (a) Interaction of dislocation with Σ57 (4 4 5) GB in terms of the energy barrier to the applied shear strain. (b) Energy barrier for dislocation-GB interaction plotted against the static GB energy for various types of GBs without and with H.

Here it is important to stress that the introduction of H atoms into the GB generally increases the energy barrier for dislocation-GB interaction (see Fig. 6.12(b)). This manifests that the GB tends to impede the slip transmission and dissociation of the incoming dislocation in the presence of H. Alternatively, the lattice dislocation is always absorbed into the GB, agreeing well with the simulation results in Figs. 6.7-6.9. Furthermore, our simulations reveal that dislocation absorption disorders the atomic structure of GBs and establishes a local stress state. These factors have been proposed to

play a critical role in achieving intergranular fracture in experiments [47, 203]. Hence, based on our simulation results and experimental evidence, the following consequences may be anticipated. When lattice dislocations interact with the GB, the segregation of H atoms is prone to impede the process of slip transmission and dislocation dissociation, and thus promote dislocation absorption. This activates the GB to a more disordered atomic structure and increases the localised strain energy stored within the GB. To relieve the accumulated energy, an alternative response such as vacancy formation and crack propagation may be initiated, causing the H-induced intergranular decohesion.

6.5 Summary

In summary, by using atomistic simulations, the interaction mechanisms between a screw dislocation and various $[1\bar{1}0]$ STGBs in Ni without and with H were studied, with special emphasis on the solute H effects on them. The main results are summarised as follows.

(1) The incident dislocation dissociated into GB dislocations while intersecting 'singular' GBs. This dissociation was achieved through the nucleation and lateral motion of GB disconnections, which contributed to the GB migration. For interactions with 'general' GBs, several possible dislocation reactions occurred depending on the specific glide planes and GB structures. When the incoming dislocation interacts with the GB, it directly transmitted into the neighbouring grain, or promoted the nucleation of new dislocations from the GB, or reflected back into the initial grain.

(2) Segregated H atoms transformed interaction mechanisms into ones involving dislocation absorption for most of GBs. The twin boundary of Σ3 GB and twin segments of Σ171 GB hardly trapped H atoms, therefore the transformation was not observed. The change from dislocation dissociation to absorption for 'singular' GBs was attributed to that H impeded the GB migration. In the case of 'general' GBs, the boundaries were prone to absorb the incident dislocation within the framework of HELP mechanism where H modifies the stress field of GB dislocations, reduces the equilibrium separation distance between GB dislocations, and stabilizes the configurational structure of GB dislocations.

(3) The energy barrier for dislocation-GB interaction was found to strongly correlate with the static GB energy in both H-free and H-charged cases. GBs with lower interfacial energy provided a higher barrier for dislocation interaction. The presence of H atoms generally increased the energy barrier for dislocation-GB interaction (dislocation

nucleation, transmission, dissociation and reflection), thereby promoting dislocation absorption. This activated the GB to a more disordered atomic structure and established a local stress state, which is expected to contribute to the H-induced intergranular fracture via vacancy formation and crack propagation.

Chapter 7 Atomistic investigation of hydrogen induced decohesion of grain boundaries

This chapter is extracted from the following publication:

Li J, Lu C*, Pei L, Zhang C, Wang R. Atomistic investigation of hydrogen induced decohesion of Ni grain boundaries. Mech Mater. 2020;150:103586.

7.1 Introduction

This chapter is focused on direct simulations of the decohesion of Ni GBs in the presence of H. To this end, two cohesive parameters including the GB cohesive strength and the fracture energy of the GB as a function of H concentrations and GB types during GB separation process were first examined. Then the GB cohesive properties aided by dislocation-GB interactions that could establish the conditions—stress state, boundary disruption and critical hydrogen concentration to cause the GB to become the weak link in metallic systems were studied. Finally, these calculations were coupled with experimental observations of high dislocation plasticity, which provide a picture of H embrittlement arising from the cooperative action of H-induced plasticity and GB decohesion.

7.2 Computational approach

All calculations were performed using the molecular dynamics code (LAMMPS) [155] and simulation samples were visualised using the OVITO [166]. The semi-empirical EAM potential for Ni-H used in the present study was first introduced by Angelo et al. [160] and then modified by Curtin et al. [28，29] to eliminate the instability of NiH hydrides. Twenty types of symmetric tilt Ni GBs with ⟨100⟩, ⟨110⟩ and ⟨111⟩ tilt axis were constructed on the basis of the CSL model, as listed in Table 7.1. The dimension of each of grains along *Y* direction was set to 60 Å. The simulation domain extends 6 repeat units (RUs) along *X* direction and 3 RUs along *Z* direction, as shown in Fig. 7.1. Periodic boundary conditions were enforced in all three directions. To avoid any effects of the second GB along *Y* direction, regions of 10 Å thickness were set as vacuum spaces on the top of grain-A and the bottom of grain-B. The bulk and free surface (FS) models have

the same dimensions as the bicrystal model. After structural initialization, the atoms in bulk, GB and FS samples were fully optimised during energy minimisation process.

The GB energy γ_{GB} is determined as the difference between the energy of GB sample and that of bulk sample, divided by the GB area:

$$\gamma_{GB} = \frac{E_{GB} - E_{bulk}}{A} \tag{7.1}$$

The propensity of H to segregate into the GB is defined by the segregation energy given by Eq. 7.2:

$$E_{seg}^{\alpha} = (E_{GB+H}^{\alpha} - E_{GB}) - (E_{bulk+H} - E_{bulk}) \tag{7.2}$$

where E_{GB}, E_{GB+H}^{α}, E_{bulk} and E_{bulk+H} are the system energy of the clean GB, the GB with H atom at trapping site α, the clean bulk Ni and the bulk sample with H atom, respectively. To find all possible trapping sites along GBs, a geometric approach of space tessellation of polyhedral packing units was used [209].

Table 7.1. Characterization of the GBs, including Σ value, tilt angle, numbers of atoms and GB energies.

Sigma ($\boldsymbol{\Sigma}$)	Angle (°)	GB energy ($\boldsymbol{J \cdot m^{-2}}$)	No. of atoms	Sigma ($\boldsymbol{\Sigma}$)	Angle (°)	GB energy ($\boldsymbol{J \cdot m^{-2}}$)	No. of atoms
13(510) ⟨100⟩	22.62	1.22	8736	17(223) ⟨110⟩	86.63	0.95	13920
17(410) ⟨100⟩	28.07	1.25	8820	17(334) ⟨110⟩	93.37	0.88	17100
5(310) ⟨100⟩	36.87	1.21	9000	3(111) ⟨110⟩	109.47	0.09	11520
5(210) ⟨100⟩	53.13	1.26	8508	11(332) ⟨110⟩	129.52	1.01	13788
17(530) ⟨100⟩	61.93	1.19	11712	9(221) ⟨110⟩	141.06	1.17	13020
5(320) ⟨100⟩	67.38	1.10	10008	19(331) ⟨110⟩	153.48	1.15	15648
19(116) ⟨110⟩	26.53	1.00	16350	13(143) ⟨111⟩	27.80	1.16	12672
9(114) ⟨110⟩	38.94	0.88	12894	7(132) ⟨111⟩	38.20	1.18	15768
11(113) ⟨110⟩	50.48	0.43	10752	19(253) ⟨111⟩	46.80	1.19	19080
3(112) ⟨110⟩	70.53	0.90	14430	3(121) ⟨111⟩	60.00	0.90	16650

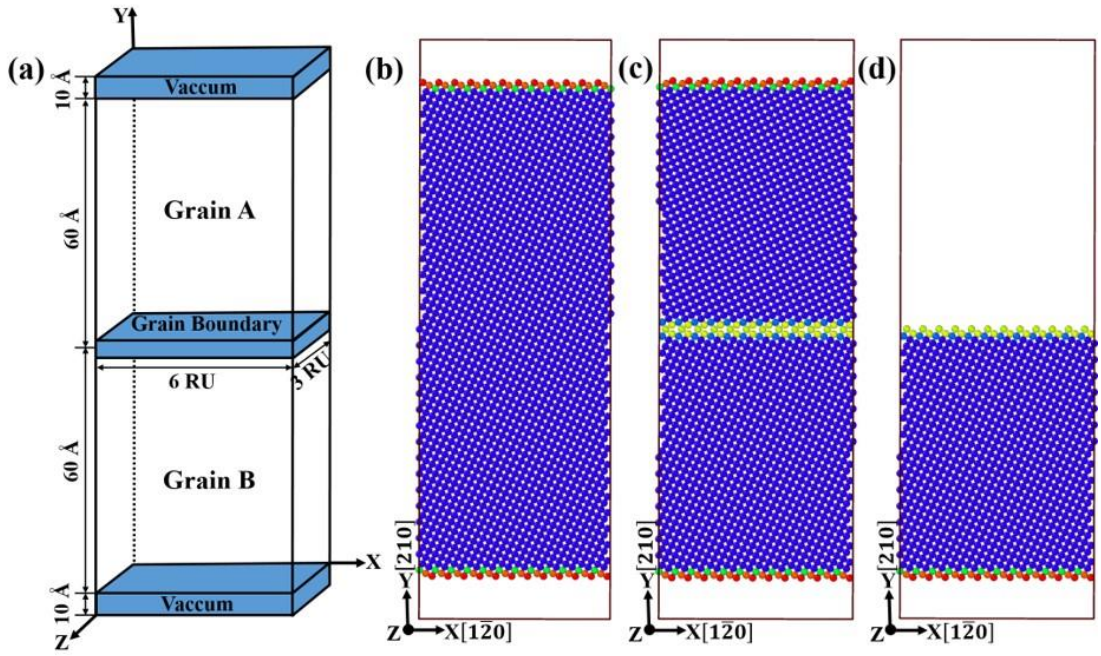

Fig. 7.1. (a) Schematic illustration of the bicrystal sample. Atomic structure of (b) Ni bulk, (c) Σ5 (210) GB and (d) Ni (210) free surface.

According to H segregation energy, the H occupation probability at site α is derived as:

$$\theta_\alpha = \frac{\theta_{bulk}\exp(-E_{seg}^{\alpha}/K_BT)}{1+\theta_{bulk}\exp(-E_{seg}^{\alpha}/K_BT)} \tag{7.3}$$

where θ_{bulk} is bulk H concentration in atomic ratio, K_B is Boltzmann's constant and T is the temperature. The bulk H concentration is set at θ_{bulk} = 0.001 where H-induced intergranular fracture has been observed [149]. The Ni-H configurations were created by inserting H atoms into 'favourable' trapping sites based on θ_α. Here all sites with a negative E_{seg}^{α} are defined as 'favourable'. In addition, to amplify the solute H effect, an extreme case was also considered, namely, all favourable trapping sites were filled by H atoms independent of θ_{bulk}. This was quantified by the maximum excess, calculated by dividing the total number of favourable sites by the GB area. After attaining Ni-H configurations with a desired H coverage, the system cell was optimised via non-linear conjugate gradient energy minimisation.

The computational tensile tests were carried out to investigate the influence of H segregation on GB cohesive properties. The cleavage plane was set a priori [29] and the two grains (grain-A and grain-B) were rigidly separated at the cleavage plane parallel to the boundary by inserting some distance (0.1, 0.2, 0.3 ….., 6 Å, etc.). After each separation, the interfacial stress σ_{yy} was directly computed according to the virial

theorem by the formula [215]:

$$\sigma_{ij} = \frac{1}{V}\sum_{\alpha=1}^{N}\left(\frac{1}{2}\sum_{\beta=1}^{N} r_{\alpha\beta}^{i} F_{\alpha\beta}^{j} - m^{\alpha} v_{i}^{\alpha} v_{j}^{\alpha}\right) \quad (5.4)$$

Here, i and j denote indices in the Cartesian coordinates and α and β are atom index numbers. m and v indicate the mass and velocity of the atom. $r_{\alpha\beta}$ and $F_{\alpha\beta}$ are the distance and force between atom α and β, respectively. V stands for the volume of system with total number of atoms N. The theoretical cohesive strength can be taken as the peak value of tensile stress. The separation energy E_{sep}, can be obtained from the difference between the real-time and initial system energies:

$$E_{sep} = \frac{E_x - E_{GB}}{A} \quad (7.5)$$

where E_x is the real-time energy of the fracture sample with a separation distance of x. The limit of the separation energy at a separation distance that the energy does not change any more, is defined as the fracture energy. Two types of calculations about fracture energy were conducted: (1) rigid separation without subsequent relaxations, E_{frac}^{u}; (2) with atomic relaxations, E_{frac}^{r}. For each GB type, several possible cleavage planes were chosen to determine the minimum theoretical cohesive strength and fracture energy surfaces as shown in Fig. 7.2.

The H diffusion process is ignored during separation in the above tensile tests. However, it is possible for solute H to diffuse over a few atomic hops from the immediate sub-surface to the fracture surface so as to change the fracture energy [29]. Due to the limit of simulation time scales, it is not possible to conduct direct simulation of such local diffusion. Herein, we move all sub-surface H into favourable trapping sites on the fracture surface by hand, and then calculate the corresponding fracture energy.

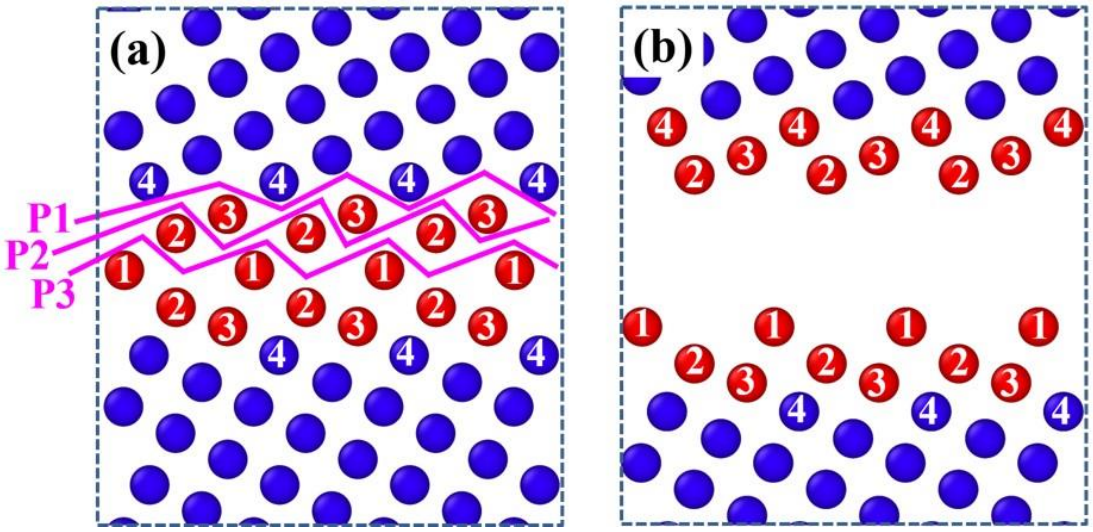

Fig. 7.2. Schematic diagram of (a) the fracture paths for the Σ5 (210) ⟨100⟩ GB and (b) the totally separated two free surfaces. P1, P2 and P3 stand for the potential cutting planes separating two grains.

7.3 Results

7.3.1 H trapping map

Fig. 7.3 shows H segregation energy maps for four typical GB/FS. The possible trapping sites are indicated by small spheres and coloured according to the segregation energy. For the GB, most of the trapping sites with segregation energy that is different from that of the bulk occur within a region ±5 Å from the boundary centre, manifesting that the GB region is energetically conducive to H segregation. As for the FS, H atoms prefer to occupy at the surface layers. Taking the Σ5 (210) GB/FS as an example, the lowest segregation energy for this GB is -0.28 eV and the corresponding sites are located at the GB centre. In contrast, trapping sites with the lowest segregation energy of -0.55 eV are on the top layer of the FS.

The summary of segregation energy maps including GB/FS energy, H segregation energy and maximum excess H concentration is plotted in Fig. 7.4. It is obvious that segregation energies vary somewhat over the misorientation range except Σ3 (111) ⟨110⟩ case. Σ3 (111) ⟨110⟩ has the segregation energy of -0.04 eV and -0.47 eV at the GB and FS, respectively, which is much higher than that at other GB/FS. This is ascribed to the atomic configuration that Σ3 (111) ⟨110⟩ GB is the most compact boundary in face-centred cubic crystals, and its coherent twin structure composed of close-packed (111) layers provides very small excess volume for H segregation. The trapping ability of GB/FS is quantitatively evaluated by the maximum excess H concentration, as marked by triangles in Fig. 7.4(a) and (b), respectively. The range of maximum excess is 0.03-

0.22 $Å^{-2}$ for a GB and 0.06-0.16 $Å^{-2}$ for a FS. Furthermore, it is found that the maximum excess H concentration is prominently varied with different tilt axis and misorientation angle, being indicative of that the H trapping ability is sensitive to the GB/FS character.

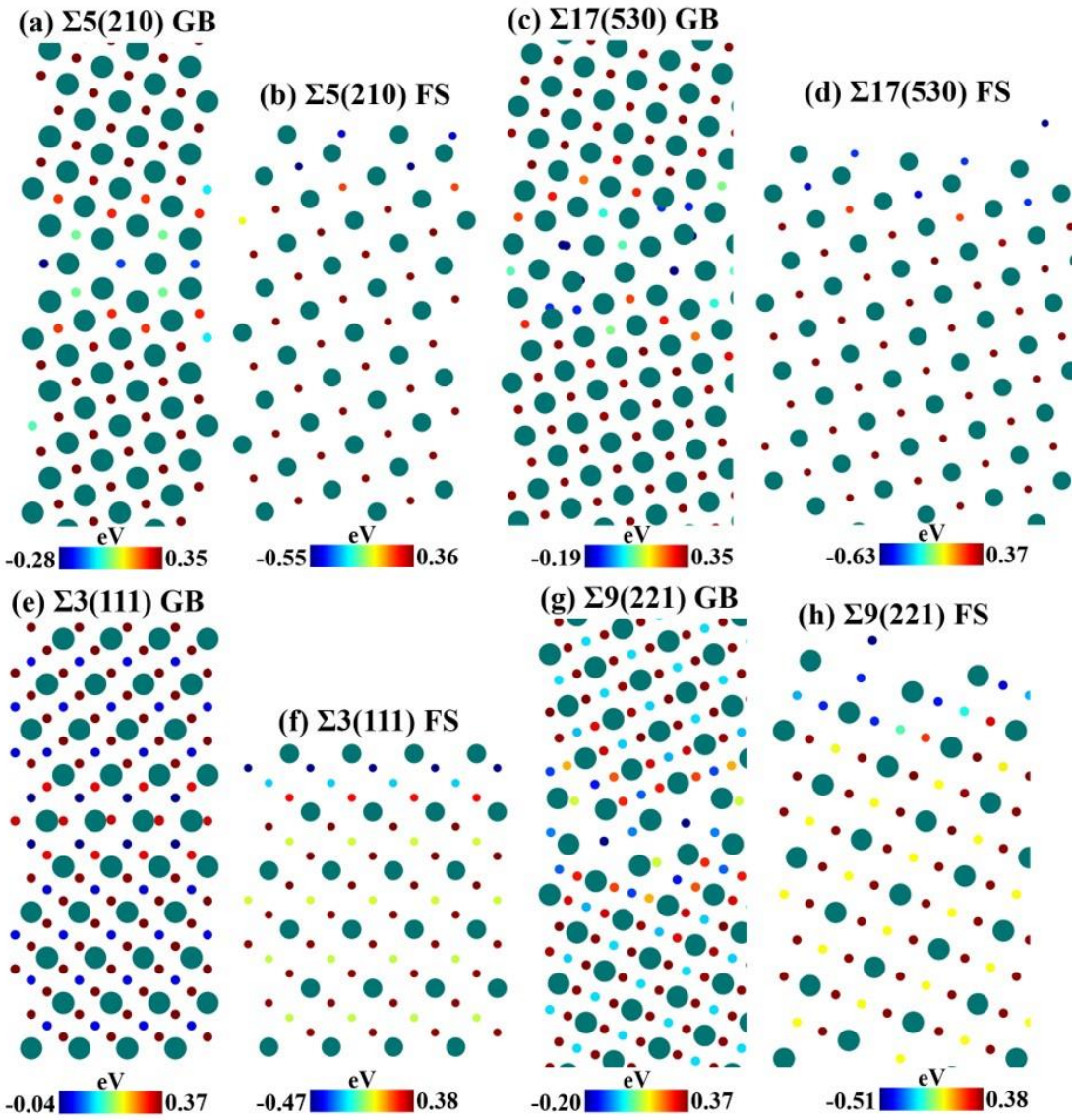

Fig. 7.3. H segregation energy maps for four types of GB/FS. Larger spheres represent Ni atoms, and smaller ones indicate possible H trapping sites.

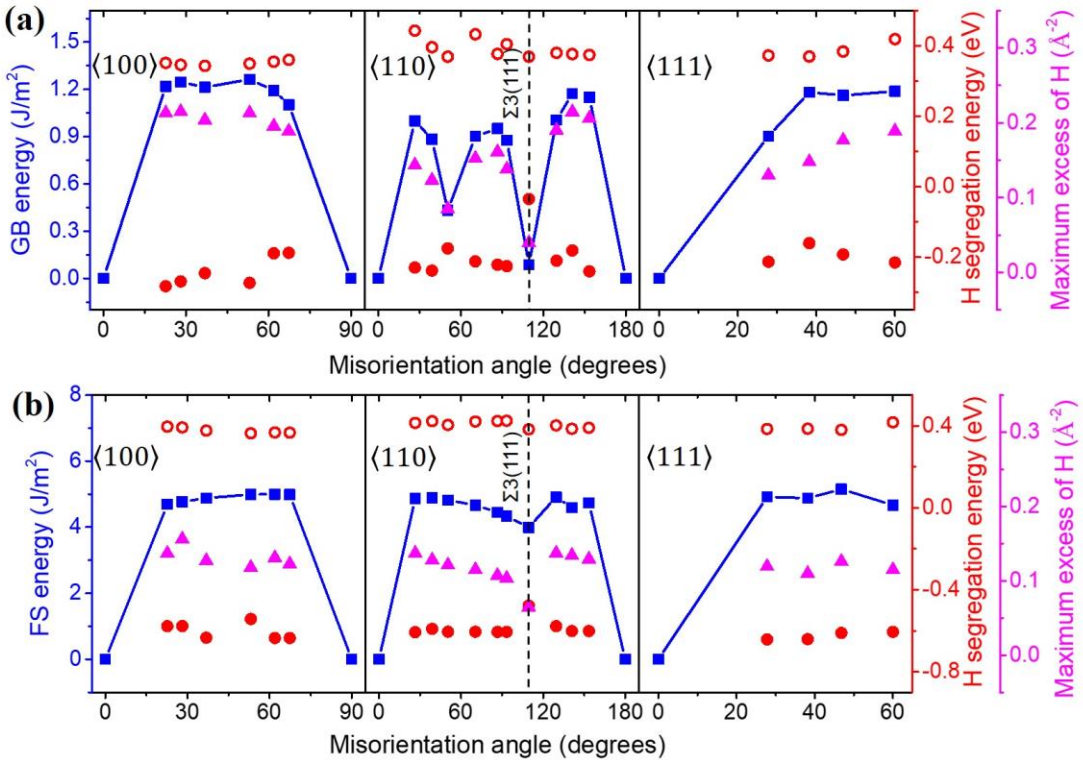

Fig. 7.4. Summary of segregation energy maps for 20 types of GB and FS tilted around ⟨100⟩, ⟨110⟩ and ⟨111⟩ axis. Squares denote GB/FS energy, solid and hollow circles denote the lowest and highest H segregation energy, respectively, and triangles denote maximum excess H concentration.

7.3.2 Computational tensile tests

Fig. 7.5 shows the rigid separation energy and tensile stress of bulk Ni, clean GB, GB with bulk H concentration of θ_{bulk} = 0.001 and maximum excess of H. For each case, the fracture plane with the minimum theoretical cohesive strength and fracture energy is chosen to plot these curves. As can be seen in Fig. 7.5, all GBs show a similar trend for cohesive properties. There is a sharp increase of the separation energy with separation distance at the beginning. Subsequently, it rises at a slower rate until the energy reaches an asymptote. By comparing separation energy of different configurations, it is found that the energy of clean GB is lower than that of bulk Ni, and the presence of H atoms decreases the separation energy of the GB. In addition, the results in Fig. 7.5(d)-(f) present that the theoretical cohesive strength of bulk Ni is the largest. Compared to the clean GB, H segregation slightly decreases the tensile strength of the GB.

The cohesive properties calculated for all the bulk/GBs under different H environments are plotted in Fig. 7.6, and some scenarios of interest are summarised in Table 7.2 and 7.3. It can be seen that the cohesive strengths of GBs are not pronouncedly changed by H at θ_{bulk} = 0.001. The maximum reduction in the tensile strength occurs at

Σ5 (210) ⟨100⟩ GB, with the value decreased by 6.60% from 27.12 GPa to 25.33 GPa. To amplify the role of H atoms, all possible trapping sites of each GB were occupied by H, and the corresponding strength was computed. As shown in Fig. 7.6(a) and Table 7.2, even though with maximum excess H concentration, there is no remarkable reduction in the strength, with a maximum drop of only 7.99% for the Σ3 (121) ⟨111⟩ GB. As a comparison, the calculation of the cohesive strength of bulk Ni separated across a fracture plane parallel to each GB is also presented. The maximum excess of H in bulk Ni is considered by filling all octahedral sites located within $\pm$5 Å from the fracture plane. Similar to the GB, H segregation causes a slight decrease in theoretical cohesive strength of bulk Ni. Taking the Ni (210) as an example, the reduction is from 27.25 GPa to 26.34 GPa, only 3.34%.

The unrelaxed and relaxed fracture energies of GBs are summarised in Table 7.2. Atomic relaxation reduces the fracture energy of each GB in the absence and presence of H. In addition, it can be seen that H segregation does not prominently decrease the unrelaxed or relaxed fracture energy. For all investigated GBs at θ_{bulk} = 0.001, the magnitude of the reduction of fracture energy is no more than 12% of clean GB cases. To investigate the local H diffusion, all sub-surface H atoms were moved to the final fracture surfaces, and the corresponding relaxed fracture energy was calculated. The diffusion process lowers the energy, but the magnitude of change remains small, with a maximum reduction of 15.75% for the Σ17 (530) ⟨100⟩ GB. By comparison, there is a precipitous drop in fracture energy when H atoms are introduced into GBs with maximum excess, ranging from 10.23% to 41.52% across all GBs. Considering the local H diffusion process, the maximum reduction can reach as high as 46.49%, obtained for Σ9 (221) ⟨110⟩ GB. According to Griffith criterion, the brittle cleavage process is mainly controlled by the critical stress intensity, expressed by the equation $K_I^c = \sqrt{E_{frac}^r / A_1}$, where A_1 is a constant depending on the anisotropic linear elasticity [132]. Therefore, even though the maximum reduction in the relaxed fracture energy (E_{frac}^r) can reach 46.49% for the GB with maximum excess of H plus local H diffusion, the critical stress intensity (K_I^c) is reduced only by 26.83%. In this regard, the tendency for significant promotion of the intergranular fracture seems small.

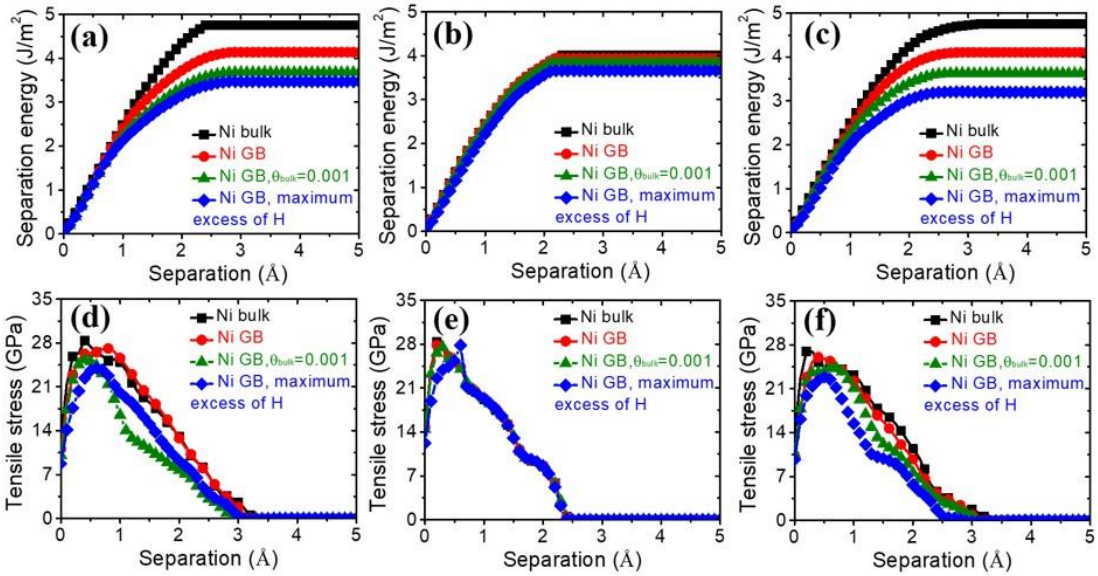

Fig. 7.5. Rigid separation energy and tensile stress as a function of separation distance for different GBs under varying H concentrations: (a) and (d) Σ5 (210) ⟨100⟩ GB, (b) and (e) Σ3 (111) ⟨110⟩ GB, (c) and (f) Σ3 (121) ⟨111⟩ GB.

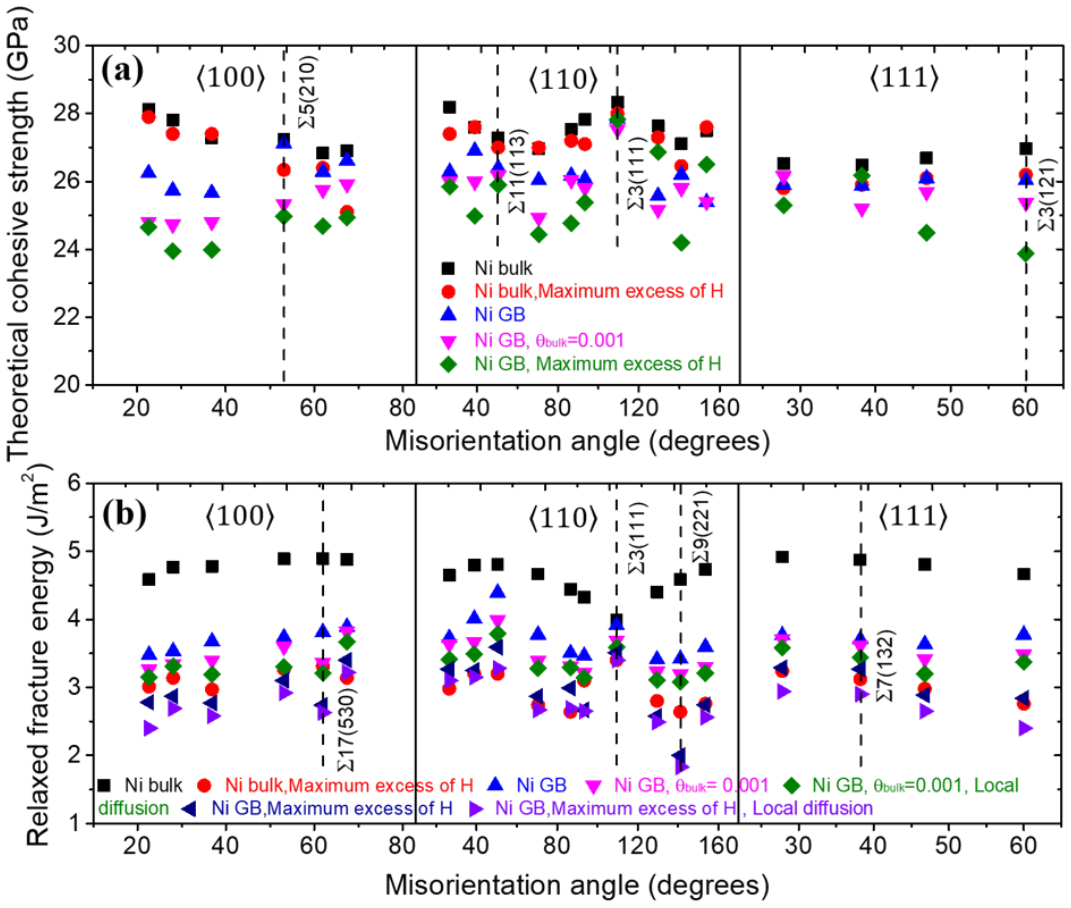

Fig. 7.6. Theoretical cohesive strength and fracture energy plotted as a function of misorientation angle with different tilt axes. The vertical dashed lines indicate the GBs of interest.

Table 7.2. Theoretical cohesive strength and fracture energy of GBs. The minimum values of cohesive properties for each GB are highlighted in bold. P1, P2 and P3 are the cleavage planes.

		Theoretical cohesive strength (GPa)			Fracture energy (J/m^2)							
		θ_{bulk}=0	θ_{bulk}=0.001	Maximum excess of H	θ_{bulk}=0		θ_{bulk}=0.001		θ_{bulk}=0.001, local diffusion	Maximum excess of H		Maximum excess of H, local diffusion
					E^u_{frac}	E^r_{frac}	E^u_{frac}	E^r_{frac}	E^r_{frac}	E^u_{frac}	E^r_{frac}	E^r_{frac}
Σ5(210) <100>	P1	**27.12**	26.05	**24.97**	5.05	**3.74**	4.87	3.70	3.51	3.81	3.35	3.35
	P2	28.96	26.81	25.67	5.21	3.86	4.89	**3.60**	3.42	4.41	**3.10**	**2.92**
	P3	27.12	**25.33**	25.61	4.14	**3.74**	3.68	3.78	**3.30**	3.47	3.20	3.09
Σ17(530)< 100>	P1	**26.28**	**25.75**	25.43	5.12	3.89	4.95	3.66	3.38	4.18	3.95	3.91
	P2	26.85	25.99	**24.68**	4.66	**3.81**	4.32	3.39	**3.21**	3.24	**2.74**	**2.63**
	P3	26.75	26.24	24.74	4.30	**3.81**	3.93	**3.36**	4.33	3.54	2.89	2.78
Σ11(113)< 110>	P1	26.50	26.73	26.14	4.90	4.79	4.87	4.70	4.11	4.46	4.11	3.97
	P2	**26.39**	**26.18**	**25.90**	5.01	**4.39**	4.80	**3.98**	**3.77**	4.12	**3.59**	**3.28**
	P3	27.61	27.10	25.94	4.60	4.41	4.34	4.02	4.02	3.84	3.64	3.44
Σ3(111) <110>	P1	**27.84**	**27.53**	**27.83**	4.01	4.00	3.99	3.96	3.71	3.75	3.70	3.59
	P2	28.02	27.65	27.92	3.94	**3.91**	3.84	**3.70**	**3.59**	3.67	**3.51**	**3.40**
	P3	28.02	27.64	27.97	3.94	**3.91**	3.85	**3.70**	3.69	3.65	3.65	3.65
Σ9(221) <110>	P1	27.05	26.62	28.50	4.76	3.62	4.63	3.25	3.17	4.04	2.70	2.34
	P2	26.78	27.20	29.92	4.51	**3.42**	4.26	**3.19**	3.19	4.19	2.89	2.11
	P3	**26.21**	**25.81**	**24.20**	3.48	3.44	3.35	3.29	**3.08**	3.01	**2.00**	**1.83**
Σ7(132) <111>	P1	**25.87**	26.40	26.18	4.96	3.79	4.92	**3.62**	3.51	4.86	3.64	3.03
	P2	26.33	**25.61**	**25.17**	4.90	**3.70**	4.82	3.63	**3.44**	4.51	3.44	3.44
	P3	27.15	27.46	27.12	4.48	3.88	4.39	3.63	3.54	3.87	**3.27**	**2.90**
Σ3(121) <111>	P1	27.54	**25.49**	24.69	4.59	4.13	4.86	4.43	4.00	4.49	3.31	2.89
	P2	**26.03**	26.37	24.70	4.40	**3.77**	3.94	**3.48**	3.40	3.54	**2.84**	**2.41**
	P3	27.08	25.80	**23.95**	4.11	**3.77**	3.63	3.53	**3.37**	3.20	3.01	2.65

Table 7.3. Theoretical cohesive strength and fracture energy of bulk Ni.

	Theoretical cohesive strength (GPa)		Relaxed fracture energy, E_{frac}^{r} (J/m^2)	
	θ_{bulk}=0	Maximum excess of H	θ_{bulk}=0	Maximum excess of H
Ni(210)	27.25	26.34	4.89	3.27
Ni(530)	26.83	26.41	4.89	3.31
Ni(113)	27.49	27.02	4.81	3.22
Ni(111)	28.33	28.15	3.99	3.46
Ni(221)	27.10	26.48	4.58	2.64
Ni(132)	26.48	25.92	4.87	3.12
Ni(121)	26.96	26.22	4.66	2.76

7.3.3 GB decohesion aided by plasticity

During the deformation and failure process in metals, dislocation plasticity could combine H atoms to cause the cohesive strength of the GB to become the weak link in metallic systems and therefore the source of crack nucleation [19, 20, 108]. Thus it is necessary to investigate the GB decohesion aided by localised plasticity. Plasticity (dynamic dislocation-GB interactions) typically provokes the GB to transform into an activated state with a more disordered atomic structure, and establishes a local stress state [216], we therefore directly quantify the influence of the two factors (boundary disruption and stress state) on the H-induced GB decohesion by computing the reduction in cohesive strength. Here, we choose three typical GBs (Σ5 (210) ⟨100⟩, Σ3 (111) ⟨110⟩ and Σ3 (121) ⟨111⟩) to identify the dependency of the GB cohesive strength on GB type. The schematics of the calculation for the GB cohesive strength with various configurations are shown in Fig. 7.7. For clean GB in Fig. 7.7(a), the transverse stresses are kept free. The model in Fig. 7.7(b) is the same as clean GB, but filled with maximum excess of H. For Fig. 7.7(c), the disordered boundary structure is obtained via displacing GB atoms randomly in all directions, followed by a local minimisation. It is obvious that after boundary disruption, GB has a higher centrosymmetry parameter value and more distorted environments. In the case of the model in Fig. 7.7(d), the transverse stresses are applied in *X* and *Z* directions to imitate the local stress state. Finally, the above all factors are combined into the model in Fig. 7.7(e).

Fig. 7.8 shows the tensile stress–separation distance curves for various GB configurations in Fig. 7.7. Due to the randomness in the boundary disruption artificially introduced on the GB, we have prepared ten models with different disordered atomic

structures. The averaged cohesive strength of these ten models is given in Table 7.4 accordingly. Similarly, five models with different transverse stress values ranging from 0 GPa to 5 GPa are used here in calculation of GB cohesive strength under stress state. As shown in Fig. 7.8 and Table 7.4, the presence of H does not reduce the cohesive strength significantly by itself, i.e., the reduction of 7.93% for the Σ5 (210) ⟨100⟩ GB, 0.04% for the Σ3 (111) ⟨110⟩ GB and 7.99% for the Σ3 (121) ⟨111⟩ GB. By comparison, the magnitude of the reduction of cohesive strength can reach as high as 29.65% for the Σ5 (210) ⟨100⟩ GB, 23.74% for the Σ3 (111) ⟨110⟩ GB and 25.12% for the Σ3 (121) ⟨111⟩ GB when localised plasticity (boundary disruption and local stress state) is considered.

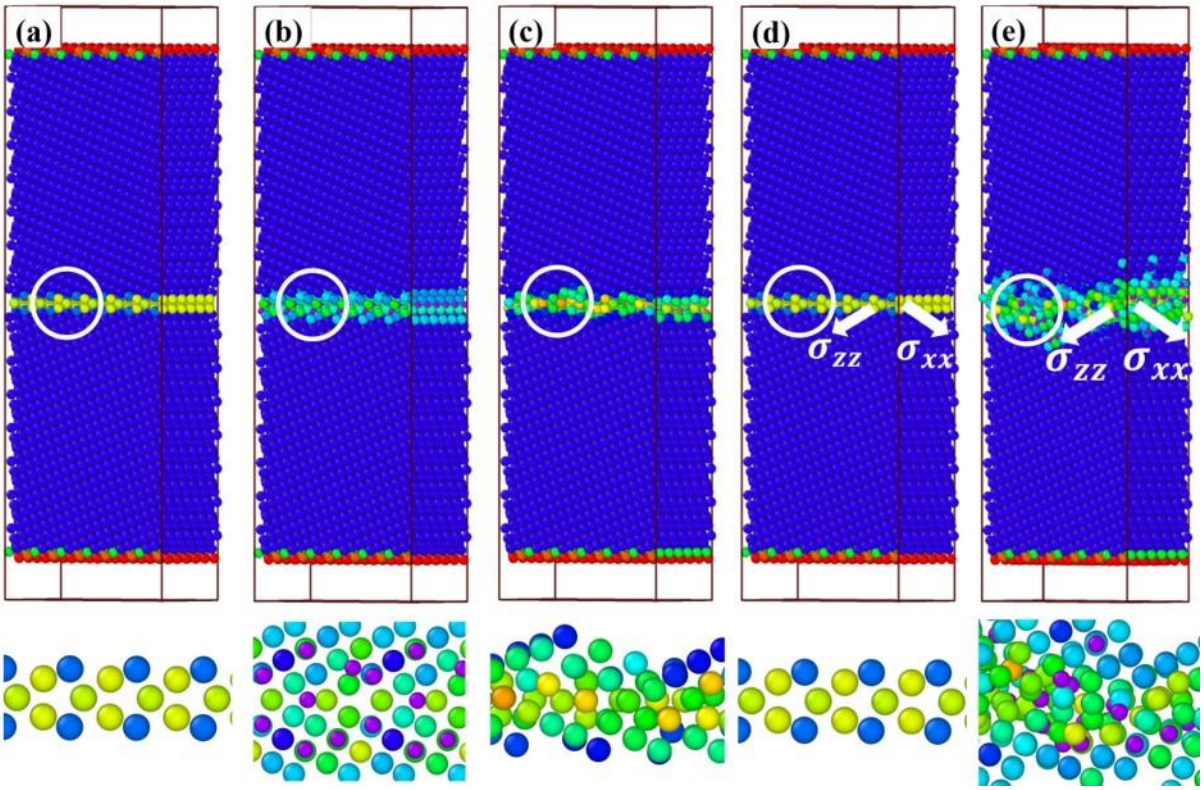

Fig. 7.7. Calculation for GB cohesive strength with various configurations: (a) Ni GB, (b) Ni GB, maximum excess of H, (c) Ni GB, boundary disruption, (d) Ni GB, local stress state and (e) Ni GB, with three factors combined. Ni atoms are coloured according to their centrosymmetry value, and H atoms are assigned in purple.

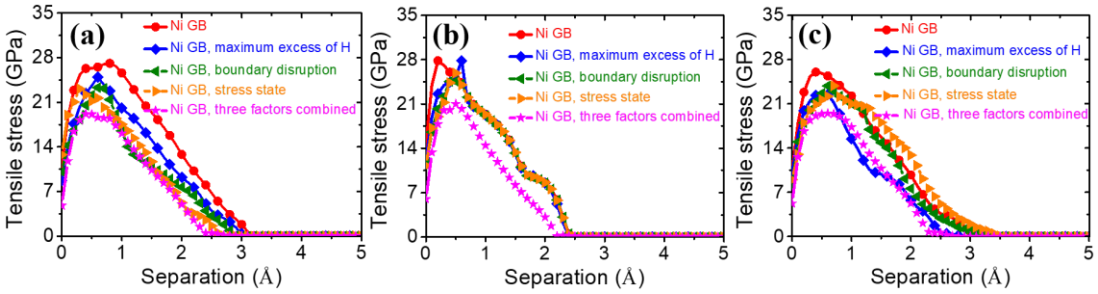

Fig. 7.8. Tensile stress-separation distance curves for tensile stretching of various GBs: (a) Σ5 (210) ⟨100⟩, (b) Σ3 (111) ⟨110⟩, and (c) Σ3 (121) ⟨111⟩.

Table 7.4. Theoretical cohesive strength of various GBs with different configurations.

Various configurations	Cohesive strength (GPa)		
	Σ5 (210) ⟨100⟩ GB	Σ3 (111) ⟨110⟩ GB	Σ3 (121) ⟨111⟩ GB
Ni GB	27.12	27.84	26.03
Ni GB, maximum excess of H	24.97	27.83	23.95
Ni GB, boundary disruption	23.31	24.59	23.85
Ni GB, stress state	21.67	25.89	23.42
Ni GB, three factors combined	19.08	21.23	19.49

7.4 Discussion

Previously, some studies directly measured the reduction in the GB cohesive strength with varying H coverage [55, 56, 150, 151]. However, H coverage was unrealistic as only some lowest-energy trapping sites were identified and filled. Furthermore, the dependency of the GB cohesive strength on H coverage should be conducted in the context of GB type as for the same H concentration, the H-induced reduction may differ from various GBs. In the present study, a powerful geometric approach of space tessellation was used for finding every possible trapping site, which provides an atomistically-based thermodynamic framework to quantify the GB fracture by H segregation in Ni. In addition, various ⟨100⟩, ⟨110⟩ and ⟨111⟩ GBs were studied to explore the influence of GB type on the relationship between the GB cohesive strength and H coverage.

By mapping H segregation energy at the GB/FS and calculating cohesive properties during GB separation along the fracture plane, it is found that the theoretical cohesive strength and fracture energy are sensitive to GB type. Among all investigated cases, Σ3 (111) ⟨110⟩ GB exhibits marginal reduction in cohesive strength and energy due to H segregation, being in concordance with the DFT calculation [56]. Under the equilibrium

H concentration where H embrittlement in Ni is observed (θ_{bulk} = 0.001), in conjunction with local H diffusion process the maximum reduction of tensile strength and fracture energy is 6.60% and 15.75% for Σ5 (210) ⟨100⟩ and Σ17 (530) ⟨100⟩ GBs, respectively. As such, one question needs to be considered: whether such weakening of the GB due to H (only a few percent of the strength reduction) is sufficient to induce a transition from transgranular to intergranular failure in experiments [149]?

Although it is abstruse to answer this question today, more recently, numerous studies of the microstructure beneath H-induced intergranular facets in structural materials such as Ni and Fe, martensitic, and austenitic steels indicate that H-enhanced plasticity (dynamic dislocation-GB interactions) plays a critical role in establishing the conditions for intergranular fracture by boundary decohesion [19, 20, 108]. Experimental evidence showed that the microstructure was comprised of extremely high density of dislocations, which was more evolved and complicated than expected for the failure strain. In fact, for the Ni case, this dislocation structure was found to extend over a significant distance from the fracture surface, suggestive of an acceleration of plasticity process and pre-failure deformation prior to crack initiation. Combining the experimental observations of accelerated plasticity and direct decohesion calculations, the mechanism of plasticity-mediated decohesion becomes evident. Under this scenario, the ultimate fracture behaviour itself is by HEDE but the conditions for achieving it are via HELP (combined effects of HEDE and HELP).

Herein, the role of HELP mechanism is assumed to be threefold: (i) the plasticity accumulation induced by slip transfer provides an effective path for H atoms to be deposited into the GB. If the dislocations intersecting with the GB are transporting H atoms, the consequence of slip transmission will accumulate H atoms on the GB. Additionally, the change in the GB structure due to dislocation-GB interactions allows the GB to accommodate more H atoms as additional favourable trappings sites are generated. In the current study, all calculations are performed at fixed segregation of H to the GB, and this dynamic H transportation process is not considered. Therefore, our calculation of the reduction in GB cohesive properties is likely an underestimate of H embrittling effect on ultimate decohesion; (ii) when the dislocations are incorporated into the GB, the segregated GB by H tends to trap the incoming dislocations [216]. The dislocation accumulation activates the GB to a more disordered structure and increases the strain energy density within the GB. By quantitative calculation in Fig. 7.8 and Table

7.4, it is found that the GB with a more disordered atomic structure can reduce the cohesive strength of the GB even without H atoms. For example, the reduction is 3.81GPa for the Σ5 (210) ⟨100⟩ GB with a boundary disruption, being comparable to 2.15 GPa for the GB in the presence of H. Based on this calculation, it is suggested that GB disruption caused by dislocation plasticity process is important in achieving H embrittling effect in metallic materials; (iii) as the GB hinders slip transfer, a local stress state on the GB is built up. Similar to the factor of boundary disruption, stress state can also help reduce the GB cohesive strength and play a crucial role in the embrittlement process. Ultimately, with these conditions combined, our results reveal that the final decohesion process (HEDE activation) is largely facilitated.

7.5 Summary

In summary, H trapping maps and H-induced change in cohesive properties of various GBs were studied using MD simulations. Under conditions typical of H-induced intergranular fracture in Ni, the maximum reduction in the GB cohesive strength and fracture energy due to H segregation was 6.60% and 15.75%. Combining these calculations with experimental observations of high dislocation plasticity, it was revealed that the realisation of H embrittling effect in metallic materials was largely assisted by the boundary disruption and local stress state concentrated on the GB through the plasticity process. These findings advance the atomic-level understanding of the GB decohesion, and suggest appropriate directions for design of new materials against H embrittlement.

Chapter 8 Hydrogen-modified behaviour of cracks along grain boundaries

This chapter is extracted from the following publication:

Li J, Lu C*, Wang L, Pei L, Godbole A, Michal G. The role of hydrogen on the behavior of intergranular cracks in bicrystalline α-Fe nanowires. Nanomaterials. 2021;11:294.

8.1 Introduction

As the occurrence of HE is frequently along GBs in polycrystalline metals, and often shows cleavage-like features, it is believed that understanding of crack behaviour along GBs is fundamental to clarify HE. Considering cleavage-like failure to happen by the propagation of sharp cracks, such a process is suppressed if dislocation emission blunts the crack tip. This points towards examining crack-tip specific behaviour (the inherent competition between brittle cleavage and ductile emission) associated with hydrogen. In this chapter, the technique of MD simulations was employed to investigate the H-modified behaviour of GB cracks in α-Fe bicrystal models. Various H concentrations, loading spectra (monotonic and cyclic) and GB types (symmetric and asymmetric) were considered for increasing complexity. The remainder of this chapter is organized as follows. The simulation methodology is described in Section 8.2. Theoretical predictions according to Griffith's and Rice's models of brittle cleavage and ductile emission, separately, and atomistic mechanisms of crack tip events in the presence of H under various loading spectra are given in Section 8.3. The results are discussed in terms of H-induced transition into intergranular failure, and a summary is concluded in Section 8.4.

8.2 Computational approach

All simulations were carried out using the Large-scale Atomic/Molecular Massively Parallel Simulator (LAMMPS) [155] with a Finnis–Sinclair-type embedded-atom-method potential for Fe-H [67, 162]. Four bicrystal models with tilt GBs were established with specified crystallographic orientations: Σ3 (1 1 2) [1 $\bar{1}$ 0] GB, Σ17 (2 2 3) [1 $\bar{1}$ 0] GB, Σ5 (2 $\bar{1}$ 0) [0 0 1] GB, and Σ11 (5 5 7)$_A$($\bar{7}$ $\bar{7}$ 1)$_B$ [1 $\bar{1}$ 0] GB, as shown

in Fig. 8.1(d)-(g). The simulation domains have dimensions $L_x \times L_y \times L_z$ of about 430 Å × 480 Å × 20 Å and a total number of atoms of about 3.6×10^5. A crack of length 100 Å was created by removing three atomic planes along the boundary, and the periodic boundary condition was imposed along the crack front direction (Z axis). The atoms within the 10 Å thick region near the free surfaces along the Y direction were fixed and frozen by setting the interatomic force to zero. An incremental displacement was applied to the frozen atoms to load the crack according to anisotropic elastic mode I stress intensity field K_I [217]. To study the effects of solute H, H atoms were randomly inserted into simulation models with four H concentrations of approximately 45, 90, 135 and 180 mass parts per million (mppm) respectively. The system was initially loaded to $K_{Iapp} = 0.6$ MPa $\sqrt{m}$ to drive H segregation around the crack tip, where K_{Iapp} represents the applied stress intensity factor. Prior to fracture simulations, the constructed models were first heated at a temperature of 700 K for 0.5 ns, then cooled to 300 K for 0.5 ns, followed by further equilibration at 300 K for 3 ns. As shown in Fig. 8.1(b) and (c), H atoms preferentially segregate onto the GB and crack surfaces due to the strong H trapping effect of defects (GBs/cracks) and high diffusion of H atoms in the α-Fe lattice. After obtaining equilibrated Fe-H configurations, the crack was loaded further by imposing successive increments of $\Delta K_{Iapp} = 0.002$ MPa $\sqrt{m}$ every 1×10^{-3} ns. For the cyclic loading cases, loading spectra are presented in Section 8.3. MD simulations were performed under the canonical ensemble (NVT) [218] with time steps of 0.5 and 1 fs for models with and without H, respectively. The Nose-Hoover method [219, 220] was used to keep the system temperature at 300 K.

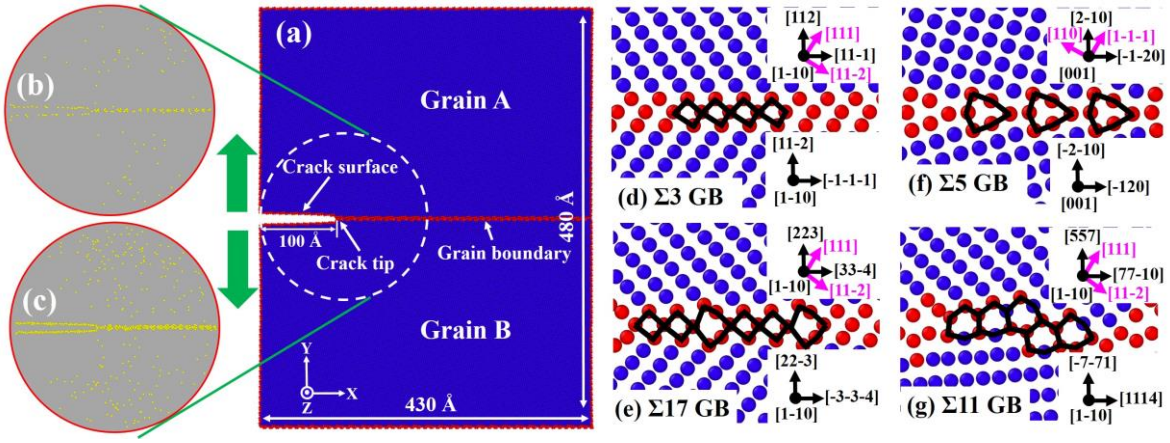

Fig. 8.1. MD simulation set-up for mode-I fracture along tilt boundary. (a) Geometry and crystallographic orientations of simulation model. (b) and (c) H distribution around the crack tip with 45 and 135 mppm H atoms. (d)-(g) Atomic configurations of the equilibrium structure of various GB types. Images are

coloured by CNA, where atoms with bcc structure are coloured in blue, atoms at the GB and free surface are coloured in red, atoms with fcc structure are coloured in green, and H atoms are assigned in yellow. The structural units of each GB are outlined by the black line. Possible dislocation slip systems are indicated with pink arrows.

8.3 Results

8.3.1 Theoretical model for embrittlement

As illustrated in Fig. 8.2, an intergranular crack is inserted along a tilt GB and propagates to the right. According to Griffith's theory, the critical stress intensity factor for cleavage propagation under mode I loading is derived as:

$$K_{Ic} = \sqrt{\gamma_i / A_1} \tag{8.1}$$

where γ_i is fracture energy, and A_1 is a constant depending on the anisotropic linear elasticity c_{ij} [56, 221]:

$$A_1 = \left[\frac{\sqrt{c_{22}}}{2}\sqrt{2c_{11} + 2c_{12} + c_{44}}\right]^{-1} \tag{8.2}$$

The calculation method of γ_i as a function of the H concentration and GB type has been presented in our previous study [209], and the corresponding results are shown in Fig. 8.2(e). It is clear that for all investigated GBs γ_i is decreased with increasing H concentration.

Rice's model of dislocation emission from a crack tip is adopted here to study the intrinsic ductility of the GB [139]. In this model, the critical stress intensity factor required for dislocation emission can be determined as:

$$K_{Ie} = \frac{1}{cos^2(\theta/2)\sin(\theta/2)}\sqrt{\frac{2G}{1-v}\gamma_{usf}[1 + (1-v)tan^2\emptyset]} \tag{8.3}$$

where G is the shear modulus, v is the Poisson ratio, θ and $\emptyset$ is the angle between the cleavage and slip planes, the angle of the crack normal and the Burgers vector, and γ_{usf} is unstable stacking fault energy. For calculating γ_{usf} by using MD, a single crystal is created and shown in Fig. 8.2(c). The generalized stacking fault energies are determined by rigidly displacing the upper block on $(1\ 1\ \bar{2})/(1\ 1\ 0)$ plane along $[1\ 1\ 1]/[1\ \bar{1}\ \bar{1}]$ direction while fixing the lower block and calculating the energy change in the whole simulation cell. In the present study, H atoms mainly occupy at the crack tip and GB, and a few H atoms exist at the slip plane. Further, some studies have revealed that H segregation into the slip plane marginally changes the γ_{usf} [26, 145, 146]. Therefore, we use the value of γ_{usf} for pure Fe in all cases.

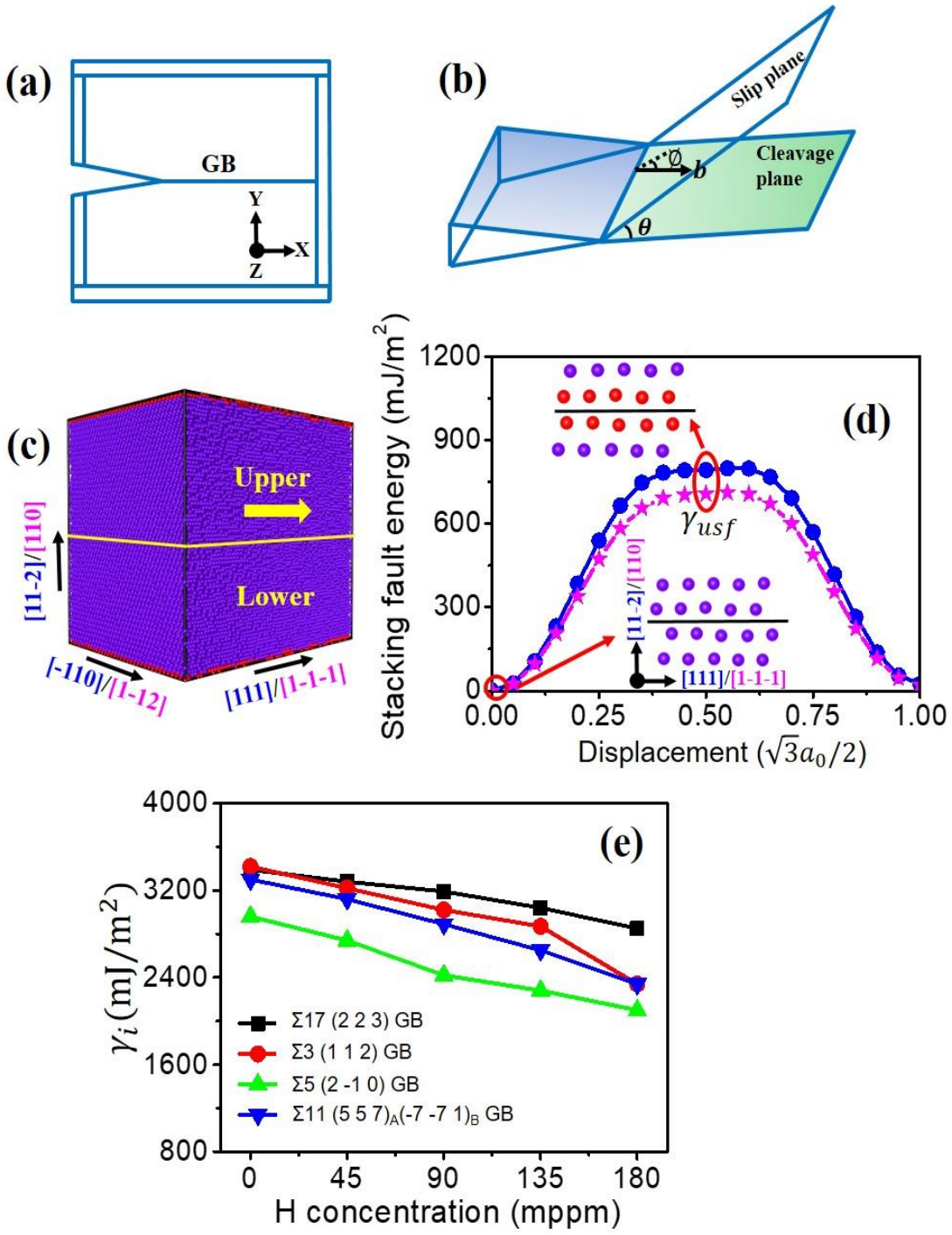

Fig. 8.2. Schematic representations of (a) a crack along a tilt GB and (b) dislocation emission on slip plane emanating from the crack tip. (c) Simulation model for calculating the generalized stacking fault in $(11\bar{2})[111]$ and $(110)[1\bar{1}\bar{1}]$ slip systems. Atoms with perfect bcc structure are coloured by dark blue, and the red atoms represent the stacking fault and the free surface. (d) The generalized stacking fault energy versus fractional displacement in $(11\bar{2})[111]$ slip system (blue circle) and $(110)[1\bar{1}\bar{1}]$ slip system (pink star). (e) Fracture energy of various GBs as a function of H concentration.

It needs to be mentioned that, directional anisotropy exists for intergranular crack

propagation. With different values of θ and $\emptyset$, ductile behaviour (dislocation emission) may be expected for one crack tip ($K_{Ie} < K_{Ic}$), while brittle behaviour (cleavage) may occur for the opposite crack tip within the GB plane ($K_{Ic} < K_{Ie}$). For example, the crack of Σ17 (2 2 3) GB exhibits ductile behaviour along [3 3 $\bar{4}$] direction, while shows brittle fracture along [$\bar{3}$ $\bar{3}$ 4] direction (see Fig. 8.3). Likewise, in the case of Σ11 (5 5 7)$_A$($\bar{7}$ $\bar{7}$ 1)$_B$ GB, [7 7 $\overline{10}$] is ductile direction, while [$\bar{7}$ $\bar{7}$ 10] is theoretically brittle direction (Fig. 6.4).

8.3.2 Dislocation emission and cleavage of crack tip under monotonic loading

Fig. 8.3(a)-(e) shows atomic configurations of the intergranular crack along the Σ17 (2 2 3) GB for two cracking directions. For crack propagation along the [3 3 $\bar{4}$] direction (see Fig. 8.3(a)), crack tip plasticity takes place by emission of twins at $K_{Iapp} = 0.86$ MPa $\sqrt{m}$ in the absence of H. This behaviour is in accordance with Rice's model ($K_{Ie} < K_{Ic}$ in Fig. 8.3(f)). Upon increasing the applied load, the nucleated twins propagate as the twinning space widens from 7.1 Å to 18.8 Å, further blunting the crack tip. Under an H environment (45 mppm H atoms), the ductile emission behaviour is similar, but Fig. 8.3(b) shows that crack tip plasticity is initiated at the opposite grain and at a lower applied load $K_{Iapp} = 0.84$ MPa $\sqrt{m}$. This can be ascribed to H segregation that disrupts the atomic structure around crack tip (compare insets in Fig. 8.3(a) and (b) at 0.6 MPa $\sqrt{m}$). The disordered structure obviously serves as a plasticity source [216], promoting slip activity from the crack tip. As H concentration increases, the fracture energy decreases (see Fig. 8.2). The corresponding K_{Ic} is therefore reduced according to Griffith's theory, as indicated by Eq. 8.1. For the model with a high H concentration (180 mppm), the calculated K_{Ic} drops to 0.78 MPa $\sqrt{m}$, less than $K_{Ie} =$ 0.82 MPa $\sqrt{m}$ (see Fig. 8.2(f)), suggesting that a ductile-to-brittle transition by H segregation at the crack tip will occur. However, the simulation results demonstrate that crack behaviour is more complex than a simple cleavage process (see Fig. 8.3(c)). At a load of 0.80 MPa $\sqrt{m}$, the crack is seen to cleave along the boundary plane without any ductile emission, whereas such a brittle cleavage stops at a higher load of 0.97 MPa $\sqrt{m}$, in which emission of twins and blunting of crack tip resumes. The process of twinning propagation continues with the applied load; crack tip thus exhibits ductile behaviour at H concentration of 180 mppm. This phenomenon may be correlated with crack trapping in GBs. The crack advances through the region of low-disorder atomic

structure (see Fig. 8.3(c) at 0.80 MPa $\sqrt{m}$) but is eventually arrested by high-disorder region (see Fig. 8.3(c) at 0.92 MPa $\sqrt{m}$). Such trapping leads to a higher K_{Iapp}, and local plasticity can be triggered in place of cleavage if $K_{Iapp} > K_{Ie}$ (see Fig. 8.3(c) at 0.97 MPa $\sqrt{m}$).

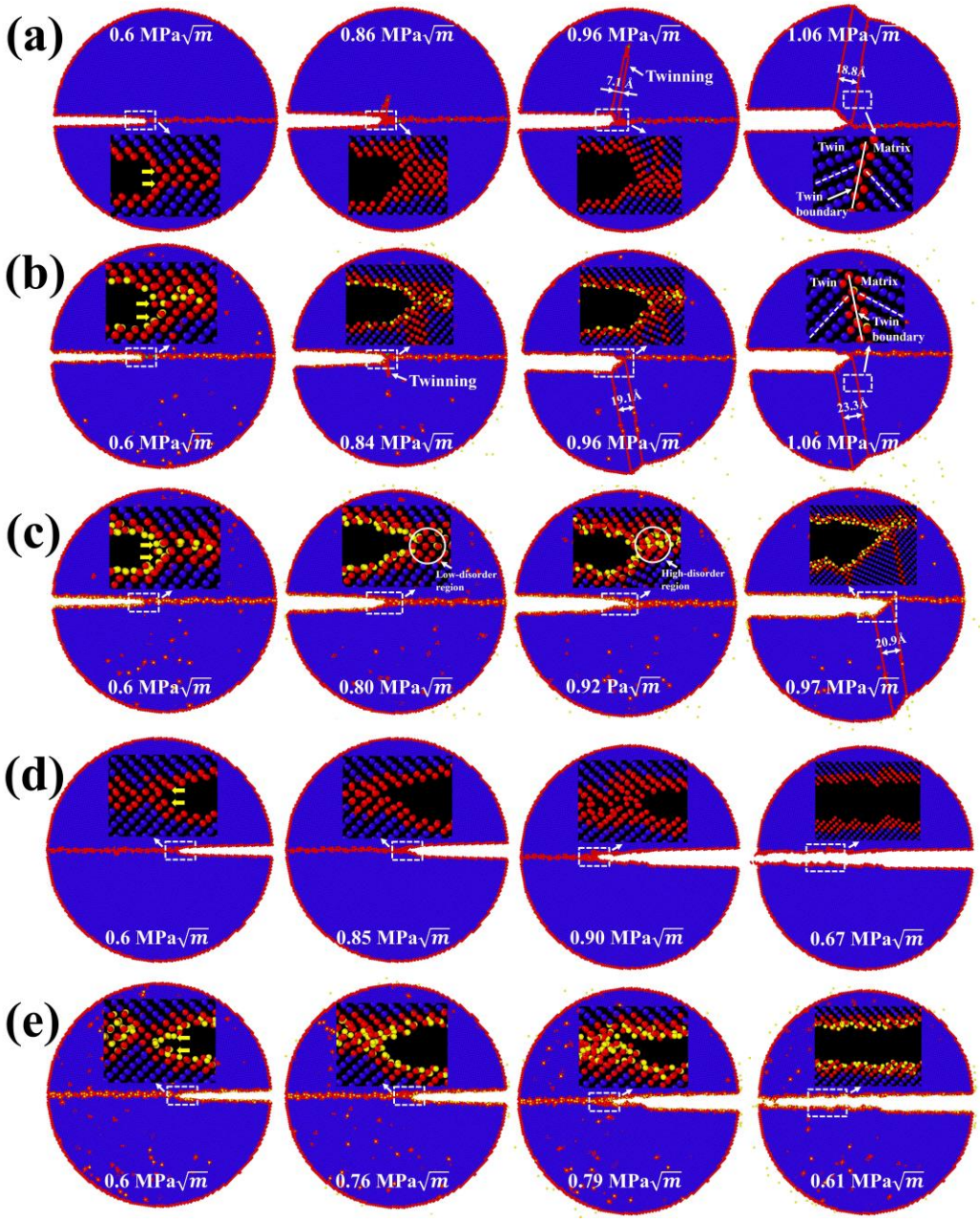

Fig. 8.3. MD snapshots illustrating the crack propagation in the simulations of Σ17 (2 2 3) GB along (a) [3 3 $\bar{4}$] direction with 0 mppm H atoms, (b) [3 3 $\bar{4}$] direction with 45 mppm H atoms, (c) [3 3 $\bar{4}$] direction with 180 mppm H atoms, (d) [$\bar{3}$ $\bar{3}$ 4] direction with 0 mppm H atoms and (e) [$\bar{3}$ $\bar{3}$ 4] direction with 180 mppm H atoms. (f) Overview of critical stress intensity factors K_{Ie} and K_{Ic}, and global applied stress intensity factor K_{Iapp} in dependence on crack orientation and H concentration. The partially filled diamonds indicate ductile emission, while solid diamonds indicate brittle cleavage. Crack propagation

distance versus the stress intensity K_{Iapp} with various H concentrations along (g) [3 3 $\bar{4}$] direction and (h) [$\bar{3}$ $\bar{3}$ 4] direction.

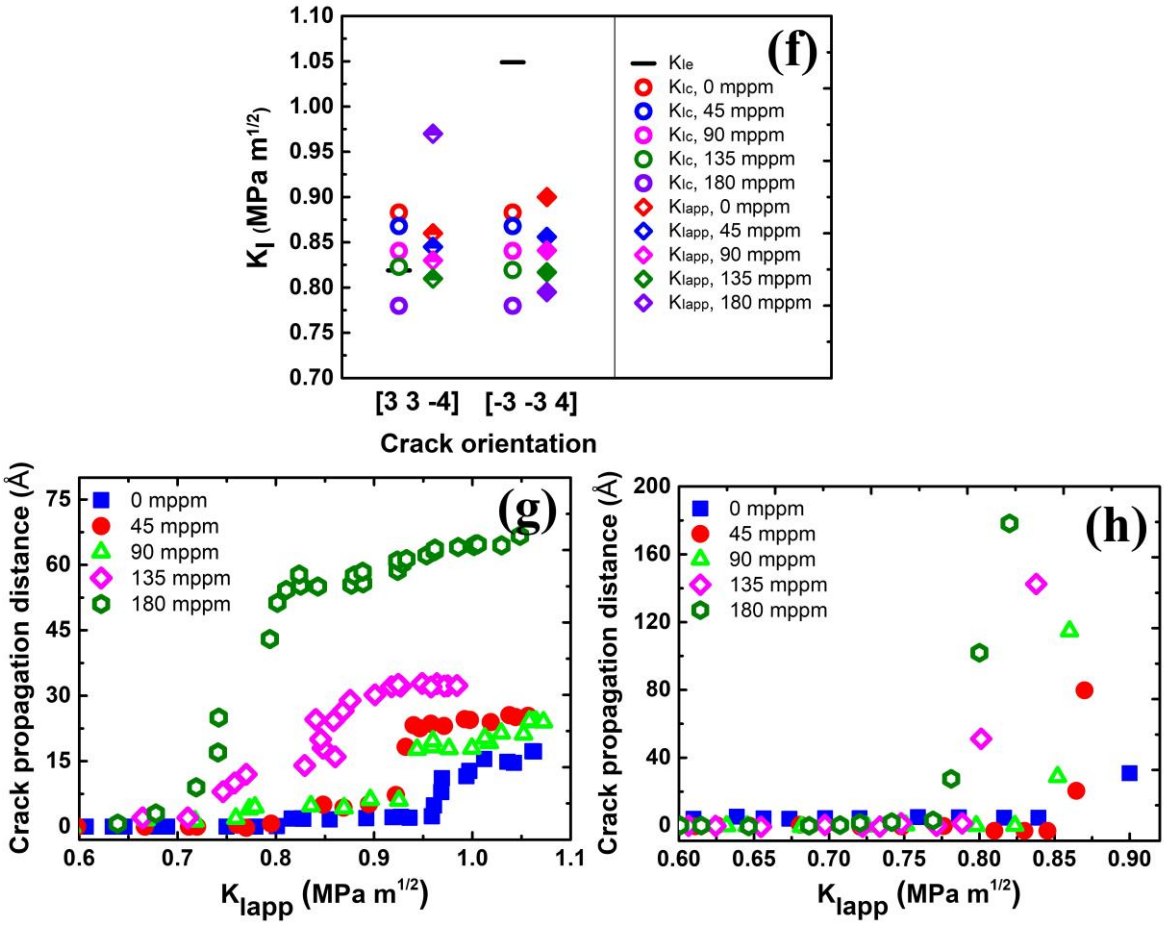

Fig. 8.3 (Continued)

In contrast to the [3 3 $\bar{4}$] cracking direction, [$\bar{3}$ $\bar{3}$ 4] is the theoretically brittle orientation (see Fig. 8.3(f)). In pure Fe, fracture along the boundary plane occurs in a perfectly brittle manner at 0.90 MPa $\sqrt{m}$ (see Fig. 8.3(d)), which is quite close to the predicted value of 0.88 MPa $\sqrt{m}$. The presence of H causes a reduction in K_{Ic}, and thus the K_{Iapp}. For example, it is seen from Fig. 8.3(e) that with H (180 mppm) the applied load is decreased to 0.79 MPa $\sqrt{m}$ for onset of cleavage. The results in Fig. 8.3(h) furthermore show that the crack propagation distance along H-charged GB is much larger than that along pure GB at the same K_{Iapp}, being indicative of that H segregation facilitates cleavage process of the GB crack in predicted brittle direction.

The crack tip behaviour for Σ11 (5 5 7)$_A$($\bar{7}$ $\bar{7}$ 1)$_B$ GB is qualitatively similar to that for the Σ17 (2 2 3) GB, as seen in Fig. 8.4. Emission of twins with Burgers vector [1 1 1]/6 dominates the plastic deformation of the crack along [7 7 $\overline{10}$] ductile

direction in the absence of H (see Fig. 8.4(a)). Low concentration of H atoms enhances the local plasticity, just as in Σ17 (2 2 3) GB. With increasing H concentration, the crack tip still exhibits ductile behaviour and no ductile-to-brittle transition is observed even though the predicted K_{Ic} is below K_{Ie} (see Fig. 8.4(c)). It is interesting to note that instead of twinning emission, an array of full dislocations with Burgers vector $[\bar{1}\ \bar{1}\ 1]/2$ nucleate at 0.88 MPa $\sqrt{m}$ after a partial cleavage, and then slip away from the crack tip. For the predicted brittle direction, cleavage advances along the boundary upon continuous loading, and H atoms make it easier for crack growth (see Fig. 8.4(d) and (e)). Similar results are also observed at Σ3 (1 1 2) and Σ5 (2 $\bar{1}$ 0) GBs, as shown in Fig. 8.5.

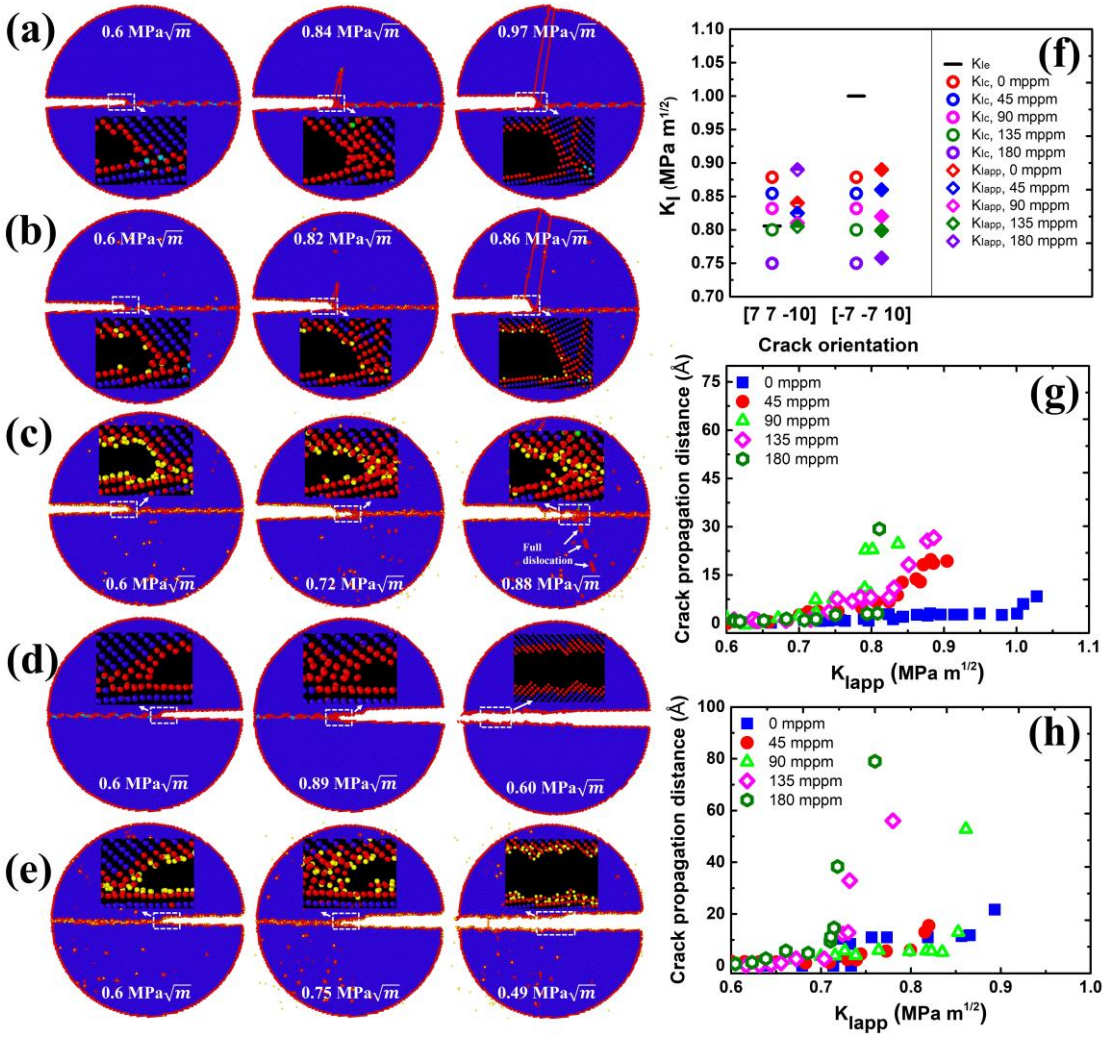

Fig. 8.4. MD snapshots illustrating the crack propagation in the simulations of Σ11 $(5\ 5\ 7)_A(\bar{7}\ \bar{7}\ 1)_B$ GB along (a) [7 7 $\overline{10}$] direction with 0 mppm H atoms, (b) [7 7 $\overline{10}$] direction with 45 mppm H atoms, (c) [7 7 $\overline{10}$] direction with 180 mppm H atoms, (d) [$\bar{7}$ $\bar{7}$ 10] direction with 0 mppm H atoms and (e) [$\bar{7}$ $\bar{7}$ 10] direction with 180 mppm H atoms. (f) Overview of critical stress intensity factors K_{Ie} and K_{Ic}, and global

applied stress intensity factor K_{Iapp} in dependence on crack orientation and H concentration. The partially filled diamonds indicate ductile emission, while solid diamonds indicate brittle cleavage. Crack propagation distance versus the stress intensity K_{Iapp} with various H concentrations along (g) [7 7 $\overline{10}$] direction and (h) [$\bar{7}$ $\bar{7}$ 10] direction.

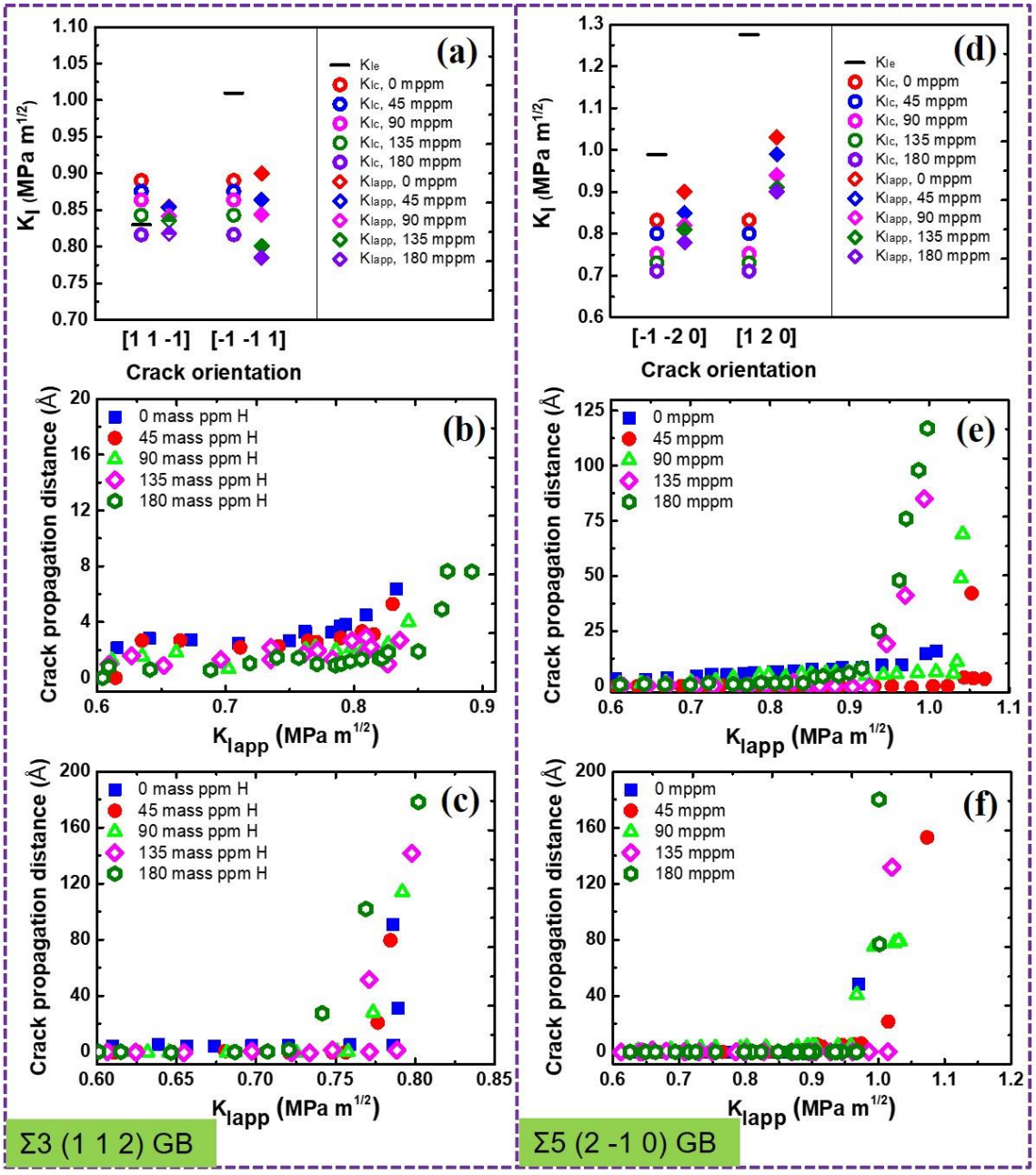

Fig. 8.5. (a) and (d) Overview of critical stress intensity factors K_{Ie} and K_{Ic}, and global applied stress intensity factor K_{Iapp} in dependence on crack orientation and H concentration. The partially filled diamonds indicate ductile emission, while solid diamonds indicate brittle cleavage. Crack propagation distance versus the stress intensity K_{Iapp} with various H concentrations along (b) [1 1 $\bar{1}$] direction, (c) [$\bar{1}$ $\bar{1}$ 1] direction, (e) [$\bar{1}$ $\bar{2}$ 0] direction and (f) [1 2 0] direction.

8.3.3 Dislocation emission and cleavage of crack tip under cyclic loading

Recent experiments in a near-neutral pH stress corrosion cracking environment have shown that H segregation significantly decreases the threshold stress intensity factor in fatigue tests, which facilitates the occurrence of brittle fracture [222-224]. Inspired by the experimental findings, we study the influence of various loading spectra on the crack tip deformation along GBs. Here, only theoretically ductile directions of Σ17 (2 2 3) [1 $\bar{1}$ 0] GB and Σ11 (5 5 7)$_A$($\bar{7}$ $\bar{7}$ 1)$_B$ [1 $\bar{1}$ 0] GB are considered. The cyclic loading spectra are shown in Fig. 8.6; the maximum value of applied stress intensity factor is 0.95 MPa $\sqrt{m}$ for Σ17 (2 2 3) GB, and 0.87 MPa $\sqrt{m}$ for Σ11 (5 5 7)$_A$($\bar{7}$ $\bar{7}$ 1)$_B$ GB, and R (K_{min}/K_{max}) is 0.4. Fig. 8.7 shows the volume density of H atoms in the GB region and the grain interior for the bicrystal models as a function of number of cycles. For calculation of the volume density of H atoms, a slab extending $\pm$1.3 nm perpendicular to the boundary plane was defined as the GB region, and a slab with the 8.0 nm thickness in the grain centre (grain A/B) was considered as the region of grain interior.

In contrast to monotonic loading cases, the ductile-to-brittle transition for GB cracks are observed at Σ17 (2 2 3) GB and Σ11 (5 5 7)$_A$($\bar{7}$ $\bar{7}$ 1)$_B$ GB under cyclic loading (see Fig. 8.8). Specifically, Fig. 8.8(a) shows that a partial cleavage starts at 0.90 MPa $\sqrt{m}$, which corresponds to the second cycle of loading phase. Continued cyclic loading leads to the successive separation of GB structure, with the final rupture occurring in the fifth cycle. As with Σ17 (2 2 3) GB, crack propagates by cleavage along the predicted ductile direction of Σ11 (5 5 7)$_A$($\bar{7}$ $\bar{7}$ 1)$_B$ GB without any plastic activity, and the two grains are ultimately separated during unloading phase in the third cycle. This transformation may be explained that cyclic loading encourages H accumulation around the crack tip along the boundary. As seen in the inserts of Fig. 8.8(a) and (c), cyclic loading concentrates the stress field ahead of the crack tip, which provides a driving force for H accumulation. During several cycles H atoms in the bulk diffuse into the GB region ahead of the crack tip, as evidenced in Fig. 8.8(b) and (d) and Fig. 8.7, where volume density of H atoms in the GB region is prominently increased, while the volume density in the grain interior is gradually reduced. With increasing H atoms on the GB, the GB fracture energy is markedly reduced (see Fig. 8.2), thus favouring brittle cleavage. Additionally, cyclic loading can aid the crack tip in overcoming the trapping; if a crack propagating along one direction is arrested by a high-disorder region,

it alternatively extends through a lower-disorder region along another direction with subsequent cycles (compare the cracking path in insets of Fig. 8.8(a) and (c)), reducing crack trapping and promoting the cleavage process. The ductile-to-brittle transition due to H accumulation and suppressed crack trapping under cyclic loading fully supports the experimental observations of large-spaced striations at the fatigue fracture surfaces in a near-neutral pH stress corrosion cracking environment [19].

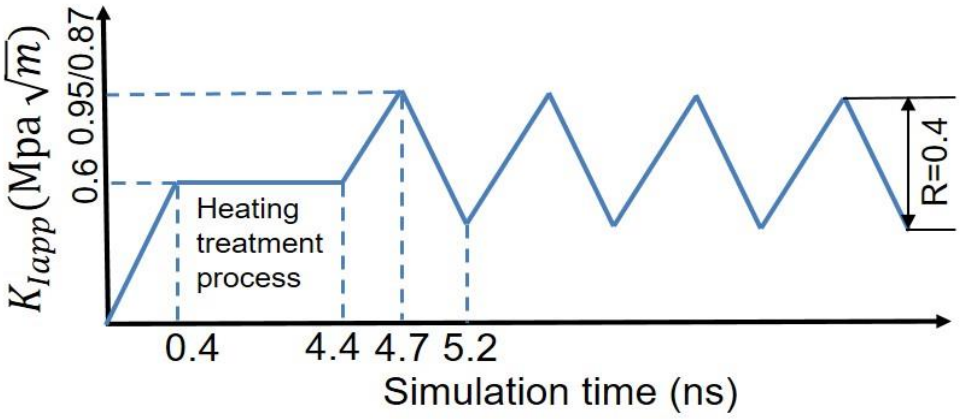

Fig. 8.6. Cyclic loading spectra in the simulations.

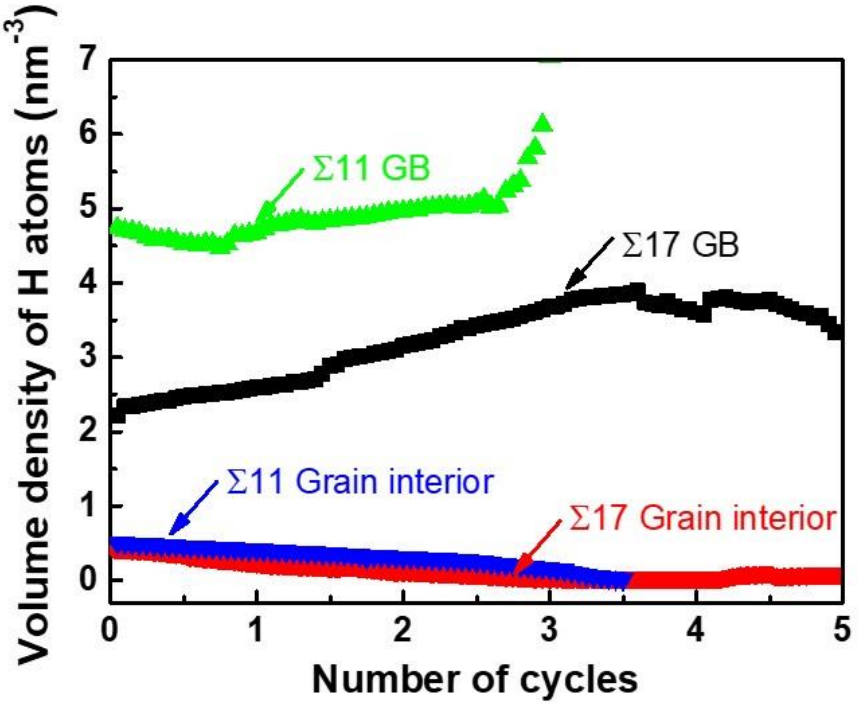

Fig. 8.7. The volume density of H atoms in the GB and the grain interior region versus number of cycles.

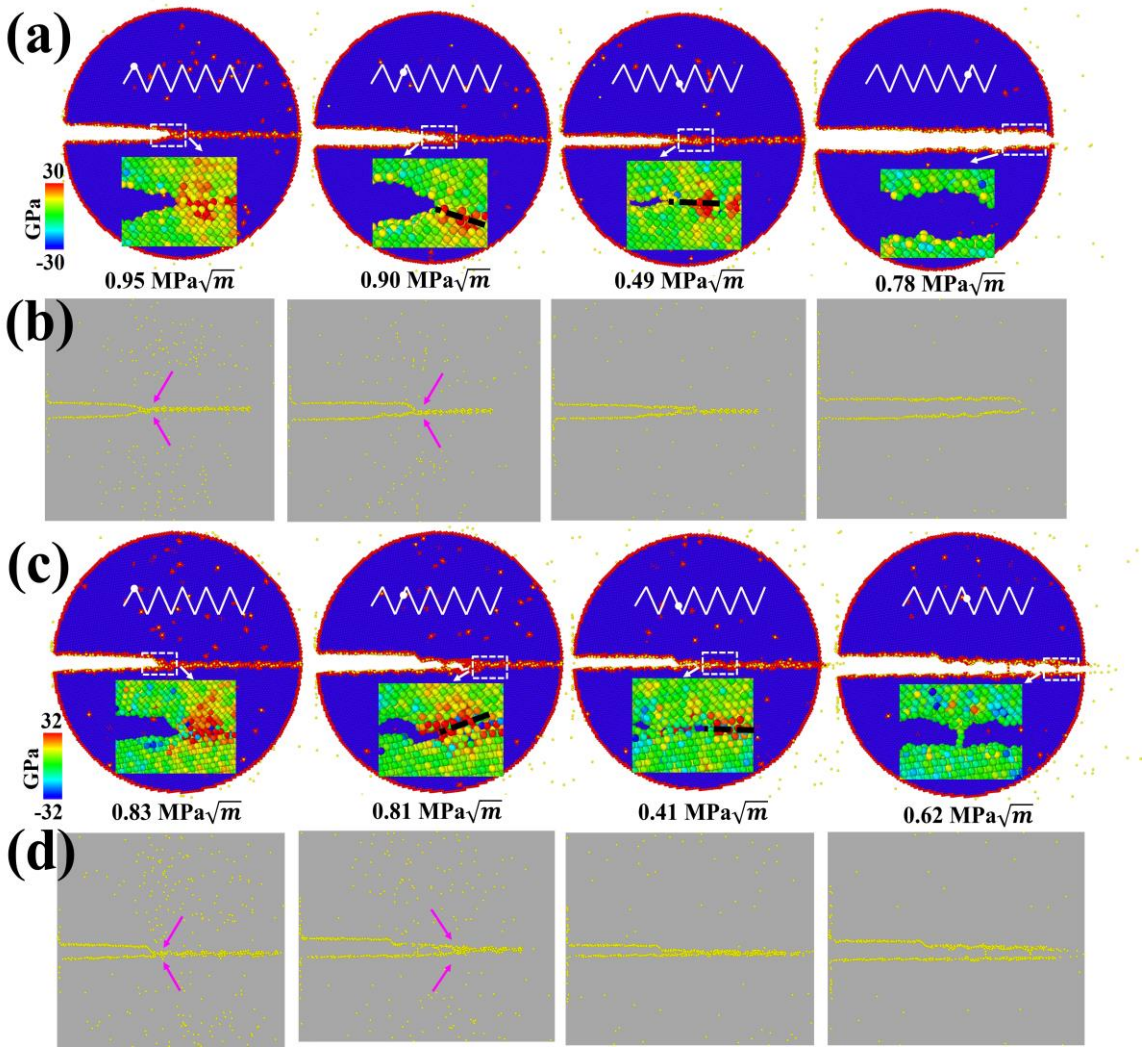

Fig. 8.8. MD snapshots illustrating the crack propagation along the predicted ductile direction of (a) Σ17 (2 2 3) GB and (c) Σ11 (5 5 7)$_A$($\bar{7}$ $\bar{7}$ 1)$_B$ GB with 135 mppm H atoms during cyclic loading. The upper inserts are loading spectra, and lower inserts of each image represent stress field distribution and are coloured by hydrostatic stress value. (b) and (d) The corresponding H distribution maps under different stress intensity. Possible cracking path is marked by dark dash, and H diffusion is indicated with pink arrows.

8.4 Discussion

The simulations show that H segregation creates no ultimate cleavage for the predicted ductile cracks along the studied GBs under monotonic loading, whereas a ductile-to-brittle transition is observed under cyclic loading. This can be ascribed to that cyclic loading helps accumulate H atoms around the crack tip along the boundary and overcome crack trapping in the GB.

Previously, some studies directly measured the reduction in the GB cohesive properties with varying H coverage and GB type [25, 44], reporting that at equilibrium concentrations for which embrittlement has been observed in experiments, the reduction due to H segregation is potentially insufficient to cause intergranular failure. By considering the intrinsic competition between cleavage fracture and dislocation emission at a crack tip, our results suggest that Fe GBs cannot be embrittled simply by equilibrium segregation of H atoms to GBs, being accordance with those calculations. Embrittlement is therefore presumably associated with H transport process. During cyclic loading, the tensile stress filed is concentrated around the crack tip. As the movement velocity of H atoms towards the crack tip is relate to hydrostatic stress, $V \propto \nabla\sigma^{hyd}$ [27], the concentrated stress results in high H movement. In addition, after several cycles H atoms in the bulk have ample time to diffuse into the GB region ahead of the crack tip. Under this scenario, ultimate failure is expected to occur.

Aside from H segregation, it is found that crack trapping can also affect the ductile-to-brittle transition. In the case of Σ17 (2 2 3) GB, brittle cleavage is predicted to occur along the [3 3 $\bar{4}$] direction with 180 mppm H atoms according to the Griffith's theory. However, atomistic simulations show that ductile emission remains the ultimate mechanism. This discrepancy can be expressed as effects due to crack trapping in GBs. Unlike single crystals, GBs typically have complicated atomic structures, crack tip can therefore be arrested by high-disorder regions of the GB. This blunts the crack tip while encouraging the occurrence of local plasticity. Under cyclic loading, the crack advances dynamically. It is less likely that the crack tip stays dormant and trapped by the GB. In other words, if the crack tip is trapped by a high-disorder region at loading phase, it may change its position and propagating path at unloading phase. In this regard, the dynamic propagation alleviates crack trapping and facilitates cleavage process.

8.5 Summary

In summary, to clarify the HE mechanism, the H-modified behaviour of intergranular cracks in bicrystal α-Fe was investigated via MD simulations. It was found that twinning emission from the crack tip was favoured in the intrinsically ductile directions, and H segregation created no ultimate cleavage. However, the presence of H atoms caused a significant reduction in the critical stress intensity factor for cleavage and facilitated brittle fracture in the theoretically brittle directions. Further, the

simulations showed that cyclic loading accumulated H atoms around the crack tip along the boundary and overcame crack trapping in the GB, and thus induced a ductile-to-brittle transition. These findings enrich our knowledge on experimental observations of H-assisted brittle cleavage failure, and suggest suitable directions for GB engineering of HE-resistant materials.

Chapter 9 Conclusions and recommendations for future work

9.1 Conclusions

In this thesis, the underlying mechanisms behind HE phenomenon on an atomic scale have been investigated. H segregation at various GBs and its influence on the structure, mechanical properties, deformation mechanisms and failure response of GBs have been examined by atomistic simulations. Simulations models cover numerous influencing factors: (1) material microstructure, such as GBs, dislocations and cracks, (2) H charging and diffusion, H interaction with various traps and trapping conditions, (3) H coverage and its local distribution around defects, and (4) mechanical loading conditions such as tensile, shear, monotonic and cyclic loading.

First of all, H segregation properties were studied in this thesis. Both tilt and twist symmetric GBs were considered as simulation models. It was found that different GBs possessed unique H segregation energy maps, and the trapping ability of H was strongly dependent on GB structures. GBs with more open structure had higher maximum excess H concentration. Of all the investigated GBs, it was found that the twin boundary seldom absorbed H. Increasing the fraction of twin boundaries by GB engineering is thus presumably one strategy for reducing the severity of HE, as shown in experiments [112]. The effects of H atoms on the mechanical behaviour and plastic deformation of various types of GBs were examined by direct MD simulations. When subjected to tensile loading, dislocation nucleation from the GB dominated the deformation mechanism. The presence of H modified this behaviour. The simulations revealed that H segregation gave rise to an increase/decrease in the yield stress for dislocation nucleation. The introduction of H caused the change in the structure, which facilitated the onset of plasticity. This softening was in accordance with the envisioned HELP mechanism. By contrast, for some types of GBs, segregated H atoms could harden the material as the result of the constrained collapse of SUs and the formation of dislocation locks. Regarding shear deformation, the coupled GB migration was the controlling mechanism of plasticity process. The segregated H atoms retarded such motion as H cannot diffuse into low-energy sites within the time scale of the shear loading. An analysis of vacancy concentration showed that during GB migration H-vacancy clusters cannot grow larger via vacancy accumulation. Therefore, it seems that the coupled GB

motion may be beneficial to resist H-induced intergranular embrittlement.

The role of H atoms in changing the interaction of dislocations with GBs was also studied by direct simulations in this thesis. The dislocations typically interacted with GBs in forms: (i) dislocation absorption followed by the formation of GB dislocations, (ii) direct dislocation transmission through the GB, (iii) dislocation reflection from the original grain, or (iv) dislocation nucleation from the GB. Segregated H atoms transformed these interaction mechanisms into ones involving dislocation absorption for most of GBs. Specifically, H induced a transition from dislocation dissociation to absorption for 'singular' GBs because H impeded the GB migration. In the case of 'general' GBs, the boundaries were prone to absorb the incident dislocation within the framework of the HELP mechanism where H modifies the stress field of GB dislocations, reduces the equilibrium separation distance between GB dislocations, and stabilizes the configurational structure of GB dislocations. The dislocation-GB interactions had two possible influences on ultimate intergranular fracture. Specifically, the absorption of incoming dislocations by the GB increased the strain energy density within the GB, and established a local stress state at the GB. During the subsequent stress relief process, the formation of extensive vacancies was observed, which is expected to cause H-induced intergranular failure by the growth and coalescence of vacancies and nano-voids.

Moreover, the decohesion of Ni GBs in the presence of H was examined via direct simulations. The computational tensile tests showed that under the equilibrium concentration of H atoms typical of embrittlement in Ni, and in conjunction with local H diffusion process, the maximum reduction of tensile strength and fracture energy was 6.60% and 15.75% for Σ5 (210) ⟨100⟩ and Σ17 (530) ⟨100⟩ GBs, respectively. Motivated by the above dislocation-GB interactions and experimental evidence of high dislocation plasticity, these decohesion parameters with boundary disruption and local stress state were calculated. The direct calculations revealed that the realisation of H embrittling effect in metallic materials was largely assisted by the plasticity process. These findings provide a picture of H embrittlement arising from the cooperative action of H-induced plasticity and GB decohesion.

The influence of H segregation at the GBs in modifying the ductile emission and brittle cleavage of the intergranular cracks was studied by atomistic simulations. The simulation of the mode I crack tip indicated that twinning emission from the crack tip

was favoured in the intrinsically ductile directions, and H segregation created no ultimate cleavage. In the theoretically brittle directions, the presence of H atoms caused a significant reduction in the critical stress intensity factor for cleavage and facilitated brittle fracture. For all investigated GB cracks, there was no tendency for H atoms to induce the ductile-to-brittle transition in Fe under monotonic loading. These observations suggested that the equilibrium segregated H atoms were insufficient to cause the intergranular failure of Fe in experiments. Further investigation of the H-modified behaviour of GB cracks under cyclic loading showed that cyclic loading accumulated H atoms around the crack tip along the boundary and overcame crack trapping in the GB, inducing a ductile-to-brittle transition. Thus, H-assisted brittle cleavage failure presumably involves mechanisms such as H diffusion or dynamic crack growth.

9.2 Recommendations for future work

Atomistic simulations in this thesis provided some insights into the plasticity and fracture related to H segregation in metallic systems, all of which can deepen our overall understanding of the HE phenomenon of metals and provide a pathway to designing new materials with high resistance to HE. However, due to the multifaceted nature of HE, this field is still open for more in-depth analysis. Some potential research areas are as follows:

In order to validate the HELP theory, the dislocation nucleation and motion in the presence of H atoms under tensile and shear loading have been probed. In parallel, the nanoindentation approach is also effective in testing the H effects on plasticity at small scales. Previous experiments stated that the presence of H often decreased the pop-in load corresponding to the onset of plasticity [104, 105, 188-233]. This phenomenon was ascribed to the decrease in dislocation line tension due to H segregation to dislocations, which facilitated homogeneous dislocation nucleation. However, there were no pre-existing dislocations underneath nanoindenter prior to the nucleation, so the reduction of dislocation line tension would not presumably occur. In addition, pop-in event originated from the simultaneous burst of dislocations, not direct homogeneous dislocation nucleation. Hence, the H-induced decrease of dislocation pop-in remains unclear so far. Wen et al. [234] performed simulations and also reported the reduced load. This phenomenon was mainly attributed to H-induced lattice swelling that led to

the development of shear stress (artifacts of the simulation). By contrast, Tehranchi and Curtin [235] proposed a physical process that explained early pop-in. Underneath the indenter, the stress field was compressive, leading to a positive misfit volume of H and a driving force of H to diffuse away from the indentation region. As a consequence of H misfit volume and non-uniform H distribution, the H diffusion process gave rise to additional stresses on the indentation region. These developed stresses enabled an early pop-in. Along these lines, further research is required to probe the mechanisms for the widely-observed pop-in.

Recent experiments in metals showed the presence of nano-voids along the fracture surface of H embrittled samples [3, 46, 47, 236-240]. These studies motivated the development of H-enhanced nano-void nucleation and growth mechanism. It was proposed that the plasticity-generated vacancies can be stabilized by H in the form of H-vacancy complexes. These complexes can be preserved during further dislocation interactions. DFT calculations indicated that complexes had a good stability in various metallic systems and might serve as the embryos for void formation [32, 241, 242]. Unfortunately, these calculations were mainly performed for studying energetics of H-vacancy complexes and cannot provide kinetic routes that explain the evolution of such complexes into nano-voids during dislocation plasticity. Further atomistic investigation is envisioned to probe the precise role of H-vacancy complexes in promoting the formation of proto nano-voids and bridge the link of atomic-scale events with the incipient macroscopic failure of HE.

In addition, the influence of solutes on enhancing or suppressing the HE in metals should also be investigated. For example, there are always carbon atoms in iron and steels in the form of interstitial solutes that precipitate as carbides, segregate at dislocations in Cottrell atmospheres, or segregate into the GBs [243, 244]. It has been reported that impurities such as carbon atoms play a pivotal role in altering the cohesive strength of the GB and dislocation-GB interactions [245-247]. These carbon interstitials, carbide precipitates, and Cottrell atmospheres can affect the motion of dislocations and the evolution of dislocation substructures at a larger scale, thereby changing the occurrence and frequency of dislocation-GB interactions. The effects of carbon atoms on the HE in the ferrous alloys can be then examined and analysed accordingly.

References

1. Johnson WH, Thomson W. II. On some remarkable changes produced in iron and steel by the action of hydrogen and acids. Proc R Soc London. 1875;23(156-163): 168-79.

2. Holzworth ML. Hydrogen Embrittlement of Type 304L Stainless Steel. Corrosion. 1969; 25:107-15.

3. Neeraj T, Srinivasan R, Li J. Hydrogen embrittlement of ferritic steels: Observations on deformation microstructure, nanoscale dimples and failure by nanovoiding. Acta Mater. 2012; 60:5160-71.

4. Gangloff RP, Wei RP. Gaseous hydrogen embrittlement of high strength steels. Metall Trans A. 1977;8:1043-53.

5. Gest RJ, Troiano AR. Stress Corrosion and Hydrogen Embrittlement in an Aluminum Alloy. Corrosion.1974;30:274-9.

6. Kamoutsi H, Haidemenopoulos GN, Bontozoglou V, Pantelakis S. Corrosion-induced hydrogen embrittlement in aluminum alloy 2024. Corros Sci. 2006;48:1209-24.

7. Song RG, Dietzel W, Zhang BJ, Liu WJ, Tseng MK, Atrens A. Stress corrosion cracking and hydrogen embrittlement of an Al–Zn–Mg–Cu alloy. Acta Mater. 2004;52:4727-43.

8. Shih DS, Robertson IM, Birnbaum HK. Hydrogen embrittlement of α titanium: In situ tem studies. Acta Metall. 1988;36:111-24.

9. Nelson HG, Williams DP, Stein JE. Environmental hydrogen embrittlement of an α-β titanium alloy: Effect of microstructure. Metall Mater Trans B. 1972;3:473-9.

10. Alvarez AM, Robertson IM, Birnbaum HK. Hydrogen embrittlement of a metastable β-titanium alloy. Acta Mater. 2004;52:4161-75.

11. Kholtobina AS, Pippan R, Romaner L, Scheiber D, Ecker W, Razumovskiy VI. Hydrogen Trapping in bcc Iron. Materials (Basel). 2020;13:2288.

12. Venezuela J, Liu Q, Zhang M, Zhou Q, Atrens A. A review of hydrogen embrittlement of martensitic advanced high-strength steels. Corros Rev. 2016;34:153-86.

13. Hydrogen Strategy Group, Hydrogen for Australia's Future, COAG Energy Council, (Australian Government, 2018).

14. Zhou, X-Y., Yang, X-S., Zhu, J-H. et al. Atomistic simulation study of the grain-size effect on hydrogen embrittlement of nanograined Fe. Int J Hydrogen Energy. 45, 3294-306 (2020).
15. Troiano AR. The role of hydrogen and other interstitials in the mechanical behavior of metals. Trans ASM 1960;52:54-80.
16. Oriani RA. A mechanistic theory of hydrogen embrittlement of steels. Berichte Bunsenges Phys Chem 1972;76:848-57.
17. Bechtle S, Kumar M, Somerday BP, Launey ME, Ritchie RO. Grain-boundary engineering markedly reduces susceptibility to intergranular hydrogen embrittlement in metallic materials. Acta Mater. 2009;57:4148-57.
18. Martin ML, Dadfarnia M, Nagao A, Wang S, Sofronis P. Enumeration of the hydrogen-enhanced localized plasticity mechanism for hydrogen embrittlement in structural materials. Acta Mater. 2019;165:734-50.
19. Wang S, Martin ML, Sofronis P, Ohnuki S, Hashimoto N, Robertson IM. Hydrogen-induced intergranular failure of iron. Acta Mater. 2014;69:275-82.
20. Robertson IM, Sofronis P, Nagao A, Martin ML, Wang S, Gross DW, et al. Hydrogen Embrittlement Understood. Metall Mater Trans A 2015;46:2323-41.
21. Spearot DE, Tschopp MA, Jacob KI, McDowell DL. Tensile strength of <100> and <110> tilt bicrystal copper interfaces. Acta Mater. 2007;55:705-714.
22. Spearot DE, Jacob KI, McDowell DL. Nucleation of dislocations from [0 0 1] bicrystal interfaces in aluminum. Acta Mater. 2005;53:3579-3589.
23. Cahn JW, Mishin Y, Suzuki A. Duality of dislocation content of grain boundaries. Philos Mag. 2006;86:3965-3980.
24. Tehranchi A, Curtin WA. Atomistic study of hydrogen embrittlement of grain boundaries in nickel: II Decohesion. Modell Simul Mater Sci Eng. 2017;25:075013.
25. Wang S, Martin ML, Robertson IM, Sofronis P. Effect of hydrogen environment on the separation of Fe grain boundaries. Acta Mater. 2016;107:279-288.
26. Song J, Soare M, Curtin W. Testing continuum concepts for hydrogen embrittlement in metals using atomistics. Modell Simul Mater Sci Eng. 2010;18(4):045003.
27. Song J, Curtin WA. Atomic mechanism and prediction of hydrogen embrittlement in iron. Nat Mater 2013;12:145–51.
28. Song J, Curtin WA. A nanoscale mechanism of hydrogen embrittlement in metals. Acta Mater. 2011;59(4):1557–69.

29. Tehranchi A, Curtin WA. Atomistic study of hydrogen embrittlement of grain boundaries in nickel: I. Fracture. J Mech Phys Solids. 2017;101:150–65.
30. Takai K, Shoda H, Suzuki H, Nagumo M. Lattice defects dominating hydrogen-related failure of metals. Acta Mater. 2008;56:5158-5167.
31. Doshida T, Nakamura M, Saito H, Sawada T, Takai K. Hydrogen-enhanced lattice defect formation and hydrogen embrittlement of cyclically prestressed tempered martensitic steel. Acta Mater. 2013;61:7755-7766.
32. Lu G, Kaxiras E. Hydrogen embrittlement of aluminum: the crucial role of vacancies. Phys Rev Lett. 2005;94:155501.
33. Momida H, Asari Y, Nakamura Y, Tateyama Y, Ohno T. Hydrogen-enhanced vacancy embrittlement of grain boundaries in iron. Phys Rev B. 2013;88:144107.
34. Ashby MF, Spaepen F, Williams S. Structure of grain-boundaries described as a packing of polyhedra. Acta Metall. 1978;26:1647–1663.
35. Xie D, Li S, Li M, Wang Z, Gumbsch P, Sun J, et al. Hydrogenated vacancies lock dislocations in aluminium. Nat Commun. 2016;7:13341.
36. Song J, Curtin WA. Mechanisms of hydrogen-enhanced localized plasticity: An atomistic study using α-Fe as a model system. Acta Mater. 2014;68:61-9.
37. Shen Z, Wagoner RH, Clark WAT. Dislocation and grain boundary interactions in metals. Acta Metall. 1988;36:3231-42.
38. Djukic MB, Bakic GM, Sijacki Zeravcic V, Sedmak A, Rajicic B. The synergistic action and interplay of hydrogen embrittlement mechanisms in steels and iron: Localized plasticity and decohesion. Eng Fract Mech. 2019:106528.
39. Lynch SP. Hydrogen embrittlement (HE) phenomena and mechanisms. In Stress Corrosion Cracking; 2011. p. 90–130.
40. Popov BN, Lee J-W, Djukic MB. Hydrogen permeation and hydrogen induced cracking. In: Kutz M, editor. Handbook of environmental degradation of materials 3rd ed. William Andrew, Elsevier; 2018. p. 133–62.
41. Lynch SP. Hydrogen embrittlement phenomena and mechanisms. Corros Rev. 2012;30(3–4):105–23.
42. Dadfarnia M, Novak P, Ahn DC, Liu JB, Sofronis P, Johnson DD, et al. Recent advances in the study of structural materials compatibility with hydrogen. Adv Mater. 2010;22(10):1128–35.
43. Robertson IM, Sofronis P, Nagao A, Martin ML, Wang S, Gross DW, et al.

Hydrogen embrittlement understood. Metall Mater Trans B. 2015;46:1085–103.
44. Dadfarnia M, Nagao A, Wang S, Martin ML, Somerday BP, Sofronis P. Recent advances on hydrogen embrittlement of structural materials. Int J Fracture. 2015;196(1–2):223–43.
45. Gerberich WW, Stauffer DD, Sofronis P. A coexistent view of hydrogen effects on mechanical behavior of crystals: HELP and HEDE effects of hydrogen on materials. In: Somerday B, Sofronis P, Jones R, editors. Effects of hydrogen on materials: proceedings of the 2008 international hydrogen conference; 2008 Sep 7-10; Jackons Lake Lodge, Grand Teton National Park, Wyoming, USA. Ohio: ASM International; 2009. p. 38–45.
46. Martin ML, Fenske JA, Liu GS, Sofronis P, Robertson IM. On the formation and nature of quasi-cleavage fracture surfaces in hydrogen embrittled steels. Acta Mater. 2011; 59(4): 1601-6.
47. Martin ML, Robertson IM, Sofronis P. Interpreting hydrogen-induced fracture surfaces in terms of deformation processes: a new approach. Acta Mater. 2011;59(9):3680–7.
48. Deng Y, Barnoush A. Hydrogen embrittlement revealed via novel in situ fracture experiments using notched micro-cantilever specimens. Acta Mater. 2018;142:236–47.
49. Bak SH, Abro MA, Lee DB. Effect of hydrogen and strain-induced martensite on mechanical properties of AISI304 stainless steel. Metals. 2016;6(7):169.
50. Hajilou T, Hope MSB, Zavieh AH, Kheradmand N, Johnsen R, Barnoush A. In situ small-scale hydrogen embrittlement testing made easy: An electrolyte for preserving surface integrity at nano-scale during hydrogen charging. Int J Hydrogen Energy. 2018;43(27):12516–29.
51. Tapia-Bastidas CV, Atrens A, Gray EM. Thermal desorption spectrometer for measuring ppm concentrations of trapped hydrogen. Int J Hydrogen Energy 2018;43(15):7600–17.
52. Escobar DP, Verbeken K, Duprez L, Verhaege M. Evaluation of hydrogen trapping in high strength steels by thermal desorption spectroscopy. Mater Sci Eng A. 2012;551:50–8.
53. Chen Y-S, Lu H, Liang J, Rosenthal A, Liu H, Sneddon G, et al. Observation of hydrogen trapping at dislocations, grain boundaries, and precipitates. Science. 2020;367:171-5.
54. Chen Y-S, Haley D, Gerstl SSA, London AJ, Sweeney F, Wepf RA, et al. Direct

observation of individual hydrogen atoms at trapping sites in a ferritic steel. Science. 2017;355:1196-9.
55. Alvaro A, Thue Jensen I, Kheradmand N, Løvvik OM, Olden V. Hydrogen embrittlement in nickel, visited by first principles modeling, cohesive zone simulation and nanomechanical testing. Int J Hydrogen Energy. 2015;40(47):16892–900.
56., Carter EA. First principles assessment of ideal fracture energies of materials with mobile impurities: implications for hydrogen embrittlement of metals. Acta Mater. 2004;52(16):4801–7.
57. Jiang DE, Carter EA. Diffusion of interstitial hydrogen into and through BCC Fe from first principles. Phys Rev B 2004;70(064):102.
58. Hickel T, Nazarov R, McEniry E, Leyson G, Grabowski B, Neugebauer J. Ab initio based understanding of the segregation and diffusion mechanisms of hydrogen in steels. JOM 2014;66(8):1399–405.
59. Counts W, Wolverton C, Gibala R. First-principles energetics of hydrogen traps in α-Fe: point defects. Acta Mater 2010;58(14):4730–41.
60. Novak P, Yuan R, Somerday BP, Sofronis P, Ritchie RO. A statistical, physical-based, micro-mechanical model of hydrogen-induced intergranular fracture in steel. J Mech Phys Solids 2010;58(2):206–26.
61. Yu H, Olsen JS, Olden V, Alvaro A, He J, Zhang Z. Cohesive zone simulation of grain size and misorientation effects on hydrogen embrittlement in nickel. Eng Fail Anal. 2017;81:79–93.
62. Yu H, Olsen JS, Alvaro A, Olden V, He J, Zhang Z. A uniform hydrogen degradation law for high strength steels. Eng Fract Mech 2016;157:56–71.
63. Olden V, Thaulow C, Johnsen R, Østby E, Berstad T. Application of hydrogen influenced cohesive laws in the prediction of hydrogen induced stress cracking in 25%Cr duplex stainless steel. Eng Fract Mech 2008;75(8):2333–51.
64. Wua W, Wang Y, Tao P, Li X, Gong J. Cohesive zone modeling of hydrogen-induced delayed intergranular fracture in high strength steels. Results Phys 2018;11:591–8.
65. Jemblie L, Olden V, Akselsen OM. A review of cohesive zone modelling as an approach for numerically assessing hydrogen embrittlement of steel structures. Phil Trans R Soc A. 2017;375(2098):20160411.
66. Matsumoto R, Seki S, Taketomi S, Miyazaki N. Hydrogen-related phenomena due to decreases in lattice defect energies-Molecular dynamics simulations using the

embedded atom method potential with pseudo-hydrogen effects. Comp Mater Sci. 2014;92:362–71.
67. Solanki KN, Tschopp MA, Bhatia MA, Rhodes NR. Atomistic investigation of the role of grain boundary structure on hydrogen segregation and embrittlement in α-Fe. Metall Mater Trans A. 2013;44(3):1365–75.
68. Solanki KN, Ward DK, Bammann DJ. A nanoscale study of dislocation nucleation at the crack tip in the nickel-hydrogen system. Metall Mater Trans A. 2011;42(2):340–7.
69. Ramasubramaniam A, Itakura M, Ortiz M, Carter EA. Effect of atomic scale plasticity on hydrogen diffusion in iron: quantum mechanically informed and on-the-fly kinetic Monte Carlo simulations. J Mater Res. 2008;23(10):2757–73.
70. Jothi S, Croft TN, Wright L, Turnbull A, Brown SGR. Multi-phase modelling of intergranular hydrogen segregation/trapping for hydrogen embrittlement. Int J Hydrogen Energy. 2015;40(42):15105–23.
71. Jothi S, Winzer N, Croft TN, Brown SGR. Meso-microstructural computational simulation of the hydrogen permeation test to calculate intergranular, grain boundary and effective diffusivities. J. Alloys Compd. 2015;645:S247–51.
72. Kumar BS, Kaina V, Singhd M, Vishwanadh B. Influence of hydrogen on mechanical properties and fracture of tempered 13wt% Cr martensitic stainless steel. Mater Sci Eng A. 2017;700:140–51.
73. Fan YH, Zhang B, Yi HL, Hao GS, Sun YY, Wang JQ, et al. The role of reversed austenite in hydrogen embrittlement fracture of S41500 martensitic stainless steel. Acta Mater. 2017;139:188–95.
74. Hu Y, Dong C, Luo H, Xiao K, Zhong P, Li X. Study on the hydrogen embrittlement of Aermet100 using hydrogen permeation and SSRT techniques. Metall Mater Trans A. 2017;48:4046–57.
75. Gerberich WW. Modelling hydrogen induced damage mechanisms in metals. In: Gangloff R, Somerday B, editors. Gaseous hydrogen embrittlement of materials in energy technologies: mechanisms, modelling and future developments. Cambridge, UK: Elsevier Inc.; 2012. p. 209–46.
76. Gerberich WW, Oriani RA, Lii M, Chen X, Foecke T. The necessity of both plasticity and brittleness in the fracture thresholds of iron. Phil Mag A. 1991;63(2):363–76.

77. Serebrinsky A, Carter EA, Ortiz M. A quantum-mechanically informed continuum model of hydrogen embrittlement. J Mech Phys Solids. 2004;52(10):2403–30.
78. Dadfarnia M, Sofronis P, Somerday BP, Balch DK, Schembri P. Degradation models for hydrogen embrittlement. In: Gangloff R, Somerday B, editors. Gaseous hydrogen embrittlement of materials in energy technologies: mechanisms, modelling and future developments. Cambridge, UK: Elsevier Inc.; 2012. p. 326–77.
79. Dadfarnia M, Nagao A, Somerday BP, Schembri PE, Foulk III JW, Nibur KA, et al. Modeling hydrogen-induced fracture and crack propagation in high strength steels. In: Somerday BP, Sofronis P, editors. Materials performance in hydrogen environments, proceedings of the 2016 international hydrogen conference, Jackson Lake Lodge, Moran, WY, USA. Ohio: ASM International, Warrendale, PA; 2017, p 572–80.
80. Harris ZD, Dolph JD, Pioszak GL, Rincon Troconis BC, Scully JR, Burns JT. The effect of microstructural variation on the hydrogen environment-assisted cracking of Monel K-500. Metall Mater Trans A. 2016;47(7):3488–510.
81. Bal B, Sahin I, Uzun A, Canadinc D. A new venue toward predicting the role of hydrogen embrittlement on metallic materials. Metall Mater Trans A. 2016;47(11):5409–22.
82. Ahn DC, Sofronis P, Dodds Jr. RH. On hydrogen-induced plastic flow localization during void growth and coalescence. Int J Hydrogen Energy. 2007;32(16):3734–42.
83. Marchi CS, Somerday BP. Technical reference on hydrogen compatibility of materials. Tech Rep. SAND2012–7321.
84. Djukic MB, Sijacki Zeravcic V, Bakic GM, Sedmak A, Rajicic B. Hydrogen damage of steels: A case study and hydrogen embrittlement model. Eng Failure Anal. 2015;58:485-98.
85. Takakuwa O, Mano Y, Soyama H. Increase in the local yield stress near surface of austenitic stainless steel due to invasion by hydrogen. Int J Hydrogen Energy. 2014;39(11):6095–103.
86. Siddiqui RA, Abdullah HA. Hydrogen embrittlement in 0.31% carbon steel used for petrochemical applications. J Mater Process Technol. 2005;170:430-5.
87. Gangloff RP. Hydrogen assisted cracking of high strength alloys. Technical report, DTIC Document, 2003;31-101.
88. Nanninga NE, Levy YS, Drexler ES, Condon RT, Stevenson AE, Slifka AJ. Comparison of hydrogen embrittlement in three pipeline steels in high pressure gaseous

hydrogen environments. Corros Sci. 2012;59:1–9.
89. Lawrence SK, Yagodzinskyy Y, Hänninen H, Korhonen E, Tuomisto F, Harris ZD, et al. Effects of grain size and deformation temperature on hydrogen-enhanced vacancy formation in Ni alloys. Acta Mater. 2017;128:218-26.
90. Rehrl J, Mraczek K, Pichler A, Werner E. Mechanical properties and fracture behavior of hydrogen charged AHSS/UHSS grades at high- and low strain rate tests. Mater Sci Eng A. 2014;590:360–7.
91. Djukic MB, Bakic GM, Sijacki Zeravcic V, Rajicic B, Sedmak A, Mitrovic R, et al. Towards a unified and practical industrial model for prediction of hydrogen embrittlement and damage in steels. Proc Struct Integr. 2016;2:604–11.
92. Stenerud G, Johnsen R, Olsen JS, He J, Barnoush A. Effect of hydrogen on dislocation nucleation in alloy 718. Int J Hydrogen Energy. 2017;42(24):15933–42.
93. Kim YS, Kim DW, Kim SS, Nam WJ, Choe H. Effects of hydrogen diffusion on the mechanical properties of austenite 316L steel at ambient temperature. Mater Trans. 2011;52:507–13.
94. Murakami Y, Kanezaki T, Mine Y. Hydrogen effect against hydrogen embrittlement. Metall Mater Trans A 2010;41(10):2548–62.
95. Matsui H, Kimura H, Moriya S. The effect of hydrogen on the mechanical properties of high purity iron I. Softening and hardening of high purity iron by hydrogen charging during tensile deformation. Mater Sci Eng 1979;40(2):207–16.
96. Zhao Y, Seok M-Y, Choi I-C, Lee Y-H, Park S-J, Ramamurty U, et al. The role of hydrogen in hardening/softening steel: Influence of the charging process. Scr Mater 2015;107:46–9.
97. Robertson IM, Birnbaum HK. An HVEM study of hydrogen effects on the deformation and fracture of nickel. Acta Metall. 1986;34:353-66.
98. Ferreira PJ, Robertson IM, Birnbaum HK. Hydrogen effects on the interaction between dislocations. Acta Mater. 1998;46:1749-57.
99. Tabata T, Birnbaum HK. Direct observations of the effect of hydrogen on the behavior of dislocations in iron. Scripta Metallurgica. 1983;17:947-50.
100. Bond GM, Robertson IM, Birnbaum HK. The influence of hydrogen on deformation and fracture processes in high-strength aluminum alloys. Acta Metall. 1987;35(9):2289-2296.
101. Birnbaum HK, Sofronis P. Hydrogen-enhanced localized plasticity-a mechanism

for hydrogen-related fracture. Mater Sci Eng A. 1994;176(1-2):191-202.
102. Sofronis P, Robertson IM. Transmission electron microscopy observations and micromechanical/continuum models for the effect of hydrogen on the mechanical behaviour of metals. Philos Mag A. 2002;82(17-18):3405-3413.
103. Sofronis P. The influence of mobility of dissolved hydrogen on the elastic response of a metal. J Mech Phys Solid. 1995;43(9):1385-1407.
104. Barnoush A, Vehoff H. In situ electrochemical nanoindentation: A technique for local examination of hydrogen embrittlement. Corrosion Science. 2008;50(1):259–267.
105. Gaspard V, Kermouche G, Delafosse D, Barnoush A. Hydrogen effect on dislocation nucleation in a ferritic alloy fe–15cr as observed per nanoindentation. Mater Sci Eng A, 2014;604:86–91.
106. Lassila DH, Birnbaum HK. Intergranular fracture of nickel: the effect of hydrogen-sulfur co-segregation. Acta Metall. 1987;35(7):1815–1822.
107. Bond GM, Robertson IM, Birnbaum HK. On the mechanisms of hydrogen embrittlement of Ni3Al alloys. Acta Metall. 1989;37:1407-13.
108. Martin ML, Somerday BP, Ritchie RO, Sofronis P, Robertson IM. Hydrogen-induced intergranular failure in nickel revisited. Acta Mater. 2012;60:2739-45.
109. Martin ML. A New Approach to Discovering the Fundamental Mechanisms of Hydrogen Failure, PhD Dissertation, University of Illinois at UrbanaChampaign, 2012.
110. Keller C, Hug E, Feaugas X. Microstructural size effects on mechanical properties of high purity nickel. Int J Plast. 2011;27(4):635-654.
111. Gahr S, Grossbeck ML, Birnbaum HK. Hydrogen embrittlement of Nb I—Macroscopic behavior at low temperatures. Acta Metall. 1977;25:125-34.
112. Lynch SP. Environmentally assisted cracking: overview of evidence for an adsorption-induced localised-slip process. Acta Metall. 1988;20: 2639-2661.
113. Lynch SP. Metallographic contributions to understanding mechanisms of environmentally assisted cracking. Metallography. 1989;23:147-171.
114. Lynch SP. Comments on “ A unified model of environmentassisted cracking ” . Scripta Mater. 2009;61:331-334.
115. Kirchheim R. Reducing grain boundary, dislocation line and vacancy formation energies by solute segregation. I. Theoretical background. Acta Mater. 2007;55:5129-38.
116. Kirchheim R. Reducing grain boundary, dislocation line and vacancy formation

energies by solute segregation: II. Experimental evidence and consequences. Acta Mater. 2007;55:5139-48.
117. Pedersen A, Jónsson H. Simulations of hydrogen diffusion at grain boundaries in aluminum. Acta Mater. 2009;57:4036-45.
118. Zhou H-B, Liu Y-L, Jin S, Zhang Y, Luo GN, Lu G-H. Investigating behaviours of hydrogen in a tungsten grain boundary by first principles: from dissolution and diffusion to a trapping mechanism. Nucl Fusion. 2010;50:025016.
119. Du YA, Ismer L, Rogal J, Hickel T, Neugebauer J, Drautz R. First-principles study on the interaction of H interstitials with grain boundaries in α- and γ-Fe. Phys Rev B. 2011;84:144121.
120. Di Stefano D, Mrovec M, Elsässer C. First-principles investigation of hydrogen trapping and diffusion at grain boundaries in nickel. Acta Mater. 2015;98:306-12.
121. Zhou X, Marchand D, McDowell DL, Zhu T, Song J. Chemomechanical origin of hydrogen trapping at grain boundaries in fcc metals. Phys Rev Lett. 2016;116(7):075502.
122. Zhou X, Song J. Effect of local stress on hydrogen segregation at grain boundaries in metals. Mater Lett. 2017;196:123-7.
123. Huang S, Chen D, Song J, McDowell DL, Zhu T. Hydrogen embrittlement of grain boundaries in nickel: an atomistic study. npj Computational Materials. 2017;3:28.
124. Zhao Y, Lu G. QM/MM study of dislocation—hydrogen/helium interactions in α-Fe. Modell Simul Mater Sci Eng. 2011;19:065004.
125. Tehranchi A, Zhang X, Lu G, Curtin WA. Hydrogen–vacancy–dislocation interactions in α-Fe. Modell Simul Mater Sci Eng. 2016;25(2):025001.
126. Wen M, Li Z, Barnoush A. Atomistic study of hydrogen effect on dislocation nucleation at crack tip. Adv Eng Mater. 2013;15(11):1146–51.
127. Matsumoto R, Taketomi S, Matsumoto S, Miyazaki N. Atomistic simulations of hydrogen embrittlement. Int J Hydrogen Energy. 2009;34(23):9576–84.
128. Taketomi S, Matsumoto R, Hagihara S. Molecular Statics Simulation of the Effect of Hydrogen Concentration on {112} <111> Edge Dislocation Mobility in Alpha Iron. ISIJ Int. 2017;57:2058-64.
129. von Pezold J, Lymperakis L, Neugebeauer J. Hydrogen-enhanced local plasticity at dilute bulk H concentrations: the role of H-H interactions and the formation of local hydrides. Acta Mater. 2011;59(8):2969–80.

130. Zhou X, Ouyang B, Curtin WA, Song J. Atomistic investigation of the influence of hydrogen on dislocation nucleation during nanoindentation in Ni and Pd. Acta Mater. 2016;116:364-9.
131. Tehranchi A. Atomistic mechanisms of hydrogen embrittlement. Tech. rep. EPFL; 2017
132. Lu G, Orlikowski D, Park I, Politano O, Kaxiras E. Energetics of hydrogen impurities in aluminum and their effect on mechanical properties. Phys Rev B. 2002;65:064102.
133. Van der Ven A, Ceder G. The thermodynamics of decohesion. Acta Mater. 2004;52:1223-35.
134. Van der Ven A, Ceder G. Impurity-induced van der Waals transition during decohesion. Phys Rev B. 2003;67:060101.
135. Jiang DE, Carter EA. First principles assessment of ideal fracture energies of materials with mobile impurities: implications for hydrogen embrittlement of metals. Acta Mater. 2004;52:4801-7.
136. Yamaguchi M, Ebihara K-I, Itakura M, Kadoyoshi T, Suzudo T, Kaburaki H. First-Principles Study on the Grain Boundary Embrittlement of Metals by Solute Segregation: Part II. Metal (Fe, Al, Cu)-Hydrogen (H) Systems. Metall Mater Trans A. 2011;42:330-9.
137. Zhu YT, Wu XL. Ductility and plasticity of nanostructured metals: differences and issues. Mater Today Nano. 2018;2:15-20.
138. Kumar KS, Suresh S, Chisholm MF, Horton JA, Wang P. Deformation of electrodeposited nanocrystalline nickel. Acta Mater. 2003;51:387-405.
139. Rice JR. Dislocation nucleation from a crack tip: An analysis based on the Peierls concept. J Mech Phys Solids. 1992;40:239-271.
140. Gumbsch P, Beltz GE. On the continuum versus atomistic descriptions of dislocation nucleation and cleavage in nickel. Modelling Simul Mater Sci Eng. 1995;3:597–613.
141. Sun Y, Beltz GE. Dislocation nucleation from a crack tip: A formulation based on anisotropic elasticity. J Mech Phys Solids. 1994;42:1905-32.
142. Zimmerman JA, Gao HJ, Abraham FF. Generalized stacking fault energies for embedded atom FCC metals. Modelling Simul Mater Sci Eng. 2000;8:103–115.
143. Olden V, Alvaro A, Akselsen OM. Hydrogen diffusion and hydrogen influenced

critical stress intensity in an API X70 pipeline steel welded joint – Experiments and FE simulations. Int J Hydrogen Energy. 2012;37:11474-86.
144. Oriani RA. The diffusion and trapping of hydrogen in steel. Acta Metall. 1970;18:147-57.
145. Xing X, Yu M, Chen W, Zhang H. Atomistic simulation of hydrogen-assisted ductile-to-brittle transition in α-iron. Comput Mater Sci. 2017;127:211-221.
146. Xing X, Zhang H, Cui G, Liu J, Li Z. Hydrogen inhibited phase transition near crack tip – An atomistic mechanism of hydrogen embrittlement. Int J Hydrogen Energy. 2019;44:17146-17153.
147. Taketomi S, Matsumoto R, Miyazaki N. Atomistic study of the effect of hydrogen on dislocation emission from a mode II crack tip in alpha iron. Int J Mech Sci. 2010;52:334-8.
148. Jothi S, Croft TN, Brown SGR. Influence of grain boundary misorientation on hydrogen embrittlement in bi-crystal nickel. Int J Hydrogen Energy. 2014;39:20671-88.
149. Bechtle S, Kumar M, Somerday BP, Launey ME, Ritchie RO. Grain-boundary engineering markedly reduces susceptibility to intergranular hydrogen embrittlement in metallic materials. Acta Mater. 2009;57:4148-4157.
150. Barrows W, Dingreville R, Spearot D. Traction–separation relationships for hydrogen induced grain boundary embrittlement in nickel via molecular dynamics simulations. Mater Sci Eng A. 2016;650:354-364.
151. Barrows W. Traction-Separation Relationships for HydrogenInduced Grain Boundary Embritlement in Nickel via Molecular Dynamics Simulations: University of Arkansas; 2015.
152. O'Brien CJ, Foiles SM. Misoriented grain boundaries vicinal to the twin in Nickel part II: thermodynamics of hydrogen segregation. Philos Mag. 2016;96:1463-84.
153. Kuhr B, Farkas D, Robertson IM. Atomistic studies of hydrogen effects on grain boundary structure and deformation response in FCC Ni. Comput Mater Sci. 2016;122:92-101.
154. Djukic MB, Bakic GM, Sijacki Zeravcic V, Sedmak A, Rajicic B. The synergistic action and interplay of hydrogen embrittlement mechanisms in steels and iron: Localized plasticity and decohesion. Eng Fract Mech. 2019:106528.
155. Plimpton S. Fast parallel algorithms for short-range molecular dynamics. J Comput Phys. 1995;117:1-19.

156. Hu Z, Fukuyama S, Yokogawa K, Okamoto S. Hydrogen embrittlement of a single crystal of iron on a nanometre scale at a crack tip by molecular dynamics. Modell Simul Mater Sci Eng. 1999;7(4):541.
157. Xu X, Wen M, Hu Z, Fukuyama S, Yokogawa K. Atomistic process on hydrogen embrittlement of a single crystal of nickel by the embedded atom method. Comput Mater Sci. 2002;23(1):131–8.
158. Chandler MQ, Horstemeyer M, Baskes M, Gullett P, Wagner G, Jelinek B. Hydrogen effects on nanovoid nucleation in face-centered cubic single-crystals. Acta Mater. 2008;56(1):95–104.
159. Li J, Lu C, Pei L, Zhang C, Wang R, Tieu K. Atomistic simulations of hydrogen effects on tensile deformation behaviour of [0 0 1] twist grain boundaries in nickel. Comput. Mater. Sci. 2019;159:12-23.
160. Angelo JE, Moody NR, Baskes MI. Trapping of hydrogen to lattice defects in nickel. Modell Simul Mater Sci Eng. 1995;3(3):289.
161. Baskes M, Sha X, Angelo J, Moody N. Trapping of hydrogen to lattice defects in nickel. Model Simul Mater Sci Eng. 1997;5(6):651.
162. Ramasubramaniam A, Itakura M, Carter EA. Interatomic potentials for hydrogen in α–iron based on density functional theory. Phys Rev B. 2009;79(17):174101.
163. Ackland GJ, Mendelev MI, Srolovitz DJ, Han S, Barashev AV. Development of an interatomic potential for phosphorus impurities in α-iron. J Phys: Condens Matter. 2004;16:S2629-S42.
164. Li J. AtomEye: an efficient atomistic configuration viewer. Modelling and Simulation in Materials Science and Engineering. 2003;11:173-177.
165. Stukowski A. Visualization and analysis of atomistic simulation data with OVITO–the Open Visualization Tool. Model Simul Mater Sci Eng. 2010;18:015012.
166. Begau C, Hartmaier A, George EP, Pharr GM. Atomistic processes of dislocation generation and plastic deformation during nanoindentation. Acta Mater. 2011;59:934-942.
167. Cheung KS, Yip S. Atomic-level stress in an inhomogeneous system. Appl Phys. 1991;70: 5688–5690.
168. Kelchner CL, Plimpton SJ, Hamilton JC, Dislocation nucleation and defect structure during surface indentation. Phys Rev B. 1998;58:11085-11088.
169. Schiøtz J, Di Tolla FD, Jacobsen KW. Softening of nanocrystalline metals at very

small grain sizes. Nature. 1998;391:561–563.
170. Stukowski A, Bulatov VV, Arsenlis A. Automated identification and indexing of dislocations in crystal interfaces. Modell Simul Mater Sci Eng. 2012;20:085007.
171. Frank FC. LXXXIII. Crystal dislocations.—Elementary concepts and definitions. The London, Edinburgh, and Dublin Philosophical Magazine and Journal of Science. 1951;42:809-19.
172. Rycroft Chris H. VORO++: A three-dimensional Voronoi cell library in C++. Chaos. 2009;19: 041111.
173. Oudriss A, Creus J, Bouhattate J, Conforto E, Berziou C, Savall C, et al. Grain size and grain-boundary effects on diffusion and trapping of hydrogen in pure nickel. Acta Mater. 2012;60:6814-28.
174. Spearot DE. Evolution of the E structural unit during uniaxial and constrained tensile deformation. Mech Res Comm. 2008;35:81-8.
175. Fleischer RL. Cross slip of extended dislocations, Acta Metall.1959;7:134-135.
176. Abraham DP, Altstetter CJ. Hydrogen-enhanced localization of plasticity in an austenitic stainless steel. Metall Mater Trans A. 1995;26:2859-2871.
177. Tschopp MA, McDowell DL. Dislocation nucleation in Σ3 asymmetric tilt grain boundaries. Int J Plast. 2008;24:191-217.
178. Sutton AP, Vitek V. On the structure of tilt grain boundaries in cubic metals I. Symmetrical tilt boundaries. Philos T Roy Soc A. 1983;309:1–36.
179. Cahn JW, Mishin Y, Suzuki A. Coupling grain boundary motion to shear deformation. Acta Mater. 2006;54:4953-4975.
180. Frank FC. in: Symposium on the Plastic Deformation of Crystalline Solids (Office of Naval Research, Pittsburgh, 1950), p. 150.
181. Bilby BA. Continuous distributions of dislocations. Prog Solid Mech. 1960;1:329–398.
182. Homer ER, Foiles SM, Holm EA, Olmsted DL. Phenomenology of shear-coupled grain boundary motion in symmetric tilt and general grain boundaries. Acta Mater. 2013;61:1048-1060.
183. Niu L-L, Zhang Y, Shu X, Gao F, Jin S, Zhou H-B, et al. Shear-coupled grain boundary migration assisted by unusual atomic shuffling. Sci Rep. 2016;6:23602.
184. Lu G, Kaxiras E. Hydrogen embrittlement of aluminum: the crucial role of vacancies. Phys Rev Lett. 2005;94:155501.

185. Namilae S, Chandra N, Nieh TG. Atomistic simulation of grain boundary sliding in pure and magnesium doped aluminum bicrystals. Scripta Mater. 2002;46:49-54.
186. Elsener A, Politano O, Derlet PM, Van Swygenhoven H. Variable-charge method applied to study coupled grain boundary migration in the presence of oxygen. Acta Mater. 2009;57:1988-2001.
187. Niu L-L, Peng Q, Gao F, Chen Z, Zhang Y, Lu G-H. Effects of interstitial defects on stress-driven grain boundary migration in bcc tungsten, J. Nucl. Mater. 512 (2018) 246-251.
188. Doshida T, Suzuki H, Takai K, Oshima N, Hirade T. Enhanced lattice defect formation associated with hydrogen and hydrogen embrittlement under elastic stress of a tempered martensitic steel. ISIJ Int. 2012;52:198-207.
189. Fukai Y. Superabundant vacancies formed in metalhydrogen alloys. Phys Scripta. 2003;T103:11.
190. Zhu Y, Li Z, Huang M. Solute hydrogen effects on plastic deformation mechanisms of a-Fe with twist grain boundary. Int J Hydrogen Energy. 2018;43:10481-95.
191. Li S, Li Y, Lo Y-C, Neeraj T, Srinivasan R, Ding X, Sun J, Qi L, Gumbsch P, Li J. The interaction of dislocations and hydrogen-vacancy complexes and its importance for deformation-induced proto nano-voids formation in a-Fe. Int J Plast. 2015;74:175-91.
192. Zhu Y, Li Z, Huang M, Fan H. Study on interactions of an edge dislocation with vacancy-H complex by atomistic modelling. Int J Plast. 2017;92:31-44.
193. Hirth JP, Lothe J. Theory of dislocations. 2nd ed. New York: Wiley; 1992.
194. Jin ZH, Gumbsch P, Ma E, Albe K, Lu K, Hahn H, Gleiter H. The interaction mechanism of screw dislocations with coherent twin boundaries in different face-centred cubic metals. Scripta Mater. 2006;54:1163-8.
195. Jin ZH, Gumbsch P, Albe K, Ma E, Lu K, Gleiter H, Hahn H. Interactions between non-screw lattice dislocations and coherent twin boundaries in face-centered cubic metals. Acta Mater. 2008;56:1126-35.
196. Li J, Lu C, Pei L, Zhang C, Wang R, Tieu K. Effects of H segregation on shear-coupled motion of <1 1 0> grain boundaries in α-Fe. Int J Hydrogen Energy. 2019;44(33):18616-27.
197. Seita M, Hanson JP, Gradečak S, Demkowicz MJ. The dual role of coherent twin boundaries in hydrogen embrittlement. Nat. Commun. 2015;6:6164.
198. Watanabe T. The impact of grain boundary character distribution on fracture in

polycrystals. Mater Sci Eng A. 1994;176:39-49.
199. Palumbo G, Aust KT. Solute effects in grain boundary engineering. Can Metall Q. 1995;34:165-73.
200. Bollmann W. Crystal defects and crystalline interfaces. New York: Springer-Verlag; 1970.
201. O'Brien CJ, Medlin DL, Foiles SM. Misoriented grain boundaries vicinal to the twin in nickel Part I: thermodynamics & temperature-dependent structure. Philos Mag 2016;96(13):1285-304.
202. Lee JH, Holland TB, Mukherjee AK, Zhang XH, Wang HY. Direct observation of Lomer-Cottrell Locks during strain hardening in nanocrystalline nickel by in situ TEM. Sci Rep. 2013;3:1061.
203. Lassila DH, Birnbaum HK. The effect of diffusive hydrogen segregation on fracture of polycrystalline nickel. Acta Metall. 1986;34:1237-1243.
204. Bachurin DV, Weygand D, Gumbsch P. Dislocation-grain boundary interaction in <111> textured thin metal films. Acta Mater. 2010;58:5232-41.
205. De Koning M, Miller R, Bulatov VV, Abraham FF. Modelling grain-boundary resistance in intergranular dislocation slip transmission. Philos Mag A: Physics of Condensed Matter, Structure, Defects and Mechanical Properties. 2002;82:2511-27.
206. De Koning M, Kurtz RJ, Bulatov VV, Henager CH, Hoagland RG, Cai W, Nomura M. Modeling of dislocation-grain boundary interactions in FCC metals. J Nucl Mater 2003;323:281-9.
207. Yu W, Wang Z. Interactions between edge lattice dislocations and S11 symmetrical tilt grain boundaries in copper: a quasi-continuum method study. Acta Mater. 2012;60:5010-21.
208. Cheng Y, Mrovec M, Gumbsch P. Atomistic simulations of interactions between the 1/2-111- edge dislocation and symmetric tilt grain boundaries in tungsten. Philos Mag. 2008;88(4):547-60.
209. Li J, Lu C, Pei L, Zhang C, Wang R, Tieu K. Influence of hydrogen environment on dislocation nucleation and fracture response of <1 1 0> grain boundaries in nickel. Comput Mater Sci. 2019;165:40-50.
210. Robertson IM. The effect of hydrogen on dislocation dynamics. Eng Fract Mech. 2001;68:671-92.
211. Birnbaum HK, Sofronis P. Hydrogen-enhanced localized plasticity-a mechanism

for hydrogen-related fracture. Mater. Sci. Eng. A., Struct. Mater., Prop. Microstruct. Process.1993;A176:191-202.
212. Chateau JP, Delafosse D, Magnin T. Numerical simulations of hydrogen-dislocation interactions in fcc stainless steels: part I: hydrogen-dislocation interactions in bulk crystals. Acta Mater. 2002;50:1507-22.
213. Ferreira PJ, Robertson IM, Birnbaum HK. Hydrogen effects on the character of dislocations in high-purity aluminum. Acta Mater. 1999;47:2991-8.
214. Sangid MD, Ezaz T, Sehitoglu H, Robertson IM. Energy of slip transmission and nucleation at grain boundaries. Acta Mater. 2011;59(1):283-96.
215. Sirk TW, Moore S, Brown EF. Characteristics of thermal conductivity in classical water models. J Chem Phys. 2013;138(6):064505.
216. Li J, Lu C, Pei L, Zhang C, Tieu K. Influence of solute hydrogen on the interaction of screw dislocations with vicinal twin boundaries in nickel. Scripta Mater. 2019;173:115-9.
217. Cherepanov GP, Balankin AS, Ivanova VS. Fractal fracture mechanics: a review. Eng Fract Mech.1995;51(6):997–1033.
218. Metropolis N, Rosenbluth AW, Rosenbluth MN, Teller AH, Teller E. Equation of state calculations by fast computing machines. J Chem Phys. 1953;21:1087-1092.
219. Hoover WG. Canonical dynamics: Equilibrium phase-space distributions. Phys Rev A. 1985;31:1695-1697.
220. Nosé S. A unified formulation of the constant temperature molecular dynamics methods. The Journal of Chemical Physics. 1984;81:511-519.
221. Wu Z, Curtin WA. Brittle and ductile crack-tip behavior in magnesium. Acta Mater. 2015;88:1-12.
222. Yu M, Chen W, Kania R, Van Boven G, Been J. Crack propagation of pipeline steel exposed to a near-neutral pH environment under variable pressure fluctuations. Int J Fatigue. 2016;82:658-66.
223. Yu M, Chen W, Kania R, Van Boven G, Been J. Underload-induced crack growth behaviour of minor cycles of pipeline steel in near-neutral pH environment. Fatigue Fract Eng M. 2015;38:681-92.
224. Murakami Y, Kanezaki T, Mine Y, Matsuoka S. Hydrogen embrittlement mechanism in fatigue of austenitic stainless steels. Metall Mater Trans A. 2008;39(6):1327-1339.

225. Golovin YI. Nanoindentation and mechanical properties of solids in submicrovolumes, thin near-surface layers, and films: A Review. Physics of the Solid State. 2008;50:2205-36.
226. Katz Y, Tymiak N, Gerberich WW. Nanomechanical probes as new approaches to hydrogen/deformation interaction studies. Eng Fract Mech. 2001;68:619-46.
227. Glowacka A, Wozniak MJ, Swiatnicki WA. Nanoindentation measurements of austeno-ferritic stainless steel submitted to hydrogen charging. Reviews on Advanced Materials Science. 2004;8:66-8.
228. Gao X. Displacement burst and hydrogen effect during loading and holding in nanoindentation of an iron single crystal. Scripta Mater. 2005;53:1315-20.
229. Bahr DF, Nibur KA, Morasch KR, Field DP. Hydrogen and deformation: Nano- and microindentation studies. JOM. 2003;55:47-50.
230. Nibur KA, Bahr DF, Somerday BP. Hydrogen effects on dislocation activity in austenitic stainless steel. Acta Mater. 2006;54:2677-84.
231. Durst K, Backes B, Franke O, Göken M. Indentation size effect in metallic materials: Modeling strength from pop-in to macroscopic hardness using geometrically necessary dislocations. Acta Mater. 2006;54:2547-55.
232. Barnoush A, Yang B, Vehoff H. Effect of hydrogen and grain boundaries on dislocation nucleation and multiplication examined with a NI-AFM. Advances in Solid State Physics2008. p. 253-69.
233. Barnoush A, Vehoff H. Recent developments in the study of hydrogen embrittlement: Hydrogen effect on dislocation nucleation. Acta Mater. 2010;58:5274-85.
234. Wen M, Zhang L, An B, Fukuyama S, Yokogawa K. Hydrogen-enhanced dislocation activity and vacancy formation during nanoindentation of nickel. Phys Rev B. 2009;80(9):094113.
235. Tehranchi A, Curtin WA. The role of atomistic simulations in probing hydrogen effects on plasticity and embrittlement in metals. Eng Fract Mech. 2019;216:106502.
236. Sakaki K, Kawase T, Hirato M, Mizuno M, Araki H, Shirai Y, Nagumo M. The effect of hydrogen on vacancy generation in iron by plastic deformation. Scr Mater. 2006;55:1031-1034.
237. Takai K, Shoda H, Suzuki H, Nagumo M. Lattice defects dominating hydrogen-related failure of metals. Acta Mater. 2008;56:5158-5167.

238. Doshida T, Nakamura M, Saito H, Sawada T, Takai K. Hydrogen-enhanced lattice defect formation and hydrogen embrittlement of cyclically prestressed tempered martensitic steel. Acta Mater. 2013;61:7755-7766.
239. Hatano M, Fujinami M, Arai K, Fujii H, Nagumo M. Hydrogen embrittlement of austenitic stainless steels revealed by deformation microstructures and strain-induced creation of vacancies. Acta Mater. 2014;67:342-353.
240. Marchi CS, Somerday BP, Nibur KA, Stalheim DG, Boggess T, Jansto S. Fracture and fatigue of commercial grade API pipeline steels in gaseous hydrogen. In: Proceedings of the ASME Pressure Vessels and Piping Conference, Bellevue, WA, 2010, pp. 939-948.
241. Tateyama Y, Ohno T. Stability and clusterization of hydrogen-vacancy complexes in alpha-Fe: an ab initio study. Phys Rev B. 2003;67:174105.
242. Tanguy D, Wang Y, Connétable D. Stability of vacancy-hydrogen clusters in nickel from first-principles calculations. Acta Mater. 2014;78:135-43.
243. Chen Y-S, Lu H, Liang J, Rosenthal A, Liu H, Sneddon G, et al. Observation of hydrogen trapping at dislocations, grain boundaries, and precipitates. Science. 2020;367:171-5.
244. Wan L, Geng WT, Ishii A, Du J-P, Mei Q, Ishikawa N, et al. Hydrogen embrittlement controlled by reaction of dislocation with grain boundary in alpha-iron. Int J Plast. 2019;112:206-19.
245. Zhang D, Shintaku Y, Suzuki S, Komizo Y-I. In situ observation of phase transformation in low-carbon, boron-treated steels. Metall Mater Trans. 2011;43(2):447-458.
246. Wang J, Janisch R, Madsen GKH, Drautz R. First-principles study of carbon segregation in bcc iron symmetrical tilt grain boundaries. Acta Mater. 2016;115:259-268.
247. Aksyonov DA, Lipnitskii AG, Kolobov YR. Grain boundary segregation of C, N and O in hexagonal close-packed titanium from first principles. Model Simulat Mater Sci Eng. 2013;21(7):075009.